UNIVERSITY OF CALIFORNIA, MERCED

Atomic-Scale Surface Engineering for Enhancing Electrochemical Performance and Improving the Durability of Solid Oxide Cells

Submitted to the School of Engineering
In partial fulfillment of the requirement for
the degree of Doctor of Philosophy

in

Mechanical Engineering

by

Haoyu Li

Committee Members:
Prof. Mehmet Baykara
Prof. Abel Chuang
Prof. James Palko
Prof. Min Hwan Lee

SIGNATURE PAGE

The dissertation of Haoyu Li was prepared under the direction of the candidate's dissertation advisor, Prof. Min Hwan Lee, Department of Engineering, and has been approved by the members of his supervisory committee.

_____

Prof. Mehmet Baykara, Chair, and Committee Member

_____

Prof. Abel Chuang, Committee Member

_____

Prof. James Palko, Committee Member

_____

Prof. Min Hwan Lee, Ph.D. advisor, and Committee Member

TABLE OF CONTENTS

LIST OF TABLES

LIST OF FIGURES

activation energies (E_a); (b) Bare, Ce_{Inf} (Type I) and Ce_{ALDn} series (Type II), (c,d) $Ce_{Inf}Ce_{ALDn}$ and $Ce_{Inf}Y_{ALDn}$ series (Type III-A) and (e) $Ce_{Inf\text{-}sint}Y_{ALD3}$ and $Ce_{Inf\text{-}sint}Ce_{ALD6}$ (Type III-B). All the corresponding EIS curves and Arrhenius plots are provided in Fig. 4.11. (f) Reaction order (m) values obtained at 700 °C; the corresponding R_p versus pO_2 graphs presented in Fig. 4.12. The inset shows the parametric meaning of m; pO_2 is the partial pressure of O_2 applied to the cell during measurements.

Fig. 4.11 EIS curves and Arrhenius plots (inset). In the insets, the activation energies (E_a) of each sample are calculated from the least square fitting of R_p values with temperature. (a) Bare, Ce_{Inf} and Ce_{ALDn} series, (b) $Ce_{Inf}Ce_{ALDn}$ series (c) $Ce_{Inf}Y_{ALDn}$ series and (d) the samples sintered before ALD ($Ce_{Inf\text{-}sint}Y_{ALD3}$ and $Ce_{Inf\text{-}sint}Ce_{ALD6}$).

Fig. 4.12 Partial pressure dependency of polarization resistances measured at 700 °C.

Fig. 4.13 A schematic diagram of possible ORR pathways in a LNF/GDC system. $(O_2)_s$ and $(O)_s$ refer to O_2 and O adsorbed on the electrode surface, respectively; TPB stands for triple phase boundary.

Fig. 4.14 (a) Time evolution of polarization resistance (R_p), (b) characteristic frequency (f_c), and (c) capacitance (C). All are deduced from the impedance data, which were obtained intermittently at the open circuit condition during the thermal exposure at 700 °C.

Fig. 4.15 (a) An exemplary SEM image taken from $Ce_{Inf}Ce_{ALD6}$ (a,b), and (b) a close-up image in the dotted area in (a). The size of the nanoparticle defined by the black line was estimated by drawing a red circle. The resulting diameter of the red circle was quantified as the particle size.

Fig. 4.16 (a,b) Exemplary SEM images taken from two different areas of a $Ce_{Inf}Ce_{ALD6}$ sample and the resulting particle size distributions (c) and d_{20}, d_{50} and d_{80} values.

Fig. 4.17 (a-e) Size distribution of infiltrated ceria NPs in each sample after 2 h and 260 h at 700 °C, and (f) the corresponding accumulative distribution of infiltrated ceria NPs, counting from smaller NPs. Graphs are based upon the SEM images provided in Fig. 4.18 and Fig. 4.19

Fig. 4.18 (a-e) SEM micrographs of 5 different samples at the initial stage of thermal stress (after 2 h at 700 °C). (f) Accumulative number of particles versus particle size, counting from those with smaller particle size.

Fig. 6.14 (a) I-V curve of all the samples. (b) Nyquist plot of all the samples (in electrolysis cell mode) and the equivalent circuit used for fitting. (c) DRT plot of all the samples. (d) Durability test at 500 mA cm^{-2}. Evolution of fitted (e)R_H and (f)R_L over time. All the sample is tested at 700 ºC with 50% RH of hydrogen in the fuel electrode and 21% Oxygen/ 79% Nitrogen in the air electrode.

Fig. 6.15 Evolution of fitted (e)C_H and (f)C_L over time.

ACKNOWLEDGEMENT

Haoyu Li (HL) would like to acknowledge the following individuals, organizations, grants.

This work is supported by the National Science Foundation (DMR 1753383) and NASA MIRO program (Grant No. NNX15AQ01A).

HL acknowledges the MACES program for the support in the summer section.

HL acknowledges Dr Art J. Nelson for his contribution on XPS measurement and precious advice in Chapter 4.

The text of this dissertation is a reprint of the material as it appears in J. Mater. Chem. A and Int. J. Hydro. Energy. The co-authors are listed as follows:

Dr. Hung-Sen Kang (University of California, Merced)
Dr. Ziqi Liu (University of California, Merced)
Dr. Simranjit Grewal (University of California, Merced)
Orbel Barkhordarian (University of California, Merced)
Dr. Art J. Nelson (Lawrence Livermore National Laboratory)
Suhan Lee (Korea Advanced Institute of Science and Technology)
Yongjin Yoon (Korea Advanced Institute of Science and Technology)
Shin Ae Song (Korea Institute of Industrial Technology)
Dr. Min Hwan Lee (University of California, Merced)

HL would like specially thanks to the visiting scholars Dr. Dohyun Go, Dr. Hyong June Kim, and their PI, Dr. Jihwan An, from Seoul National University of Science and Technology for providing valuable information about the solid oxide fuel cell testing station and thermal atomic layer deposition system.

HL would like to thank for the support from his family, his mother Xin Shen as well as his father Baochun Li.

HL would like to express heartfelt gratitude to his wife, Anni Zhao, for her unwavering support and companionship throughout his Ph.D. journey. Anni serves as an inspiring role model in all aspects of life from academics to personal growth and research pursuits.

Lastly, HL would like to express his deepest gratitude to Prof. Min Hwan lee for serving as his esteemed Ph.D. advisor and providing invaluable guidance throughout the Ph.D. journey. Prof. Lee's unwavering patience and utmost respect have been truly inspiring. HL is deeply honored and grateful for the privilege fo being his student.

CURRICULUM VITAE

Contact : (209) 564-0649 | hli84@ucmerced.edu | https://haoyuli.me

EDUCATION

University of California, Merced Merced, CA
Ph.D. Candidate in Mechanical Engineering
September 2017 - present

- Advisor: Prof. Min Hwan Lee
- Research Topic: Atomic-scale surface engineering for solid oxide fuel cells/electrolysis.
- Degree expected in May 2023

Drew University Madison, NJ
B.A. in Physics
May 2013 – May 2017

- Baldwin Honors Scholarship: Awarded annually to undergrad students in an excellent academic standing.

Project Experience @E^{2}C lab

Surface engineering on solid oxide electrolysis cells (SOECs)
Nov 2022 - Present

- Utilized *plasma-enhanced* atomic layer deposition (PE-ALD) as the tool to introduce precious metals on the surface of either the fuel side or air side of a cell.
- Revealed the distinct effectiveness of ultra-thin layer of metallic catalysts in enhancing the kinetics of oxygen electrocatalysis and durability.
- Performed a mechanistic study to explain the underlying phenomena using various physicochemical characterization techniques.

Engineering solid oxide electrolysis cell test apparatus
Jan 2022 – Nov 2022

- Designed and implemented SOEC test stations.
- Successfully performed test-runs in a full-cell SOEC mode for both short-term and long-term tests without a concentration loss or voltametric fluctuations.

Building a thermal atomic layer deposition (ALD) system
Aug 2022 – Jan 2022

- *Built* an in-house thermal ALD system from scratch; designed, parts acquisition, assembly, and testing.
- Initially demonstrated a true ALD mode deposition with Zr precursor; now routinely used for Y_2O_3, ZrO_2, TiO_2, CeO_2, and CoO_x deposition.

Mechanism study of cation segregation of perovskite electrodes
Dec 2019 – May 2021

- Established hypotheses on the driving force of A-site dopant segregation to understand the behavior, which is a major problem against cell durability.
- Performed atomic-scale surface treatment by ALD to address the issue successfully.
- Proposed segregation mechanisms by performing data collection, analysis, and interpretation of the atomic-level treatment effect on cation segregation (specifically of Sr) by using X-ray photoelectron spectroscopy (XPS) as the main tool.

Surface engineering of solid oxide fuel cell electrodes
May 2018 – Nov 2019

- Performed surface treatment of SOFC cathodes by a wet process (e.g. impregnation) and/or ALD.
- Demonstrated the beneficial effect of additional atomic-scale ALD overcoat in further enhancing electrode kinetics and durability.
- Correlated the relationship among cell durability, electrode microstructure, and surface chemistry in a quantitative manner.

Instrumentation of Cr-free test station
May 2018 – May 2020

- Successful *i*nstrumentation of a Cr-free test station for SOFC/SOEC characterization; design, assembly, and testing.

Publications

- **H. Li**, H. Kim, J. An, M.H. Lee, "Ultra-load metallic ruthenium on solid oxide electrolysis cells by plasma-enhanced atomic layer deposition" (in preparation)
- **H. Li**, T. Garcia, H. Kim, D. Go, M. Bonab, J. An, M.H. Lee, "Surface and interface engineering for air electrode of solid oxide electrolysis cells"(in preparation)
- Z. Liu, **H. Li**, H.-S. Kang, A. T. N'Diaye, M. H. Lee, "Lattice oxygen-mediated Ni-O-O-Co formation for efficient oxygen evolution reaction in MOF@LDH core-shell structures", *Chemical Engineering Journal*, 454, 140403, 2023
- **H. Li**, H.-S. Kang, Z. Liu, O. Barkhordarian, S. Lee, Y. Yoon, M. H. Lee, "Effect of angstrom-level oxide overcoat on Sr segregation behavior of LSM electrodes", *International Journal of Hydrogen Energy*, 47, 33058, 2022
- Z. Liu, A. Macedo Andrade, S. Grewal, A. J. Nelson, K. Thongrivong, H.-S. Kang, **H. Li**, Z. Nasef, G. Diaz, M. H. Lee, Trace amount of ceria incorporation by atomic layer deposition in Co/CoO_x-embedded N-doped carbon for efficient bifunctional oxygen electrocatalysis: demonstration and Quasi-Operando observations, *International Journal of Hydrogen Energy*, 46, 38258, 2021
- D. Kim, **H. Li**, M. H. Lee, K. Kim, S. N. Lim, J. Y. Woo, H. Han, S. A. Song, Improved performance and stability of low-temperature, molten-carbonate fuel cells using a cathode with atomic layer deposited ZrO_2, *Journal of Power Sources*, 484, 229254, 2021
- **H. Li**, H.-S. Kang, S. Grewal, A. J. Nelson, S. A. Song, M. H. Lee, How an angstrom-thick oxide overcoat enhances durability and activity of nanoparticle-decorated cathodes in solid oxide fuel cells, *Journal of Materials Chemistry A*, 8, 15927, 2020
- H.-S. Kang, S. Grewal, **H. Li**, M. H. Lee, Effect of surface-specific treatment by infiltration into $LaNi_6Fe_4O_{3-d}$ cathodic backbone for solid oxide fuel cells, *Journal of The Electrochemical Society*, 166, F255, 2019

Book Chapter

- **H. Li**, T. Garcia, M. H. Lee, "SOFCs for vehicles", in Book "Fuel Cells for Transportation" edited by P. K. Das, in print, 2023

Conference and Presentation

- **H. Li**, T Garcia, H. S. Kang, Z. Liu, and M. H. Lee, Effect of Atomic-Scale Surface Overcoat By Atomic Layer Deposition on Dopant Segregation of Perovskite Cathodes, 242nd ECS 2022 (oral)

- **H. Li**, O. Barkhordarian, H. Kang, M. H. Lee, Atomic-Scale Surface Overcoat to Suppress Agglomeration and Dopant Segregation of Perovskite Cathodes, SSI-23 2022 (oral)
- Z. Liu, **H. Li**, T. Garcia, M. H. Lee, Atomic Dispersed Ce/Ti Onto Layered Double Hydroxide Substrate Via Atomic Layer Deposition for Efficient Oxygen Evolution Reaction, 242nd ECS 2022 (poster)
- H.S. Kang, T. Garcia, **H. Li**, Z. Liu, and M. H. Lee, Localized Surface Oxygen Ion Transport in STO and YSZ Observed Via Quasi in Situ Scanning Probe Microscopy, 242nd ECS 2022 (poster)
- **H. Li**, H.S. Kang, S. Grewal, M. H. Lee, Atomic-scale metal oxide overcoat on decorated ceria nanoclusters for enhanced performance and durability of solid oxide fuel cell cathodes, PRiMes 2020 (oral)
- **H. Li**, H.S Kang, A. Karimaghaloo, M. H. Lee, Atomic Layer Deposition Treatment on Infiltrated Cathodes for Solid Oxide Fuel Cells, *AiMES* 2018 (poster)
- H.S Kang, **H Li**, M.H. Lee, Comparative Study: Effect of various wet impregnations into LNF cathodic backbone for solid oxide fuel cells. *AiMES* 2018 (oral)

Teaching experience

As a Teaching Assistant

- **ME 021: Engineering Computing**
- **ME 137: Computer-Aided Engineering**
- **ENGR 057: Statics and Dynamics**
- **ENGR 065: Circuit Theory**
- **ENGR 135: Heat Transfer**

Technical Skills

Instrumentational:
Building customized SOFC/SOEC test stations
building thermal atomic layer deposition (ALD) systems
Fabrication tool:
Vacuum processes (e.g., atomic layer deposition, metallic sputtering)
Wet processes:
(e.g., screen printing, tape casting, infiltration, spin coating, ball milling), die-pressing
Electrochemical characterization:
potentiostat/galvanostat/EIS
Material characterization:

SEM, Angle-resolved XPS, XRD, TEM, TEMEDS

Computer:

MATLAB, Python, PowerPoint, Microsoft Excel, Origin Pro

ABSTRACT

Solid oxide cells (SOCs) have emerged as a promising electrochemical energy conversion and storage device, especially for large-scale applications, due to their high efficiency, fuel flexibility, and reversibility between fuel cell and electrolysis modes. However, the high operational temperature poses durability challenges, and lowering the operating temperature significantly reduces the catalytic activity, particularly in the oxygen reduction reaction (ORR) and oxygen evolution reaction (OER) occurring in air electrodes. La-based perovskites with an A-site dopant ($La_{1-x}A'_xBO_3$) are commonly employed as the air electrode owing to their high electrochemical kinetics and decent chemical stability in oxidizing environment. In this dissertation, I demonstrate that an atomically thin oxide overcoat on perovskite-based air electrodes can simultaneously address two key degradation processes: agglomeration and dopant segregation, while enhancing the electrode surface kinetics for both ORR and OER. The overcoat provides mechanical stabilization and suppresses the agglomeration of the perovskite nanoparticles, while simultaneously limiting A-site dopant segregation toward the electrode surface.

Firstly, I show that an atomic layer deposition (ALD) overcoat facilitates the ORR kinetics and improves cell durability. By employing an angstrom-level CeO_2 and Y_2O_3 overcoat via ALD on a ceria nanodot-decorated $LaNi_{0.6}Fe_{0.4}O_{3-\delta}$ (LNF) air electrode, we demonstrate that the angstrom-level metal oxide overcoat is highly effective in suppressing the nanodot agglomeration and enhancing the ORR kinetics.

Secondly, I demonstrate that an ALD overcoat of a specific type of oxides suppresses A-site dopant segregation effectively. I apply a ~ 2 Å thick metal oxide ALD coating (ZrO_2, Y_2O_3, CeO_2 and TiO_2) on a $La_{0.8}Sr_{0.2}MnO_{3-\delta}$ (LSM) air electrode and quantify the Sr segregation behavior and ORR kinetics for 250 h at 750 ºC. Results reveal that a coating of metal oxide with multi-valent cations lead to a suppression of surface segregation or even de-segregation of Sr from the electrode surface. The oxygen vacancies formed on the perovskite surface by the ALD treatment are identified as the key to controlling Sr segregation.

Lastly, I demonstrate that an ALD overcoat with metallic Ru catalyst (7.5-20 Å in nominal thickness) enhances both ORR and OER kinetics and preserves cell durability under electrolysis mode when applied on a conventional $La_{0.6}Sr_{0.4}Co_{0.2}Fe_{0.8}O_{3-\delta}$ (LSCF) air electrode via plasma-enhanced ALD (PE-ALD). The Ru catalyst reacts with surface-segregated Sr species, forming a secondary perovskite phase that suppresses further Sr segregation and improves cell stability.

These findings highlight the potential of surface engineering to effectively enhance the performance and durability of both solid oxide fuel cells (SOFCs) and solid oxide electrolysis cells (SOECs).

Chapter 1: Introduction and Objectives

1.1 Importance of Hydrogen

The increasing awareness of the adverse impact of green-house gas emissions, mostly carbon dioxide (CO_2), on the environment and human health has accelerated the global push for sustainable energy solutions. As shown in **Fig. 1.1**, the amount of CO_2 emission exponentially increases over the past decades, a transition towards a sustainable and low-carbon society is extremely necessary. As the world shifts away from carbon-based fuels, hydrogen (H_2) has emerged as a promising alternative due to its versatility, abundance, and potential to transition to a low-carbon economy.

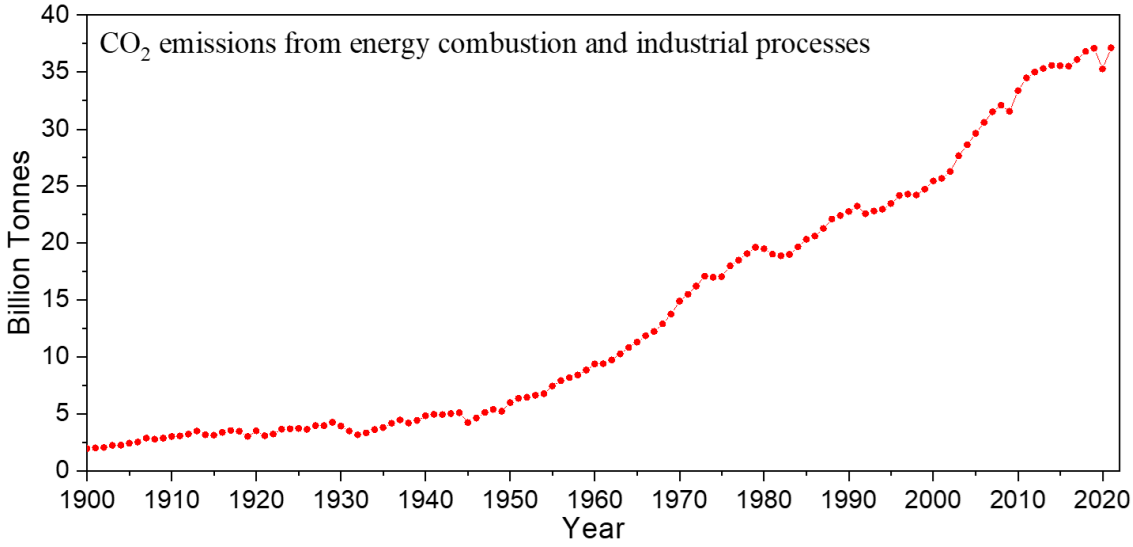

Fig 1.1 CO2 emissions from energy combustion and industrial processes over years

Hydrogen is an energy-dense (120.2 MJ kg^{-1}), clean fuel that emits only water as the by-product when either by combustion or electrochemical reaction. It can be produced from various renewable energy sources, such as wind and solar, making it a potential carrier of renewable energy. According to the International Renewable energy Agency (IRENA), hydrogen from renewable sources accounted for 5% of the overall final energy usage, with 16% of total electricity generation being devoted to producing hydrogen in 2025, reducing annual CO_2 emissions in gigatons scale[3]. Hydrogen can also be used to store and transport energy generated from intermittent renewable sources, which is much lighter and cheaper compared to lithium-ion batteries for large-scale applications, thereby addressing the challenges of energy storage and grid balancing. Furthermore, fuel/electrolysis cells can be used to convert between electricity and hydrogen with a high efficiency, providing a zero-emission alternative for various applications, such as transportation, power generation, and large-scale industrial applications. The potential of hydrogen is expected to grow substantially in the coming decades as many countries try to meet their requirements on climate goals and transition to low-carbon societies. Besides the usefulness in addressing climate

change, hydrogen can be used as a feedstock to produce synthetic fuels and chemicals, further reducing the demand on fossil fuels.

Fuel cells and electrolysis cells, especially solid oxide fuel cells (SOFCs) and solid oxide electrolysis cells (SOECs), are crucial to unlock the potential of hydrogen as an energy carrier. Solid oxide cells (SOCs, combination of SOFCs and SOECs) are fuel/electrolysis cells operating at elevated temperatures (600 - 900 ºC), in which electrochemical reactions are significantly enhanced, allowing use of relative cheap and abundance materials as the catalysts. SOFCs are electrochemical devices that convert the chemicals stored in a fuel (most notably, hydrogen) to electrical energy, with efficiency up to 60% or higher. They offer a promising solution for stationary power generation and can be integrated into large-scale projects, providing clean and reliable electricity. SOECs, on the other hand, use electricity to generate hydrogen and oxygen by water splitting, enabling the production of green hydrogen directly from renewable energy sources. The electrochemical processes are intrinsically efficient thanks to the high operating temperature, thereby there is a high potential of reducing the costs compared to low-temperature electrolysis cells. By integrating SOECs with renewable energy systems, hydrogen can be produced without the emission of CO_2 gas, supporting the decarbonization goal.

1.2 Recent Progress and Projects

The global SOFC market was valued at $339.8 million in 2021 and is projected to reach approximately $10 billion by 2030, growing at a compound annual growth rate (CAGR) of 40.7%[4]. The U.S. Department of Energy's SOFC program has invested over hundreds of millions of dollars since 2000 to advance the development of SOFC technology. Many projects have been performed, affording commercial products including Blooming Energy server (Bloom ES-5700), a 200 kW SOFC system with net electrical efficiency as high as 50%. The investments are not limited to the US. For example, South Korea has announced plans to produce 1 gigawatt (GW) of power using fuel cells by 2022, with plans to expand the capacity to 15 GW by 2024[5]. Furthermore, SOFCs have gained significant attention in the transportation sector, particularly for large-scale applications with long transport distances, such as heavy-duty trucks, maritime vessels, railways, and even aircrafts.

On the other hand, SOEC market is still in the early stages, Cummins, Inc. had been supported by U.S. Department of energy (DOE) for the development of a 100 MW SOEC system for hydrogen production[6]. The project, known as Hydrogen from Next-generation Electrolyzers of Water (H2NEW), aims to accelerate the development of cost-effective and efficient SOEC technology, targeting an electrolysis system cost of less than $2 per kilogram of hydrogen by 2025. The European commission's Horizon 2020 program had funded several SOEC projects, including the GrlnHy2.0, that focuses on integrating a 720 kW SOEC system into an operational steel plant in Germany, aiming to achieve a stack lifetime of more than 10,000 hours with overall efficiency over 80%.

The growing attention in SOCs has led to numerous international collaborations and initiatives, stimulating the development of SOC technology. The international Partnership for Hydrogen and Fuel Cells in the Economy (IPHE), established in 2003, is a leading global initiative that focuses on fostering the widespread adoption and development of hydrogen and fuel cell technologies, including SOCs. IPHE is comprised of 20 member countries, including the United States, China, Germany, Japan, South Korea, and others. The IPHE was established to facilitate the exchange of information, joint project development, and policy creation aimed at promoting the hydrogen economy. The collective efforts of these initiatives demonstrate a significant level of interest in advancing SOC technologies.

1.3 Challenges and Personal Perception

1.3.1 Challenges

A SOFC is an advanced electrochemical device that converts chemical energy from fuels like H_2 and CH_4 into electrical power with high efficiency. However, the commercialization of SOFCs has been impeded by the high operational temperatures (700°C - 900°C), which result in considerable challenges in securing decent durability. Multiple factors affect the overall cell efficiency, with the electrochemical activity and material integrity of the electrodes being particularly critical. Perovskites have been employed in the fabrication of SOFCs for many years, and pure metals, such as Pt and Ag, have predominantly been utilized in fundamental investigations of oxygen reaction reactions (ORR). More recently, metal electrode has also been incorporated into low-temperature micro-SOFCs[7,8]. Despite their application in these technologies, all such materials exhibit a significant decline in performance during prolonged, high-temperature operations.

There are three main mechanisms that cause the degradation of a fuel cell electrode. Firstly, the agglomeration of porous electrode is a significant issue at high temperatures. When agglomeration occurs, the surface area-to-volume ratio decreases significantly, leading to the decrease of active sites and thus the electrode performance. Karimaghaloo et al.[9] found that the high degradation of the Pt cathode at 600 °C is a result of the severe agglomeration. In addition, Matsui et al. reported that porous $La_{0.6}Sr_{0.4}Co_{0.2}Fe_{0.8}O_{3-\sigma}$ (LSCF) also experiences a significant particle agglomeration under high temperature operation[10]. Secondly, the segregation of A-site dopants in a perovskite (ABO_3, widely used for cathodes) is another factor of performance degradation. Sr, the usual A-site dopant, segregates to the surface of the lattice to form SrO or $Sr(OH)_2$, blocking the active surface layer and denying access to reactant (O_2)[11]. Different ideas were developed to explain the driving force of dopant segregation. Ja et al.[12] used both density functional theory (DFT) calculation and experimental results to demonstrate the effect of elastic strain caused by A-site dopants on the segregation effect. Alternatively, Sr segregation has been widely ascribed to the electrostatic interactions between positively charged oxygen vacancies and negatively charged Sr

cations[13]. Finally, interconnectors of SOFCs, which are made of alloys with high-temperature oxidation resistance, contain chromium (Cr) that forms a protective chromium oxide[14]. Cr-containing vapor species, such as CrO_3 and $CrO_2(OH)_2$, would form by combining oxygen or water vapor and be deposited on the cathode, blocking the surface. This will reduce the electrochemically active layer on the surface by prohibiting the adsorption of O_2 reactants.

On the other hand, a SOEC operates by reversing the reactants and produces of a SOFC. This results in the conversion of electrical energy into chemical energy, stored in the form of molecules such as H_2 or CH_4. However, as the development of SOECs is still in its early stages, the materials and structure utilized are similar to those used in SOFCs. As a result, SOECs not only face the same degradation challenges, such as particle agglomeration, cation segregation, and electrode poisoning, as SOFCs, but also have additional difficulties due to the high operating voltage (1.2-1.5V). The most pressing issue facing SOECs, but not SOFCs, is delamination between the air electrode and electrolyte. Theories suggest that this delamination may be caused by the accumulation of oxygen partial pressure in the interface [15], new phase formation[16], formation of nanoparticles[17], and external mechanical stress [18,19]. Furthermore, the degradation of SOECs is even more difficult to suppress due to the high operating voltage, which can further promote particle agglomeration and cation segregation. Additionally, perovskite materials, widely used in SOFCs, are designed for oxygen reaction reactions (ORR) and thus have limited kinetic for oxygen evolution reactions (OER), hindering the cell performance.

1.3.2 Advantages of surface treatments

Many techniques have been developed to enhance the performance and stability of electrodes in SOCs. The primary aim of research in this area is to achieve a high kinetics and maintain it without decreasing over time. One of the main challenges in achieving this is the poor stability of the electrode, which is primarily caused by thermal agglomeration and A-site dopant segregation. While this problem can be addressed by reducing the working temperature, the kinetics of the electrode drops exponentially with decreasing temperature. Therefore, it is critical to find alternative highly active materials or additional effective treatments to address this problem.

Currently, perovskites (or double perovskites) with Sr-doped La on A-site and transition metals on B-site are the state-of-the-art materials used for cathode electrodes. It is challenging to find materials that match the thermal expansion coefficient (TEC) of the electrolyte while simultaneously providing an order of magnitude increase in performance. However, applying additional surface treatments to existing materials can maintain the bulk material's physics properties while eliminating the need for a matching TEC between the bulk and surface treatment materials. Furthermore, certain perovskite materials, such as LSC, exhibit excellent performance but experience a decrease in kinetics by an order of magnitude after only a few hours of operation. Therefore, it is more practical to investigate the degradation mechanics and develop

preventative measures rather than searching for new materials. Analytical studies are crucial for uncovering the underlying mechanisms of degradation and identifying factors hindering electrode kinetics. Experimental research is equally critical due to the complexities of real-world scenarios and the impracticality of extensive calculations. In some cases, experimental results exhibit contrary behaviors to what was anticipated.

In my opinion, the exploration of novel materials for SOCs is a time-intensive endeavor, with a high likelihood of encountering recurring issues, such as exceptional performance coupled with poor thermal stability. The widespread commercialization of SOCs is currently hindered by this thermal instability, making it critical to identify the factors contributing to degradation and develop methods to mitigate it.

1.4 Research Approaches and Achievement

Two types of surface engineering have been employed to enhance the durability of perovskite-based cathodes in the study of SOFCs. The first approach addresses the issue of thermal agglomeration among nanoparticles that constitute the cathode backbone, while the second tackles the problem of Sr segregation. Surface engineering has been applied to address these issues related to cell performance and degradation.

The first approach for the SOFC project involves preparing a cathode material without an A-site dopant, $LaNi_{0.4}Fe_{0.6}O_{3-\sigma}$ (LNF), as the backbone to eliminate dopant segregation as a factor of electrode degradation. By selecting an A-site dopant-free electrode, the focus could be placed on the effect of electrode agglomeration. Two types of surface treatments, sol-gel impregnation (infiltration) and atomic layer deposition (ALD), were applied independently or in combination throughout the experiment. Long-term durability and catalytic activity were assessed to determine the effectiveness of each surface treatment. The results revealed that a single-step infiltration of $Ce(NO)_3$ solution yielded a ten-fold enhancement in performance, while a single-step ALD of CeO_2 resulted in a five-fold improvement. Interestingly, by applying an additional ALD treatment to the infiltrated sample, performance could be further enhanced, while the activation energy and polarization resistance displayed minimum values at specific deposition cycles (three cycles of Y_2O_3 and six cycles of CeO_2). Regarding durability, the sample with ALD exhibited extraordinary thermal stability over 250 h, whereas the sample with only one-step infiltration displayed extreme degradation after the first 150 h, suggesting that coating the surface with a few angstroms of metal oxide can maintain and enhance performance.

In the second approach for the SOFC project, a Sr-doped material, $La_{0.8}Sr_{0.2}MnO_{3-\sigma}$ (LSM), was utilized as the backbone, and four different metal oxides (TiO_2, CeO_2, ZrO_2 and Y_2O_3) were deposited by ALD to evaluate how an atomically thin layer of various oxides would affect the migration behavior of Sr species and performance stability. It was hypothesized that increasing oxygen vacancies on the surface with bivalent-state oxides would facilitate Sr incorporation, while reducing Sr segregation with oxides with single-valent cations. After quantifying the amounts of Sr

and oxygen vacancies on the surface over time, it was found that the Sr concentration decreased with TiO_2 or CeO_2 overcoat, whereas the concentration remained nearly unchanged with ZrO_2 or Y_2O_3 ALD. As for the cell durability, the bare LSM sample exhibited significant degradation over 250 h, but the sample with ALD demonstrated considerable thermal stability over an extended period. Surprisingly, the cell performance increased by 10%-15% within the first 50 h of testing for samples treated with bivalent-state oxides overcoat, which correlated positively with the Sr incorporation mechanism.

In the approach for the SOEC project, an ultra-thin overcoat of metallic Ru catalyst was deposited on $(La_{0.6}Sr_{0.4})_{0.95}Co0.2Fe_{0.8}O_{3-\sigma}$ (LSCF) using plasma-enhanced ALD (PE-ALD), focusing on both ORR and OER as well as durability behavior in electrolysis mode for intermediate-temperature SOCs (IT-SOCs). LSCF is a conventional commercialized air electrode with low catalytic activity and is prone to Sr segregation[20]. Ru is a widely utilized noble metal for low-temperature solid oxide fuel cells (LT-SOFCs), mainly in fuel electrodes [21–23]. According to the volcano theory for OER, RuO_2 is the best candidate among various metal oxide catalysts (e.g., TiO_2, PtO_2, NiO, etc.)[24,25]. Electrochemical, physical, and surface-specific characterization revealed that even an angstrom-thick Ru overcoat significantly enhances both ORR and OER kinetics. Intriguingly, Ru tends to react with surface-segregated Sr species, forming a secondary perovskite phase that suppresses further Sr segregation and improves cell durability. Moreover, detailed electrochemical measurements were obtained throughout the durability test, demonstrating that the additional secondary phase is highly effective in maintaining oxygen desorption activity in the electrolysis mode.

In summary, my research primarily focuses on enhancing the durability of perovskite-based air electrodes and improving cell performance for SOCs. The first approach addressed thermal agglomeration and electrode degradation by utilizing surface treatments such as sol-gel impregnation and ALD. Results show that a combination of these treatments considerably augmented performance and increased durability over 250 h. The second approach involved depositing different metal oxides onto a Sr-doped material to evaluate their impact on Sr migration behavior, particle size, and performance stability. The results indicated that certain ALD treatments enhanced thermal stability and cell performance, while others controlled Sr segregation. In the SOEC project, I investigated the effect of sparsely deposited metallic Ru catalysts on a conventional air electrode using PE-ALD and found that even an angstrom-level Ru overcoat significantly improves both ORR and OER. The Ru catalyst reacted with surface-segregated Sr species forming a secondary perovskite phase that suppressed further Sr segregation and improved cell sustainability. These results demonstrate the effectiveness of surface engineering in enhancing the performance and durability of both SOFCs and SOECs.

Chapter 2: Background and Characterization Skills

2.1 Short History of SOFC/SOEC Development

The fuel/electrolysis cell has long been recognized as a promising technology for a clean energy society. Among various types of fuel/electrolysis cells, solid oxide cells (SOC, a combination of SOFCs and SOECs) have garnered significant attention due to their high efficiency, fuel flexibility, and reversibility using a single system. As a result, SOCs have emerged as a promising technology for using hydrogen or other chemical substances as the energy carrier for electricity, without the extra production of harmful by-products, such as CO_2, known as the greenhouse gases causing global warming.

The development of SOFCs can be traced back to the 1930s when Baur and Preis observed oxygen ion conduction in zirconia, which set the foundation for the discovery of the first solid electrolyte materials, stabilized zirconia[26]. In the following 1950s and 1960s, researchers at Westinghouse Electric Corporation pioneered the development of SOFCs, with yttria-stabilized zirconia (YSZ) as the electrolyte material, and developed the first functional prototype for SOFCs. With such success, the first SOEC was developed in the 1980s, taking advantage of the reversibility of SOCs. Researchers realized the potential of high-temperature electrolysis using solid oxides as materials. It required less energy and preserved higher efficiency than conventional low-temperature electrolysis (which all require a relatively high voltage to initiate the production process).

Between the 1990s and 2000s, because of the low ionic conductivity of YSZ, even in elevated temperatures (>800 ºC), researchers tried to enhance the performance, and decrease the operating temperatures by exploring alternative electrolyte materials. As a result, ceria-based electrolytes, like gadolinium-doped ceria (GDC) and samarium-doped ceria (SDC), emerged as the potential alternative to YSZ. However, due to the cost and additional electronic cross-over for the ceria-based materials, the commercialization of SOCs becomes nearly impossible.

Due to the high demand for clean energy, an exponent amount of research has been done to improve the performance and study the mechanism behind chemistry. First, pure metallic electrodes, such as Platinum, had changed to perovskite with sponge-like porous, such as $LaNi_{0.6}Fe_{0.4}O_3$(LNF) and $La_{0.8}Sr_{0.2}MnO_3$(LSM). Then, mixed ionic-electronic conducting (MIEC) materials, such as $La_{0.6}Sr_{0.4}Co_{0.2}Fe_{0.8}O_3$ (LSCF) and $A_2B_2O_7$ (pyrochlores), were developed to further improve the electrocatalytic activity and performance. Nanostructure electrodes are evolving as a new trend in improving cells performance and the cells durability. In addition, surface engineering has become a handy tool to enhance surface chemistry, thus enhancing the catalytic activity for SOCs applications.

2.2 SOFC Primer

2.1.1 Reactions in SOFCs

A fuel cell is an electrochemical device that directly converts chemical energy, such as H_2 and CH_4, to electrical energy. Unlike combustion engines, which convert chemical energy to electrical energy via thermal energy, fuel cells are highly appealing due to their superior energy-conversion efficiency. SOFCs are of particular interest to researchers because they offer several advantages over other fuel cell types. All the components in the SOFC system are made of solid metal oxides, which exhibit chemical and mechanical stability. In addition, under operating temperatures (700-900 °C), SOFCs not only demonstrate higher efficiency, but also recycle the excess heat generated within the system to maintain their operating temperature. However, the high cost and limited lifetime of SOFC systems, resulting from unfavorable stability at such elevated temperatures, impede further development of this promising power generation method.

The fundamental components of the SOFC system, as depicted in **Fig. 2.1**, include the cathode, electrolyte, and anode. Unique among other types of fuel cell, the SOFC utilizes a solid electrolyte composed of a highly dense material that prevents gas penetration. The cathode and anode materials are typically porous, maximizing the contact area with gaseous reactant. **Fig. 2.1** illustrates the processes by which SOFCs generate power. Oxygen is introduced to the cathode side, where it is accompanied by electrons and reduced to oxygen ions (**Eqn. 2.1**) at the electrode. Subsequently, the

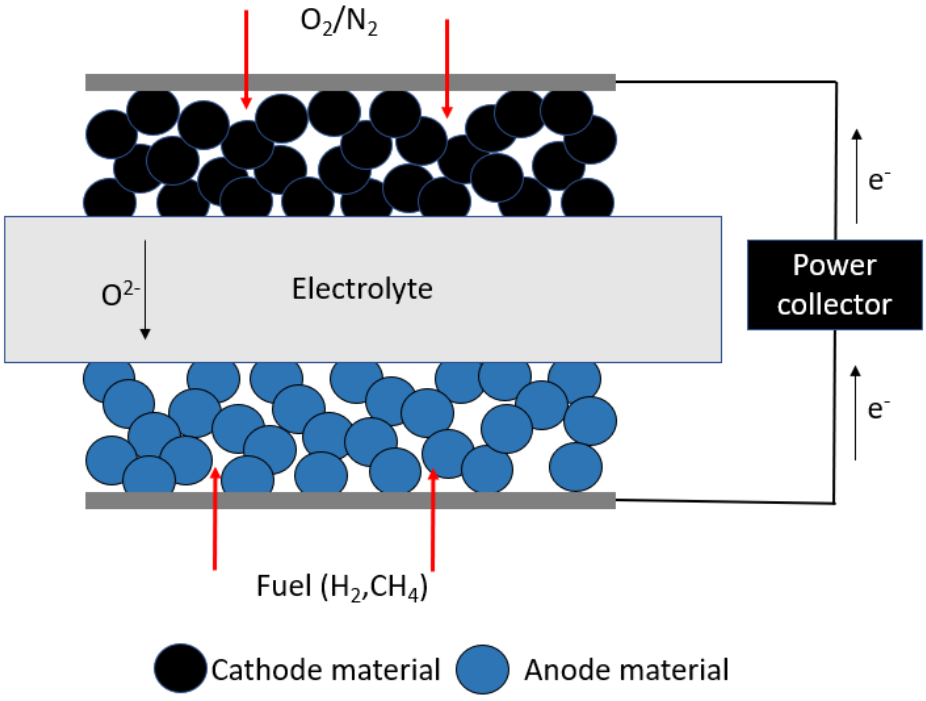

Fig 2.1 General layout of SOFC

oxygen ions migrate to the electrolyte, either from the surface or through the bulk of the cathode.

$$O_2 + 4e^- \rightleftarrows 2O^{2-} \tag{2.1}$$

Hydrogen or other hydrocarbons (e.g., methane) utilized as fuel is supplied to the anode, where it combines with oxygen ions that are transported from the electrolyte. This reaction results in the formation of water and electrons (**Eqn. 2.2 and 2.3**).

$$2H_2 + 2O^{2-} \rightleftarrows 2H_2O + 4e^- \tag{2.2}$$

$$\frac{1}{2}CH_4 + 2O^{2-} \rightleftarrows 2H_2O + \frac{1}{2}CO_2 + 4e^- \tag{2.3}$$

Electrolytes are composed of materials featuring high oxygen ion conductivity and minimal electron conductivity, ensuring the electrical current is exclusively directed through the power generator. The latest advancements in SOFC materials and their properties can be found in **Table 2.1**.

2.2.2 SOFC driving forces and performance

For electrical current to flow, a driving force is required. Similar to how a stream flows from a higher to lower elevation due to gravitational potential, the current in an electrochemical cell is driven by the electrical potential established by the differences in the electrode potential specific to the reactions in each electrode. Using O_2-H_2 system as an example, its overall reaction formula can be expressed as follows:

$$H_2 + \frac{1}{2}O_2 \rightleftarrows 2H_2O \tag{2.4}$$

In this reaction, the standard-state Gibbs-free-energy is -237 kJ/mol for liquid water as the product.

$$E^0 = -\frac{\Delta \hat{g}^0_{rxn}}{nF} \tag{2.5}$$

where E^0 is the standard-state reversible voltage and $\Delta \hat{g}^0_{rxn}$ is the standard-state free-energy change for the reaction with the number of electron transfers (n) and Faraday constant (F). At standard temperature and pressure (300 °K and 1 atm), the maximum voltage thermodynamically achievable from a single H_2-fueled fuel cell is 1.23 V. However, SOFCs operate at a higher temperature (900-1100 °K), and the thermodynamically determined open circuit potential (OCP) is as shown in **Eqn 2.6**.

$$\mathrm{E}_T = E^0 + \frac{\Delta \hat{s}}{nF}(T - T_0) \tag{2.6}$$

where E_T is the OCP at the temperature T. Here, T_0 is the standard temperature, and $\Delta\hat{s}$ is the change in entropy for the reaction. Moreover, **Eqn. 2.6** does not fully capture the real potential, as it is also dependent upon the activity of products and reactions.

$$E = E_T - \frac{RT}{nF} ln \frac{\prod a_{products}^{v_i}}{\prod a_{reactants}^{v_i}} \tag{2.7}$$

where $a_{products}$ and $a_{reactants}$ are the activities of products and reactants with v_i as the amount of i-th product or reactant. *R* is the universal gas constant. However, it is noted that the contribution of activity to the actual *E* is not significant. For example, there is a decrease of *E* only by 10 mV by changing the oxygen activity from 1 atm to 0.21 atm.

However, in practice, the actual voltage output will be significantly less than the ideal cell potential (*E*), and the amount of cell potential decrease will scale with the extracted current. There are mainly three mechanisms of cell voltage losses; namely, activation loss, ohmic loss, and concentration loss.

$$V = E - \eta_{activation} - \eta_{ohmic} - \eta_{concentration} \tag{2.8}$$

Activation loss arises from the electrochemical reaction between the reactant and product, which predominantly occurs at low current density. Ohmic loss, on the other hand, is attributed to both ionic and electronic conduction, primarily taking place within the electrolyte and prevailing at medium current density. Concentration loss transpires when the rate of mass transportation, including gas input or steam output, fails to meet the demands of the input gas, such as oxygen or fuel, or the production of steam. The cell power output (P) can be calculated as shown in **Eqn. 2.9**.

$$P = I \times V \tag{2.9}$$

where V represents the cell voltage, and I is the electrical current.

A typical I-V curve of SOFCs is depicted in **Fig. 2.2**. The power density was ascertained based on the current-voltage (I-V) curve depicted in **Fig. 2.2**. A maximum power density can be derived to evaluate the performance of the system.

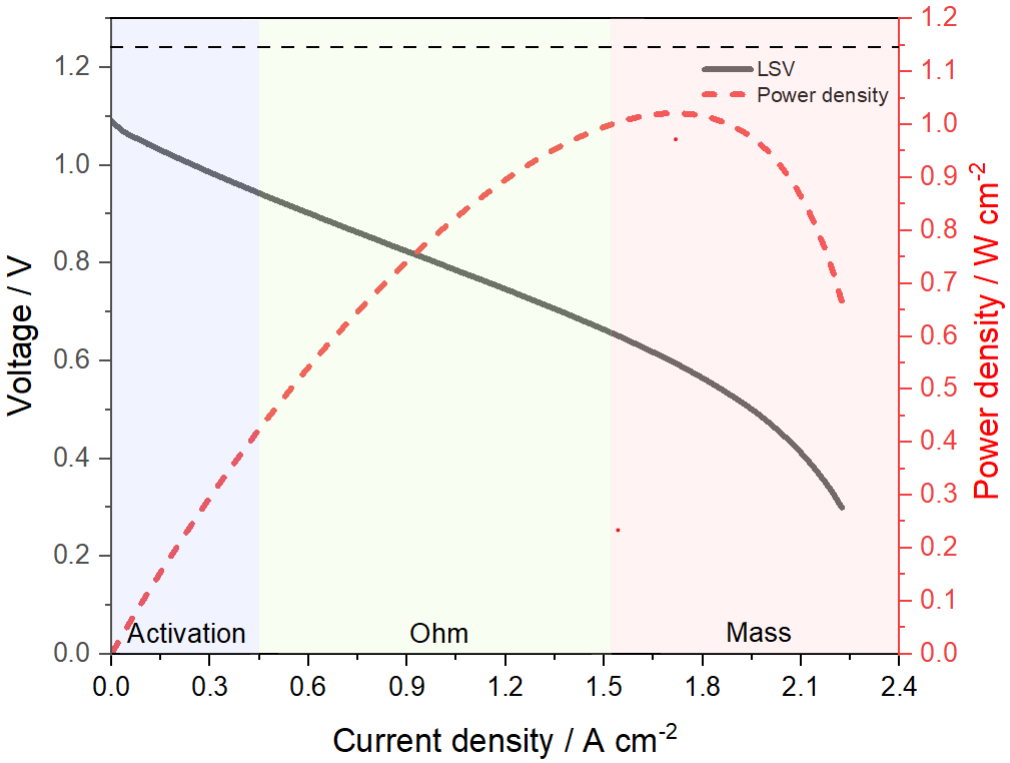

Fig. 2.2 Schematic of SOFC I-V curve (Black). The real voltage will be lower than the thermodynamically predicted voltage (dash line) due to the unavoidable losses. As well as power density curve (Red) which comes from the integration of the I-V curve.

2.2.3 SOFC materials

Numerous materials have been investigated to meet the requirements of SOFCs. The compatibility of these materials is constrained by the necessity for matching thermal expansion coefficients (TEC) to prevent cracking or dislocation within the entire stack. In addition to the overall configuration, numerous factors must be considered for each individual component, including electrical/ionic conductivity, catalytic activity, chemical compatibility, material stability, etc. The electrolyte must possess a high density to prevent gas leakage. Conversely, electrodes must adequately porous enough to allow gas penetration and minimize mass transport loss. Furthermore, the electrolyte material should have a minimum level of electrical conduction coupled with a high ionic conductivity.

Table 2.1 presents state-of-the-art materials employed in SOFC systems and their properties. Anode-supported or electrolyte-supported fuel cells are predominantly utilized, with the former experiencing greater commercialization as a result of the reduced electrolyte resistance. In both instances, the electrolyte should be highly dense and preferably thin to minimize ohmic resistance. Consequently, YSZ and GDC are the most suitable candidates. By enhancing ionic conductivity, 8% of yttria is added to zirconia, creating oxygen vacancies, and increasing stability. Although GDC

electrolytes demonstrate superior ionic conductivity and lower activation energy of ionic conduction compared to YSZ, their chemical integrity is susceptible to reducing environment, especially at high temperatures. Therefore, GDC is a viable option at lower operating temperatures.

The anode is a crucial component in the setup of an SOFC, as it comprises 90%-95% of the total material utilized. It catalyzes the fuel reaction with oxygen ions from the electrolyte and transfers the electrons generated in hydrogen oxidation reaction (HOR) to the external circuit. Anode requires a material that has a catalytical activity for HOR, as well as high ionic and electrical conductivity to transport the oxygen ions from electrolyte and electrons to the load, respectively. Nickel mixed with oxygen ion-conducting oxides (Ni-YSZ or Ni-GDC) are typically considered as an anode material. To provide sufficient electronic conduction, a good amount of Ni must be added to the anode, with a threshold value of 30 vol%. To balance TEC and electronic conductivity, researchers demonstrated that an optimal range of Ni concentration lies between 40-60 vol%[27]. As the anode required a higher sintering temperature (1000-1300°C) than the cathode and is thus produced before the cathode in the fuel cell manufacturing.

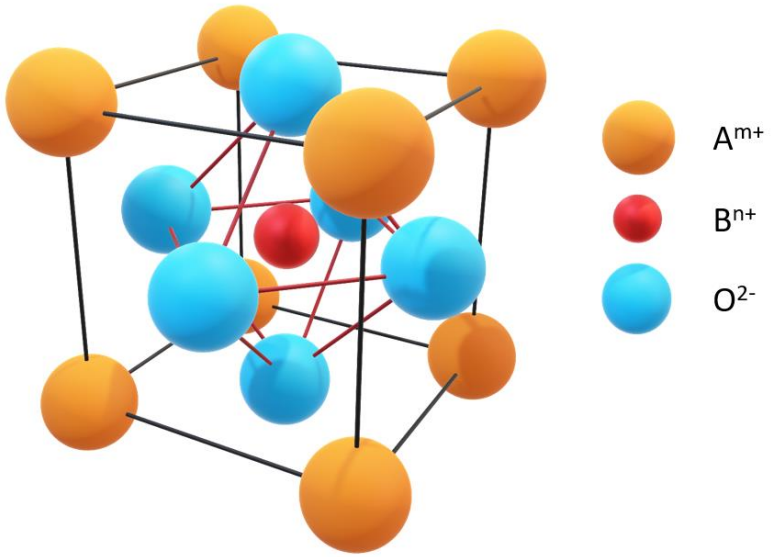

Fig. 2.3 Unit cell of the ABO_3 structure

Noble metals, such as Pt, were utilized as cathode materials in the 1990s. However, due to their poor stability, inability to allow oxygen ions to pass through the bulk, and high costs, perovskite-based materials have replaced them and are now widely used. **Fig. 2.3** illustrates the typical structure of cubic perovskite with the fundamental formula ABO_3, where A and B are cations with a total charge of 6 (m+n = 6). The A-site cation consists of a mixture of rare and alkaline earths (La, Sr, Ca, Pr, etc.) with a lower valence state and larger size. B-site cations include a transition metal (Co, Fe, Ni, Ti, etc.), creating the ionic and electrical conduction within the perovskite. The octahedral symmetry surrounding the transition metal often promotes a metallic or semiconducting band structure, making it possible to achieve high electronic conductivity at elevated temperatures. Simultaneously, oxygen vacancies can be

formed when the sum of A-site and B-site cations is less than six[28]. A proper choice of material and dopant ratio for each site will attain high ionic conductivity while maintaining great electronic conductivity. Ionic conductivity is typically achieved by doping a 2+ charge cation to the A-site, resulting in a decrease in charge that is compensated by the formation of oxygen vacancies, enabling oxygen ions to jump from one vacant site to another. Cobalt-containing material, such as $La_{0.6}Sr_{0.4}CoO_{3-\sigma}$ (LSC), typically exhibit significantly high ionic and electrical conductivity, making them ideal candidates for SOFC cathodes. However, the high cobalt composition leads to a large TEC value, as listed in **Table 2.1**, causing a tendency to delaminate or crack the electrolyte, thus limiting the usage of this type of electrode. Research has demonstrated that by doping other non-active transition metal to the B-site, the TEC value can be reduced, compensating for the reduced number of oxygen vacancies formed, which in turn strongly decreases ionic conductivity[29]. A high Co and A-site dopant (Ca, Sr, Ba) composition causes severe segregation, wherein the dopants tends to segregate to the surface and form a secondary phase, such as SrO or $Sr(OH)_2$[30]. $LaNi_{0.4}Fe_{0.6}O_{3-\sigma}$ (LNF) was developed as a Co and A-site dopant free electrode. It displayed a strong similarity in TEC and stability but suffered from low ionic conductivity, primarily due to the lack of Co and A-site dopant.

In summary, ohmic resistance, primarily originating from the ionic conduction through the electrolyte, can be reduced by simply decreasing the electrolyte's thickness or replacing it with materials with higher ionic conductivity. Most polarization resistance primarily sources from the cathode site, so greater attention has been focused on enhancing the catalytic activity and stability of the cathode. Matching the TEC of the cathode material with other components often involves a trade-off between decreasing catalytic activity and long-term stability.

Table 2.1 Properties of state-of-the-art SOFC materials.

Component	Composition	TEC[$\times10^{-6}K^{-1}$]	T [°C]	σ_e [Scm^{-1}]	σ_i [Scm^{-1}]
Anode	NiO-YSZ[31,32]	11.9	800	250	--
Anode	NiO-GDC[32]		800	1070	--
Electrolyte	$(Y_2O_3)_{0.08}(ZrO_2)_{0.92}$[33]	10.5	800	--	0.03
Electrolyte	$Ce_{0.8}Gd_{0.2}O_{1.9}$[34,35]	12.5	800	--	0.053
Cathode	$La_{0.6}Sr_{0.4}CoO_3$[36]	20.5	800	1600	0.22
Cathode	$La_{0.6}Sr_{0.4}Co_{0.2}Fe_{0.8}O_3$[36,37]	15.3	600	330	8×10^{-3}
Cathode	$Pr_{0.8}Sr_{0.2}Co_{0.2}Fe_{0.8}O_3$[36]	12.8	800	76	1.5×10^{-3}
Cathode	$LaNi_{0.4}Fe_{0.6}O_3$[38,39]	11.4	800	580	4.3×10^{-9}

2.2.4 Oxygen reduction reaction

The ORR consists of a series of steps as follows:

Mass transport of oxygen to electrode surface (step 1):

$$O_{2(bulk)} \rightarrow O_{2(near\ electrode)}$$

Molecular oxygen adsorption on activated surface (step 2)

$$O_{2(near\ electrode)} + X \rightarrow X \cdots O_2$$

Dissociation into atomic oxygen (step 3)

$$X \cdots O_2 + X \rightarrow 2(X \cdots O)$$

Surface transport of atomic oxygen (step 4)

$$X \cdots O \rightarrow X \cdots O$$

Partial reduction of O to O^- (step 5)

$$X \cdots O + e^- \rightarrow X + O^-$$

Total reduction of O to O^{2-} (step 6)

$$X + O^- + e^- \rightarrow X + O^{2-}$$

Oxygen ion transport (step 7)

$$O^{2-}_{electrode} \rightarrow O^{2-}_{electrolyte}$$

where X denotes the active site on the surface, and e^- represents free electron. Similar to a series of operations in an assembly line, the overall reaction rate is limited by the slowest step in the entire process. In most cases, steps 5 and 6 are the rate limiting step as shown in formula below.

$$X \cdots O + e^- \rightarrow X + O^- \quad (2.10)$$

$$X + O^- + e^- \rightarrow X + O^{2-} \quad (2.11)$$

As depicted in **Fig. 2.4**, for a reaction to occur, an adsorbed oxygen (red dot) should interface with both ion-conducting and electron-conducting media. The region is called the triple phase boundary (TPB)

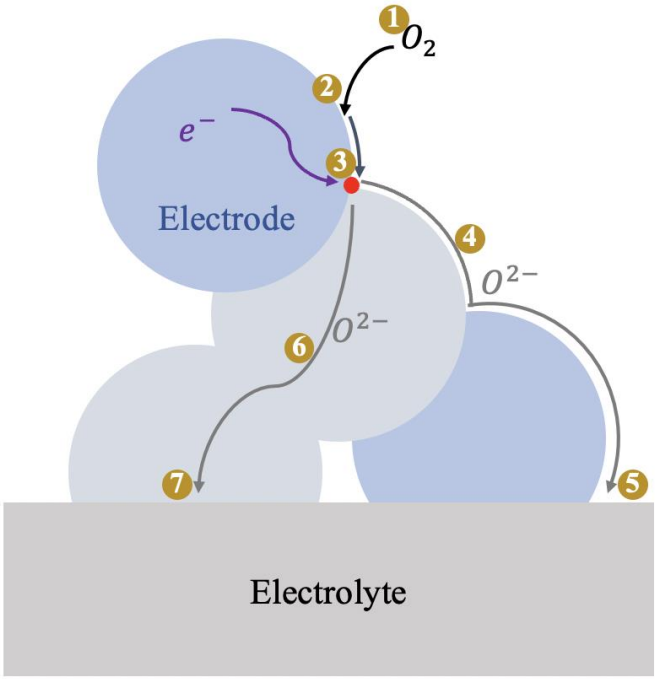

Fig. 2.4 Schematic diagram of the reaction of oxygen reduction reaction (ORR)

2.3 SOEC Primer

An SOEC is an electrochemical device that convert electrical energy directly into chemical energy with the efficiency of as high as 85% with high operating temperatures[40]. An even higher overall electricity-to-fuel conversion efficiency can be achieved when utilizing the extra-heat in generating more products. It gains significant attention as a promising technology for sustainable energy production. It offers a unique solution for converting renewable energy, such as wind and solar, into chemical energy in the form of chemical energy through the process of water electrolysis.

2.3.1 Reactions in SOECs

Thanks to the reversibility of reactions, by applying a voltage higher than open circuit voltage (OCV), the electrochemical process can be reversed from fuel cell to electrolysis cell. **Fig. 2.5** illustrates a general layout of a SOEC for water electrolysis with oxygen-ion conducting electrolyte. Electrolysis of CO_2 or co-electrolysis of H_2O/CO_2 can also be accomplished to generate CO or H_2/CO, respectively[41].

The components of SOEC systems are very similar to that of a SOFC system,

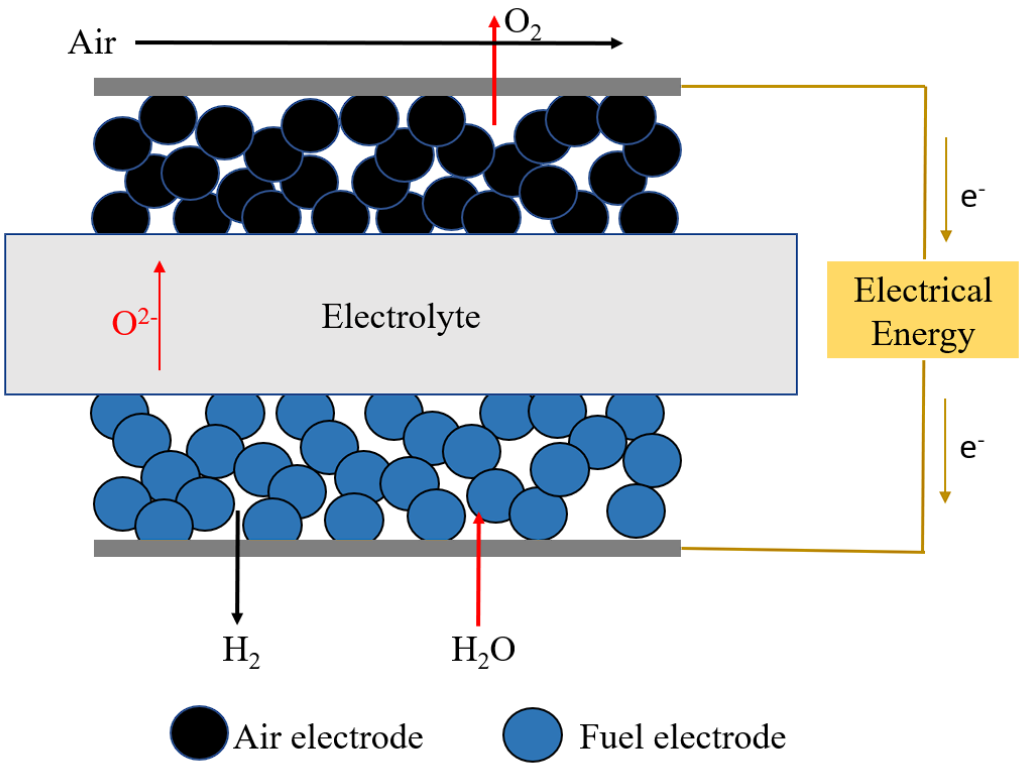

Fig. 2.5 General layout of SOEC

but the direction of reactions and resulting current is reversed. At the fuel electrode, H_2O in the form of steam is fed into the fuel electrode and split into protons and oxygen ions. The protons react with incoming electrons, evolute as hydrogen molecules, which are released from the fuel electrode (**Eqn. 2.12**). Alternatively, with CO_2 as the reactant, CO can be generated (**Eqn. 2.13**).

$$H_2O + 2e^- \rightleftarrows H_2 + O^{2-} \quad (2.12)$$

$$CO_2 + 2e^- \rightleftarrows CO + O^{2-} \quad (2.13)$$

On the air electrode, oxygen ions transferred from the electrolyte evolve to oxygen molecules via OER.

$$2O^{2-} \rightleftarrows O_2 + 4e^- \quad (2.14)$$

2.3.2 Cell potential and overpotential

The total energy required for the electrolysis process (ΔH) is the sum of the electricity energy (ΔG) and the thermal energy ($T\Delta S$) as indicated in the equation:

$$\Delta \mathrm{H} = \Delta \mathrm{G} + \mathrm{T}\Delta S \tag{2.15}$$

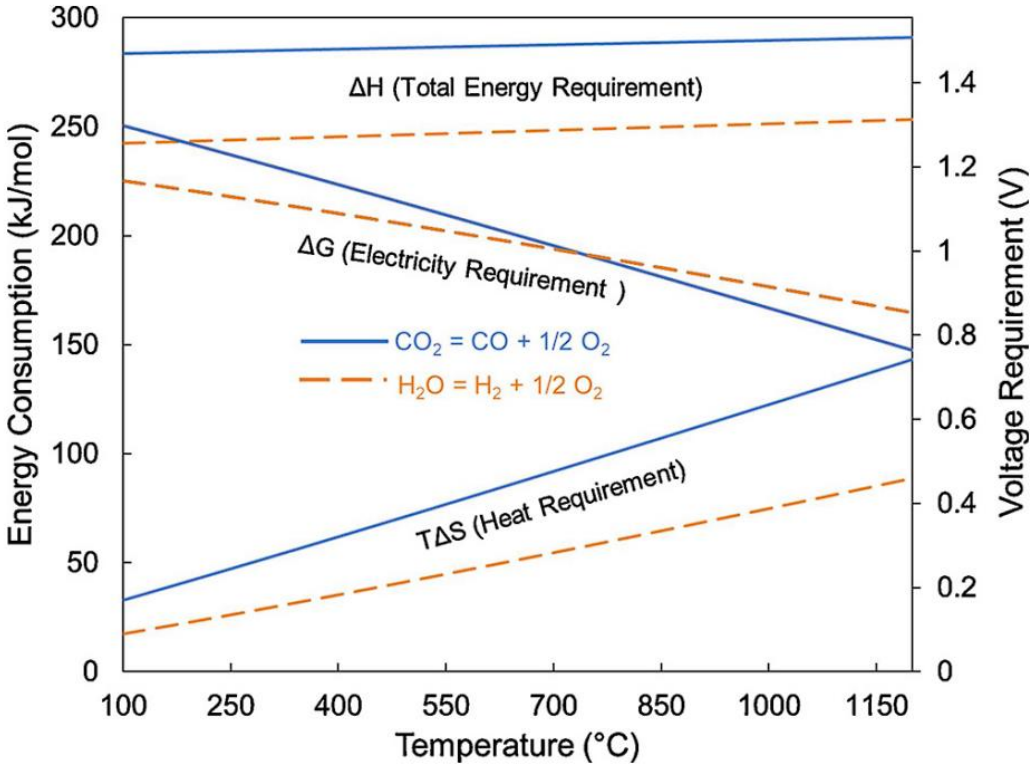

Fig. 2.6 Energy demand for H2O and CO2 electrolysis as a function of temperature. Axis on the left shows enthalpy and Gibb's free energy while the axis on the right shows electrical energy needed for the process at various temperatures[1].

The minimum potential (E) to incur an electrolytic reaction is related with Gibbs free energy change (ΔG) as shown in **Eqn. 2.16**.

$$\mathrm{E} = -\Delta \mathrm{G} \,/\, \mathrm{nF} \tag{2.16}$$

where n is the electron moles that transfer per mole of reactant during reaction and F is the Faraday constant.

As shown in **Fig. 2.6**, the cell voltage required for the electrolysis reaction decreases as the operating temperature increases[1]. This is why SOECs (operating temperature at 700-900 ºC) are intrinsically advantageous over low-temperature electrolysis cells. A state-of-the-art YSZ-based cell has been tested in different humidity levels (50, 30, and 3 relative humidity (RH)) at 700 ºC (**Fig. 2.7**). The cell OCV is ~ 1.1 V with dry H_2 and O_2 as fuel and oxidant, respectively. With a higher humidity added to H_2 (50 RH), the OCV drops to 0.97 V.

Similar to fuel cell systems, the voltage loss in an SOEC can be attributed to activation, ohmic, and concentration losses.

$$V = E + \eta_{activation} + \eta_{ohmic} + \eta_{concentration} \tag{2.17}$$

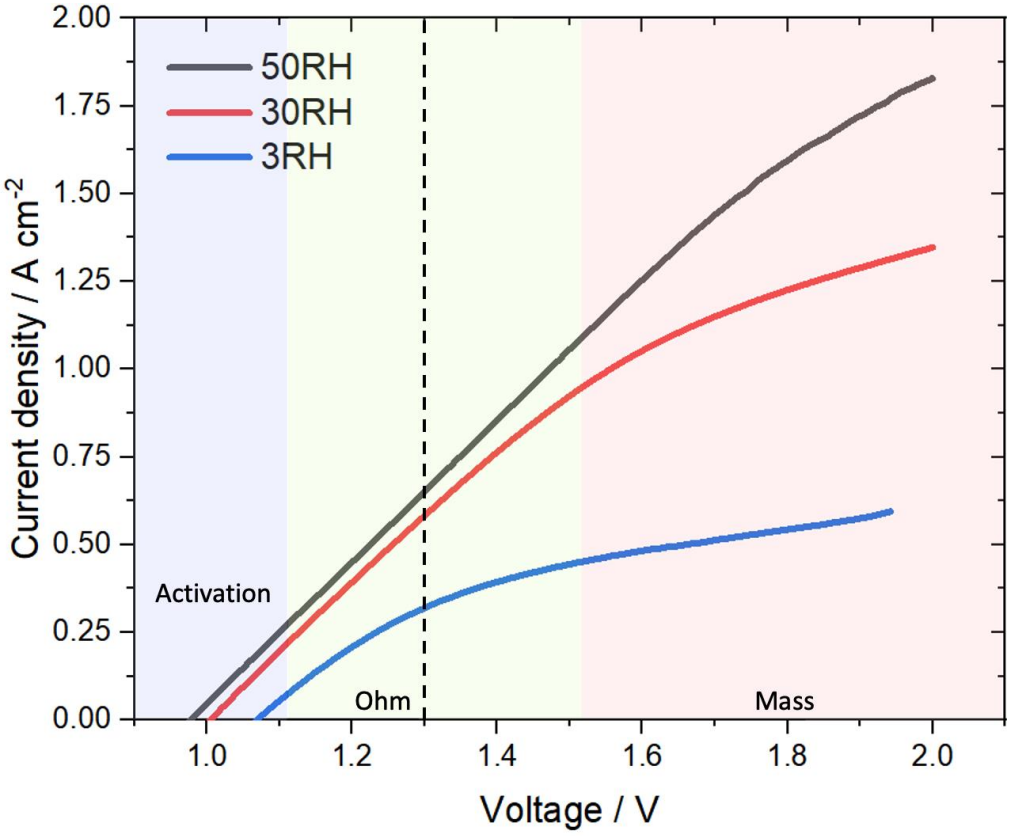

Fig. 2.7 Schematic of SOEC I-V curve with different humidity level, 50%RH, 30%RH, and 3%RH as black, red, and blue, respectively

Activation loss occurs due to the electrochemical reaction of OER. Ohmic loss results from electronic conduction and more dominantly ionic conduction, which occurs mainly in the electrolyte. Concentration loss occurs when the input rate of steam transportation cannot keep up with the requirement of the current flow.

In general, SOECs run in their stable voltage range to ensure the minimum damage on the cell, which is 1.2 V - 1.5 V at 700-1000 ºC.

2.3.3 Oxygen evolution reaction

OER, which is the reaction on the air electrode in electrolysis mode, is dependent on the efficiency and resistance of the electrolysis process. The overall process can be decomposed into serval sub-processes as shown in **Fig. 2.8.**

Oxygen ionic transportation from electrolyte to interface (step 1)

$$O^{2-}_{electrolyte} \rightarrow O^{2-}_{interface}$$

Oxygen ionic transportation from interface to electrode or through surface (step 2)

$$O^{2-}_{interface} \rightarrow O^{2-}_{electrode}$$

Partial oxidation of O^{2-} to O^{-} (step 3)

$$X + O^{2-} \rightarrow X + O^{-} + e^{-}$$

Total oxidation of O^{2-} to O (step 4)

$$X + O^{-} \rightarrow X \cdots O + e^{-}$$

Surface transport of atomic Oxygen (step 5)

$$X \cdots O \rightarrow X \cdots O$$

Evolution into Oxygen (step 6)

$$X \cdots O_2 + X \rightarrow 2(X \cdots O)$$

Molecular desorption on electrode (step 7)

$$X \cdots O_2 \rightarrow O_{2(near\ electrode)} + X$$

Mass transport of oxygen out of the system (step 8)

$$O_{2(near\ electrode)} \rightarrow O_{2(out)}$$

X denotes the active site on the surface. In most cases, oxygen oxidation reaction (**Eqn 2.18**) and oxygen desorption (**Eqn 2.19**) are the rate limiting step[42,43].

$$X + O^{2-} \rightarrow X + O + 2e^{-} \quad (2.18)$$

$$X \cdots O_2 \rightarrow O_{2(near\ electrode)} + X \quad (2.19)$$

In this equation, X denotes the active site on the electrode surface, e^{-} represents the free electron. The rection is depicted in **Fig. 2.8**.

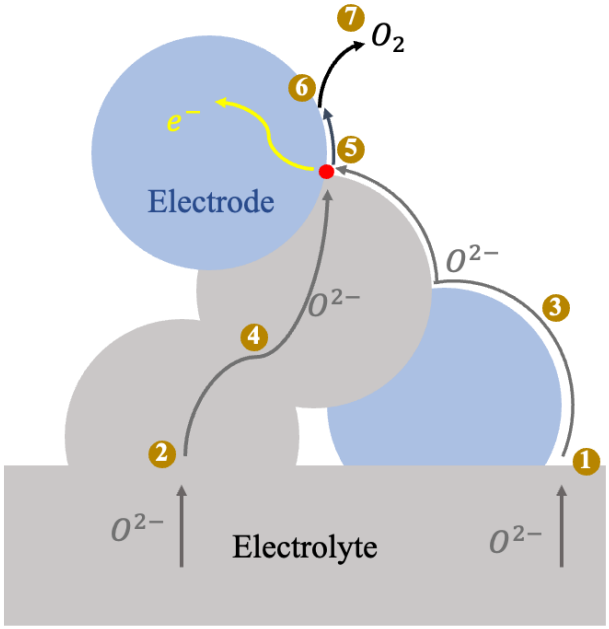

Fig. 2.8 Schematic diagram of the reaction of oxygen evolution reaction (OER)

2.4 Cells/Test Station Preparations

As a most important component of the SOCs system, the single cell typically consists of a dense electrolyte and porous electrodes. To achieve sufficient mechanical strength, electrolyte or electrode should serve as the support, while other materials build onto it. There are two general types of support, electrolyte-supported cell or fuel-electrode-supported cell, in which the thickest layer, electrolyte or fuel electrode respectively, would be in a range of 200-600 μm. Due to the low ionic conductivity of the typical electrolyte material[44], YSZ, fuel-electrode-supported cells are widely used to achieve a high performance. The supported layer is usually manufactured by tape casting methods. On the other hand, air electrodes need higher surface area and porosity to attain higher electrode reaction rate and fluent gas diffusion. Therefore, nano-power synthesis has become a significant initial process for the electrode building process. A simple and efficient process, usually referred to as “screen printing” process has been conducted to deposit nano-powers on a selected area via slurry deposition followed by a sintering process.

However, the performance tends not to be high enough to meet the requirement of commercialization. To further enhance the cell performance, additional nanoparticles or films are decorated on an electrode backbone by infiltration or ALD process. A brief introduction for each individual process is provided below.

2.4.1 Nano-powder synthesis

The solid-state reaction method is the typical procedure for preparation of ceramic compounds due to its simplicity and low cost. However, it requires high temperature, poor compositional uniformity as well as large particle sizes with unpredictable size distribution. It is not an ideal option for the air electrode material for SOCs due to these disadvantages[45]. Therefore, various other chemical synthetic techniques have been explored to produce nano-powder for electrodes, such as solution combustion synthesize, co-precipitation, sol-gel, polymeric complexing, and hydrothermal methods.

Among these chemical synthetic techniques, solution combustion synthesis (SCS) has emerged as a widely used technique, in which an exothermic redox reaction occurs between oxidizer, such as nitrates, and organic fuels, such as glycine or urea. An example is made on a previous report[46], where LNF powder was synthesized first with lanthanum (III) nitrate hexahydrate, nickel (II) nitrate hexahydrate, iron (III) nitrate nonahydrate, glycine and deionized water. Nitrate precursors with a weight ratio of 1:0.403:0.373 (La: Ni: Fe) were dissolved in minimal amount of deionized water while stirring on a hot plate. Glycine was slowly added into the solution while stirring (with 1:0.877 weight ratio between nitrate precursors and glycine), which changes the color of solution into dark red. Once all were dissolved, water was evaporated at ~150°C until the mixture became gel-like. Then the temperature was set at 325°C for a combustion reaction. After cooling down, the reaction product was crushed into smaller clusters and calcined at 850°C for 3 h in a ceramic container. **Fig. 2.9** indicates the synthesize of iron oxide nanoparticles, similar to the step we performed for the preparation of LNF nano-particles. It provides the following advantages[47].

1. Enhanced control in particle size and morphology
2. High scalability
3. Uniform distribution of desired elements
4. Environmentally friendly

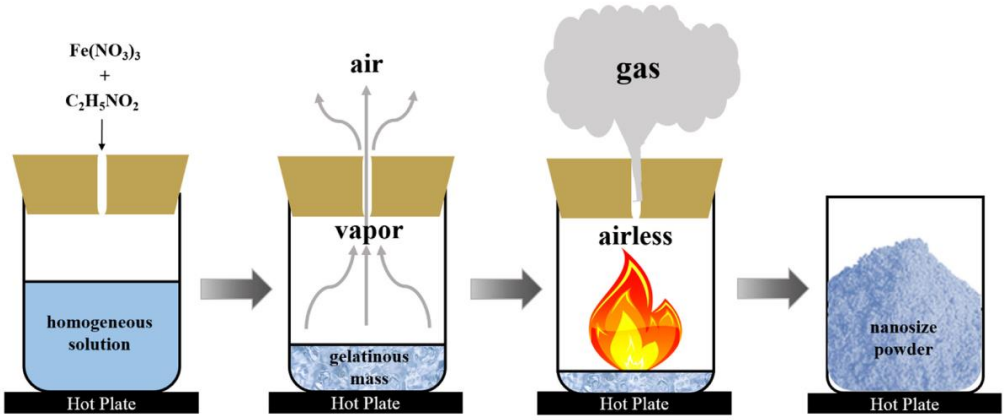

Fig. 1. Schematic illustration of SCS process for the ferric nitrate-glycine reaction system.

Fig. 2.9 Schematic diagram of the Nitrate-Glycine combustion process

2.4.2 Screen printing

The performance of SOCs is highly dependent on the manufacturing process employed to fabricate their component, in which screen-printing method is widely used and well-established technique and had become a promising approach for the fabrication of SOC component. Its versatility and cost-effectiveness offer numerous advantages in terms of material utilization, processing time, and scalability[48].

Fig. 2.10 The electrode deposition process by screen printing

As described in **Fig. 2.10**, prior to the screen-printing process, a slurry is made from electrode nano-powders, binder, solvent, and dispersant. In the screen-printing process, the electrode slurry can be deposited with the designed area. A sintering process is required to consolidate the structure as well as evaporate the solvent, binder, and dispersant. An example is made on the recent paper, where a GDC slurry is first prepared by mixing Hypermer KD-1 (Croda, dispersant) for 24 h at 50 °C. GDC nano-powders (FuelCellMaterials; 20 wt% GDC; surface area: 35.3 m^2 g^{-1}) and ethyl cellulose (Sigma Aldrich, binder) are then added to the mixture and stirred for another 24 h at 50 °C. The final slurry is composed of 40 wt% terpineol, 10 wt% Hypermer KD-1, 2 wt% ethyl cellulose, and 48 wt% GDC nano-powder. LSCF slurry is prepared using the same method as the GDC slurry but with different compositions. It consists of 35 wt% of terpineol, 5 wt% of Hypermer KD-1, 3 wt% of ethyl cellulose, and 57 wt% of LSCF powers (FuelCellMaterials). After preparing the slurry, the GDC slurry is screen printed on the YSZ side with a specific area and then sintered at 1150 °C for 5 h at a rate of 3°C/min, with additional stops at 80 °C for 1 h and 500 °C for 30 mins to evaporate the solvent and binders, respectively. LSCF slurry is then screen printed on the GDC and sintered at 850 °C for 3 h, with the same stops with sintering GDC slurry. There are several advantages for the screen-printing process:

1. Precise deposition of materials in the desired pattern
2. Fast processing time
3. High scalability
4. High versatility
5. High control over thickness and uniformity

Overall, screen printing offers a versatile and cost-effective approach for the fabrication of SOCs components.

2.4.3 Tape casting

Tape casting is a well-known technique in ceramics industry and it an attractive approach for manufacturing thin, uniform layers. The flexibility and cost-effectiveness of such technique provide lots of advantages.

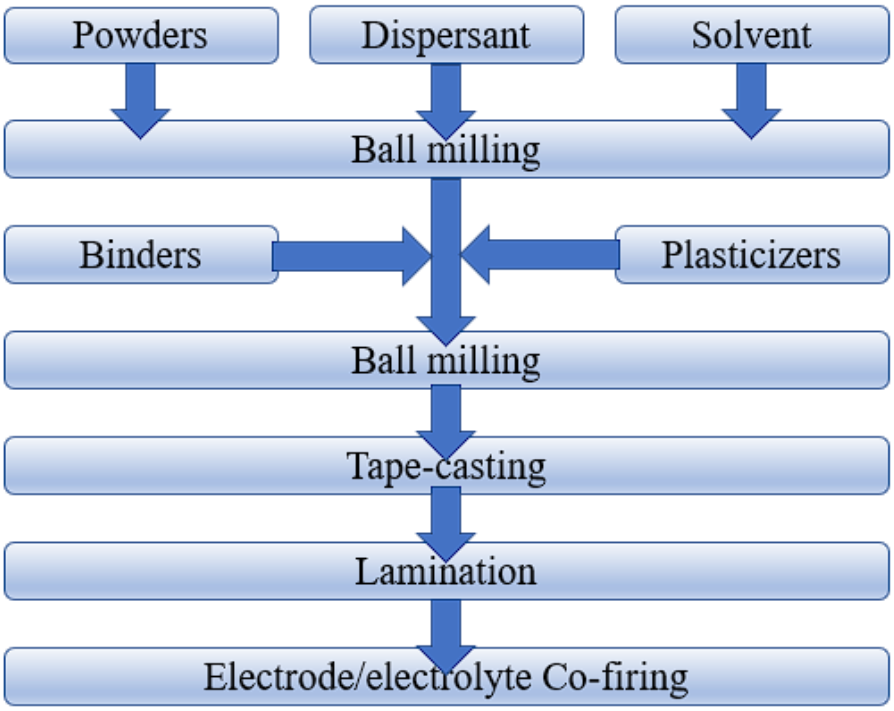

Fig. 2.11 Schematic diagram of the general process of tape casting

As depicted in **Fig. 2.11**, the process starts from mixing ceramic powders, dispersant and solvent to prepare the slurry. Due to the high viscosity of the slurry, a ball miller is used to utilize the mixing process. After ball milling for ~ 24 h, binders and plasticizers are then added to the slurry, flowing with additional ball-milling process for 24 h. The result slurry then performs the de-airing process by putting the slurry into a vacuum condition. Finally, the tape casting process is performed with desired thickness level by changing the height of doctor blade, followed by a lamination (if there is an additional layer) and sintering process to consolidate the structure.

2.4.4 Infiltration

High operating temperatures are necessary to ensure proper contact between the electrode and electrolyte; consequently, thermal expansion coefficient must be compatible, such as LSM (11.3) and YSZ (10.5). Conventional methods involving the infiltration on green-stage electrodes are ineffective for high-temperature SOFCs. Thus, to incorporate nanoparticles into a high-temperature fuel cell, backbone electrodes must undergo a pre-sintering process before infiltration. The infiltration/impregnation treatment involves precipitating and decomposing metal precursor solutions into porous

backbone materials, either electrode or electrolyte materials, depending on the specific circumstances[49].

Fig. 2.12a illustrates a typical method for synthesizing nanoparticles infiltration onto an electrode/electrolyte framework. A sintering process, performed at a lower temperature than that of electrode sintering temperature, is conducted either once or multiple times as needed. For example, in my first project on SOFC, CeO_2 nanoparticles were introduced via a single wet infiltration of $Ce(NO)_3$ metal salt solution into a pre-fired LNF backbone. A drop of 1M $Ce(NO)_3$ solution, approximately 5 µL, was introduced on top of the LNF electrode and positioned into a vacuum chamber. Jiang et al.[50] demonstrated that due to the capillary pressure acting as the driving force for the solution to permeate the porous electrode, a vacuum environment facilitates the precipitation of the precursor solution. The infiltrated LNF is subsequently sintered at 450 ºC for 1 hour to decompose the metal precursor. Since the CeO_2 catalytic phase forms at a significantly lower temperature than the operating temperature (750 °C in this instance), grain growth is prevented, resulting in the formation of nanoparticles CeO_2 overcoat on the LNF surface (**Fig. 2.12b)**.

Infiltrated catalytic particles can create discrete or continuous nanoparticles, as demonstrated in **Fig. 2.12bc**. The scaffold can exhibit both electronic and ionic conductivity such as LSCF or LSM-YSZ, or it can be a pure ionic conductor like GDC or YSZ. When the latter is chosen as the porous framework, infiltrated electrode materials must be continuous to achieve adequate electronic conductivity, necessitating the addition of a surfactant (e.g., Triton-X100) to the precursor or multiple infiltrations. To create a continuous and uniform nanoparticle overcoat, various additives have been tested. Sholklapper et al[51]. and Lu et al.[52] employed additional urea and polymeric

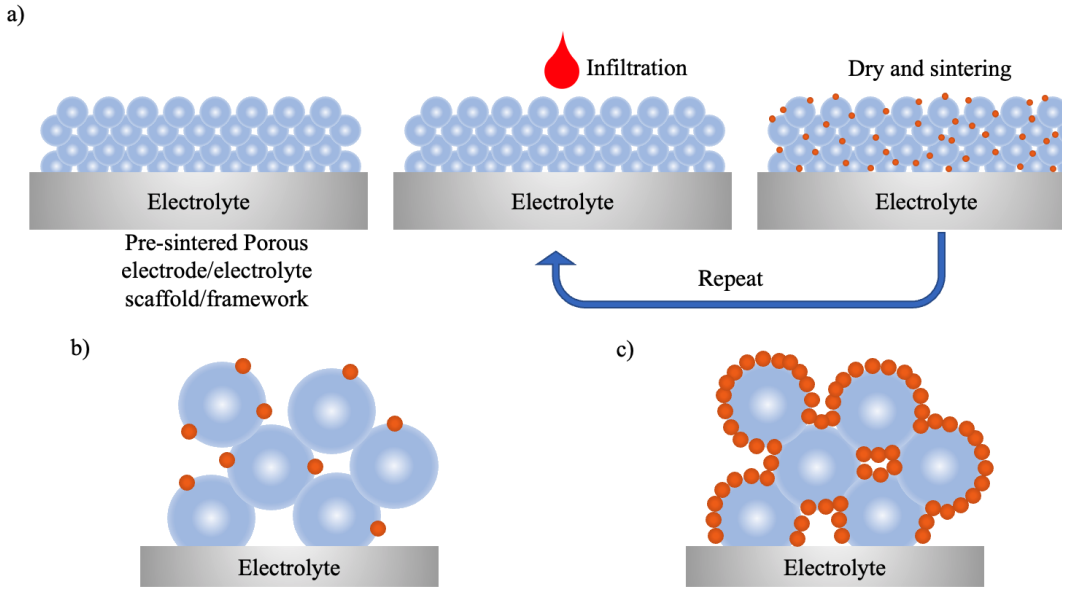

Fig. 2.12 a) typical process for infiltration of metal precursor on to pre-fired porous backbone. Scheme of b) discrete nanoparticles or c) continuous nanoparticles by infiltration on porous scaffold skeleton.

dispersants to facilitate the formation of the perovskite phase. Li et al.[53] also confirmed that the distribution and connectivity of the Cu nanoparticle phase on Cu-YSZ composite is enhanced by adding urea.

2.4.5 Atomic layer deposition

In addition to solution-based techniques like infiltration, vacuum-based thin-film fabrication techniques encompass physical vapor deposition (PVD) and chemical vapor deposition (CVD). PVD typically involves methods such as plasma layer deposition (PLD) and sputtering, in which an electrode target is hit by the surrounding gases molecules being transformed into plasma phase and physically deposited on the desired sample surface. On the other hand, CVD employed vaporized precursors as carriers that react with sample surface chemically, forming strong bonds and producing thin films. Atomic layer deposition (ALD), distinct from other types of CVD, exhibits self-limiting behavior between the precursors and substrate surface. Consequently, the thickness of the overcoat film created by ALD can be precisely controlled at the angstrom level, maintaining high uniformity[54].

A typical ALD process involves sequential and isolated supply of precursors within a heated, vacuumed environment. For instance, if Ce_2O_3 is chosen as the overcoat material through ALD, the procedure includes separate steps as depicted in **Fig. 2.13**: (1) The cerium precursor is introduced into the chamber, and the chemical $Ce(iPrCp)_3$ binds to the substrate surface. (2) after reaction saturation, in which the substrate is coated with a single layer of precursor, any excess precursor is purged using an inert gas (in this case, N_2). (3) An oxidizer (in this case, H_2O) is subsequently

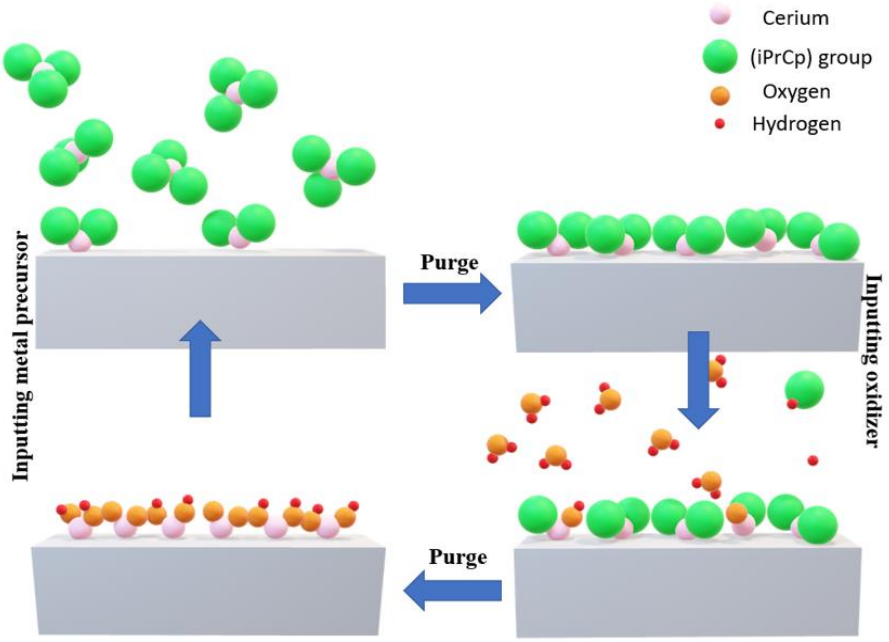

Fig. 2.13 Chemical deposition process of atomic layer deposition

supplied to the system to react with the precursor's functional group, leaving an OH group attached to the cerium element. (4) The reactant and excess oxidizer are purged using an inert gas. One ALD cycle consists of four steps, resulting in a single atomic layer or less. By performing several cycles, a uniform and well-organized thin film is produced with a growth rate of 0.1-2 Å.

The growth of thin films by ALD comprises two stages: nucleation and constant growth. The growth of metal oxide via ALD begins with the formation of nanoparticle nuclei, followed by an increase in nuclei size and the generation of additional nuclei. Subsequently, these nanoparticles coalesce into islands, forming a continuous film on the substrate upon which growth continues at a constant rate[55]. The latter stage involves one layer stacking atop another, with a linear dependence between the number of cycles and total thickness. The primary parameter affecting the growth rate is the operating temperature. It has been demonstrated that ALD reactions are optimized within a specific temperature range, referred to as the 'ALD window'. Operating beyond or below the ALD window results in significant changes in growth rate and a loss of ALD characteristics[56]. However, nucleation is not a linear process and predominantly occurs at the onset of film growth. ALD nucleation is challenging due to the requirement for high nucleation density, which leads to the accelerated formation of a continuous layer with uniform surface.

2.5 Instrumentational Projects

Instrumentation plays a significant role in my research. There are two instrumentation projects, which are the instrumentation of SOEC testing station, and that of ALD system. The first one involves upgrading from a symmetrical-cell SOFC testing station to a full-cell SOFC/SOEC testing station. The second one involved building an entirely new ALD system from scratch. The purpose of building a new ALD is to (1) expand the total number of precursors we can deposit in the same time, and (2) increase amount of feasible precursors we can implemented, such as Co and Ce.

2.5.1 SOECs testing station

As a transition from SOFC to SOEC research, instrumentation work is crucial for three main reasons. (1) Full cell testing is critically necessary for SOECs, necessitating a change from symmetrical cell to fuel cell configuration. (2) Hydrogen and oxygen must be provided separately through two channels, ensuring that hydrogen does not leak into the system and cause a drop in open-circuit voltage (OCV). (3) an additional external bubbler is required to supply a steam/hydrogen mixture to the fuel electrode channel input.

Fig. 2.14 presents a schematic diagram of the modified test station tailored for SOEC testing purposes. The entire system is composed of Inconel-600 nickel alloy due to its electrical conductivity, high-temperature tolerance (up to 800 °C), and robust mechanical stability. The test cell is sandwiched between two additional current-collecting plates (also made of Inconel), with nickel foam and platinum mesh serving as the current collectors for the fuel electrode and air electrode, respectively. A ceramic

sealant is applied around the fuel electrode and a copper ring is placed between the fuel electrode current collecting plate and the Inconel support to act as a seal, preventing hydrogen gas leakage. To ensure solid contact between each layer, a 3kg weight is applied from the top of the testing station throughout the entire testing process.

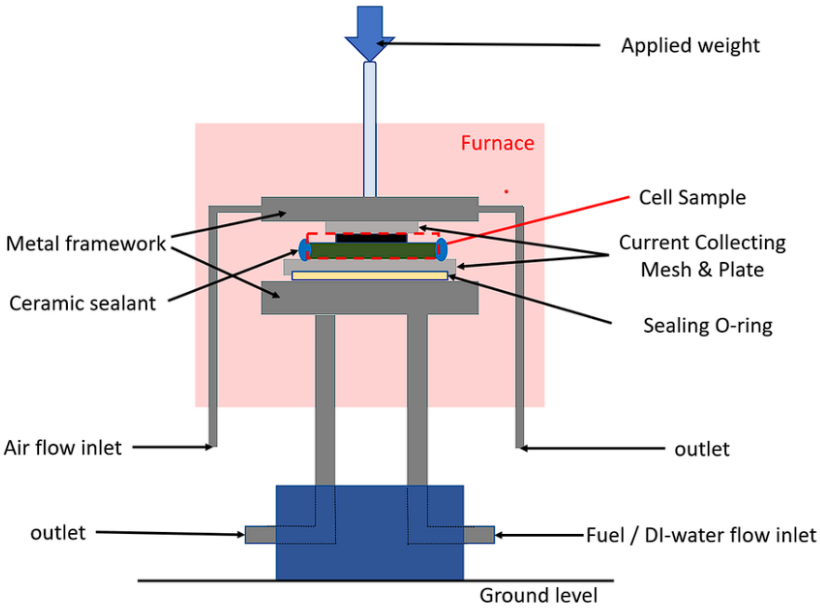

Fig. 2.14 schematic diagram of Testing station

A mixture of oxygen and nitrogen is supplied to the air electrode through the 'air flow inlet' by a mass flow rate controller (MFC), where the ratio between the two gases can be adjusted by altering their individual flow rates, maintaining a sum of 100 sccm. In order to supply hydrogen and steam to the fuel electrode for SOEC purposes, the hydrogen gas must pass through a bubbler to 'carry' the steam into the fuel electrode inlet chamber. **Fig. 2.15** illustrates a schematic diagram of the bubbler configuration I designed. All tubes are made of stainless steel, and their temperature is controlled at

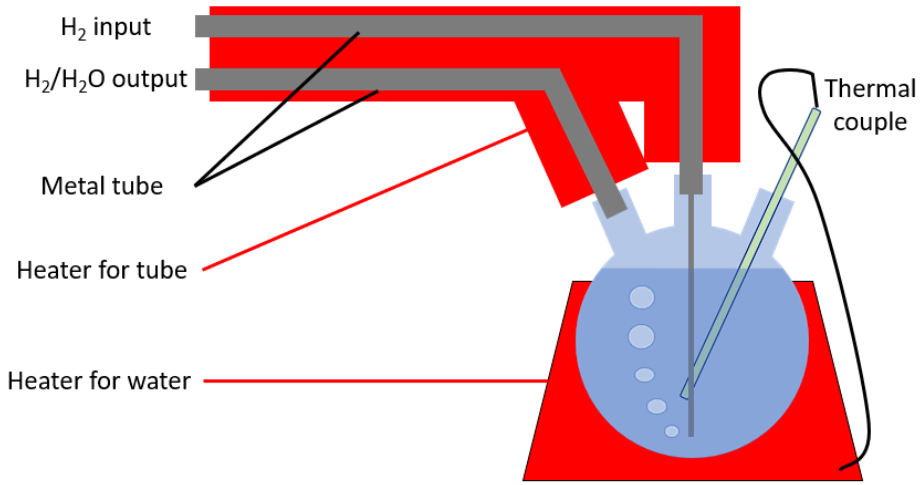

Fig. 2.15 schematic diagram of bubbler configuration

170 °C to prevent water condensation. A three-neck round-bottom flask is used as the bubbler, with a separate thermocouple (TC) directly touching the water bath to accurately control the bath temperature. To calculate the temperature required for a specific relative humidity (RH), the following equation has been employed:

$$RH = 100 \times \frac{P_w}{P_{ws}} \tag{2.20}$$

Here, P_w represents vapor pressure, and P_{ws} denotes the saturation vapor pressure. Alternatively, P_w is the saturated vapor pressure of the air temperature, and P_{ws} is the actual vapor pressure at the dewpoint temperature. The air pressure temperature just above the water level can be estimated as 100 °C, where the P_w is 102.23 kPa. Thus, to achieve 50% RH of hydrogen, P_{ws} needs to be half of 102.23kPa, which is 51.16 kPa, and the dewpoint temperature associated with that is 81.8 °C (required water bath temperature). Similarly, 30 RH and 3 RH correspond to a water-bath temperature of 69.6 and 24.5 °C, respectively.

Fig. 2.16 displays an overview of the entire testing station, where the output channel is also heated to 170 °C to prevent water condensation. Four-point electrochemical measurements are conducted for the cell testing to eliminate the contact resistance between connectors and the additional electrical resistance from the Inconel interconnectors.

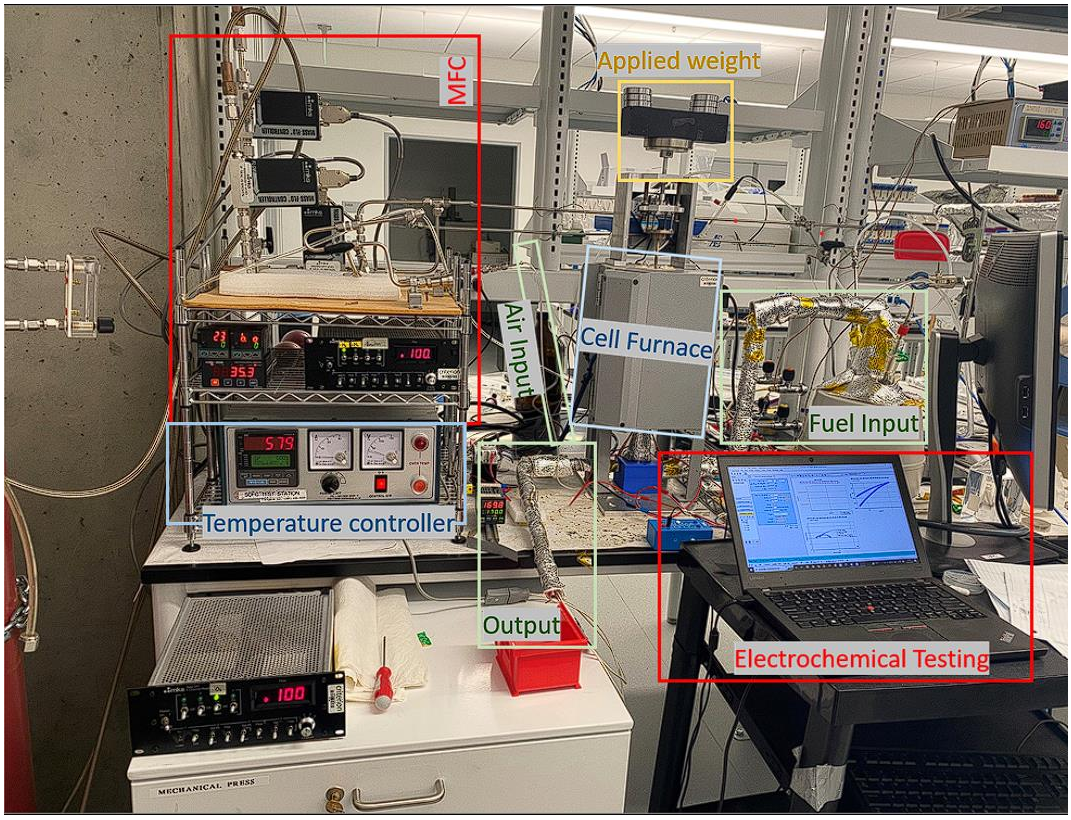

Fig. 2.16 A picture of customized SOEC testing station

2.5.2 Thermal ALD system

To enhance the versatility and multi-channel capabilities of the ALD, a new customized ALD system has been constructed to meet the desired requirements. A schematic diagram is displayed in **Fig. 2.16**, which features a customized ALD chamber (depicted in dark gray) made of stainless steel. Argon is utilized as the carrier and purge gas within the system.

The pneumatic valves (represented by brown squares in **Fig. 2.16**) are controlled by pneumatic solenoid valves, which have switched by an electrical voltage (24V DC). These valves are programmed using custom-designed LabVIEW software through a data translation. Furthermore, the temperature of the ALD chamber and precursors are regulated by a PID temperature controller coupled with individual heating tapes.

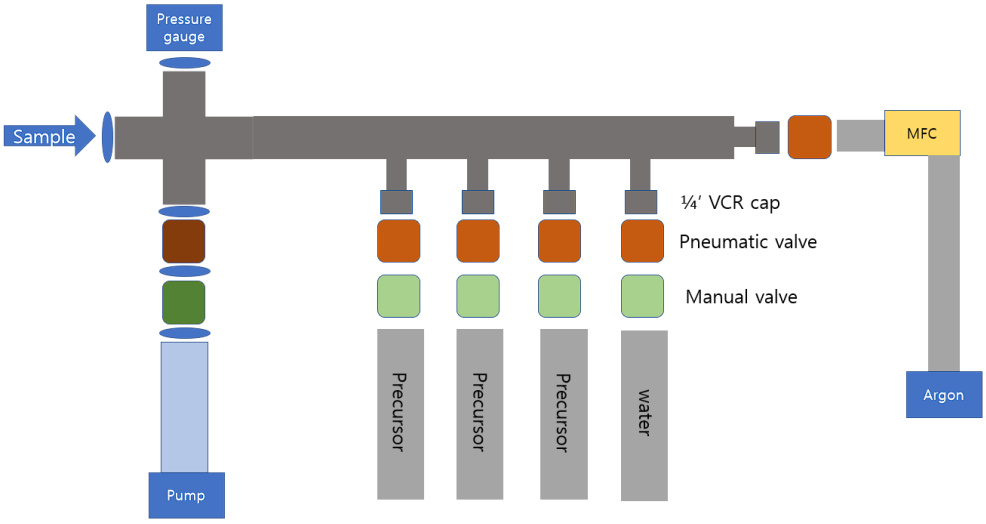

Fig. 2.17 schematic diagram of ALD design

The base pressure was tested in the absence of inputting Argon purging gas. A based pressure of <10 mtorr was achieved, confirming a suitable environment for ALD conditions. The ALD system was tested by depositing a well-known thin layer of ZrO_2 on a silicon wafer using $Zr(NMe_2)_4$ as precursor and H_2O as oxidant. The thin film exhibited ALD properties and validated the effectiveness of the ALD system. **Fig. 2.18** provides an overview of the entire ALD system. In addition to heating the chamber and precursors, the pump line was also heated to 100 °C to prevent the precursors condensation.

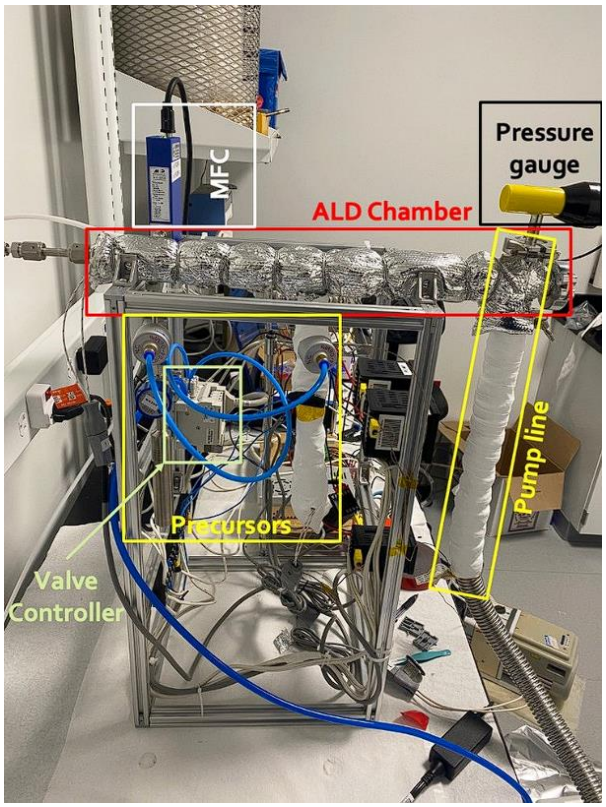

Fig. 2.18 A picture of customized ALD system

2.6 Materials Characterization

Materials characterization technique provides important information about the physical, chemical, and structural properties of SOCs materials. It provides a deeper understanding of the physical properties of materials, which can help researchers and engineers to design and fabricate high performance, highly durable and reliable SOCs. Typically, it includes microscopy, diffraction pattern, and spectroscopy. Scanning electron microscopy (SEM) and transmission electron microscopy (TEM) provide information about the morphology and microstructure of the materials. X-ray diffraction (XRD) gives the crystallinity and structure of the materials. X-ray photoelectron spectroscopy (XPS) and Raman spectroscopy provide information about the chemical composition and bonding of materials.

2.6.1 Scanning electron microscope

The SEM is a type of microscope for examining the surface of a wide range of materials at high magnifications. It used an electron beam to generate images with high resolution and depth of field, allowing to observe the surface topography, composition, and morphology of materials with magnification as large as 100k. It is a powerful and versatile tool that can obtain high-resolution images of the surface of various materials with nanometer scale.

Fig 2.19 shows the schematic diagram of SEM, and the key components of an SEM include, (1) Electron Gun, which is the source of the high-energy electron beam

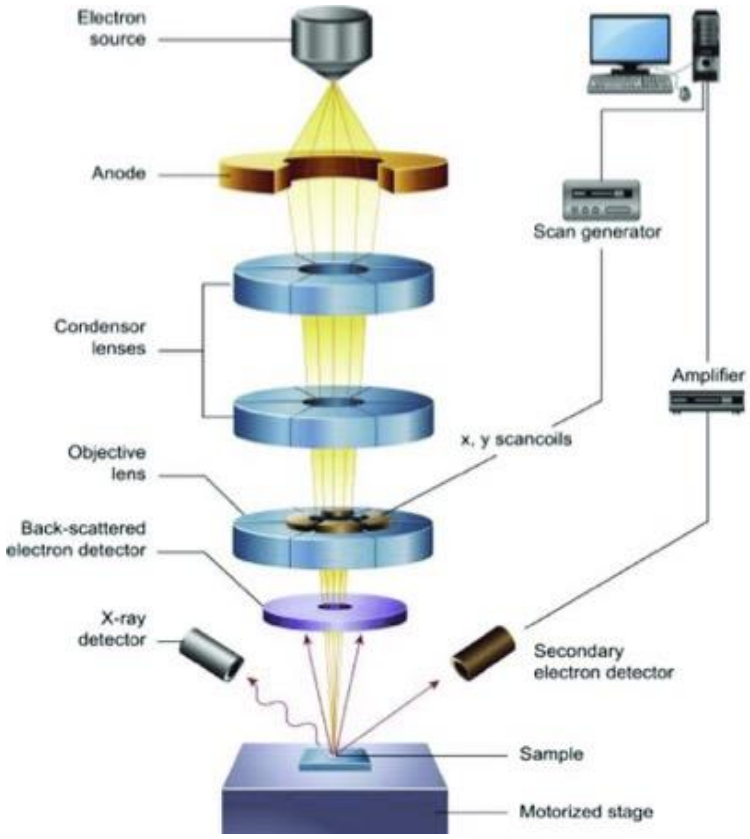

Fig. 2.19 Schematic diagram of Scanning electron microscope[171]

and typically uses either a thermionic or a field emission gun as the electron source, (2) electromagnetic lenses, that control and focus of electron beam and responsible for the resolution and magnification of the images, (3) sample stages, where the sample can be moved, tilted or rotated for precise positioning of the sample, and (4) detectors, where various signal are collected and analyzed according to different requirements.

There are generally 3 types of signals that are created by the interaction of the electron beam with the sample: backscattered electron (BSE), secondary electron (SE2), and X-ray. BSE is the electrons that are scattered back from the sample after interacting with the primary electron beam. These electrons are the reflected electron from the electron source, not ejected from the atoms within the sample. They are high energy electrons ranging from 100 eV to 10 keV, depending on the power of electron source. Due to the high energy, BSE can penetrate through the sample surface and make it less sensitive to surface topography. In addition, SE2 is the secondary electrons with low energy electrons that are emitted from the surface of the sample as a result of interactions with the high-energy primary electron beam. SE2 usually has relatively low energies (<50 eV), and it can only penetrate just a few nanometers below the sample's surface. It is highly sensitive to the surface topography and morphology of the tested sample, so SEM images based on the secondary electron signals provide excellent information about the sample's surface features and topography, making the grain boundaries, surface textures, and edges more visible. To have a clear contract between

those two electron sources, **Fig. 2.20** shows two SEM images resolved from different electron sources, (a) BSE and (SE2), from a same position. It is obvious that the SEM image resolved from SE2 shows incredible topography information, while SEM images derived from BSE shows clear distinction of Metallic particle (in this case, Ni is the lighter spot) verse the ceramic particles (in this case, YSZ is the darker spot).

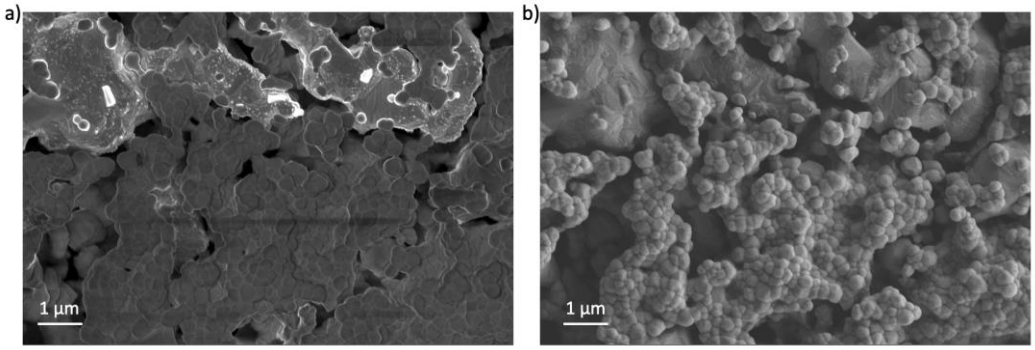

Fig. 2.20 High-resolution SEM images of Ni-YSZ examined by (a) BSE and (b) SE2.

Furthermore, the X-ray emitted from the surface by electron source is also very useful because it can provide valuable information about the elemental composition and distribution in the sample. In addition to SEM, an energy-dispersive X-ray Spectroscopy (EDS) can be coupled to evaluate the characteristic X-rays produced on the sample surface. These X-rays have specific energies that correspond to the difference in energy levels between the electron shells involved, which are unique to each element. An elemental map can thus be generated in parallel with the topography information.

2.6.2 X-ray diffraction

XRD is a powerful non-destructive analytical technique for examine the material crystallinity[57]. The theory behind this technique is based on the elastic scattering of X-rays by the atoms in the material that have a certain crystalline order, resulting in a constructive interference under certain conditions, as known as Braggs law as indicated in the following equation,

$$n\lambda = 2d\ \sin\theta \tag{2.21}$$

Where n is an integer, λ stands for inputting X-ray wavelength, d is the interplanar spacing between the atomic planes in the crystal lattice, and θ indicates the angle of incidence beam. **Fig. 2.21** illustrate the graphical view of the Bragg's law, where a monochromatic X-ray beam shots directly toward the atoms in the crystal, and the scattered X-ray from different atomic planes by different incidence angle will either constructive or destructive interference with each other, forming peaks and troughs respectively. The XRD device will then measure the intensity of diffracted beam as a function of 2θ, creating a diffraction map, also as known as X-ray diffractogram. The map can then be compared and characterized by the pre-existed XRD data, calculating the crestline structure of the tested sample.

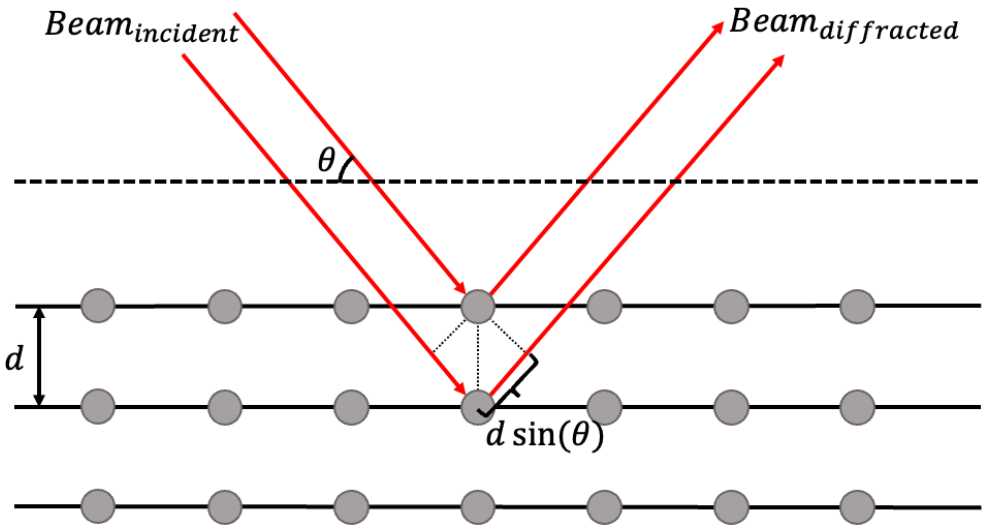

Fig. 2.21 Bragg's law for X-ray diffraction.

Based on the XRD analysis, detailed information about the material's properties and structure can be resolved. Some of the key features and benefits include (1) determining crystal structure (2) study of lattice strain and defect, (3) phase identification, and (4) crystal orientation analysis.

2.6.3 X-ray photoelectron spectroscopy

XPS, also known as electron Spectroscopy for Chemical Analysis (ESCA), is a widely used analytical technique that provides the chemical composition, element valent state as well electronic environment on the very surface (6-10 nm) of the substrate. It is an extremely useful technique for investigating surface properties and composition. Its diverse applications and importance on surface chemistry make it a fundamental tool for researchers and industry professionals alike.

The working principle of XPS is based on the photoelectric effect. As described in **Fig. 2.22**, an incident x-ray with high energy is provided first, then the electrons from the substrate eject and emit photoelectrons. The kinetic energy of the emitted photoelectrons is then identified and can be used to calculate the binding energy (BE) of the electrons using **Eqn 2.22**,

$$BE = hv - (E_{kin} + \Phi) \tag{2.22}$$

where *hv* is the known x-ray incident energy, E_{kin} is the measured photoelectrons kinetic energy, and Φ is a work function-like term for the specific surface of the substrate.

An XPS spectrum is obtained by plotting the intensity of the detected photoelectrons energy with calculated binding energy. The corresponding peaks can be used to identify the elemental composition, and according to the shape and area under the peak, the ratio of chemical energy state can be quantified.

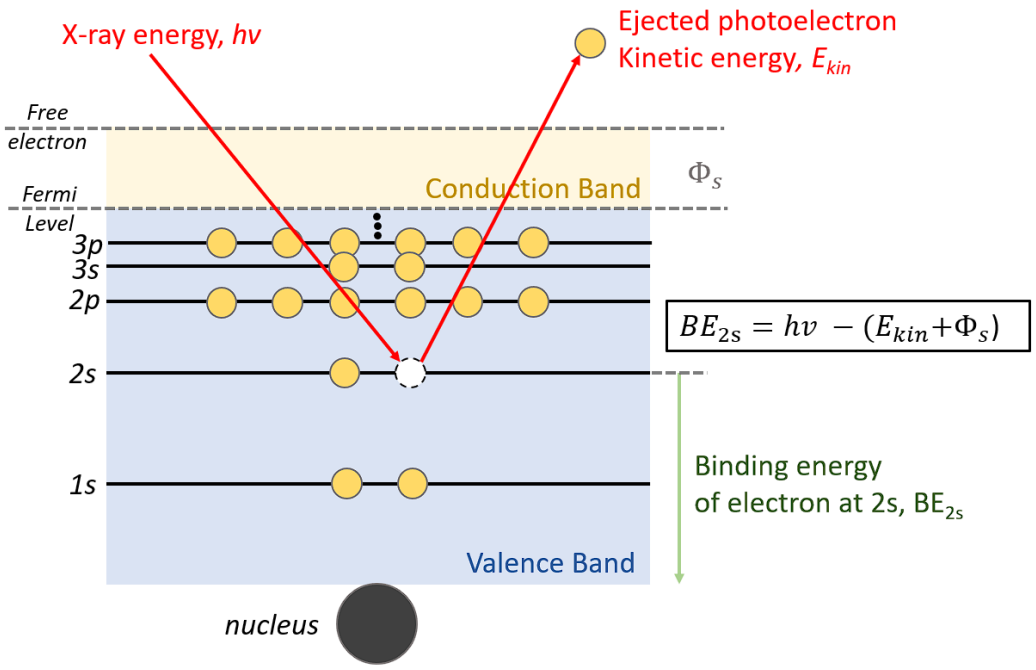

Fig. 2.22 Principle of X-ray photoelectron spectroscopy

2.6.4 Transmission electron microscopy

TEM is a high-resolution imaging technique that can examine the internal structure, morphology, and composition of various materials in the atomic scale. TEM can be sued in a wide variety of fields, such as biology, geology, material science, and nanotechnology.

The working principle of TEM is based on the transmission of electron beam with high energy through an extremely thin specimen. As indicated in the schematic diagram in **Fig. 2.23**, the electron beam is first generated by the electron gun, which is similar to that of SEM. Then, the electron beam is amplified and controlled by a series of electromagnetic lenses and apertures. When the electron interacts with the thin specimen, the electrons can be transmitted, blocked, or scattered by the sample, and detected by the fluorescent screen or the detector, forming image or diffraction pattern according to different electron collecting methods.

There are lots of advantages of TEM that is beyond the limit of SEM. TEM is able to provide detailed information about a material's properties as well as structure and some key applications includes (1) Atomic-level resolution imaging, where it offers exceptional spatial resolution and visualization of the internal structure in atomic scale, (2) structural determination, where enable to characterize the crystal structure, lattice parameters as well as defect analysis, (3) high resolution elemental mapping, where additional EDS feature can be added to resolve the elemental distribution, and (4) in-situ analysis, where allow environmental, such as temperature and bias, changes while imaging.

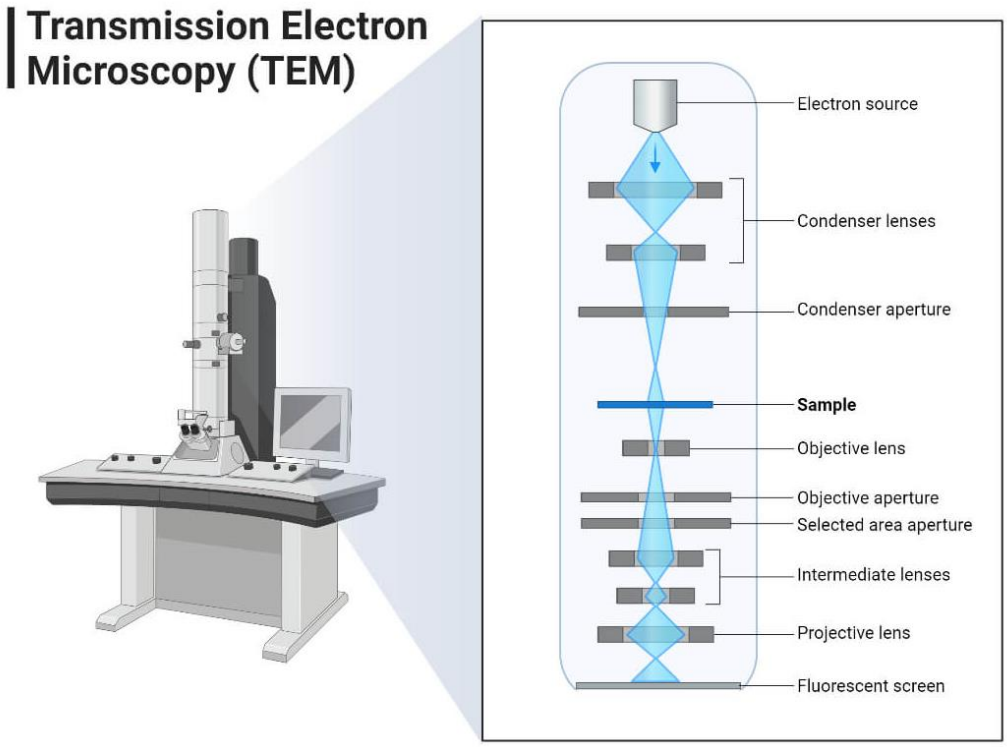

Fig. 2.23 Schematic diagram of Transmission electron microscope[172]

2.7 Electrical Characterization

Besides physical characterizations, electrical characterization is important in understanding the performance, efficiency, and durability of a cell. It provides valuable insights into each electrochemical process, which in turn enables us to further improve the cell performance and durability.

2.7.1 Measurements

Linear scan voltammetry (LSV)

LSV is an electro-analytical technique used to study the redox behavior of the materials by measuring the current response as a function of an applied potential. **Fig. 2.24** indicates the electrochemical system for one of the bare samples for SOCs, in which the potential is linearly swept from 0.3-2V (black) and 2-0.3V (red) with a scan rate of 20 mV s^{-1}, while the current is continuously measured, providing an overall picture of the electrochemical activity of the system. According to the two LSV curves, the two lines exactly overlap except the first 0.1 V of swiping, indicating high reversibility of the system.

There are two main advantages for LSV technique. First, it provides information about the redox properties of the materials, including the number and type of redox species, as well as the thermodynamic and kinetic of the redox reaction. Second, LSV is a very simple technique which can be applied to various systems.

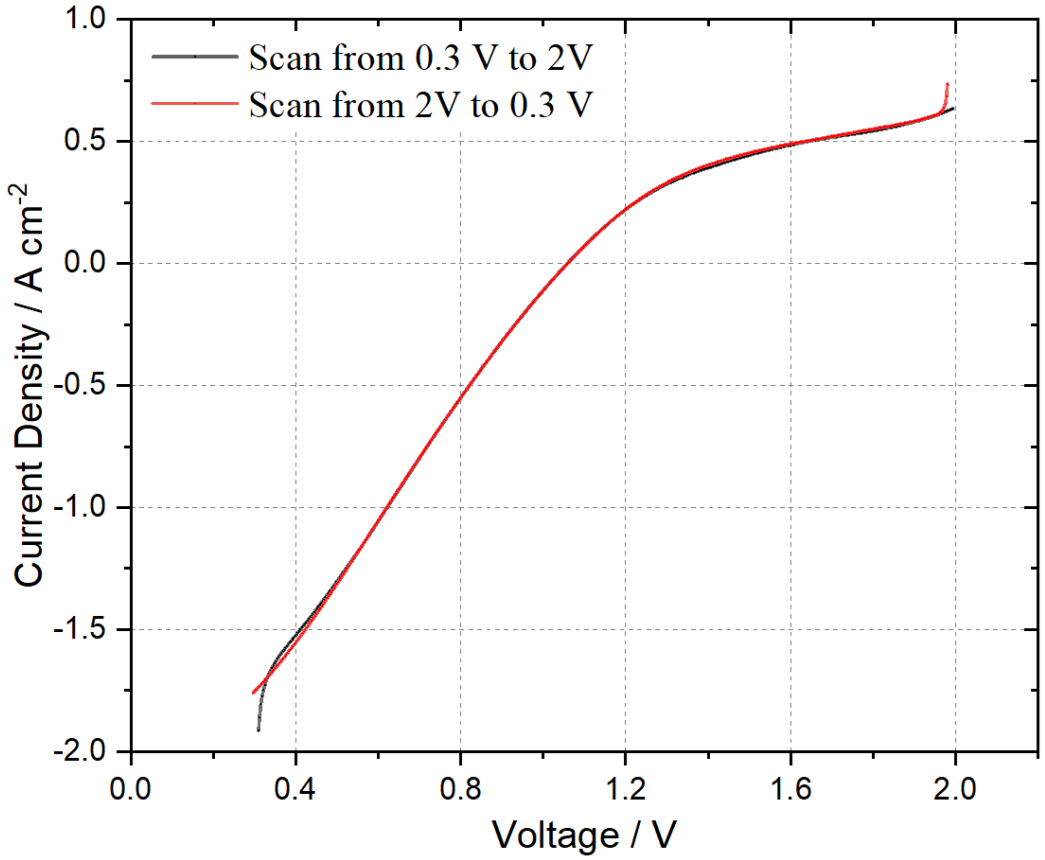

Fig. 2.24 LSV with different scanning direction: Black (from low to high voltage), Red (from high to low voltage).

Electrochemical impedance spectroscopy (EIS)

EIS is widely used to investigate the electrical properties of materials including electrode, electrolyte, and interlayers. The working principle of EIS is to apply a small amplitude sinusoidal voltage (or current) at a specific voltage (or current) load, typically at OCV, measuring the current response. By varying the frequency of the applied sinusoidal voltage, the resulting impedance response is plots, so called Nyquist plot. **Fig. 2.25** shows a series of EIS plots for a typical SOFC at different applied voltage (V). By lowering the potential of a fuel cell, the polarization resistance decreases, which agrees with the theoretical behavior of a fuel cell. EIS is a powerful tool that can provide valuable information about electrochemical processes. The next section will discuss the analytical approaches to understand the electrochemical properties and processes of EIS.

Another advantage of EIS is that it is a non-destructive technique to measure the system response. The measurement can be taken without changing the entire system's properties or structures. This is very powerful for the durability test since the

testing condition is always *in situ* and the additional EIS measurement have little affect while monitoring the electrochemical behavior at the same time.

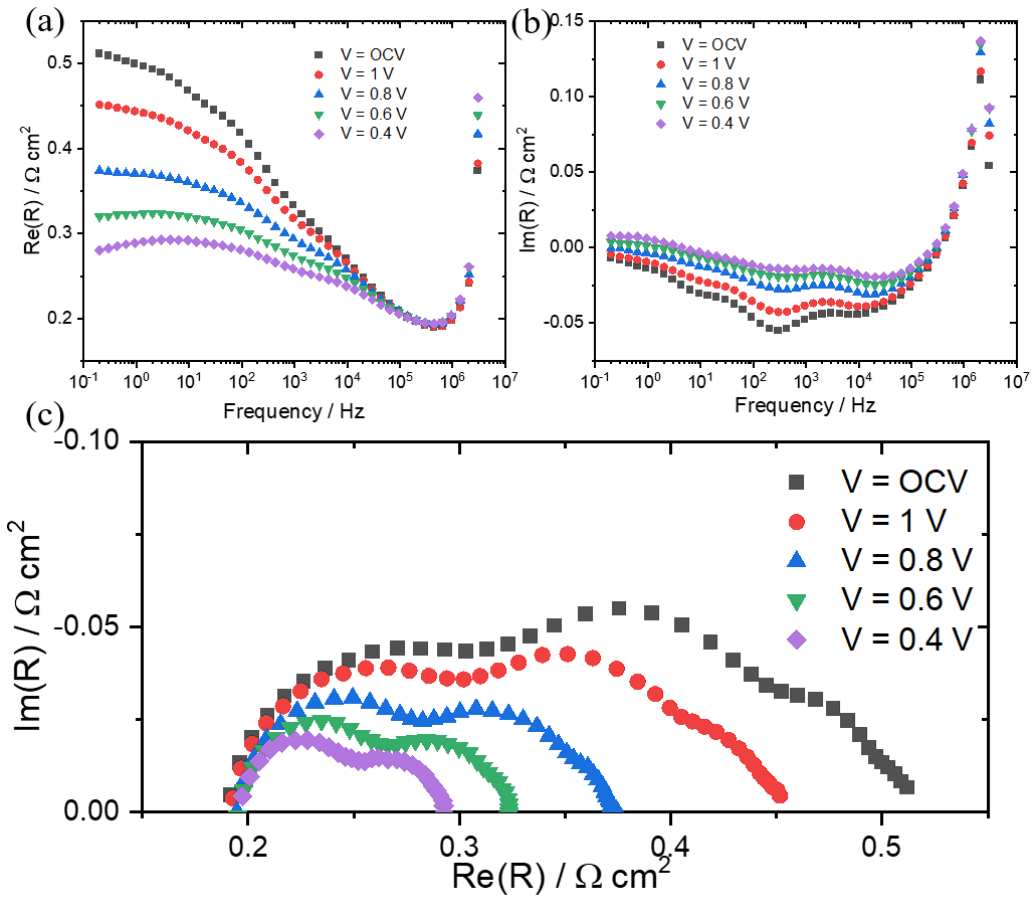

Fig. 2.25 EIS plot at different applied voltages. Frequency verse (a) Re(R) and (b) Im(R) as well as (c) Nyquist plot

2.7.2 Analysis

Equivalent circuit modeling

Equivalent circuit modeling is a power tool to analyze and interpret the data obtained from EIS. Due to the complexity of the EIS data, an equivalent circuit is a simplified electrical network that represents the complex impedance behavior of an electrochemical system. The circuit is composed of common electronic components, including resistors, capacitors as well as inductors, with each element representing a specific electrochemical process occurring at the system's interface.

By simulating the EIS data by an equivalent circuit, it allows us to obtain a more detailed understanding of the electrochemical process occurred in the SOCs system, including information about the number and speed of the different electrochemical procedure. For example, **Fig 2.26** represents an equivalent circuit with the respect of the Nyquist plot of a SOFC sample, where L, R, and Q are inductance, resistance, and constant phase element (CPE), respectively. Because the R_O is in series with the other

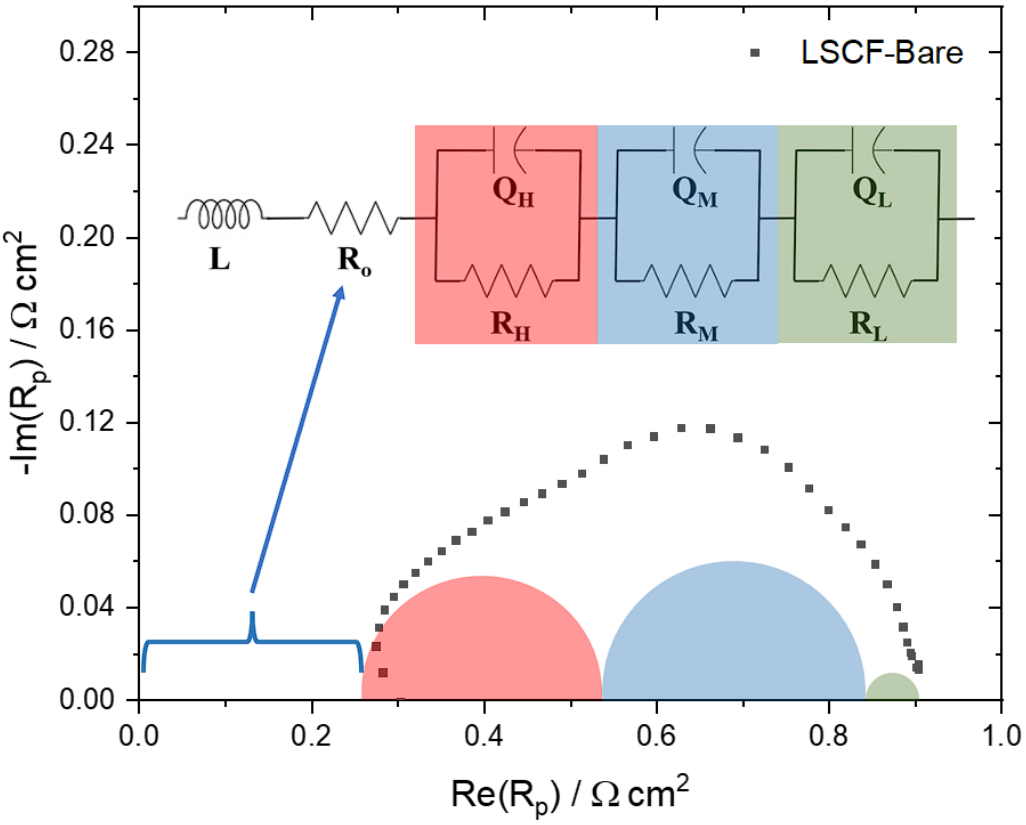

Fig. 2.26 EIS plot and its equivalent circuit

component, the source of R_O can be attributed to the SOC components with no chemical/physical processes involved. Therefore, R_O is attributed ohmic resistance sourced from the ionic movement within electrolyte material (YSZ, GDC, and electrode framework) and connectivity between the electrolyte and electrodes. R//Q component can be used to model the behavior of an electrochemical process, where the resistor represents the resistance of the process, while the constant phase element represents the imperfect capacitance that created based on that electrochemical process. The categories of electrochemical processes are distinguished by its characteristic frequency (f_c) that is correlated with the capacitance of the R//C circuit as shown in **Eqn 2.23**.

$$f_c = \frac{1}{2\pi RC} \tag{2.23}$$

where R and C represent the corresponding resistance and capacitance (translated from CPE). As presented in different colors, the term (R_H//Q_H), (R_M//Q_M), and (R_L//Q_L) denote the RC couples within the high f_c range of 10^3-10^4 Hz, middle f_c range of 10^2-10^3 Hz and low f_c range of 10-10^2 Hz, respectively. In addition, each R//C components can be attributed to (1) oxygen reduction reaction (ORR), (2) oxygen absorption and, (3) gas diffusion process with descending order of f_c.

The advantage of equivalent circuit modeling is that it allows us to design a suitable electrochemical system for specific applications. By fitting the parameters, we

can identify and address issues related to each individual electrochemical process. From the above analysis based on the equivalent circuit modeling, we might conclude that the ORR and oxygen absorption preserved the highest resistance, and the performance can be enhanced by adding catalyst on those two electrochemical processes.

In summary, equivalent circuit modeling is an important tool for analyzing EIS data because it provides a detailed understanding of the electrochemical processes within the system, allowing us to optimize the performance based on the existing assumptions.

Distribution of relaxation time (DRT)

The DRT is a mathematical approach for translating and analyzing EIS data. It is important because it provides a more detailed and precise understanding of the electrochemical behavior of the system. The distribution reflects the range of time scales associated with different electrochemical processes, with the longer/shorter relaxation times indicates the electrochemical process is slow/fast, respectively. The calculation of DRT can be represented as **Eqn 2.24**,

$$Z^*(\omega) = R_\infty + j\omega L + \int_{-\infty}^{+\infty} \frac{\gamma(\ln \tau)}{1 + j\omega\tau} d(\ln(\tau)) \tag{2.24}$$

Where R_∞ is the ohmic resistance, L is the system induction, and $\gamma(\ln \tau)$ is the DRT, which is a function that describes the time relaxation characteristics for a selected electrochemical system. $\tau = RC$ is the relaxation time, where R and C are effective resistance and capacitance, respectively. ω is the angular frequency.

For example, **Fig. 2.26a** shows an EIS plot of a fuel-cell SOFC test with LSCF as the air electrode (same plot as the previous section), and the EIS can be deconvoluted into three R//C components by looking at the graph itself. However, by applying DRT analysis (**Fig. 2.26b)**, five distinctive can be observed as indicated by different colors, which is more complicated than the modeled equivalent circuit. By comparing and correlating the frequency back the EIS plot(as indicated in the same colors), we might

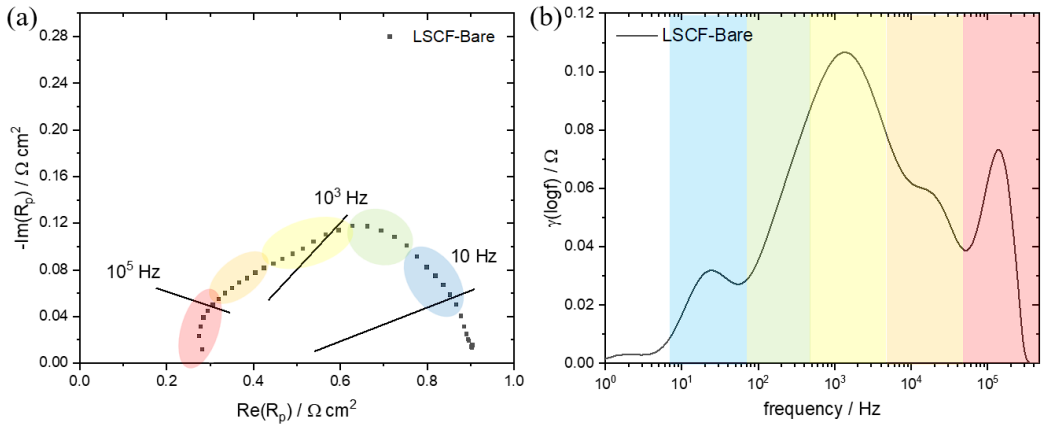

Fig. 2.27 (a)EIS plot and its corresponding (b)DRT plot.

conclude that the red peak is not represented in the EIS plot, and the first R//C component relates to the combination of orange and yellow peaks in the DRT, the second R//C component relates to the combination of yellow and green peaks in the DRT, and the last R//C component relates to the blue peak in DRT. We, therefore, have a deeper understanding of the system's behavior and ultimately correlated it with the assumptions. Furthermore, from the DRT plot, the peak at 10^3-10^4 Hz is significantly higher than that of the other f_c, indicating the bottle neck of the system is the electrochemical process corresponding to a f_c within10^3-10^4 Hz.

In conclusion, DRT is a powerful tool for analyzing EIS data, especially when the electrochemical behavior is very complex and cannot be easily adequately described by a simple equivalent circuit model. In addition, DRT also provides information about the speed of the electrochemical process at each f_c, allowing us to have a deeper understanding of the system and design more effective electrochemical systems.

Activation energy (E_a)

The E_a of an electrode is a measure of energy required to initiate an electrochemical reaction at the electrode in SOCs. EIS data can be used to estimate the E_a by analyzing the polarization resistance (R_p) with different applied temperatures.

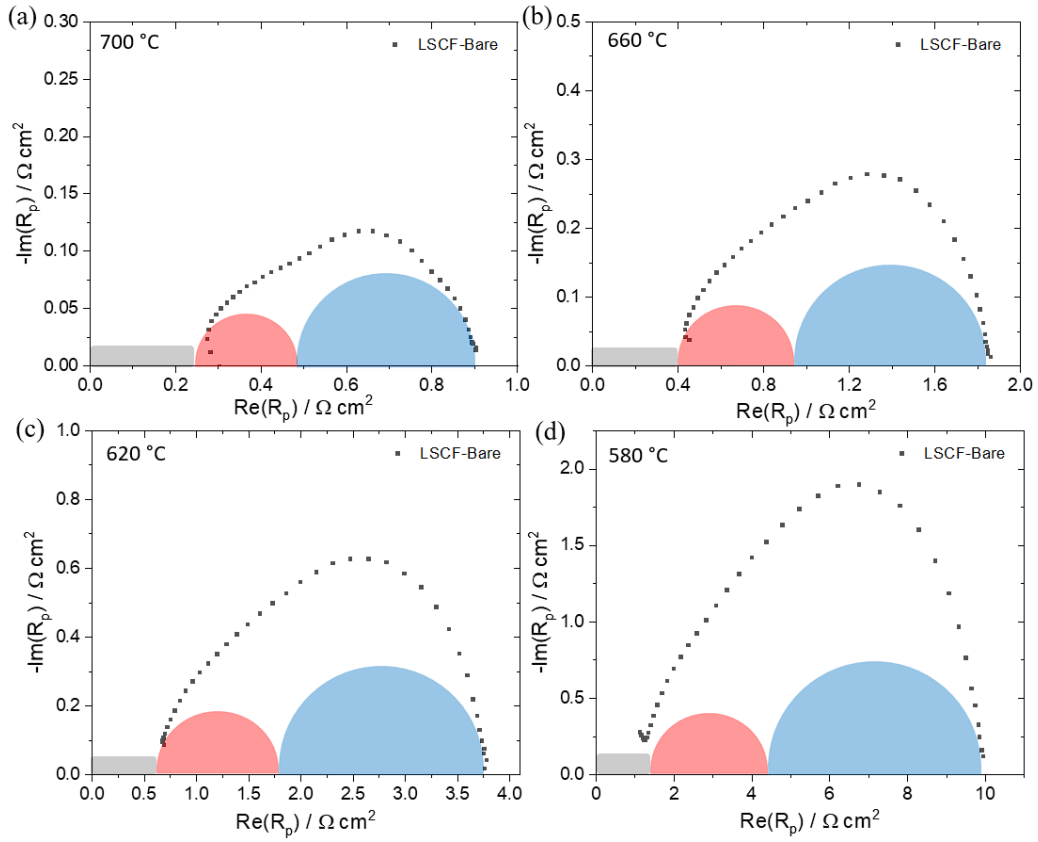

Fig. 2.28 EIS measurement at (a)700 ºC, (b)660 ºC, (c)620 ºC, and (d)580 ºC. Resistance colored in gray, red, and blue indicate R_{ohm}, R_p with high f_c and R_p with low f_c, respectively.

The activation energy of the SOFCs is temperature dependance and can be calculated by the Arrhenius relationship as indicated in **Eqn 2.25**.

$$R_p = A\, e^{-E_a/k_B T} \tag{2.25}$$

Where A is the pre-exponential factor, k_B is the Boltzmann constant. Normally the E_a is in a unit of [eV], so here $k_B = 8.617 \times 10^{-5}\ eV/K$.

Fig. 2.28 shows the EIS measurement over a range of temperatures and data can be deconvoluted into three part, R_{ohm}, $R_{p\text{-}HF}$, and $R_{p\text{-}LF}$ which correspond to ohmic resistance, polarization resistance respective to high f_c, and polarization resistance respective to low f_c. The Arrhenius plot can thus be plotted as shown in **Fig. 2.29**, where the E_a can be calculated based on the slope (k) of the linear fitted data.

$$E_a = k * k_B \tag{2.26}$$

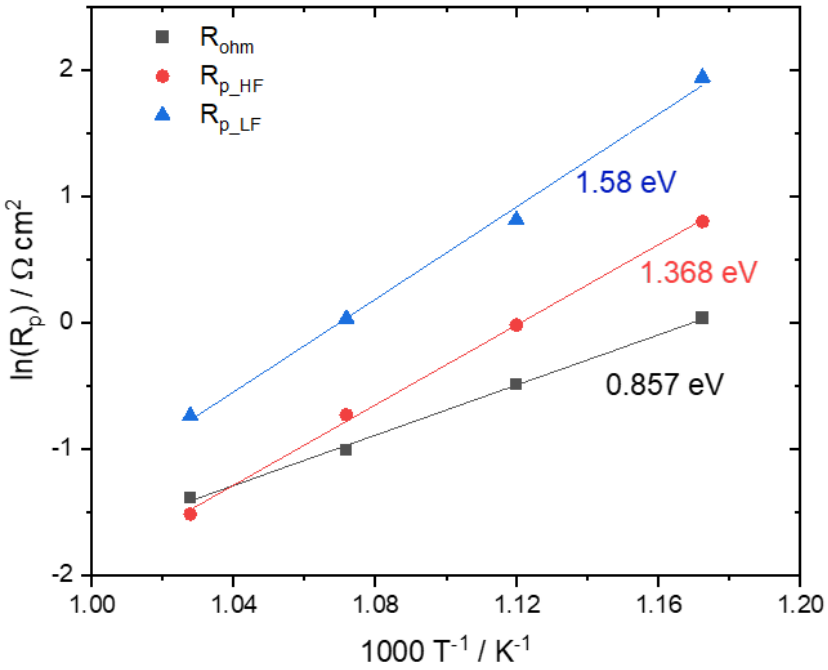

Fig. 2.29 Arrhenius plots for each resistance colored in black, red, and blue indicating R_{ohm}, R_p at high f_c and R_p at low f_c, respectively.

Therefore, the E_a is an important parameter that can provide insights into the kinetics and speed of electrochemical reactions occurring within the electrode. By understanding the activation energy of the electrode, researchers can optimize the electrodes for specific requirements, such as improving ORR or OER kinetics, enhancing gas diffusion, and facilitating gas absorption process.

Rate limiting step

The performance of SOCs is often limited by the rate of the electrochemical reactions at the electrodes. Determining the rate limiting step is crucial for understanding the bottleneck and optimizing the electrodes of SOCs. One way to identify the rate limiting step is to evaluate the impedance with varying environmental factors, such as partial pressure of oxygen (P_{O2}) or hydrogen (P_{H2}). In my study, different impedances are measured at various P_{O2}, while keeping other parameters constant. The rate limiting step can then be estimated using the following relationship,

$$R_p \propto {P_{O2}}^m \tag{2.26}$$

Where R_p is the polarization resistance, and m is the determination of rate-limiting step where it is oxygen absorption (m = 1), oxygen dissociation and diffusion (m = 1/2), charge transfer (m = 1/4), and ionic incorporation (m = 0).

Fig. 2.30 are the EIS curves in different P_{O2} of a symmetrical cell with LNF as the electrode. EIS curves obtained for the cell could be reasonably well fitted to a double arc-based L-R_o-(R_H//Q_H)-(R_L//Q_L) model, where R_H is the R_p at high f_c, and where R_L is the R_p at low f_c. It is clear from **Fig. 2.30b** that the rate limiting step of R_H is the combination of ionic incorporation and charge transfer, and that of R_L is the combination of oxygen adsorption and oxygen dissociation and diffusion. This makes sense because the additional low-frequency arc that appears at low oxygen activities (< 0.1 atm) can be ascribed to a mass transport polarization, which is aligned with the m value.

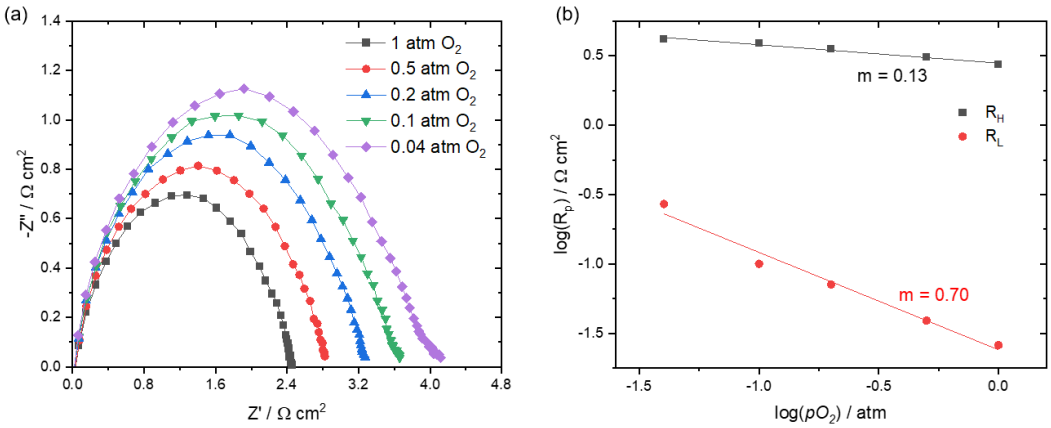

Fig. 2.30 (a) Nyquist plot of LNF bare sample obtained at various pO_2 and (b) corresponding polarization resistances versus pO_2 graph; here, the polarization resistances are acquired by fitting the EIS data to R-L-R_o-(R_H//Q_H)-(R_L//Q_L). R_H and R_L corresponds to polarization resistances with higher and lower characteristic frequencies.

In conclusion, determining the rate-limiting step is critical for optimizing the performance of SOCs. Similar to the other three factors mentioned above, researchers can optimize the electrodes for specific requirements.

Chapter 3: Literature Review

3.1 Cathode Degradation Mechanisms

3.1.1 Particle agglomeration

Agglomeration refers to the process in which small particles merge to form large ones. This phenomenon is undesirable for SOFC electrodes, as it leads to a reduction in the surface-active area. Agglomeration occurs through various mechanisms, such as chemical, mechanical, physical, and electrical interactions. As SOFCs primarily operate at elevated temperatures ranging from 600~1000 °C, the high surface energy between particles becomes the main driving force for agglomeration. For example, Matsui et al. observed significant agglomeration of the LSCF phase after 400 hours of operating at 1000 °C[58]. This results in a considerable reduction in the triple-phase boundary (TPB) length of the electrode, leading to performance degradation.

Cation segregation is another driving factor of agglomeration. Cations segregate from the lattice and form oxide or hydroxide on the surface, which will form a bridge between particles and further agglomerate the electrode. As depicted in **Fig. 3.1**, when particle agglomeration occurs, the surface area significantly decreases, and the performance will drop substantially.

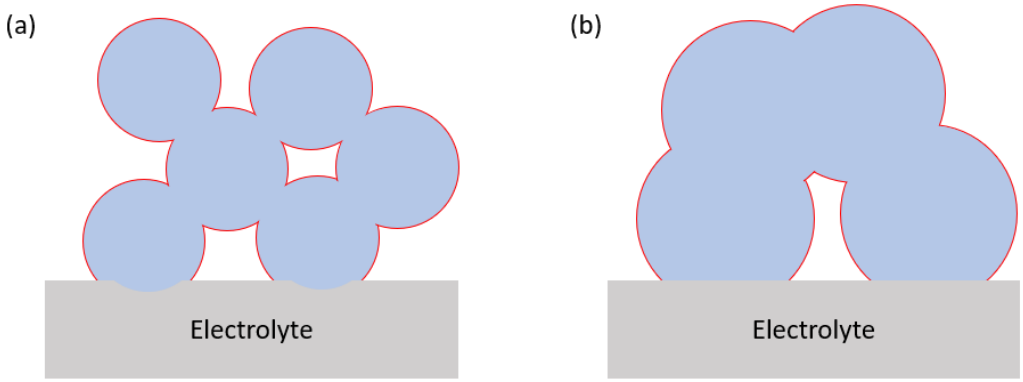

Fig 3.1 Schematic diagram of particles at (a) initial stage and (b) final stage of operating at evaluated temperature. Red line indicated the surface activate site.

3.1.2 Cation segregation

Cation segregation itself is another major cause of performance degradation and is associated with the distribution of cations and the accumulation of surface cation oxides. The segregation of A-site dopants, especially Sr, in advanced electrode materials such as LSCF, LSC, and LSM plays a significant role in the long-term performance of air electrodes. The segregated Sr tends to form SrO or $Sr(OH)_2$, occupying active sites for both oxygen reduction reaction (ORR) and oxygen evolution reaction (OER). Segregated SrO or $Sr(OH)_2$ are highly mobile on the electrode surface

and can promote particle agglomeration or react with electrolyte materials, forming an insulating $SrZrO_3$ layer[59]. Moreover, surface-segregated SrO or $Sr(OH)_2$ can react with volatile materials in interconnectors or impurities in the surrounding gas, forming inert products such as $SrCrO_4$ and $SrSO_4$, which poison the electrode and cause significant performance degradation[60]. While many researchers have established that A-site segregation, especially with Sr, has a detrimental effect on material performance, there is some conflicting evidence suggesting otherwise. For example, Yipeng et al.[61] calculated each individual active sites on the surface and posited that additional Sr on the electrode surface is not inherently negative. The work suggested that the catalytic activity of Sr is much higher than La in the same A-site although it is lower than that of Co in the B-site, In addition, Dawei et al.[62] performed an *in situ* study to demonstrate that electrode degradation is not caused by segregated Sr element, but rather the hydroxide group on the surface.

Among the existing theories regarding the driving force and mechanisms of Sr segregation in perovskite materials under operating conditions, electrostatic and elastic interactions are the most widely accepted explanations. Due to the size mismatch between A-site elements, La and Sr, Sr^{2+} in the lattice undergoes a compressive strain as size of Sr^{2+} ion is 5.9% larger than that of La^{3+}. Consequently, Sr^{2+} in the lattice tends to migrate to the surface and release its stress, eventually forming SrO and $Sr(OH)_2$. According to this theory, the magnitude of Sr segregation can be reduced or enhanced by applying additional compressive or tensile strain on the electrode material. Sharma et al.[63] performed a first-principles calculation to find that higher oxygen pressure causes more oxygen atoms to incorporate into the lattice and leads to lattice size shrinkage. As a result, dopants experience higher strain energy, which accelerates Sr surface segregation.

Due to the substitution of Sr^{2+} with A-site La^{3+} in perovskite structure material, a negatively charged defect Sr'_{La} is produced along with oxygen vacancies $V_O^{\bullet\bullet}$ for charge neutralization. On the surface, the oxygen vacancy concentration is typically much higher than in the lattice due to structural inbalances. The electrostatic force created by the Sr'_{La} and $V_O^{\bullet\bullet}$ drives Sr toward the surface, where it combines with oxygen from the air to form SrO or $Sr(OH)_2$. When additional cathodic polarization is applied to increase the amount of oxygen vacancies on the surface, LSC-based electrodes exhibit significant Sr segregation[64]. However, for LSM electrodes, the opposite behavior is observed under cathodic polarization[65]. Sr de-segregation (incorporation) is observed for LSM when extra oxygen vacancies are introduced on the surface.

3.1.3 Chromium deposition and poisoning

Cr deposition and poisoning is an issue[66] not because of the cell itself, but the surrounding environment. SOFCs typically utilize chromia-forming alloy as the material of interconnector. At operating temperatures ranging from 800-1000 °C,

volatile Cr species are generated from the interconnector, which eventually deposit onto and poison the electrode surface. Over time, the surface becomes covered by these inert species, resulting in reduced overall performance.

The volatility of Cr species tends to increase under high oxygen and water partial pressure, making the vaporization and poisoning of Cr species a primary concern at the cathode site of SOFCs. Thermodynamic calculations indicate that $CrO_2(OH)_{2(g)}$ is the dominant vapor species within the temperature of 800 °K to 1600 °K. Cr volatility peaks when oxygen and water content are approximately equal and drops significantly if either O_2 or H_2O content reduce[66].

In addition to Cr deposition via vaporization, Cr contamination can also occur through direct contact between the cell and Fe-Cr alloy interconnector. Tucker et al.[67] found that MnO_x and Co_3O_4 oxides incur significant Cr surface diffusion, forming $Mn_xCr_{3-x}O_4$ and $Cp_{3-x}Cr_xO_4$, as well as SrO. However, under SOFC operating conditions, formation of $SrCrO_4$ is mainly observed between LSCF and Fe-Cr alloy.

The volatility of Cr species from chromia-forming alloys not only depends on the oxygen-to-water ratio, the presence of metal oxides on the sample surface and at the sample-interconnector interface, but also on the composition of the interconnector itself. For instance, the transport or vaporization of Cr species can be significantly reduced by coating an additional layer of $(CrMn)_3O_4$ spinel material. Moreover, the vaporization rate of iron-based alloys is much lower than that of chromium-based alloys[68]. Studies on Cr poisoning using LSM cathode materials have shown that employing a Ni-Mo-Cr alloy as interconnector as could massively reduce the Cr deposition and poisoning compared to conventional Fe-Cr alloy[69].

3.2 Approaches to Improve Cell Performance/Durability

3.2.1 Alloying

Alloying is a technique that combines multiple materials, creating a multi-phase structure for the electrode. Distinct from a single-phase electrode, incorporating an additional electrolyte phase can extend the activation sites and improve durability. Furthermore, contemporary MIEC cathode materials with high ionic conductivity typically exhibit a relatively high TEC (refer to **Table 2.1**) compared to common electrolyte materials. Alloying with additional electrolyte materials enables the reduction of the TEC. Li et al.[70] assessed the TEC for LSCF with different concentrations of GDC observed a decreasing trend as the amount of GDC increase.

Alloying also promotes the combination of each individual material. For instance, strontium-doped lanthanum manganite (LSM) possesses excellent electronic conductivity (approximately 200S cm^{-1} at 800 °C[71]) but negligible ionic conductivity (approximately 10^{-16} cm^2 s^{-1} at 700 °C[72]). As a result, most of the reactions occur at the electrode-electrolyte interface. As illustrated in **Fig.3.2** the majority of the oxygen reduction reaction (ORR) takes place in the area marked in red. By introducing an additional electrolyte phase (**Fig. 3.2b**), the activation site expands from a 2-

dimensional area between the electrolyte and electrode (**Fig.3.2**) to a 3-dimensional volume throughout the electrolyte path. Murray and Barnett[73,74] demonstrated that the addition of GDC or YSZ to an LSM backbone significantly reduces electrode polarization resistance (R_p).

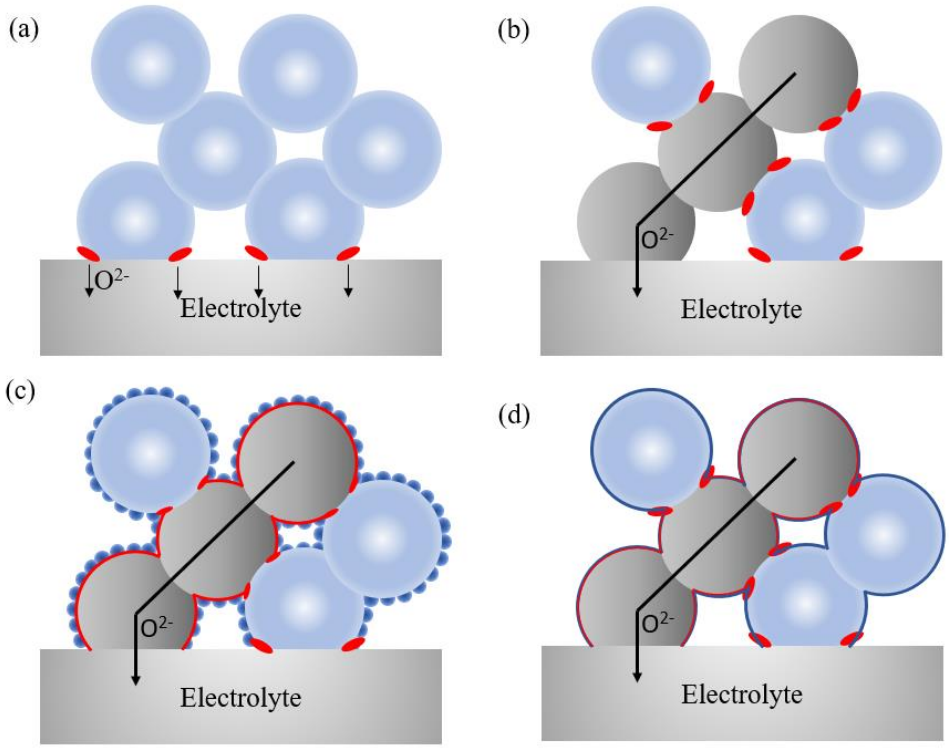

Fig. 3.2 Illustration of activated site marked by red area. (a) electrode with pure cathode material. (b) electrode with mixed cathode/electrolyte material. (c) solution-based infiltrated on mixed cathode/electrolyte material. (d) mixed cathode/electrolyte material with catalytic materials by ALD

3.2.3 Doping

Doping is a technique that involves the deliberate introduction of impurities into a backbone material. Perovskite materials, which possess an ABO_3 structure as described in the former chapter, are frequently employed for this purpose. By doping different elements at the A-site or B-site, it is possible to facilitate electrical, electrochemical, or thermal expansion characteristic tailored to the requirements of SOFCs. However, doping necessitates the re-synthesis of chemicals from the initial stage and primarily alters the intrinsic properties of the material (e.g., enhancing conductivity, reducing material strain, etc.), while most reactions occur on the surface.

By substituting the lower oxidation state Sr^{2+} with La^{3+} on A-site oxygen vacancies are generated due to charge and size mismatches, resulting in ionic conduction within the material. The material also exhibits significant electronic conductivity, attributable to p-type conduction influenced by oxygen vacancies.

Nevertheless, Sr^{2+} is prone to surface segregation, forming an inert SrO or $Sr(OH)_2$ layer while reducing the dopant percentage in the lattice and subsequently diminishing its ionic and electronic conductivity. Investigations involving various dopants have been conducted to elucidate the underlying cause and to mitigate or eradicate the segregation. For example, by modifying the Sr^{2+} dopant percentage on the Asite, researchers identified a trend wherein decreasing the Sr content led to reduced segregation[75,76]. Other elements akin to Sr^{2+}, such as Ca^{2+} or Ba^{2+}, have been co-doped onto the A-site alongside Sr^{2+} to diversify material properties.

Although incorporating dopants with reduced oxidation state can diminish the overall positive charge with the lattice, the formation of oxygen vacancies is heavily reliant on the reducibility of B-site transition metals[77] (Co, Fe, Ti, Mn, etc.) as outlined in **Eqn 3.1**.

$$2B_B^{\times} + O_O^{\times} \rightarrow V_O^{\bullet} + 2B_B' + \frac{1}{2}O_2 \tag{3.1}$$

In this equation, '•' and '′' denote positive negative overcharges, respectively, while '×' indicates neutral charge.

Thus, doping at the B-site is equally crucial for altering material properties. For instance, oxygen vacancies tend to be produced by the B-site cation with a lower oxidation state, where the cation's size is larger than its initial state. By doping an element with smaller ionic radius, the B-site cation is compelled to expand its size, leading to a lower oxidation state and the formation of additional oxygen vacancies [78]. A similar analogy can be applied to the A-site, Merkle et al.[79] employed density functional theory (DFT) calculations and discovered that by doping A-site cations with larger Ba^{2+} cations on LSC electrode, the formation energy of oxygen vacancies could be reduced by 0.3 eV, potentially resulting in lattice expansion and low-valence state of Co on the B-site.

3.2.3 Surface engineering

The chemical behavior of an electrode's surface can significantly difference from that of its bulk, primarily due to the varying completeness of surrounding molecules, with half of the elements exposed to the air, are less stable compared to those within the lattices. Moreover, since electrochemical reactions occur at TPBs where ions, gases, and electrons converge, surface engineering serves as a more direct approach to enhance catalytic activity and address durability issues.

Maintaining the consistency of thermal expansion coefficients (TECs) between electrode and electrolyte materials is crucial, which consequently limits electrode selection. Surface treatment and substrate engineering can introduce a range of materials with high catalytic activity but poor compatibility, without significantly altering the TEC of the electrode material. Surface treatment methods can be broadly categorized into chemical or physical deposition. Infiltration/impregnation is a technique that physically deposits metal precursors into a rigid and pre-fired electrode

or electrode scaffold[49] using a liquid precursor solution. Following an additional sintering process, a nanoscale electrode forms on the electrode backbone. This technique not only significantly enhances electrochemical activity but also vastly extends TPB activation sites from the electrode-electrolyte interface to the entire electrolyte surface when applied to an electrode/electrolyte mixed framework, as illustrated in **Fig. 3.3c**. Similar structures can be created by immersing a sample cell in a liquid solvent containing a formulated metal precursor, followed by drying and sintering. However, the distribution of nanoparticles formed by infiltration is not uniform, as the solvent tends to follow according to gravitational force. Researchers have attempted to improve uniformity by adding additional surfactants or complexing agents [51,52].

ALD and chemical vapor deposition (CVD) are methods that chemically deposit precursors onto the electrode surface through a gaseous medium. Unlike infiltration, ALD and CVD can create an even finer and more uniform overcoat layer. Catalytic activity can be modified by an ultra-think overcoat, as evidenced by the reduction in R_p [80]. Nonetheless, due to the overcoat's low thickness and absence of p=type or n-type conduction, electronic conductivity is limited, hindering electron transportation from the activation site.

Plasma layer deposition (PLD) is a technique that deposits an atomic-level controlled amount of overcoat onto an electrode surface. Although the deposition process is precise, its rate is low, rendering it suitable for commercialized mass production. PLD is an ideal tool for single-crystal electrolyte or electrode research. For instance, Cai at al.[30] employed PLD to grow LSC on single crystal YSZ (100) at 450 and 650 °C with 200 nm thickness, discovering a phase change from Sr to $SrO/Sr(OH)_2$ at higher temperature, while no phase change was detected at 450 ºC. Jalili et al.[81] deposited a 10-nm-thick LSM film onto single crystal STO (001) and LAO (001) using PLD to observe in-plane tensile strain and compression strain, finding that SrO segregation has a positive relationship with surface oxygen vacancies. Such studies are vital for understanding the underlying causes of low catalytic activity or poor durability in SOFCs.

3.3 Application of Infiltration/Wet Impregnation

3.3.1 Infiltration for SOFCs

In recent years, infiltration has been significantly developed, resulting in a diverse range of operations. The most prominent advantage of solution-based infiltration/ impregnation is the substantial improvement of electrochemical performance. This technique is typically employed in two primary categories of electrode skeleton: mixed ionic and electronic conducting (MIEC) electrodes and ion-conducting electrodes.

In the case of MIEC backbones, the electrochemical properties on the electrode surface can be significantly enhanced through the additional phases generated by

infiltration, while the backbone ensures electron conductivity throughout the electrode. For instance, the electrode polarization resistance (R_p) of conventional porous LSM at 700 °C is approximately 11.7 Ω cm^2. Jiang et al.[82] demonstrated a 56-fold reduction (0.22 Ω cm^2) of R_p with infiltration of 5.8 mg cm^{-2} GDC nanoparticle upon the LSM backbone. The phase of the infiltrated particles also plays a crucial role in the surface activity. Xu et al.[83] infiltrated Co_3O_4 nanotubes with exposed (001) planes into LSM electrode backbone, achieving a peak power density of 500 mW cm^{-2} at 600 °C, whereas the commercial Co_3O_4 (with no orientation) yielded only 179 mW cm^{-2} at 600 °C. It was determined that Co_3O_4 with (001) planes exhibited the lowest oxygen adsorption and oxygen dissociation energies compared to other planes. Additionally, precious metals or oxides were also employed as potential candidates for infiltration. For example, Sahibzada et al.[84] and Chen et al.[85] infiltrated Palladium (Pd) and Pd-Ce onto the LSCF electrode, revealing that the additional infiltration nanoparticles not only decreased the electrode R_p, but also significantly reduced the activation energy. Furthermore, Wang et al.[86] and Mori et al.[87] utilized Ag as the precursor for infiltration, resulting in a marked improvement in performance and reduction in cell R_p.

On the other hand, the performance of infiltrated MIEC materials on electrolyte skeleton backbone is also noteworthy compared to traditional mixed electrode/electrolyte electrodes. Liang et al.[88] investigated the performance difference between LSM/YSZ composite electrodes and infiltrated LSM nanoparticles on porous YSZ backbones under identical operating conditions at 600 °C, observing a 44-fold R_p reduction in the latter case. The most distinct advantage of solution-based infiltration is the flexibility in material selection. Due to the compatibility requirement between the electrode and electrolyte material, highly active materials cannot be incorporated. However, infiltration permits the use of these materials without altering the structural properties of the electrode. For instance, Pd is a noble metal with excellent catalytic activity at intermediate temperatures. Liang et al.[89] fabricated nano structured Pd/YSZ by infiltrating Pd onto a porous YSZ electrolyte framework, resulting in an R_p of 0.22 0.22 Ω cm^2 of R_p at 700 °C, which is significantly better than traditional electrode/electrolyte composite electrodes.

Nonetheless, the high operating temperature can pose challenges. If the infiltrated nanoparticles within the electrode operate at an elevated temperature, these nanoparticles tend to agglomerate, thereby reducing the catalytic active site and cell performance. Long-term durability remains an issue, even though the initial performance is significantly enhanced.

3.3.2 Infiltration for SOECs

As the cell structure and components are nearly identical between SOFCs to SOECs, the infiltration can also be applied on two general categories of electrode skeleton: MIEC electrodes and pure ion-conducting electrodes. To enhance the electrochemical activity of the MIEC type of electrode, Ge et al.[90] demonstrate a simple strategy to significantly enhance the catalytic activity of conventional air electrode,

such as LSM, LSC and LSCF, through a one-step urea-based infiltration of Pr_6O_{11}. The approach increased the current density at 1.28V from 69 mA cm^{-2} to 308 mA cm^{-2} (LSM backbone), from 109 mA cm^{-2} to 235 mA cm^{-2} (LSCF backbone), and from 150 mA cm^{-2} to 293 mA cm^{-2} (LSC backbone). The enhancement in performance is explained by the higher surface kinetics for the OER reaction. In addition, infiltration of single-phase precious metal oxide nanoparticles, such as PdO, PtO, RuO, can improve the catalytic activity of the conventional electrode and greatly improve the maximum power density. However, these nanoparticles tend to grow and agglomerate, decreasing the catalytically active surface area and causing poor cell stability. To address the issue, Tan et al.[91] applied a co-infiltration of PdO with ZrO_2, which enhanced the electrocatalytic activity and stabilization from agglomeration. The cell with additional PdO/ZrO_2 infiltration reached 2.322 A cm^{-2} at 2.0 V at 750 ºC, and the increase in performance is attributed to the enlargement of active sites on the electrode and length of TPB, while the PdO particle catalysts promote the mass transport process. Furthermore, Tong et al.[92] applied a hybrid catalyst coating that combines GDC with Pr_6O_{11} on the LSF backbone air electrode and reported a high current density of 1.62 A cm^{-2} at 1.3V at 750ºC, as well as promising durability behavior. The active surface area is enlarged by the GDC nanoparticles, and the enhanced performance mainly occurs in the characteristic frequency range from 10^1 to 10^2 Hz, which can be attributed to the OER reaction.

In addition to single-phase nanoparticles, MIEC materials have also been used as infiltration agents. Zhang et al. [93] reported a more than 2-fold increase in current density (from 0.23 A cm^{-2} to 0.54 A cm^{-2}) by infiltrating $SrTi_{0.3}Fe_{0.6}Co_{0.1}O_{3-\delta}$ (STFC) into LSM-YSZ electrode backbone at 1.3 V at 650 ºC. The performance enhancement is correlated with the reduction in response peak at ~10^2 – 10^3 Hz, which corresponds to the OER reaction in the air electrode. Lee et al.[94] applied urea-based infiltration of highly active-nano catalyst, $Sm_{0.5}Sr_{0.5}CoO_3$ (SSC), to a LSCF-GDC composite backbone and observed extremely fine nanoparticle crystals anchored on the backbone, resulting in a performance enhancement from 0.9 A cm^{-2} to 1.8 A cm^{-2} at 1.29V at 750 ºC. The presence of SSC nanoparticles is attributed to accelerating the rate-limiting step and reducing the low-frequency impedance arc. Furthermore, Yoon et al.[95] developed a model to study the correlation between the performance and infiltrated nanoparticles, and their results provided evidence for the effectiveness of infiltration in enhancing the electrochemical activity of air electrodes.

The infiltration technique can also be applied to ion only conducting scaffolds, as opposed to MIECs, which offer several advantages, such as wider and continuous paths for oxygen ion transportation and thermal stability under typical operating temperatures. However, infiltrating catalytically active species on these scaffolds requires a larger load of surface-infiltrated particles to secure decent electronic pathway between each individual nanoparticles and the current collecting mesh [96]. Fan et al.[97] showed that infiltrating $La_{0.6}Sr_{0.4}FeO_{3-\delta}$ (LSF) nanoparticles into a porous YSZ scaffold increased current density due to the extension of TPBs. Wang et al.[96] achieved

extraordinary electrolysis performance, 5.31 A cm^{-2} and 4.09 A cm^{-2} at 1.3V at 800 ºC and 750 ºC, respectively, by infiltrating Pr_6O_{11}-SDC and Ni-SDC on the SDC scaffold on the air and fuel side, respectively. Chen et al.[98] also implemented the infiltration technique on both electrodes, achieving 2.05 A cm^{-2} at 1.3V at 800 ºC by infiltrating SDC nanoparticles on a YSZ scaffold on the fuel side and Nd_2O_3-$Nd_2NiO_{4+\delta}$ (Nd_2O_3+NNO) nanoparticles on an SSZ air electrode.

3.4 Application of Atomic Layer Deposition

3.4.1 ALD for SOFCs

ALD has emerged as a leading surface treatment technique to address the challenges associated with SOFC electrodes, particularly in terms of poor long-term stability and low catalytic activity. While there has been a significant improvement in the initial performance of SOFCs, ensuring long-term sustainability remains a critical obstacle for successful commercialization. The uniform and ultra-thin layers produced by ALD make it an optimal solution for reducing surface energy without compromising the inherent catalytic activity of the electrodes.

Gong et al.[99,100] demonstrated that applying a uniform ZrO_2 overcoat through ALD on LSC or LSCF-GDC electrode results in exceptional stability, maintaining performance over an impressive 4000 hours of operation at 700 °C. This remarkable stability enhancement is a key factor in increasing the operational lifespan of SOFCs and, consequently, their commercial viability. In addition to benefiting perovskite materials, metal-based cathodes for intermediate-temperature SOFCs (IT-SOFCs) can also leverage the advantages offered by ALD. Chang et al.[101,102], Neoh et al.[103] and Li et al.[104] observed a significant enhancement in long-term stability and triple phase boundary (TPB) density by depositing SnO_2, CeO_x, and YSZ using ALD. This improvement in stability and TPB density can lead to more efficient energy conversion and increased power output from SOFCs.

An ultra-thin metal oxide overcoat with a high catalytic activity serves multiple purposes. Firstly, it increases the amount of TPB region and catalytic activity of the sites, which promotes more effective electrochemical reactions. Secondly, it prevents thermal agglomeration of the metal electrode at high temperatures by reducing the surface energy, ensuring that the electrode's structural integrity and performance are maintained. However, it is important to consider that a relatively dense layer of chemically inert material, such as ZrO_2 and YSZ, may result in the passivation of activation sites, leading to a reduction in electrochemical performance. Striking the right balance in the thickness of the deposited layer is crucial for optimizing performance.

Despite its advantages, ALD does have some limitations, Due to its high cost and low deposition rate, it may not be an appropriate method for constructing bulk electrodes. Holme et al.[105] fabricated a cell with an LSM electrode created entirely by ALD and discovered a peak power density as low as 0.2 μW cm^{-2} at 450 °C. This low

performance can be attributed to the poor kinetics and low oxygen diffusivity generated by the ALD process. Nevertheless, ALD required fewer materials to achieve comparable performance level [106], highlighting the potential advantages of this technique in specific applications.

3.4.2 ALD for SOECs

The applications of ALD on SOECs are very limited, and only a few reports have been done. For example, Shen et al.[107] used three different coatings techniques, ALD for Co_2O_3, electroplating deposition (ED) for Co_2O_3, and electrophoretic deposition (EPD) for $CuMn_{1.8}O_4$ on metal supported. The cell performance significantly improved from 0.65 A cm^{-2} for bare cells to 0.83 A cm^{-2} for ALD cells 1.4 V at 700 ºC. As the cells are metal supported, containing elements such as Fe, Cr, Mo, and Si, the ohmic resistance for each overcoated cell decreased by over 30%. This reduction can be attributed to diminished oxidation of the metal support and a decreased Cr reaction with the oxygen catalyst. However, the polarization resistance of the cell coated by ALD improves to a lesser extent than that of samples with EPD and ED overcoats. The primary reason for this discrepancy is the minimal amount of precursors deposited by ALD, rendering it ineffective in creating a blocking layer.

In conclusion, while ALD has its limitations, it offers substantial benefits for enhancing the performance and stability for SOCs. Further research and development in this area may lead to the discovery of new methods and materials that can improve the efficiency, stability, and long-term performance of these fuel cells, paving the way for broader commercialization and adoption of this clean energy technology.

Chapter 4: Atomic-scale metal oxide overcoat on decorated ceria nanoclusters for enhanced performance and the durability of solid oxide fuel cell cathodes

4.1 Introduction

Infiltration of catalytically active species onto a cathodic backbone structure is a widely used approach to improve the ORR activity of intermediate temperature SOFCs.[108] This is achieved by enhancing the electrode surface area (and thus enlarging chemisorption and charge transfer sites) and/or exposing more active sites on the surface (by infiltrating materials of high oxygen exchange rate).[109] However, the tiny infiltrated nanoparticles (NPs) naturally carries a high surface energy (due to a high percentage of low-coordination sites), making the NPs susceptible to severe agglomeration during high-temperature operations.[109,110]

In this chapter, we demonstrate how a true atomic-scale ALD oxide overcoat affects the performance and durability of a ceria NP-infiltrated $La_{0.6}Ni_{0.4}FeO_{3-\delta}$ (LNF) cathode. Since LNF does not have A-site Sr, it does not suffer from Sr segregation, a major degradation mechanism,[111] simplifying the analysis of degradation in this study. The structural stability of LNF is sensitive to the Ni-to-Fe ratio,[112] but a Ni:Fe molar ratio of 6:4 is known to render an excellent stability in rhombohedral structure.[113] The NPs formed on LNF backbones are prone to agglomeration unless properly engineered due to their small size (5 – 20 nm). Based upon electrochemical and physical characterization of a series of infiltrated and/or ALD-treated samples, we discuss the impact of surface treatment on the nanoscale morphology, surface chemistry and electrode performance. In addition, we provide a quantitative analysis of the thermal agglomeration of NPs with and without ALD treatment and prove the close correlation between the NP agglomeration and electrode performance degradation.

4.2 Experimental

4.2.1 Cell Preparation

All the cells are in symmetric configuration, comprised of a YSZ electrolyte, a GDC interlayer, a surface-engineered LNF layer (namely, active layer; AL) and an additional LNF layer for current collecting. The cell area of 0.35 cm^2 is defined by the LNF layer patterned in circle. The GDC layer (~ 5 μm thick) is placed to prevent any unexpected reaction between YSZ and LNF layers that forms insulating secondary phases (e.g. $La_2Zr_2O_7$).[114] First, a GDC slurry was screen-printed on both sides of a 8 mol% YSZ electrolyte substrate (270 μm thick, FuelCellMaterials), dried at 80 °C for 1 h and sintered at 1150 °C for 5 h. Then, an LNF slurry was screen-printed onto both sides of the GDC layer, dried at 80 °C for 1 h and sintered at 850 °C for 5 h. The LNF and GDC slurries were prepared with the approach reported earlier.[115] Briefly, the LNF

slurry was prepared by mixing house-made LNF powder, dispersant (Hypermer KD-1, Croda) and binder (ethyl cellulose) in terpinol. The GDC slurry was made of GDC nanopowder (FuelCellMaterials), ethyl cellulose, hypermer KD-1 and terpineol.
On top of the resulting LNF layer, infiltration (ceria) and/or ALD (yttria or ceria) was performed. Ceria infiltrated samples without an ALD treatment is categorized as Type I while ALD-treated samples without an infiltration is categorized as Type II. For ceria infiltration, 1 M aqueous solution of cerium(III) nitrate hexahydrate (99%, Aldrich) was prepared with deionized water. Sol impregnation was then performed on both sides of the cell onto the LNF backbone, let idle for 1 h under a house vacuum, and then dried at 450 °C for 0.5 h in a furnace. For ALD of ceria and yttria, tris(i-propylcyclopentadienyl)cerium(III) [$Ce(iPrCp)_3$] and tris(methylcyclopentadienyl) yttrium(III) [$Y(MeCp)_3$] were used as the precursors while distilled water and nitrogen was used as co-reactant and purging gas, respectively. The canister temperatures for Ce and Y were 145 °C and 150 °C with the chamber temperature of 250 °C. The pulsing time of 3 s was used for Ce and Y precursor, and 0.4 s for water. Before an ALD treatment is performed on a ceria-infiltrated LNF, a sintering process (850 °C for 2 h) can be added; the one without the additional sintering process is categorized as Type III-A and the one with the sintering process as Type III-B. Finally, an additional layer of LNF was screen-printed on top of the infiltrated and/or ALD-treated LNF layer to use as the current collecting layer. The resulting symmetric cell was and dried at 80 °C for 1 h and sintered at 850 °C for 3 h with the heating/cooling rate of 3 °C min^{-1}. For all the samples for X-ray photoelectron spectroscopy (XPS) analysis, the sintering process (850 °C for 3 h) was performed without the additional LNF layer.

A separate set of samples were prepared for X-ray diffraction (XRD) analysis to reveal the chemical information of the cathode only without being obscured by the presence of the GDC/YSZ electrolyte. To make LNF pallet-supported sample for this purpose, LNF powders was first ball-milled and pressed under a uniaxial press. After sintering the resultant LNF pallet at 850 °C for 5 h, either an infiltration or an ALD process was performed before sintering at 850 °C for 3 h. Transmission electron microscopy (TEM) samples were prepared by grinding surface-treated LNF into powders, suspending them in ethanol and drop-casting the particle suspension upon a 3 mm lacey-carbon grid (Ted Pella).

4.2.2 Physical characterization

A field-emission scanning electron microscopy (SEM, Zeiss Gemini 500) was used at 3 kV to observe the microstructures. The structure and size of NPs were characterized by transmission electron microscopy and scanning transmission electron microscopy (STEM) which were recorded on a 200 kV FEI monochromated F20 UT Tecnai system. The STEM image was obtained with a convergence angle of 10 mrad and a detection angle of 30 mrad. Energy filtered transmission electron microscopy (EFTEM) was used to visualize elemental distributions. The energy dispersive X-ray spectroscopy (EDS) (Oxford X-max mm2 SDD 127eV at 50k cps) was performed on a Talos F200C G2 TEM system; X-FEG electron source, 0.18 lattice resolution and 0.30 nm point to point resolution was set to the tip. XPS was performed on a PHI Quantum

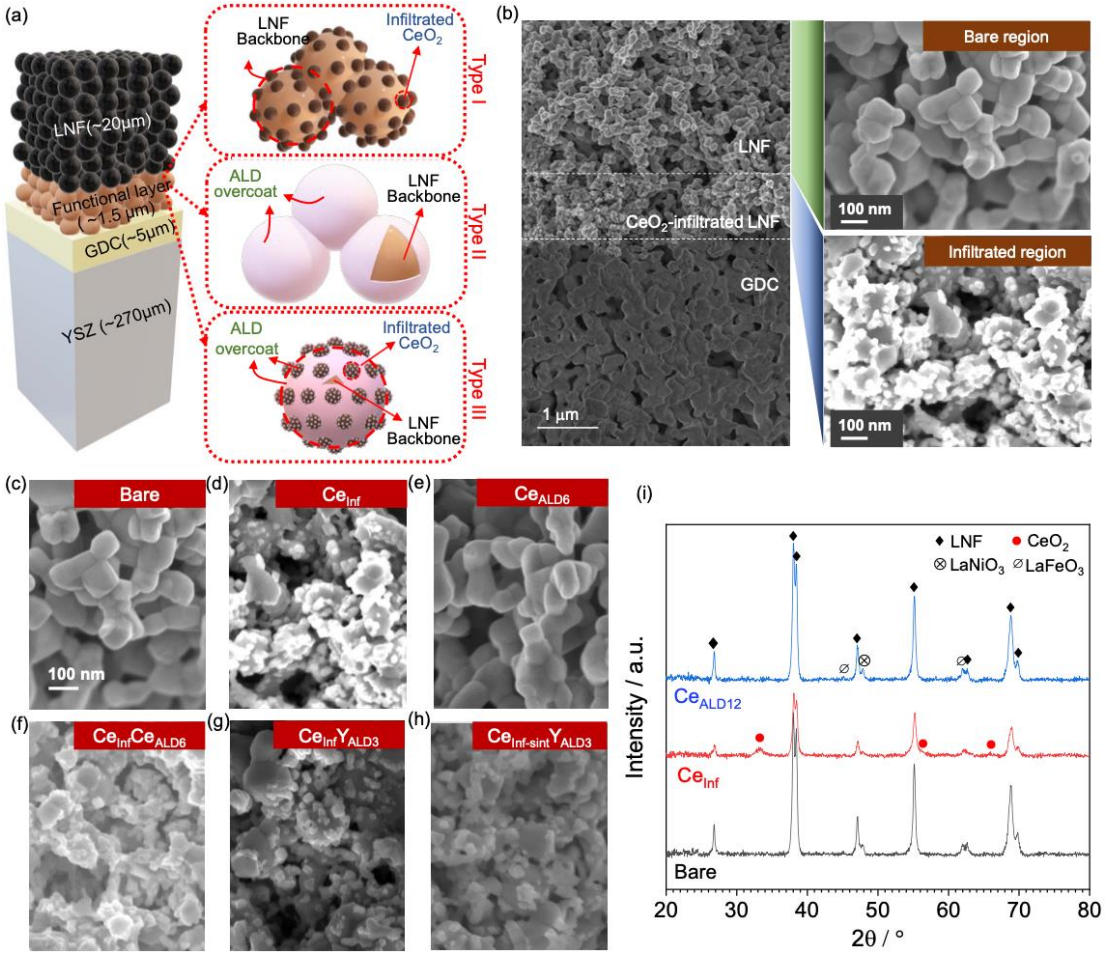

Fig. 4.1 (a) A schematic diagram of our cell configuration depicting three different classes of surface treatment. (b) A cross-sectional SEM image in the vicinity of LNF/GDC interface and zoomed-in images in the bare and infiltrated region of LNF backbone. (c-h) SEM images of bare, infiltrated and/or ALD-treated samples. (i) XRD spectra of bare, CeInf and CeALD12 samples; obtained using Co Kα radiation (λ = 1.78897 Å).

2000 system using a focused, monochromatic Al Kα X-ray (1486.6 eV) source for excitation and a spherical section analyzer (200 μm diameter X-ray beam incident to

the surface normal; detector set at 45°). For XPS, samples were prepared without the LNF current collecting layer to expose the functional layer surface for analysis. The phase and composition of samples were evaluated by XRD using a PANalytical X'Pert Pro system with Co Kα radiation (λ = 1.78897 Å).

4.2.3 Electrochemical characterization

Electrochemical properties were analyzed by electrical impedance spectroscopy (EIS) with 20 mV of ac perturbation at the open circuit condition (Bio-Logic SP-240) in a customized SOFC test station. Pt mesh was placed on both sides of the sample to collect current and a weight of 5 kg was applied to ensure a solid contact between the cell and current collector. Different oxygen partial pressures (pO_2) were realized by changing the ratio of O_2 and N_2 gas flow rates while maintaining the total flow rate at 100 sccm. Sample was heated at a rate of 3 °C/min and held at each temperature of

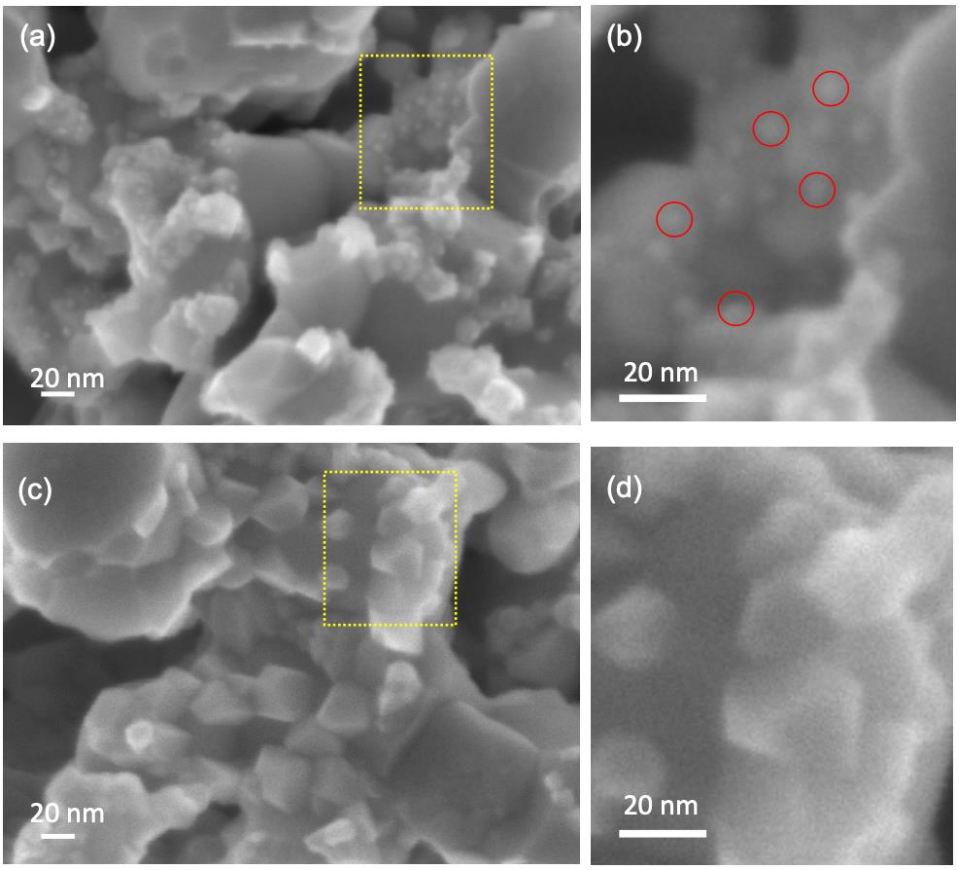

Fig. 4.2 SEM images of $Ce_{Inf\text{-}sint}Ce_{ALD6}$ (a,b) and $Ce_{Inf\text{-}sint}Y_{ALD3}$ (c,d) after 260 h at 700 °C. The dotted area in (a) is shown in (b). Some of ALD CeO_2 nanodots are circled in red.

interest for > 30 min before testing. Cell durability tests were performed at 700 °C by obtaining EIS data every hour in a different customized SOFC test setup free of Cr components. O_2 gas was continuously fed into the chamber at 200 sccm throughout the test.

4.3 Result and Discussion

4.3.1 Cell set-up

Three different classes of surface treatments were performed on LNF backbone as depicted in **Fig. 4.1a**: cells treated with an infiltration process only (Type I; Ce_{Inf}), an ALD process only (Type II; Ce_{ALDn} series) and an infiltration followed by an ALD process (Type III). Within Type III, there are two sub-categories: those sintered (at 850 °C) after both an infiltration and ALD processes are performed (namely, Type III-A; e.g. $Ce_{Inf}Ce_{ALDn}$), and those where an additional sintering process is inserted between the infiltration and ALD treatment (namely, Type III-B; e.g. $Ce_{Inf\text{-}sint}Ce_{ALDn}$). As described in the Methods section, the surface treatment (infiltration and/or ALD) was performed on a porous screen-printed LNF backbone (~10 μm). For electrochemical characterization, another ~10 μm thick LNF layer is deposited on top of the surface treated LNF layer for current collecting. The infiltrated CeO_2 NPs are mostly located in the vicinity of the GDC/LNF interface with a width of ~1.5 μm (we call it the active layer; AL), leaving the upper part of the backbone virtually uncoated as shown in **Fig. 4.1b**. This is likely due to a relatively low viscosity of precursor solution used for the infiltration, which would make the solution readily permeate through the porous LNF backbone (driven by both capillary action and gravity) and accumulate around the interface with GDC. The ceria-infiltrated cell (Type I; Ce_{Inf}) has 5 – 20 nm ceria NPs on the LNF backbone whose granular feature is sized ~ 100 nm (**Fig. 4.1b** and **Fig. 4.1d**). On the other hand, the ALD overcoat do not form a noticeable feature in any of the Type II (**Fig. 4.1e**) and Type III cells (**Fig. 4.1f-h**). However, after a long-term thermal exposure (260 h at 700 °C), ALD-induced ceria nanodots of 3 – 4 nm are resolved in $Ce_{Inf\text{-}sint}Ce_{ALDn}$ series (Type III-B) as shown in **Fig. 4.2a-b** while the feature was not observed in any other samples including the other Type III-B samples ($Ce_{Inf\text{-}sint}Y_{ALDn}$ series; **Fig. 4.2c-d**) even after the long-term heating. Interestingly, the ALD ceria nanodots are preferentially located on infiltrated ceria NPs only (in particular, more at the "neck" formed between infiltrated NPs) as opposed to the LNF backbone surface as shown **Fig. 4.2a-b** and schematically expressed in the "Type III" rectangle of **Fig. 4.1a**. Since the LNF backbone has a very high effective aspect ratio (~10 μm of backbone thickness versus ~ 100 nm of pore size) for the transport of ALD precursor, the ALD growth rate should be diminished with depth.[116] For this reason, the growth rate is quantified directly from the distribution of ALD-based nanodots formed in the AL (**Fig. 4.2a-b**).

To calculate the growth rate of CeO_2 and Y_2O_3. There are several articles reporting the growth rate of ceria by ALD using tris(i-propylyclopentadienyl)cerium(III) and H_2O as the precursor and oxygen source (the same as those used in this study). Wang et al. reported a CeO_2 film thickness of 1.3 nm after 80 ALD cycles on anatase TiO_2 nanoparticles at 250 °C, which is equivalent to ~ 0.163 Å per cycle.[117] Gupta et al. reported a ceria growth rate of 0.33 Å per cycle on a flat SiO_2 substrate at the

chamber temperature of 250 °C.[118] While these two growth rates are within a reasonable proximity, majority others reported much higher growth rates of 2.5 – 3.0 Å per cycle.[119] As Rahmanipour et al. noted, the measured growth rate varies widely dependent upon the geometry and surface chemistry of substrates and other deposition conditions.[120] Herein, we quantified the ALD growth rate of our samples (by leveraging high-magnification SEM images) as shown below instead of simply relying upon prior reports.

In the zoomed-in SEM image of $Ce_{Inf\text{-}sint}Ce_{ALD6}$ shown in **Fig. 4.2a-b**, the size of each ceria nanodots formed by ALD is ~ 3 nm in diameter. It is noted that only those deposited on infiltrated CeO_2 NPs (sized ~20 nm) forms nanodots while those deposited on the LNF backbone surface is not visible in the eyes of SEM. Therefore, we quantify the growth rate by focusing on the infiltrated CeO_2 NP region in **Fig. 4.2b**. With the aid of ImageJ software, we found that ~ 7.3% of the infiltrated CeO_2 surface is covered by the ALD-based ceria nanodots. Assuming the ceria nanodots are in a full sphere shape, we calculate the nominal thickness using the following simple relations.

$$A \cdot t = \left(\frac{4}{3}\pi r^3\right) \cdot N \tag{4.1}$$

$$(\pi r^2) \cdot N = 0.073 \cdot A \tag{4.2}$$

where *t*, *A*, *N* and *r* corresponds to the nominal thickness (when assumed a uniform deposition), substrate surface area, total number of nanodots on a substrate of area *A*, and the radius of nanodots (1.5 nm). From this, we find the nominal ALD thickness of 1.46 Å. Since 6 cycles were performed to achieve this nominal thickness, the ceria growth rate is estimated to be ~ 0.24 Å per cycle.

however, could not be applied to our yttria deposition because there was not a localized morphological protrusion incurred by yttria ALD (**Fig. 4.2d**). Since the yttria growth rates reported by previous studies using the same precursor (tris(methylcyclopentadienyl) yttrium(III)), oxygen source (water) and chamber temperature (250 °C) are 0.8 – 3.5 Å per cycle on well-defined flat surfaces,[121–123] which is within a similar range as those of ceria, we assume the same growth rate for yttria ALD on our porous electrode surface (i.e. 0.24 Å per cycle).

4.3.2 Physical properties

The XRD spectra (**Fig. 4.1i**) reveal that the backbone comprises mostly rhombohedral LNF (R-3c space group) with a minor presence of $LaNiO_3$ and $LaFeO_3$ (both R-3c space group). The Ce_{Inf} sample shows additional peaks corresponding to cubic CeO_2 (Fm-3m space group) including the one at 33.3° for (1 1 1) plane. However, the ALD-coated sample (Ce_{ALD12}) did not show a discernible ceria peak due to the tiny amount of ALD-derived ceria. This is the case for the Type-III samples; only the peaks corresponding to LNF backbone and infiltrated ceria are detected without a trace of Y from ALD in $Ce_{Inf}Y_{ALD15}$ (**Fig. 4.3**).

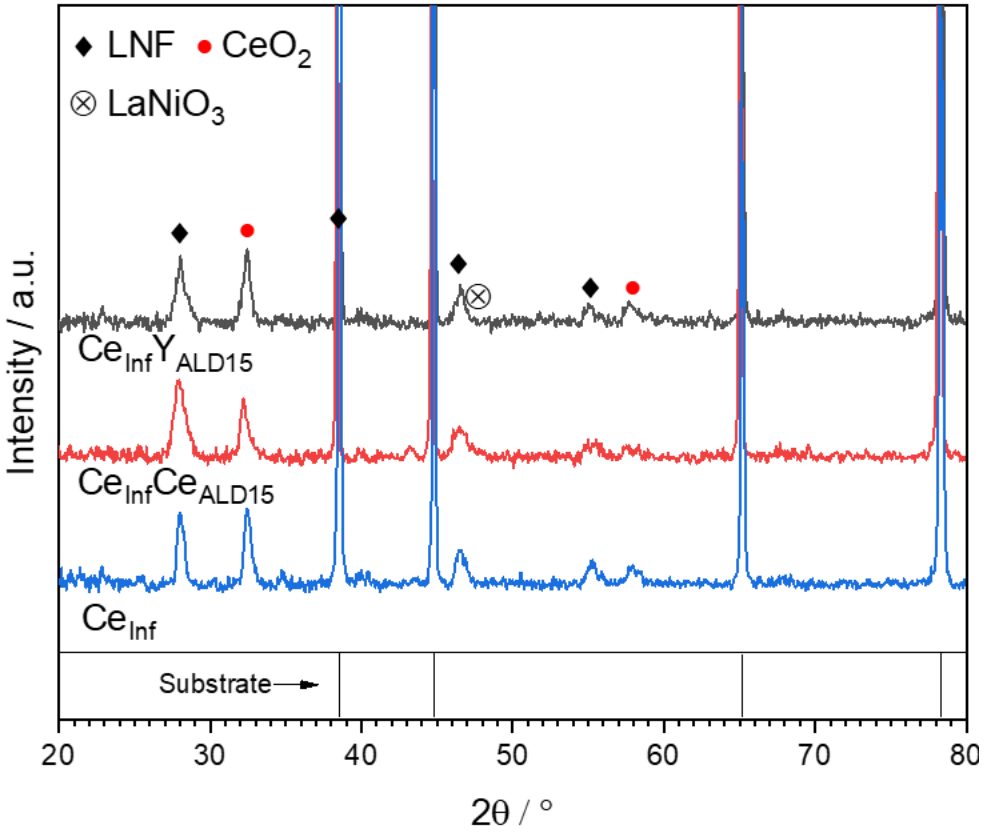

Fig. 4.3 XRD spectra of Ce_{Inf}, $Ce_{Inf}Ce_{ALD15}$ and $Ce_{Inf}Y_{ALD15}$ samples. Note that a much smaller amount of samples were placed on a substrate compared to the amount placed for Fig. 4.1i when performing XRD, resulting in a stronger peaks corresponding to the substrate.

To better resolve the surface-treated species, a set of TEM imaging and EFTEM elemental mapping was performed as shown in **Fig. 4.4**. The HRTEM images in **Fig. 4.4a** and **Fig. 4.4g** are captured at locations close to the very surface of an infiltrated ceria NP. The $Ce_{Inf}Ce_{ALD6}$ (**Fig. 4.4a**) shows CeO_2 and Ce_2O_3 nanocrystals sized between 3 – 7 nm. Considering the XRD spectrum of Ce_{Inf} (**Fig. 4.1i**) showed only cubic CeO_2 without a trace of Ce_2O_3, the Ce_2O_3 crystals shown in the HRTEM are likely formed in a tiny amount on the very surface by ALD. The existence of thermodynamically unstable Ce_2O_3 is supported by a recent study by Gupta et al.[124] that

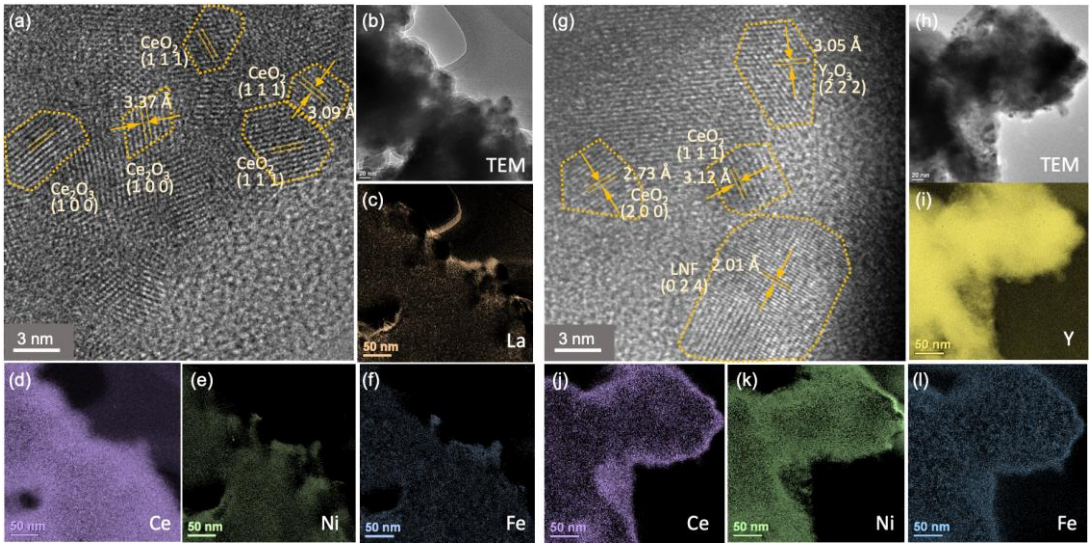

Fig. 4.4 HRTEM images and EFTEM elemental maps of $Ce_{Inf}Ce_{ALD6}$ (a-f) and $Ce_{Inf}Y_{ALD3}$ (g-l). In the HRTEM images (a, g), the boundaries of nanocrystals and identified lattice *d*-spacings are marked.

showed a nucleation of Ce_2O_3 phase in the first ~ 1.5 nm by a $Ce(iPrCp)_3/H_2O$-based ceria ALD (the ALD chemistry used in this work). The Ce elemental map in **Fig. 4.4d** also indicate that ceria species are uniformly distributed throughout the surface of LNF backbone. The HRTEM of $Ce_{Inf}Y_{ALD3}$ in **Fig. 4.4g** also confirms the presence of Y_2O_3 nanocrystals formed by ALD, and the EFTEM elemental map of Y (**Fig. 4.4i**) shows its uniform distribution throughout the LNF surface; see also To confirm the present of

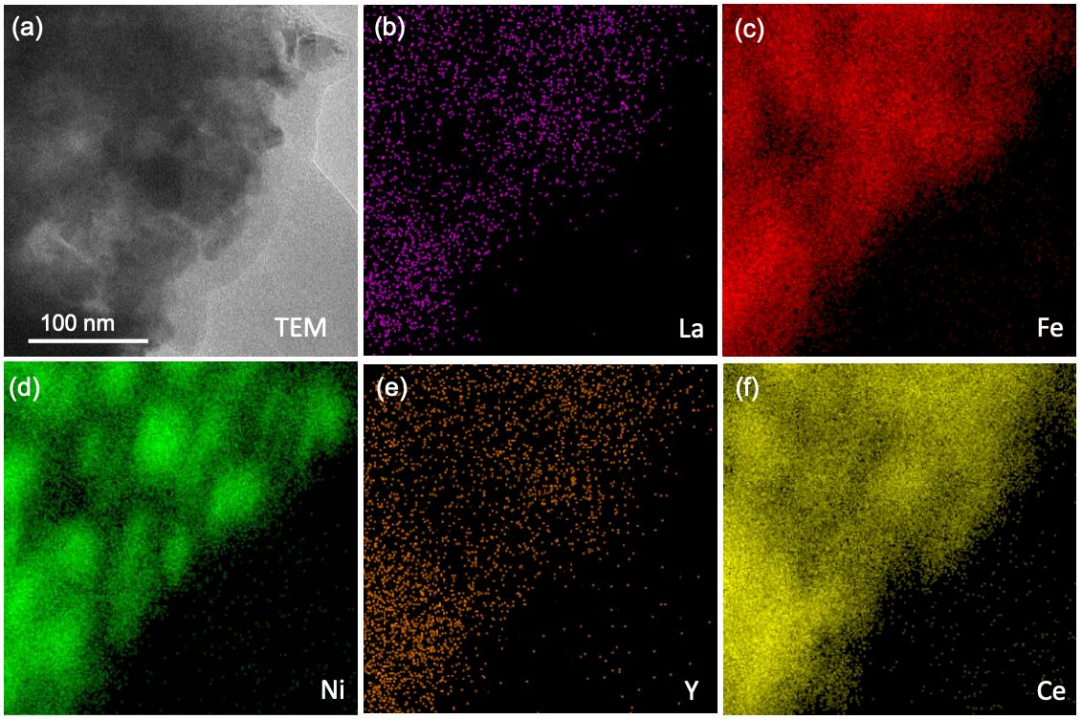

Fig. 4.5 A TEM image of $Ce_{Inf}Y_{ALD15}$ (a) and its corresponding EDS elemental mapping (b-f).

Y2O3, TEM-EDS elemental mapping (**Fig.4.5**) and TEM-EDS spectra of $Ce_{Inf}Y_{ALD15}$ (**Fig. 4.6**) was performed.

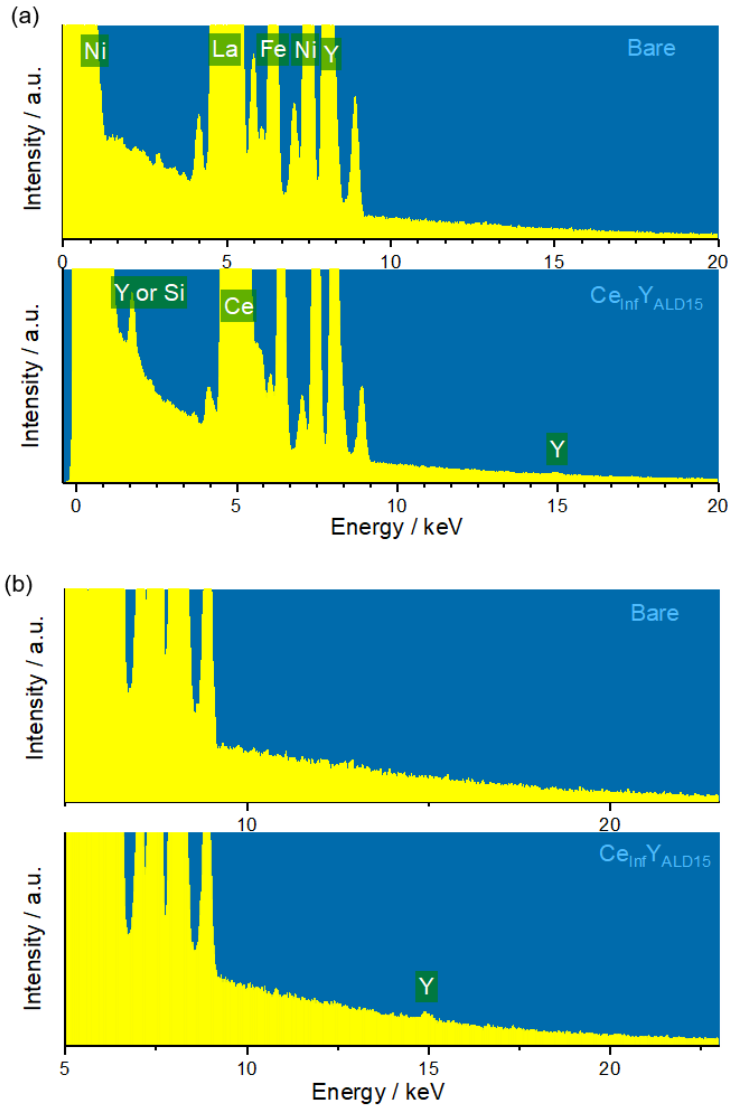

Fig. 4.6 EDS spectra of bare LNF and $Ce_{Inf}Y_{ALD15}$ powder. (b) is zoomed in y-axis to reveal the presence and absence of Y more explicitly.

XPS analysis was performed to reveal the chemical bonding states at the very surface of three samples: Ce_{Inf} (Type I), Ce_{ALD12} (Type II), and $Ce_{Inf}Ce_{ALD6}$ (Type III). By applying Maslakov et al.'s approach,[125] The fraction of Ce3+ and Ce4+ species from Ce 3d spectra was quantified by following relationship:

$$p(Ce^{3+}) = \frac{1 - \frac{3}{2}a_0(\frac{I_0}{I})}{1 + \frac{3}{2}(\frac{I_0}{I})} \quad (4.3)$$

$$p(Ce^{4+}) = 1 - p(Ce^{3+}) \quad (4.4)$$

Where $a_0 = \frac{I_S}{\frac{3}{2}I_o}$, $I_0 = I(u_4)$, $I_s = I(v_1) + I(v_3)$, $I = I(v_0) + I(v_1) + I(v_2) + I(v_3)$. The ratios of Ce^{3+} to Ce^{4+} are quantified to be 5.96% and 12.6% for Ce_{Inf} and $Ce_{Inf}Ce_{ALD6}$, respectively, from the Ce 3d spectra shown in **Fig. 4.7a**; **Table 4.1** indicates the Area under each peak. While molar fraction of O-Ce3+ and O-Ce4+ form O 1s spectra was quantified by following relationship:

$$p(O - Ce^{3+}) = \frac{I(O - Ce^{3+})}{I(O - Ce^{3+}) + I(O - Ce^{4+})} \quad (4.5)$$

$$p(O - Ce^{4+}) = 1 - p(O - Ce^{3+}) \quad (4.6)$$

The Ce^{3+} content is even higher in Ce_{ALD12} (13.4%). This is well aligned with the O 1s spectra in that the relative amount of O-Ce^{3+} in Ce_{ALD12} (48.3%) and $Ce_{Inf}Ce_{ALD6}$ (40.2%) are larger than that of Ce_{Inf} (37.5%); see **Table 4.2**. A trivalent Ce can be related to either an oxygen vacancy formation in CeO_{2-x} or a lattice Ce in Ce_2O_3. In either case, their unstable surfaces as compared to that of stoichiometric CeO_2 is likely to make it advantageous in the oxygen exchange kinetics.[126] On the other hand, the Ce 3d spectrum of Ce_{ALD12} is shifted to a higher binding energy by an unexpectedly large margin (5.7 eV) with respect to the other two samples. Considering a new O 1s peak appearing at an unusually high binding energy (~534.8 eV; not relevant to a lattice

Table 4.1 XPS Ce 3d peak analysis.

	Ce_{Inf}		**$Ce_{Inf}Ce_{ALD6}$**		**Ce_{ALD12}**	
Peak	B.E. [eV]	Area [a.u.]	B.E. [eV]	Area [a.u.]	B.E. [eV]	Area [a.u.]
u_4	916.29	1028.51	916.29	1147.38	921.90	621.13
u_3	906.91	994.63	907.22	1136.65	912.80	650.42
u_2	903.40	136.24	902.90	410.89	908.40	156.86
u_1	900.76	903.20	900.69	962.69	906.30	410.96
u_0	899.10	49.19	899.10	57.50	904.10	104.65
v_4	897.69	1542.77	897.70	1721.07	903.30	931.69
v_3	888.44	1491.95	888.78	1704.97	894.38	975.62
v_2	882.24	1354.79	882.15	1444.04	887.70	616.44
v_1	884.18	204.37	884.3	616.33	890.20	235.30
v_0	880.90	73.78	881.1	86.24	885.90	156.98
$P(Ce^{3+})$	**5.96%**		**12.6%**		**13.4%**	

Table 4.2 XPS O 1s peak analysis.

	Ce_{Inf}		$Ce_{Inf}Ce_{ALD6}$		Ce_{ALD12}	
Peak	B.E. [eV]	Area [a.u.]	B.E. [eV]	Area [a.u.]	B.E. [eV]	Area [a.u.]
O-Ce^{4+}	528.6	2200.9	528.6	2562.0	528.5	1623.2
O-Ce^{3+}	531.1	1320.2	531.1	1727.1	531.1	1514.2
Absorbed O_2	531.9	1099.3	532.0	1115.3	532.1	795.4
M-O	529.9	284.5	529.8	311.0	529.7	256.9
Ligand					534.8	276.4
p(O-Ce^{3+})	**37.5%**		**40.2%**		**48.3%**	

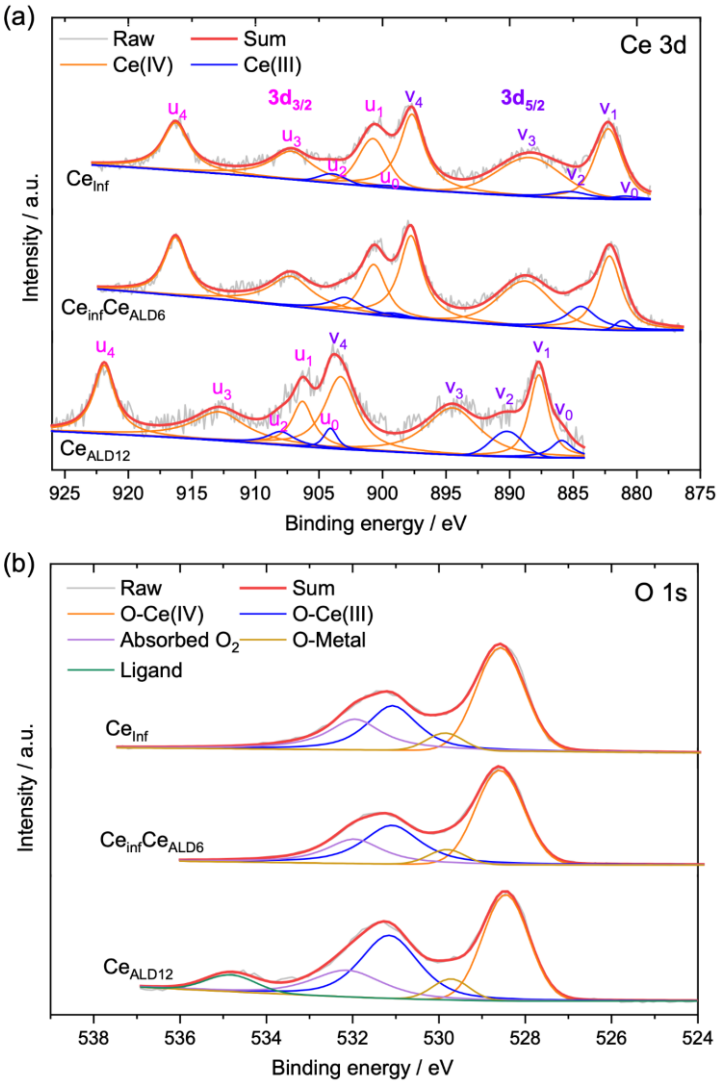

Fig. 4.7 Ce 3d and O 1s XPS peaks obtained from Ce_{Inf}, Ce_{ALD12} and $Ce_{Inf}Ce_{ALD6}$.

oxygen) and a distinct difference in C 1s spectrum, but without a noticeable difference in the spectra of La 3d, Ni 2p and Fe 2p (**Fig. 4.8**), it is conjectured that the large Ce 3d binding energy shift of Ce_{ALD12} is originated from a strong electronegativity of unidentified ligand(s) attached to Ce.

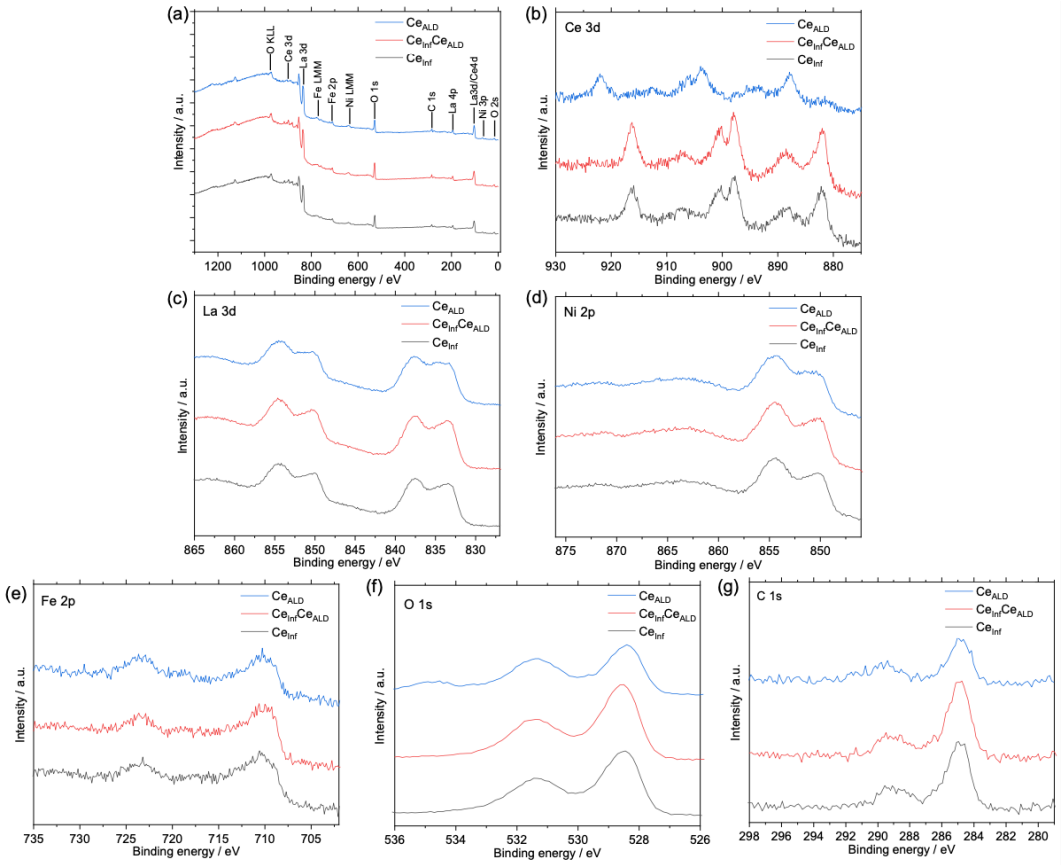

Fig. 4.8 XPS spectra. (a) Survey spectrum, (b) Ce 3d, (c) La 3d, (d) Ni 2p, (e) Fe 2p, (f) O 1s and (g) C 1s spectra.

4.3.3 Electrochemical properties on performance

Most of EIS curves obtained for the study (except for those obtained at low oxygen activities as shown in **Fig. 4.9** below) could be reasonably well fitted to a single arc-based L-R_o-(R_p//Q_p) model. An additional low-frequency arc appears at low oxygen activities (< 0.1 atm), which is ascribed to a mass transport polarization. However, even at the lowest pO_2 in our study, the newly appearing arc is almost ten-fold smaller than the other main arc, and thus the corresponding R_p is negligible compared to the main R_p as shown in **Fig. 4.9** in most cases. Therefore, we fitted all the presented data using the single arc-based model.

Fig. 4.10 presents electrochemical data obtained from a bare sample and surface-treated samples; Nyquist plots and Arrhenius plots for all the studied samples

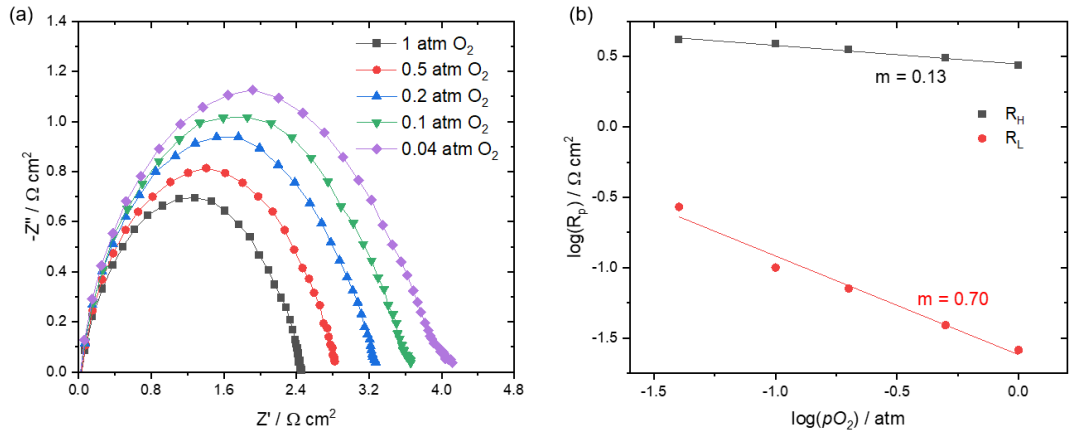

Fig. 4.9 (a) Nyquist plot of LNF bare sample obtained at various pO_2 and (b) corresponding polarization resistances versus pO_2 graph; here, the polarization resistances are acquired by fitting the EIS data to R-L-R_o-(R_H//Q_H)-(R_L//Q_L). R_H and R_L corresponds to polarization resistances with higher and lower characteristic frequencies.

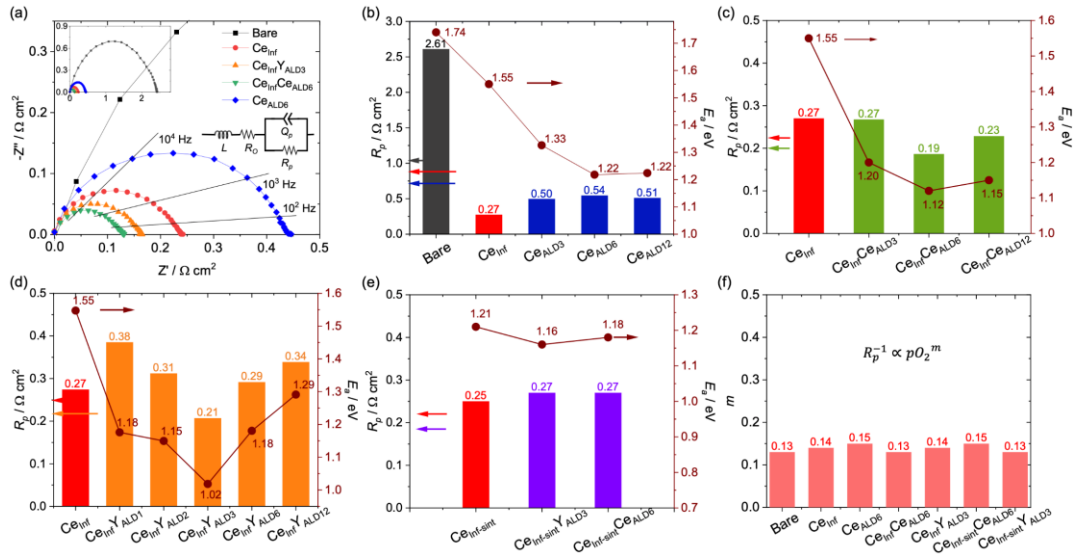

Fig. 4.10 (a) EIS curves of several selected samples obtained at 700 °C and the equivalent circuit used for fitting. The inset is a zoomed-out Nyquist plot to show the full spectrum of bare sample. (b-e) The fitted polarization resistances (R_p) and their activation energies (E_a); (b) Bare, Ce_{Inf} (Type I) and Ce_{ALDn} series (Type II), (c,d) $Ce_{Inf}Ce_{ALDn}$ and $Ce_{Inf}Y_{ALDn}$ series (Type III-A) and (e) $Ce_{Inf\text{-}sint}Y_{ALD3}$ and $Ce_{Inf\text{-}sint}Ce_{ALD6}$ (Type III-B). All the corresponding EIS curves and Arrhenius plots are provided in Fig. 4.11. (f) Reaction order (m) values obtained at 700 °C; the corresponding R_p versus pO_2 graphs presented in Fig. 4.12. The inset shows the parametric meaning of m; pO_2 is the partial pressure of O_2 applied to the cell during measurements.

are presented in **Fig. 4.11**. Since most samples show a single smooth arc in the Nyquist plot, a simple L-R_o-(R_p//Q_p) is used to fit all the presented impedance data; R_o, R_p, and Q_p refers to ohmic resistance, electrode polarization resistance and constant phase

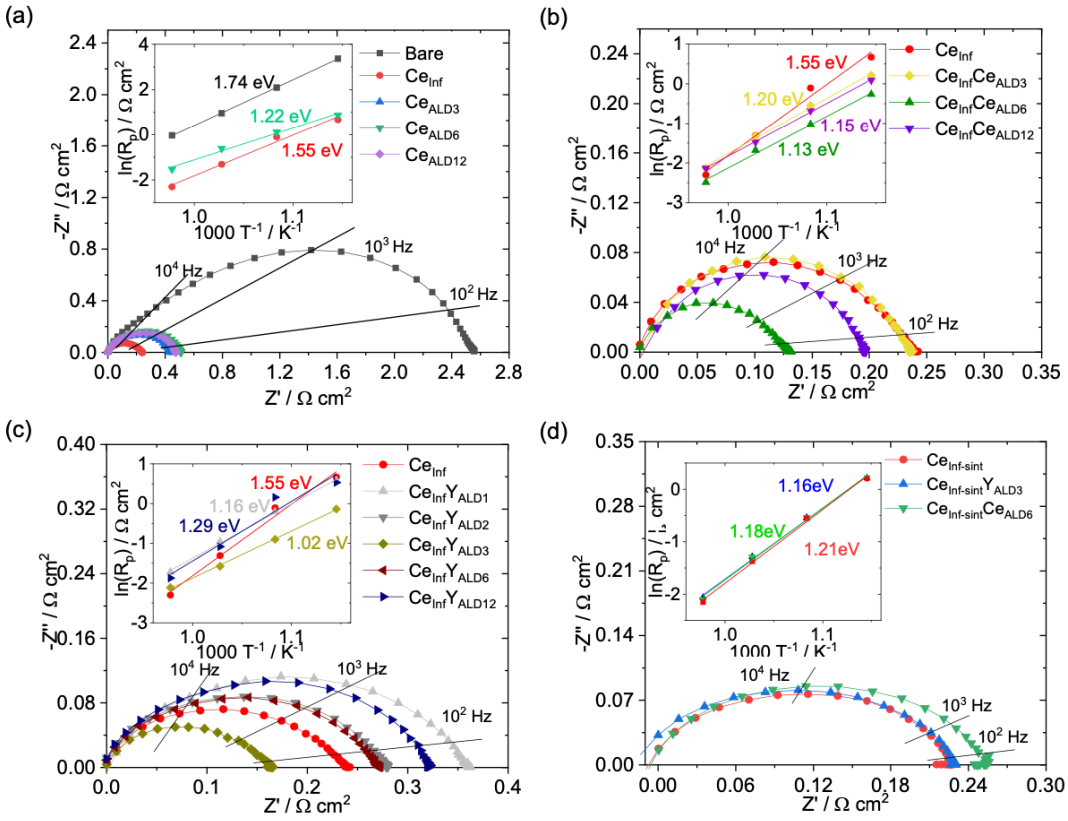

Fig. 4.11 EIS curves and Arrhenius plots (inset). In the insets, the activation energies (E_a) of each sample are calculated from the least square fitting of R_p values with temperature. (a) Bare, Ce_{Inf} and Ce_{ALDn} series, (b) $Ce_{Inf}Ce_{ALDn}$ series (c) $Ce_{Inf}Y_{ALDn}$ series and (d) the samples sintered before ALD ($Ce_{Inf\text{-}sint}Y_{ALD3}$ and $Ce_{Inf\text{-}sint}Ce_{ALD6}$).

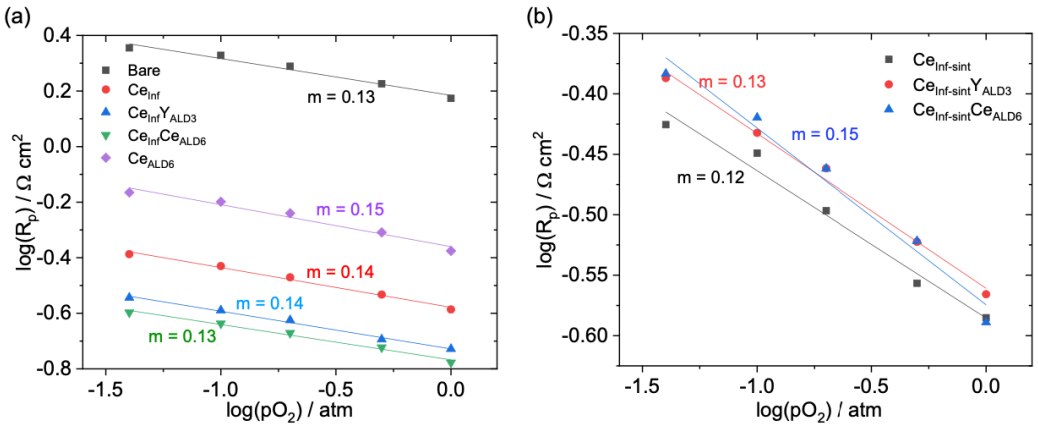

Fig. 4.12 Partial pressure dependency of polarization resistances measured at 700 °C.

element (CPE), respectively; see fitted parameters in **Table 4.3** and **Table 4.4**. All the resistance values are presented after a normalization by the cell area for a facile comparison. First, the bare sample (without an infiltration or ALD process) shows a large R_p (2.61 Ω cm^2 at 700 °C) and high activation energy of electrode polarization

Table 4.3 Ohmic resistance (R_{ohm}), Polarization resistance (R_p) and their corresponding capacitance (C) calculated with CPE parameters (α and Q).

	R_{ohm} [Ω cm^2]	R_p [Ω cm^2]	α	Q [F s$^{1-\alpha}$]	C [F cm^{-2}]
Bare	1.37	2.61	0.77	2.4×10^{-4}	1.5×10^{-5}
Ce_{Inf}	0.92	0.27	0.63	4.41×10^{-3}	8.45×10^{-5}
Ce_{ALD6}	0.95	0.54	0.71	1.26×10^{-3}	6.41×10^{-5}
$Ce_{Inf}Ce_{ALD6}$	0.96	0.19	0.60	7.03×10^{-3}	8.52×10^{-5}
$Ce_{Inf}Y_{ALD3}$	0.82	0.21	0.62	4.44×10^{-3}	6.17×10^{-5}

resistance (E_a = 1.74 eV). This is mainly ascribed to the extremely small concentration of oxygen vacancies in a bare LNF (oxygen non-stoichiometry < 0.005 in the usual SOFC condition)[127] and the resulting high energy barrier for dissociative adsorption of O_2.[115,128] A single-step infiltration (Ce_{Inf}) decreased R_p and E_a by a significant amount (**Fig. 4.10b**). An infiltration of external hetero-species doped ceria has been reported to facilitate oxygen adsorption and dissociation kinetics.[115,129] Although we infiltrated ceria NPs without an explicit doping, we still observe a drastic improvement in oxygen electrode performance by reducing R_p from 2.61 to 0.27 Ω cm^2 at 700 °C. This is ascribed to the widely known characteristics of ceria: flexible cationic valence state and facile oxygen vacancy formation,[130] which provides reversible oxygen exchange and high oxygen storage capacity.[131,132]

A considerable decrease in Rp was achieved by a 3, 6 and 12 cycles of ceria ALD as well (Type II; **Fig. 4.10b**). With 3 cycles of ceria ALD (only 0.72 Å of nominal thickness) on a bare LNF, Rp decreased by a factor of 5.2 (down to 0.50 Ω cm2) at 700 ºC. Although the amount of performance enhancement was larger by an infiltration than by an ALD overcoat, the effect of ALD is surprising in that the volume of ceria added by a 3 cycle ALD is only ~ 0.044% of the LNF. A one-step infiltration forms an oxide volume much larger than a few cycles of ALD, but a small volume compared to the backbone (~ 3%).[115] By taking the average size of infiltrated ceria NPs to be ~ 15 nm (see **Fig. 4.17**) and ALD growth rate of 0.24 Å per cycle, the volumetric ratio of ALD-deposited ceria or yttria nanodots ($V_{ALD} = 4\pi {r_{Inf,NP}}^2 \cdot t_{ALD}$ where VALD and tALD are the volume and nominal thickness of ALD-based film, and rInf,NP is the radius of infiltrated ceria nanoparticles) to the infiltrated ceria ($V_{inf} = \frac{4}{3}\pi {r_{inf}}^3$ where Vinf is the volume of infiltrated ceria) is found to be 0.0048 × (number of ALD cycle). For

Table 4.4 Summary of polarization resistances (R_p) at different temperatures and their activation energies (E_a).

	750 °C [Ω cm^2]	**700 °C [Ω cm^2]**	**650 °C [Ω cm^2]**	**600 °C [Ω cm^2]**	***E*$_a$ [eV]**
Bare	0.9683	2.6028	8.1029	28.9322	1.75
Ce$_{Inf}$	0.1001	0.2737	0.8983	1.9548	1.55
Ce$_{Inf}$Y$_{ALD1}$	0.1787	0.3848	0.814	1.7868	1.18
Ce$_{Inf}$Y$_{ALD2}$	0.1494	0.3115	0.6612	1.4096	1.15
Ce$_{Inf}$Y$_{ALD3}$	0.1208	0.2067	0.4065	0.8727	1.02
Ce$_{Inf}$Y$_{ALD6}$	0.1369	0.2912	0.6346	1.3697	1.18
Ce$_{Inf}$Y$_{ALD12}$	0.1534	0.3385	1.1723	1.6986	1.29
Ce$_{Inf}$Ce$_{ALD3}$	0.1179	0.2674	0.5784	1.2420	1.20
Ce$_{Inf}$Ce$_{ALD6}$	0.0828	0.1862	0.3598	0.7693	1.13
Ce$_{Inf}$Ce$_{ALD12}$	0.1183	0.2282	0.5093	1.0967	1.15
Ce$_{ALD3}$	0.2151	0.4956	1.3003	2.7843	1.33
Ce$_{ALD6}$	0.2172	0.5439	1.1261	2.4115	1.22
Ce$_{ALD12}$	0.2147	0.5087	1.0623	2.3993	1.22
Ce$_{Inf-sint}$	0.1164	0.2536	0.5749	1.2268	1.21
Ce$_{Inf-sint}$Y$_{ALD3}$	0.1270	0.2762	0.5819	1.2413	1.16
Ce$_{Inf-sint}$Ce$_{ALD6}$	0.1225	0.2756	0.5829	1.2481	1.18

example, considering a Type-III sample with 6 cycles of ALD, the volume of ALD-based ceria or yttria is 2.88% of infiltrated ceria volume (0.0048 × 6 = 0.0288). Considering the amount of single-step infiltration forms ~3% of volume with respect to the LNF backbone,[115] the amount of 6 cycle ALD-based ceria or yttria is only 0.087% of the backbone. No morphological corrugations by an ALD process were observed on the surface LNF backbone, either. Therefore, while it is clear that the enhancement in the electrode kinetics is enabled by a facilitation of a highly surface-specific process

(as opposed to a bulk process), it cannot be ascribed to a change of surface area nor triple phase boundary area. Based upon the quantified E_a (1.22 – 1.33 eV) and reaction order values (m ~ 0.15; **Fig. 4.10f**), we ascribe the performance enhancement to a considerable facilitation of dissociation and partial reduction of O_2 (namely, "O_2 activation"), which we identified as the rate-determining step (RDS) of ORR in the backbone LNF;[115] This is supported by the large amount of Ce^{3+} species (13.4%) in Ce_{ALD12}, even much larger than that of Ce_{Inf} (5.96%) as quantified by XPS. **Fig. 4.10b** shows that the R_p values of Ce_{ALDn} samples prepared with 3, 6 and 12 cycles of ceria ALD are similar to each other. Since the nominal thickness (the thickness estimated when assuming a perfectly uniform film) is only ~ 2.88 Å even with 12 cycles, it is likely to take a much larger number of cycles to fully passivate the LNF surface and suppress the electrode kinetics.

The schematic diagram in **Fig. 4.13** shows possible ORR pathways in the studied system. In this section, we discuss about what specific elemental step of ORR was dominantly affected by the surface treatment (infiltration and/or ALD) and how the treatment impacted the overall ORR kinetics. It is reminded that the reaction order (m) values of all the samples presented in **Fig. 10** are 0.13 – 0.15 while the activation energies (E_a) and polarization resistances (R_p) become much smaller by a surface treatment.

The most sluggish step is often considered to be the bottleneck step (i.e. RDS), but this is the case only in a process where each step (sub-process) is arranged sequentially through a single route without a parallel pathway. In a process with parallel pathways, the most sluggish pathway may not be experimentally captured because the overall reaction rate will be determined by faster pathway(s) in this case. In our system, two different types of parallel pathways–bulk pathway (green) and surface pathway

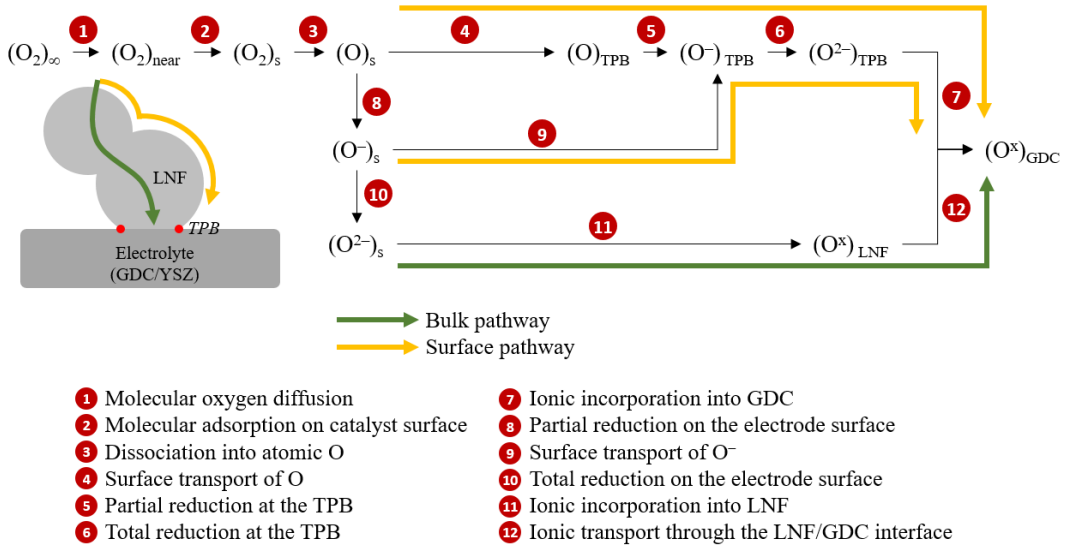

Fig. 4.13 A schematic diagram of possible ORR pathways in a LNF/GDC system. $(O_2)_s$ and $(O)_s$ refer to O_2 and O adsorbed on the electrode surface, respectively; TPB stands for triple phase boundary.

(yellow)–can be considered. Between the two, however, the bulk pathway is neglected (considered too resistive to compete against the surface pathway) based upon the following reasoning: (a) The extremely small concentration of oxygen vacancies in the LNF backbone should result in a negligible ionic conductivity,[115,127,128] and (b) the capacitance value measured from the EIS (on the order of 1×10^{-4} F cm^{-2}) is too small to correspond to a bulk process.[133] Herein, we consider the surface pathways only (corresponding to **Steps 1 – 9** in **Fig. 4.13**). Among these, Steps 1, 2, 4, and 9 are not expected to have played a dominant role in enhancing the overall ORR kinetics by the surface treatment, and thus are not expected to comprise an RDS. The following lists the justification.

Step 1: *Since the overall microstructure (geometry/porosity) was rarely changed by the highly surface-specific treatments (infiltration and/or ALD), the mass transport of gaseous O_2 should not have been affected.*
Step 2: *If the molecular adsorption step were the RDS, the reaction order (m) should be close to 1, but the m values of all the studied samples are much smaller than that (~ 0.15). In addition, the high-surface-area morphology of the LNF backbone (as opposed to a dense layer) should have provided abundant O_2 adsorption sites, making it even less likely to be an RDS.*
Steps 4 and 9: *If the surface diffusion of the electroactive oxygen species (O or O^-) were the RDS, m is expected to be close to 0.5. In addition, their slow kinetics (driven by diffusion) results in a low characteristic frequency (f_c), which is not aligned with the high f_c range we observe ($10^3 – 10^4$ Hz). Furthermore, specifically in the case of ceria infiltration, while the ceria infiltration (Ce_{Inf}) resulted in a significant decrease in R_p, the surface area where the infiltrated species occupy is only a small fraction of the whole LNF surface area, making it difficult to believe that the surface adatom diffusion is highly facilitated by the infiltrated particles.*

Now, Steps 3, 5, 6, 7 and 8 are the remaining candidates. Among these, Steps 5, 6 and 7 are charge transfer reactions occurring at the TPB region where gas, cathode and electrolyte meet altogether. Although we cannot fully exclude the possibility of enhancing the electrochemical activity of TPB region by the surface treatment, it is unlikely to achieve 10-fold improvement in electrode performance by adding some additional ceria in the highly localized TPB region when considering the electrolyte material interfacing with the cathode is another ceria-based material (GDC). On the other hand, the majority of earlier studies report LSM and LNF are rate-limited by dissociation[134–138] or dissociation with a charge transfer reaction.[115,128] (Here, the similarity in the RDS between LSM and LNF is justified by their similar characteristics including extremely low oxygen vacancy concentration under operational oxygen activity, high activation energy for O_2 dissociation, and high electronic conductivity with negligible ionic conductivity.[115])

For these reasons, we conclude that Steps 3 and 8 are responsible for the drastic improvement of overall electrode performance by the surface treatment, and thus the overall reaction rate is co-limited by dissociation and the subsequent partial reduction.

The impedance data of Type III-A cells are presented in **Fig. 4.10c-d**. In both $Ce_{Inf}Ce_{ALDn}$ (**Fig. 4.10c**) and $Ce_{Inf}Y_{ALDn}$ series (**Fig. 4.10d**), there is an optimum number of cycles for performance, presenting a V-shape behavior in the R_p versus ALD cycle relation. The $Ce_{Inf}Ce_{ALD6}$ and $Ce_{Inf}Y_{ALD3}$ show even lower R_p values than Ce_{Inf} showing the promise of further activity enhancement of infiltrated electrodes by an ALD treatment. The V-shape behavior makes good sense in that an excessive ALD overcoat will fully block the underlying catalytically active surface while a negligible amount of ALD species will make little effect on the performance. However, the reason behind the increase of R_p caused by only a single cycle ALD of yttria (**Fig. 4.10f**) is not clear at this point. It is noted that ALD treated samples show E_a values ranging 1.02 – 1.29 eV, considerably lower than that of the infiltration-only sample (1.55 eV). A synchronous behavior of E_a with R_p among the ALD-treated samples is additionally noted; the samples with minimum R_p show the smallest E_a in each sample series. These indicate a significant decrease of the barrier height for O_2 activation or even a possible shift in the RDS of oxygen reaction by a sub-nanometer scale ALD. This is again in accordance with the XPS result showing a high Ce^{3+} content of ALD-treated samples compared to Ce_{Inf}. On the other hand, Type III-B samples ($Ce_{Inf\text{-}sint}Y_{ALD3}$ and $Ce_{Inf\text{-}sint}Ce_{ALD6}$; **Fig. 4.10e**) show slightly higher R_p values than their corresponding Type III-A samples ($Ce_{Inf}Y_{ALD3}$ and $Ce_{Inf}Ce_{ALD6}$). This is likely because the additional sintering process performed before ALD treatment (Type III-B samples) have the infiltrated NPs agglomerated, resulting in a decrease of surface area (see **Fig. 4.17f** and the green bars in **Fig. 4.17a-e**; longer trails toward bigger NP sizes beyond ~ 40 nm is found in Type III-B samples unlike Type I and Type III-A samples). The additional surface roughness on infiltrated NPs of $Ce_{Inf\text{-}sint}Ce_{ALD6}$ (by the presence of ceria nanodots as revealed by the SEM images in **Fig. 4.2**) does not seem to play a determining role in the performance of electrodes studied in this report.

4.3.4 Electrochemical properties on durability

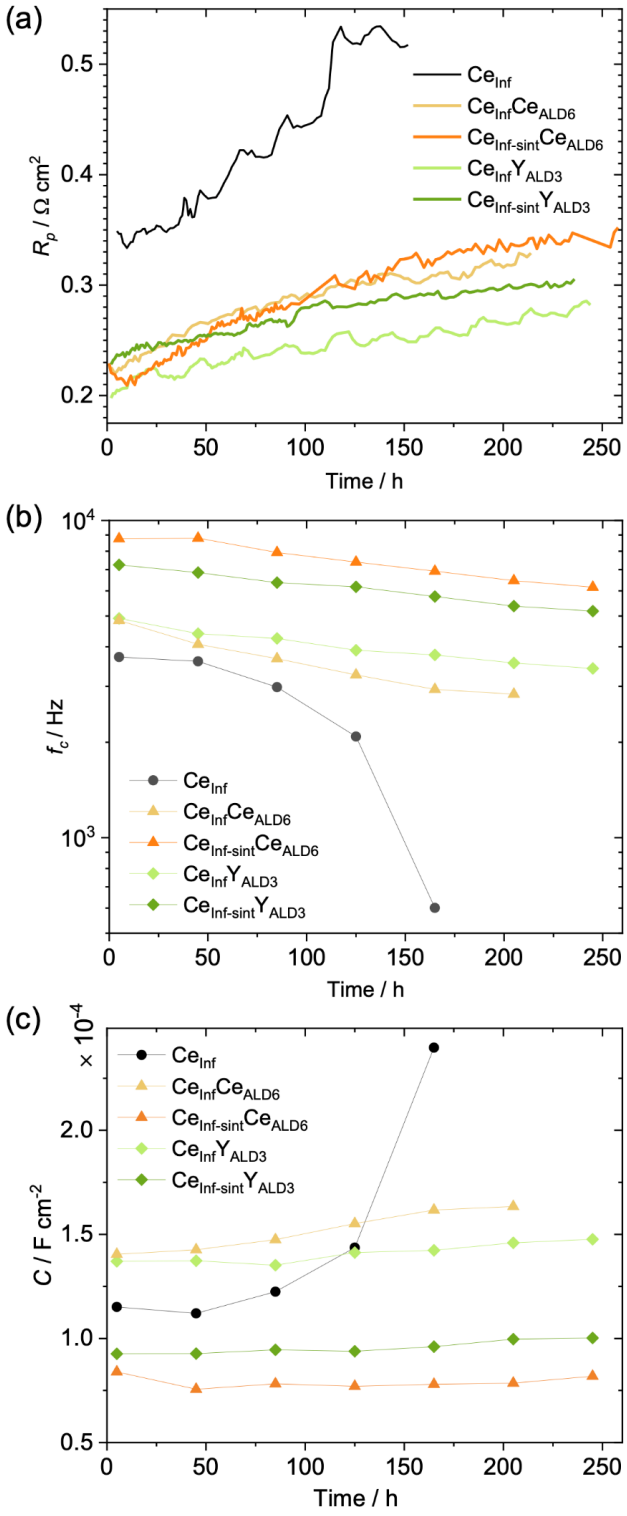

Fig. 4.14 (a) Time evolution of polarization resistance (R_p), (b) characteristic frequency (f_c), and (c) capacitance (C). All are deduced from the impedance data, which were obtained intermittently at the open circuit condition during the thermal exposure at 700 °C.

The ALD treatment on an infiltrated electrode is also found to improve the thermal stability of the electrode significantly. As shown in **Fig. 4.14**, Ce_{Inf} shows a rapid degradation; R_p changed from 0.33 to 0.53 Ω cm^2 in 150 h at 700 °C, which translates into a degradation rate of 1.33 mΩ cm^2 h^{-1}. By treating the infiltrated surface with ALD (Type III), however, we observe a significantly improved thermal stability. By coating 6 ALD cycles of ceria ($Ce_{Inf}Ce_{ALD6}$), the degradation rate decreased to 0.48 mΩ cm^2 h^{-1} (from 0.22 to 0.32 Ω cm^2 in 200 h), and 3 cycles of yttria ($Ce_{Inf}Y_{ALD3}$) resulted in an even lower degradation rate of 0.30 mΩ cm^2 h^{-1} (from 0.21 to 0.27 Ω cm^2 in 220 h). The enhanced durability is further visualized with the evolution of characteristic frequencies (f_c) and capacitance (C) of electrode process as shown in **Fig. 4.14b** and **Fig. 4.14c**; here, the capacitance is quantified using $C = (R_p \cdot Q)^{1/\alpha}/R_p$ where Q is a non-ideal capacitance specific to CPEs and α is the similarity to an ideal capacitor (α = 1: an ideal capacitor). While Ce_{Inf} exhibits a dramatic shift in f_c in 150 h (from 3,713 Hz to 601 Hz), ALD-treated samples show relatively mild changes ($Ce_{Inf}Ce_{ALD6}$: from 4,841 to 2,835 Hz in 200 h; $Ce_{Inf}Y_{ALD3}$: from 4,916 to 3,417 Hz in 250 h), confirming the enhanced thermal stability by ALD treatment. All the Type III samples maintain the f_c values within $10^3 – 10^4$ Hz and the capacitance values within $0.7 \times 10^{-4} – 1.6 \times 10^{-4}$ F cm^{-2} throughout the thermal exposure. Combined with the initial m values of ~0.15 (**Fig. 4.14e**), it can be reasonably asserted that the RDS of all the studied Type III samples is dissociation combined with an electron transfer process (i.e. O_2 activation). However, the non-ALD treated Ce_{Inf} shifts its f_c to a much lower values over time suggesting the RDS shifts to a more sluggish, non-electrochemical process such as surface diffusion of electroactive oxygen.[115]

The degradation of infiltrated SOFC cathodes has been ascribed largely to the agglomeration of infiltrated NPs, hence the loss of active surface area.[126] In light of this, we examined the change in the size of infiltrated NPs by an extended thermal exposure at 700 °C for 260 h. It is noted that the test was performed in a Cr-free chamber, eliminating Cr poisoning[139] from a possible factor of cell degradation. the size of ceria particles was quantified for all the particle that is less than ca. 60 nm from 760 × 520 nm^2 field emission SEM images. The SEM images that have ca. 200 or more of infiltrated NPs are chosen to provide a meaningful size distribution. As presented in **Fig. 4.1b**, we could resolve nanodots as small as 3 – 6 nm from images acquired from the same SEM system. The size of the ceria particles was obtained on a magnified version of the original SEM images by drawing a circle that fits best to the eyes with the perimeter of each infiltrated NP as presented in **Fig. 4.15b**, and denoting the diameter of the fitted circle. For a particle whose shape deviates significantly from a circle, the size was taken from the average between its longest length and the length in the direction perpendicular to the longest side. When estimating the size of each particle, a size with step of 3 nm were taken with error tolerance of ±1.5 nm (e.g. 3±1.5 nm, 6 ±1.5 nm, 9±1.5 nm, …).

To test whether this method enables a convincing approximation, we applied this approach to two different SEM images from a specific sample ($Ce_{Inf}Ce_{ALD6}$) and presented the resulting distribution in **Fig. 4.16**. As demonstrated, not only the overall distribution (**Fig. 4.16c**) but also the d_{20}, d_{50} and d_{80} values are in a close proximity to each other (**Fig. 4.16d**).

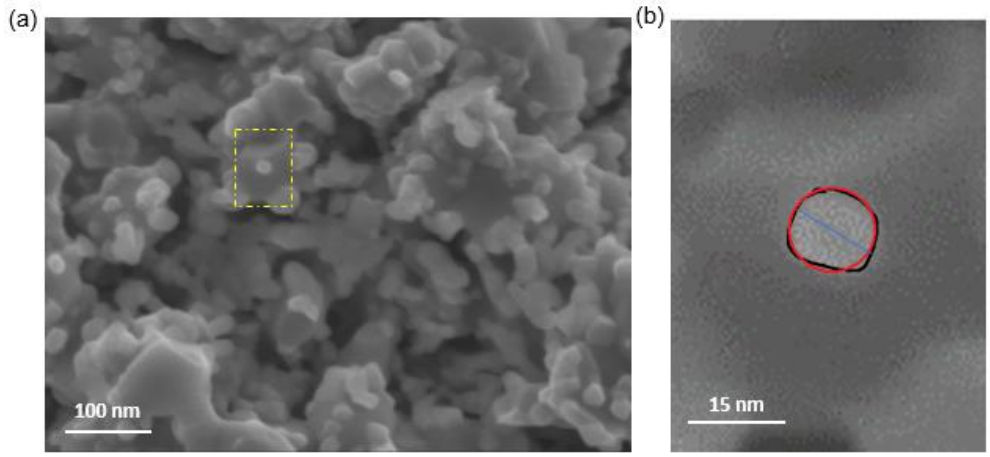

Fig. 4.15 (a) An exemplary SEM image taken from $Ce_{Inf}Ce_{ALD6}$ (a,b), and (b) a close-up image in the dotted area in (a). The size of the nanoparticle defined by the black line was estimated by drawing a red circle. The resulting diameter of the red circle was quantified as the particle size.

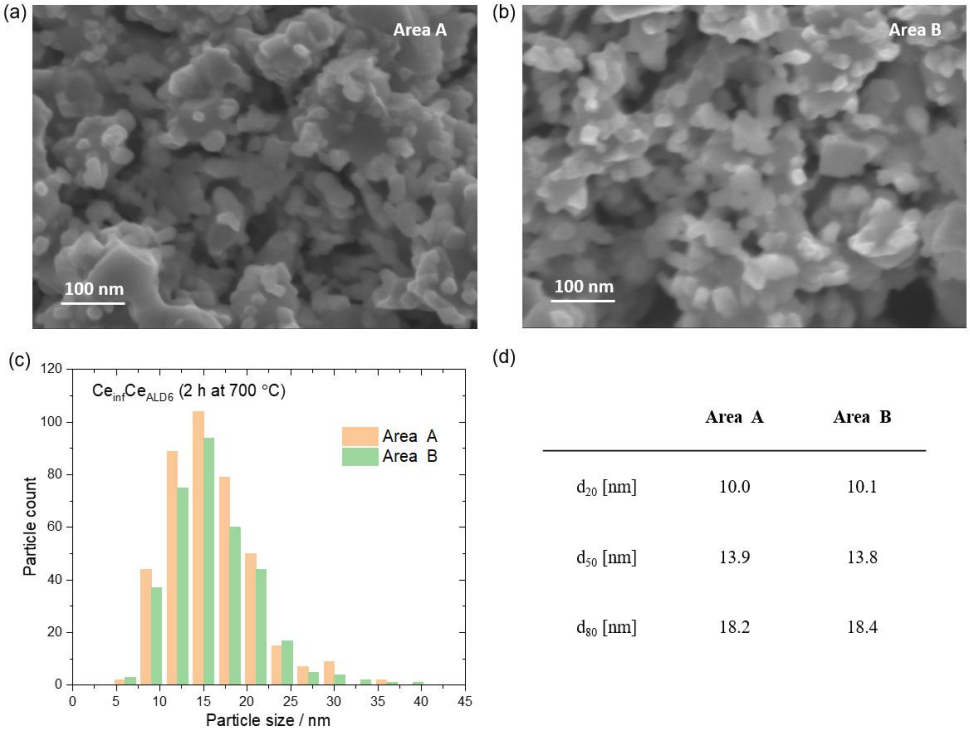

(d)

	Area A	Area B
d_{20} [nm]	10.0	10.1
d_{50} [nm]	13.9	13.8
d_{80} [nm]	18.2	18.4

Fig. 4.16 (a,b) Exemplary SEM images taken from two different areas of a $Ce_{Inf}Ce_{ALD6}$ sample and the resulting particle size distributions (c) and d_{20}, d_{50} and d_{80} values.

Fig. 4.17a-e show the size distribution of infiltrated NPs at the initial (2 h) and final stage (260 h) of the thermal stress. The bar charts show that even 3 – 6 cycles of ALD treatment (corresponding to the nominal thickness of 0.72 – 1.44 Å) is highly effective in suppressing agglomeration. While the distribution of Ce_{Inf} shifted prominently toward larger sizes after 260 h (**Fig. 4.17a**), those of ALD-treated samples (**Fig. 4.17b-e**) are much better preserved during the same duration. For a quantitative analysis, accumulative distributions of NP sizes in each sample are given in **Fig. 4.17f**. It is quantified that 80% of the infiltrated ceria NPs in $Ce_{Inf\text{-}sint}Y_{ALD3}$ are equal to or less than 20.9 nm (namely, d_{80} = 20.9 nm) at the initial stage (2 h), and the d_{80} value quantified at the final stage (260 h) is virtually unaltered (22.2 nm), indicating that $Ce_{Inf\text{-}sint}Y_{ALD3}$ exhibits an excellent resistance against thermal agglomeration of infiltrated NPs. In terms of agglomeration resistance among the Type III samples as gauged by the average d_{80} value change per hour ($\Delta d_{80}/h$) in [pm h^{-1}], $Ce_{Inf\text{-}sint}Y_{ALD3}$ (5.0) is followed by $Ce_{Inf}Ce_{ALD6}$ (24.2), $Ce_{Inf}Y_{ALD3}$ (36.5) and $Ce_{Inf\text{-}sint}Ce_{ALD6}$ (39.2). On the

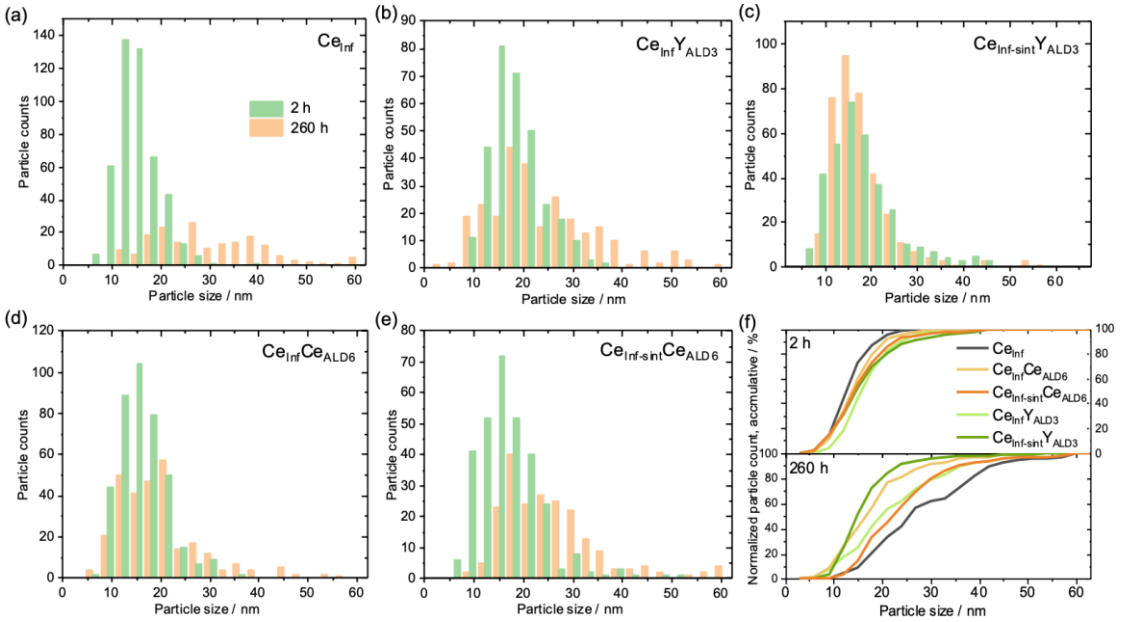

Fig. 4.17 (a-e) Size distribution of infiltrated ceria NPs in each sample after 2 h and 260 h at 700 °C, and (f) the corresponding accumulative distribution of infiltrated ceria NPs, counting from smaller NPs. Graphs are based upon the SEM images provided in Fig. 4.18 and Fig. 4.19

other hand, d_{80} of Ce_{Inf} changed significantly from 16.7 nm to 38.4 nm in ~ 260 h ($\Delta d_{80}/h$ = 83.5 pm h^{-1}), reflecting the most severe NP growth among the 5 samples. (The d_{80} values are tabulated in **Table 4.5**) It is also noted that, from **Fig. 4.14** and **Fig. 4.17**, there is a clear positive correlation between the durability of electrochemical performance and thermal stability of electrode morphology; the samples with the highest and the lowest agglomeration rate ($Ce_{Inf\text{-}sint}Y_{ALD3}$ and Ce_{Inf}, respectively; from **Fig. 4.17**) are concomitantly those with the highest and the lowest rate of performance degradation (from **Fig. 4.14**).

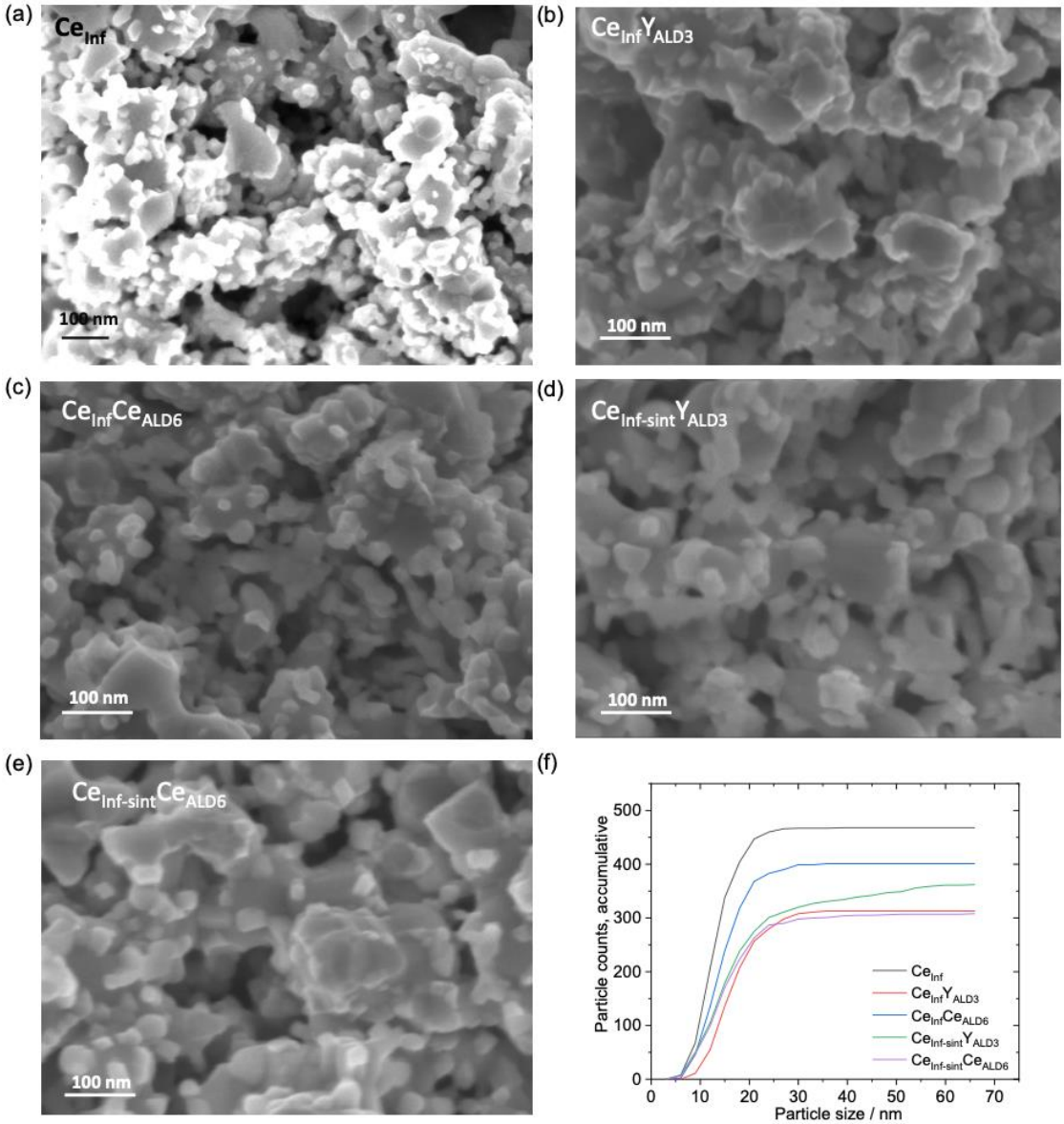

Fig. 4.18 (a-e) SEM micrographs of 5 different samples at the initial stage of thermal stress (after 2 h at 700 °C). (f) Accumulative number of particles versus particle size, counting from those with smaller particle size.

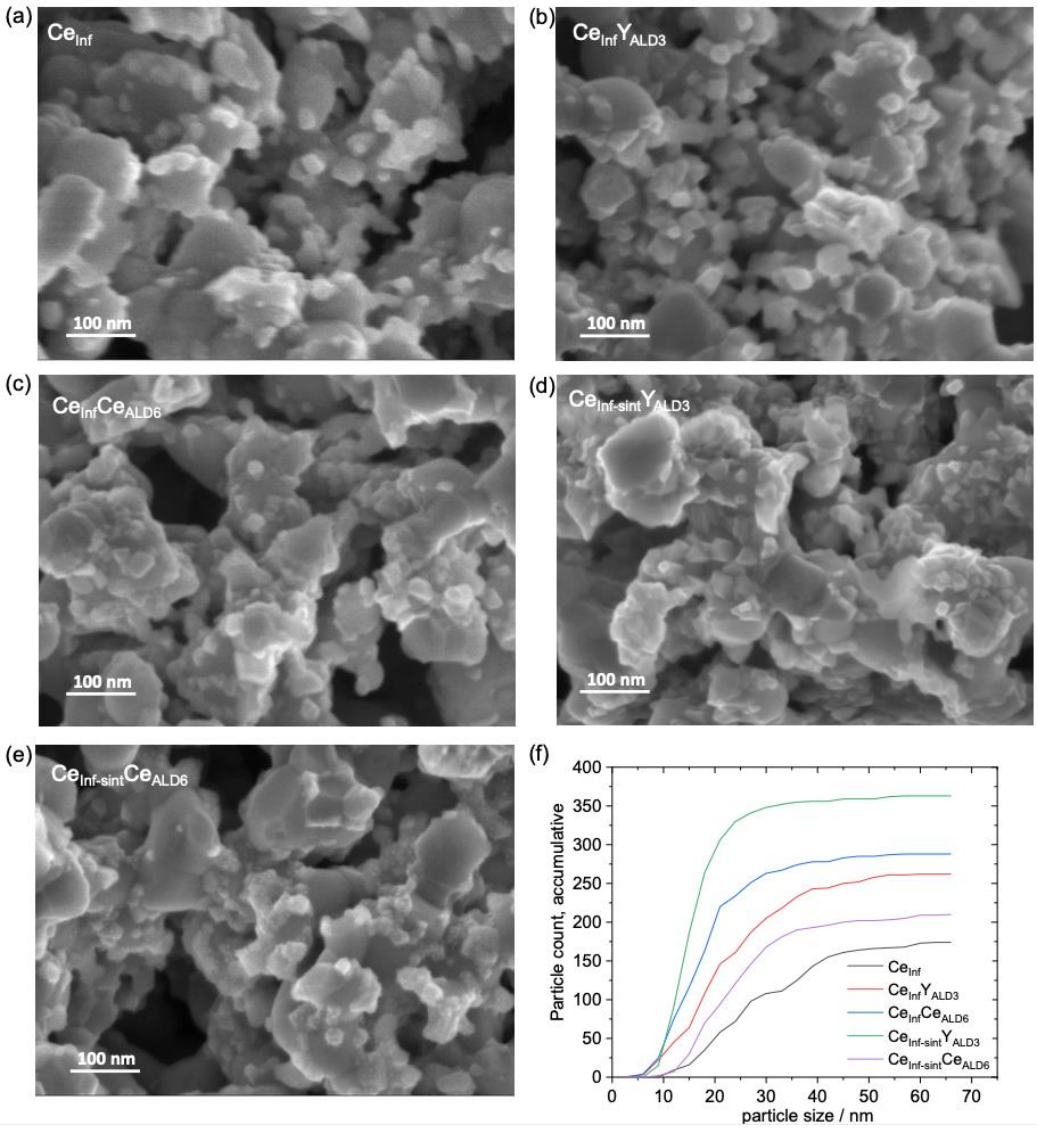

Fig. 4.19 (a-e) SEM micrographs of 5 different samples after 260 h at 700 °C. (f) Accumulative number of particles versus particle size, counting from those with smaller particle size.

Table 4.5 Summary of d_{20}, d_{50} and d_{80} values of each sample after 2 h and 260 h at 700 °C.

Samples		d_{20} [nm]	d_{50} [nm]	d_{80} [nm]
Ce_{Inf}	2 h	9.6	12.6	16.7
	260 h	18.0	25.7	38.4
$Ce_{Inf}Y_{ALD3}$	2 h	12.3	15.9	20.6
	260 h	13.2	19.7	30.1
$Ce_{Inf}Ce_{ALD6}$	2 h	10.0	13.9	18.2
	260 h	11.0	16.8	24.5
$Ce_{Inf\text{-}sint}Y_{ALD3}$	2 h	10.2	14.7	20.9
	260 h	11.3	15.0	22.2
$Ce_{Inf\text{-}sint}Ce_{ALD6}$	2 h	9.9	14.3	19.8
	260 h	15.9	22.2	30.0

4.4 Conclusion

While infiltrated NPs on a porous backbone often enhances the electrode performance by a significant margin, the high surface energy of NPs tends to make them highly susceptible to thermal agglomeration. In this report, we show that an ALD-based atomic-scale (0.7 – 1.5 Å) overcoat of ceria or yttria over a ceria infiltrated LNF is highly effective in suppressing the thermal agglomeration of infiltrated ceria NPs, and that the effect is directly correlated to the thermal durability of electrode performance, via a systematic and quantitative approach. In addition, we demonstrate that the atomic-scale ALD overcoat dramatically enhances the electrode performance in terms of polarization resistance and its activation energy for both bare LNF and ceria-infiltrated LNF electrodes. The improved electrode activity from ALD treatment is mainly ascribed to a significant facilitation of O_2 activation (i.e. O_2 dissociation followed by a partial reduction) by the additional surface-specific oxygen-deficient and catalytically active ceria.

Chapter 5: Effect of Angstrom-level Oxide Overcoat on Sr Segregation Behavior of LSM Electrodes

5.1 Introduction

The driving force of dopant segregation has been mainly attributed to elastic energy in the lattice and electrostatic interactions of the dopant with other species in the oxide [140,141]. First, elastic energy is incurred largely by the size mismatch between the host and dopant cations at the A-site; Sr^{2+} dopant is larger than the host cation, La^{3+} by ~5.9% [142]. Koo et al. studied the relation between the strain applied to the system and Sr segregation and observed that the surface Sr species become less populated with lower compressive strains [143]. On the other hand, the electrostatic interaction-based Sr segregation is ascribed to the positively charged oxygen vacancies ($V_O^{\cdot\cdot}$ in the Kröger-Vink notation) heavily accumulated on the surface [144–147]. Oxygen vacancies are readily formed on the surface because of its lower coordination compared to the bulk [141]. The surface oxygen vacancies attract negatively charged Sr (Sr_A' in the Kröger-Vink notation) toward the surface and facilitates Sr segregation. Tsvetkov et al. demonstrated that an addition of cations with low reducibility on the surface of $La_{0.8}Sr_{0.2}CoO_3$ (LSC) decreases the surface $V_O^{\cdot\cdot}$ concentration and suppresses Sr surface segregation [144]. More recently, Choi et al. showed that an overcoat of few nanometer-thick $Gd_{0.1}Ce_{0.9}O_{2-\delta}$ (GDC) on the surface of $Sm_{0.5}Sr_{0.5}CoO_{3-\delta}$ (SSC) reduces the oxygen vacancy concentration on the SSC surface and suppresses surface segregation of Sr_{Sm}', affording an excellent electrode durability [148].

In this chapter, we present a behavior seemingly contradicting to the aforementioned mechanism of electrostatic force-driven Sr segregation; we observe that a higher concentration of oxygen vacancies on the surface of LSM tends to suppress Sr segregation toward surface or even incorporate Sr species back into the lattice of LSM. A different mechanism – diffusion of oxygen vacancies – is proposed based upon a series of X-ray photoelectron spectroscopy observations. To induce a change in the oxygen vacancy concentration on LSM surface, four different metal oxides with an angstrom-level thickness are coated by atomic layer deposition (ALD). ALD affords a precise thickness and uniformity control at a sub-nanometer level. By utilizing layer-by-layer deposition where each layer deposition is self-limited, the thickness of a film can be tailored by the number of ALD cycles [149]. The sequential and self-limiting characteristics of ALD enables an unprecedented control over the thickness and uniformity even on a substrate with highly complicated geometry.

5.2 Experimental

5.2.1 Cell Preparations

The LSM powder was synthesized by using the glycine-nitrate combustion method. $La(NO_3)_3 \cdot 6H_2O$, $Sr(NO_3)_2$, and $Mn(NO_3)_2 \cdot 4H_2O$ with a molar ratio of 0.8:0.2:1 were dissolved in a minimal amount of deionized water while being stirred on a hot plate. Glycine was used as the reducing agent. The molar ratio between the sum of the nitrates and glycine was 1:1. Combustion was performed after the mixture was dehydrated in air. The resulting powder was sintered at 850 ºC for 3 h in a zirconia container to obtain LSM. The crystallography of LSM powder was confirmed by X-ray diffraction (XRD) analysis.

The cells used for electrochemical impedance spectroscopy (EIS) testing are in a symmetric configuration. On a commercial YSZ substrate (thickness: 250~300 μm; diameter: 20 mm; Fuelcellmaterials.com), a 10 μm thick $Ga_{0.2}Ce_{0.8}O_2$ (GDC) interlayer was screen printed on both sides of YSZ. Onto each GDC layer, a layer of LSM (namely, functional layer) was deposited again by screen-printing, followed by a sintering at 850 °C for 3 h. An atomic layer deposition (ALD) was performed onto each side of the functional layers; 8 cycles of TiO_2, 10 cycles of CeO_2, 3 cycles of ZrO_2 and 3 cycles of Y_2O_3 (namely, LSM-Ti, LSM-Ce, LSM-Zr, and LSM-Y, respectively). Finally, two more layers of LSM were screen-printed and sintered at 850 °C for 3 h to use as the current collecting layer. The GDC interlayer is placed to prevent any unexpected reactions between YSZ and LSM layers. The slurries for GDC and LSM were made by mixing GDC nano-powder or LSM power with ethyl cellulose, Hypermer KD-1, and terpineol in an appropriate ratio. A circular reaction area of 0.35 cm^2 was formed in all symmetric cells.

The ALD was performed in a commercial ALD system (ICOT Inc). $Zr(NMe_2)_4$, $Y(MeCp)_3$, $Ce(iPrCp)_3$, and $Ti(NMe_2)_4$ were used as the precursors of Zr, Y, Ce, and Ti respectively. Nitrogen (99.9%) and deionized water were used as the purging gas and oxygen source, respectively. The chamber temperature was set at 250 ºC, and the canister temperatures for Zr, Y, Ce, and Ti precursors were 80, 150, 150, and 80 ºC, respectively. Purging gas was fed at a constant flow rate of 3 sccm.

5.2.2 Physical Characterization

A field-emission scanning electron microscopy (FE-SEM, Zeiss Gemini 500) was used at 3 kV to observe the microstructure. X-ray photoelectron spectroscopy (XPS) was performed on a Nexus system (Thermo Fisher Scientific) using monochromated, micro-focused, low power Al Kα X-ray source for excitation and a 180º, double-focusing, hemispherical analyzer with 128-channel detector (10-400 μm spot size with adjustable sample holder incident to X-ray beam from 0º to 60º). The phase and composition of samples were evaluated by XRD using a PANalytical X'Pert Pro system with Co Kα radiation (λ = 1.78897 Å).

5.2.3 Electrochemical characterization

Electrochemical characterization was performed by electrochemical impedance spectroscopy (EIS; Bio-Logic SP-200) with 20 mV of AC perturbation at the open circuit condition. Durability tests were performed in a custom-made Cr-free SOFC test station in air to avoid possible Cr poisoning during operation. For durability test, silver mesh was to collect current. A 5 kg load was applied through the cell to ensure a solid contact between the cell and current collecting mesh.

5.3 Result and Discussion

5.3.1 Cell set-up

Each of the four different metal oxides (ZrO_2, Y_2O_3, CeO_2, and TiO_2) with a similar nominal thickness (2 – 3 Å) was introduced by ALD on a LSM backbone. As shown in **Fig. 5.1**, the ALD treatment was performed on the first layer of porous LSM backbone (~20 μm), and we call it the functional layer (FL). Two additional LSM layers were further screen-printed on top of the FL for current collection. Due to the low ionic conductivity of LSM [150], most ORR reaction is expected to occur in a close vicinity to the electrode-electrolyte interface within the FL.

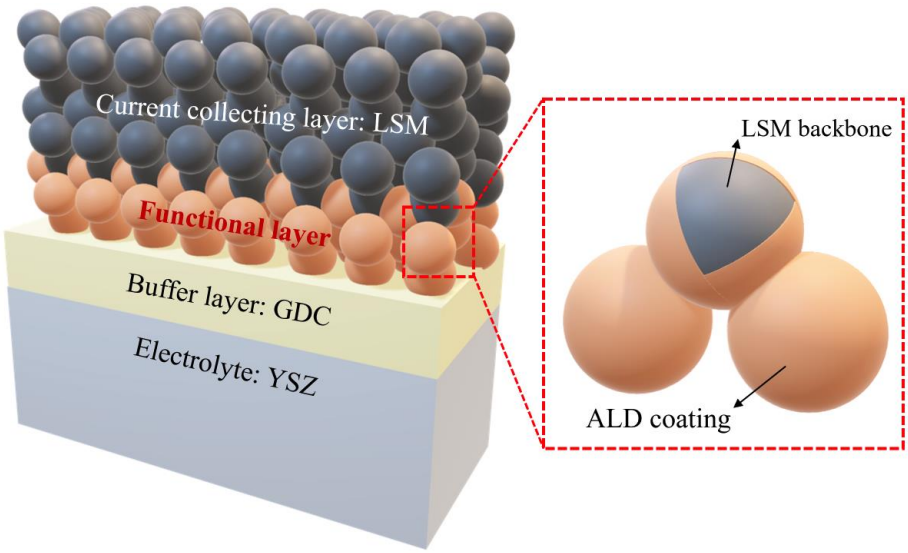

Fig. 5.1 A schematic diagram of the cell configuration, showing half of a symmetric cell.

5.3.2 Physical properties

First, XRD analysis is performed to identify the crystal phase of LSM powder synthesized through the glycine nitrate combustion method. **Fig. 5.2** shows that LSM is in a rhombohedral phase ($R\bar{3}c$ space group) without a noticeable trace of $Sr(OH)_2$ and SrO phase. There is no additional peak appearing after a prolonged exposure to 750 ºC for 50 h or 250 h. ALD treated samples do not exhibit discernible peaks other than

those found in the bare LSM either, which is likely because the amount of ALD-derived oxide is negligible compared to the LSM pellet [151].

To better understand the effect of angstrom-level metal oxide overcoat on the surface chemistry, XPS analysis is performed on each of 5 samples (LSM-bare and four ALD-coated LSM samples) at 3 different stages of aging at 750 °C: 0 h, 50 h, and 250 h. Sr 3d spectra are deconvoluted into two constituents as shown in **Fig. 5.3a–c** and **Fig. 5.4:** Sr_α (~132.1 eV) assigned to lattice Sr, and Sr_β (~133.7 eV) assigned to surface Sr species such as SrO, $Sr(OH)_2$ and $SrCO_3$ [144]. Once Sr species reach the surface by segregation, they subsequently react with surrounding gas and form compounds such as hydroxides and carbonates [145]. Unlike the other samples, those with TiO_2 and CeO_2

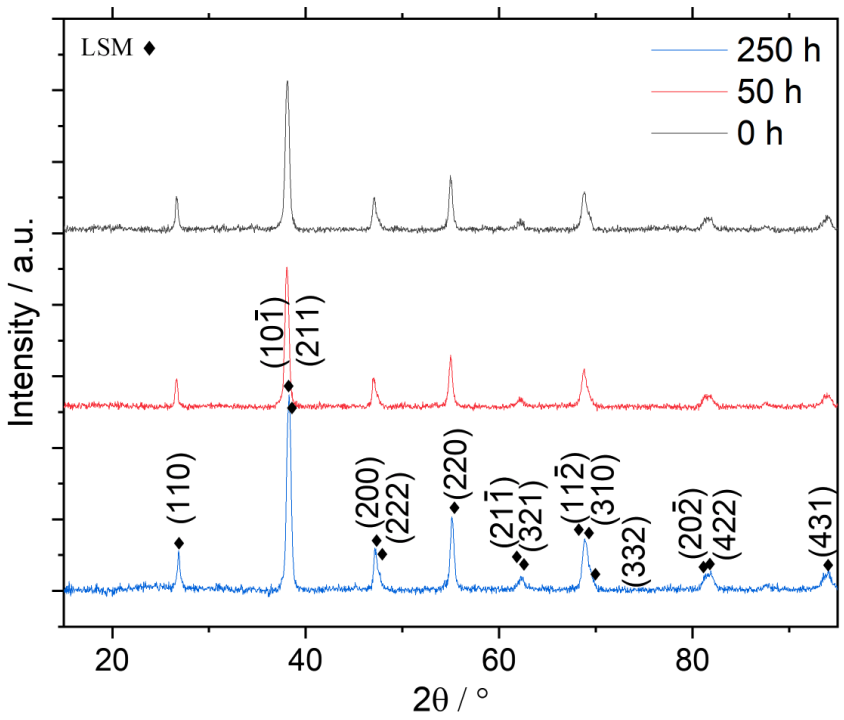

Fig. 5.2 XRD spectra of LSM-bare after exposing it to air at 750 °C for 0 h, 50 h and 250 h.

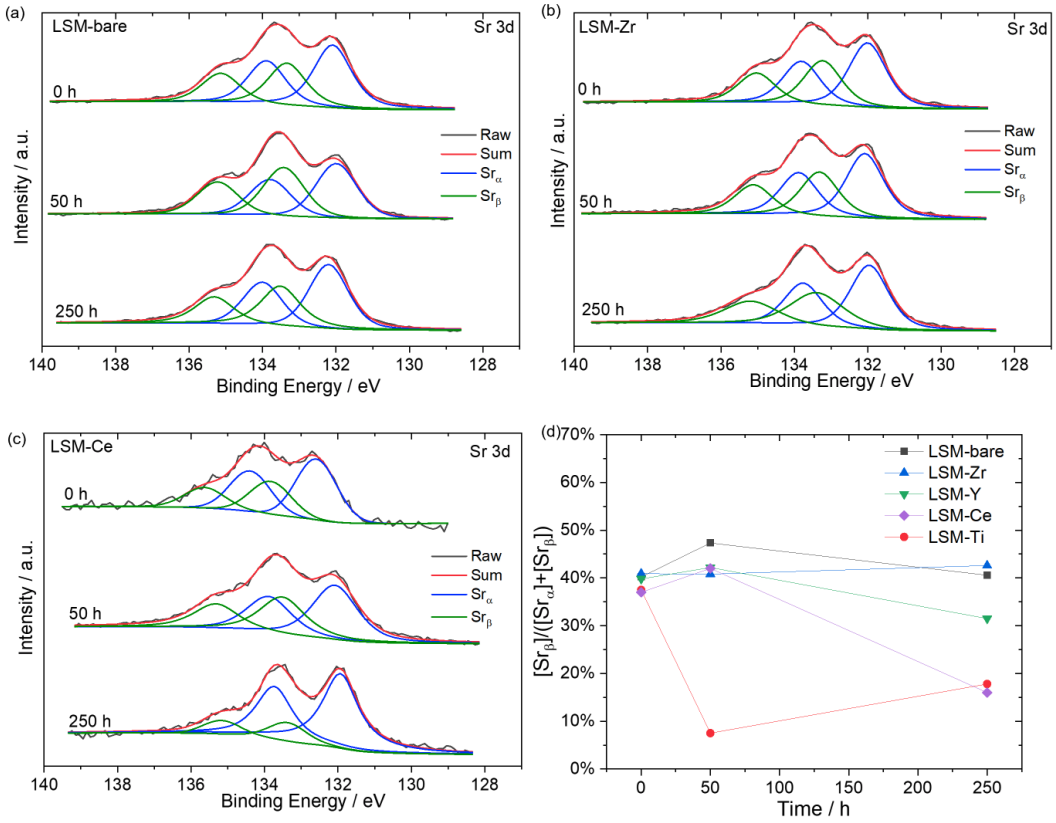

Fig. 5.3 (a-c) Sr 3d spectra of (a) LSM-bare, (b) LSM-Zr, and (c) LSM-Ce after exposing them to air at 750°C for 0, 50, and 250 h. The spectra are deconvoluted into two parts: surface Sr (green) and lattice Sr (blue). d) Relative concentrations of surface Sr as a function of thermal exposure time. All data are obtained at the collection angle of 0°.

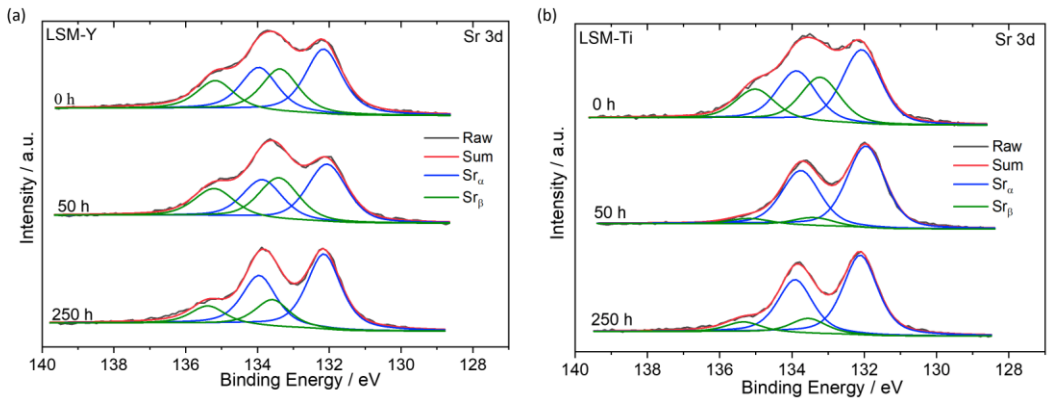

Fig. 5.4 XPS Sr 3d spectra of (a) LSM-Y and (b) LSM-Ti after exposing them to air at 750°C for 0, 50, and 250 h. The XPS spectra are obtained at the collection angle of 0°.

overcoat (i.e., LSM-Ti and LSM-Ce) show a significant decrease in the surface Sr content after 250 h, as shown in **Fig. 5.3d**. The fraction of surface Sr quantified by

$[Sr_\beta]/([Sr_\alpha] + [Sr_\beta])$ in LSM-Ti decreased from 37.5% to 17.8% after 250 h, and the fraction in LSM-Ce decreased from 37.0% to 16.0%.

As an alternative method of gauging the degree of segregation, an angle resolved XPS (ARXPS) was also performed. By varying the angle at which the emitted electrons are detected with respect to the sample direction, one can obtain spectra relevant to different depths of the sample. While the usual XPS probes a depth of ~10 nm, a shallower depth is probed by detecting emitted electrons at a tilted angle [152]. In our system, the intensity ratio of the signals obtained at the collection angle of 60° to those at 0° is ~ 0.29 for an LSM-bare sample, indicating that the detection depth for sample with 60° emission angle is less than 2.9 nm. Here, the collection angle means the angle formed between the direction of incident beam and the direction normal to the sample surface. Although the samples are porous and corrugated, as opposed to uniform and dense, the ARXPS characterization is expected to provide at least qualitative sense of how the chemical states in the very vicinity of the surface are different from those within the lattice considering the size of each particle-like feature is >~50 nm, significantly larger than the detection depth. A normalized parameter, Sr^* is defined to indicate the degree of Sr segregation toward surface as

$$Sr^* = \frac{[Sr_{60°}]/([Sr_{60°}] + [La_{60°}])}{[Sr_{0°}]/([Sr_{0°}] + [La_{0°}])} \tag{5.1}$$

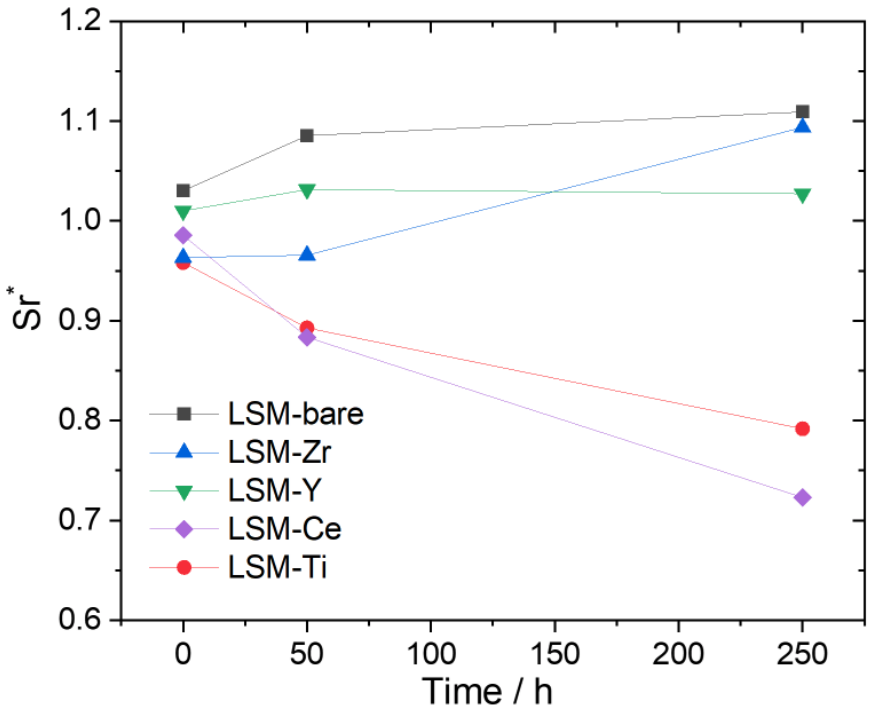

Fig. 5.5 Surface Sr analysis based on the total amount of Sr in XPS data, normalized by La in the same condition.

where $[Sr]$ and $[La]$ are the atomic concentrations of Sr and La, respectively, obtained from the spectra at their corresponding collection angles. As shown in **Fig. 5.5**, all the samples exhibit an initial Sr^* value of 1 ± 0.05, indicating a uniform depth-wise distribution of Sr species in the beginning. While LSM-bare and LSM-Zr exhibit a slight increase of Sr^* after 250 h, LSM-Ti and LSM-Ce show a significant decrease in Sr^*, reflecting a desegregation behaviour (meaning Sr movement from the surface to the bulk) during the heat exposure. This is well aligned with the data in **Fig. 5.3** that show a decreased surface Sr species in both LSM-Ti and LSM-Ce. The similarity in the time evolution of Sr species as observed from the two separate approaches – peak deconvolution (**Fig. 5.3**) and ARXPS analysis (**Fig. 5.5**) – convincingly suggest that an atomic scale overcoat by TiO_2 and CeO_2 is highly effective in desegregating Sr species from surface into the bulk. On the other hand, the samples coated with Y_2O_3 and ZrO_2 (i.e., LSM-Y and LSM-Zr) show relatively minor difference from LSM-bare in the segregation behaviour.

Looking at the results presented above, we recognize that samples coated with an oxide of multi-valent cations (i.e., LSM-Ce and LSM-Ti; namely, OMC) show a

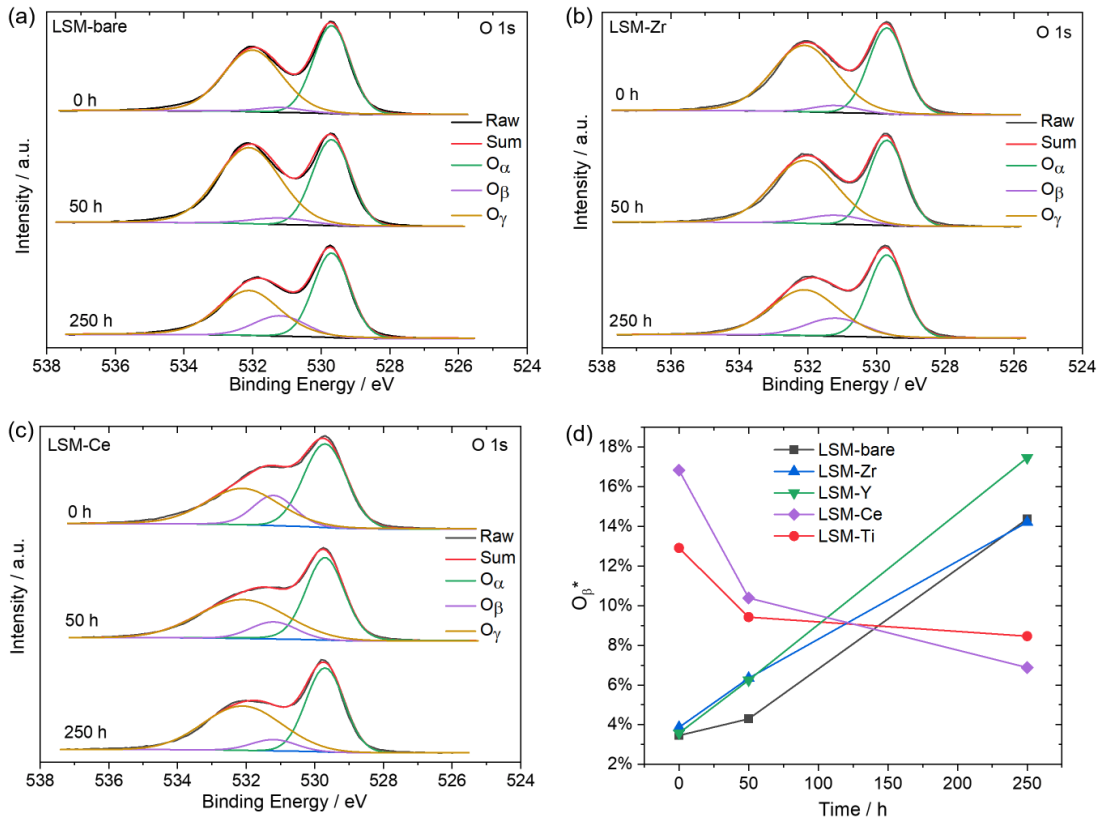

Fig. 5.6 (a-c) O 1s spectra of (a) LSM-bare, (b) LSM-Zr and (c) LSM-Ce after exposing them to air at 750°C for 0, 50, and 250 h at the electron collection angle of 0°. The spectra are deconvoluted into three parts: lattice oxygen (green), oxygen vacancy (purple) and surface oxygen (brown). (d) Relative concentrations of oxygen vacancies quantified based upon the peak deconvolution, as a function of thermal exposure time.

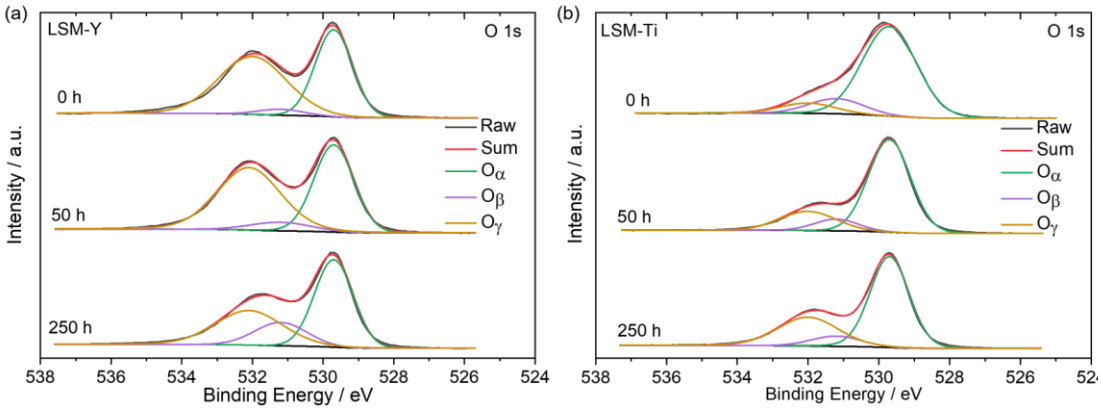

Fig. 5.7 XPS O 1s spectra of (a) LSM-Y and (b) LSM-Ti after exposing them to air at 750°C for 0, 50, and 250 h. The XPS spectra are obtained at the collection angle of 0°.

continuous desegregation behaviour whereas those coated with an oxide of single valent cations (i.e., LSM-Zr and LSM-Y; OSC) show a minor Sr segregation. To better understand the correlation between the cationic multi-valency and segregation behaviour, the evolution of O 1s peak is additionally observed as shown in **Fig. 5.6** and **Fig. 5.7**; the spectra for LSM-bare, LSM-Zr, and LSM-Ce are presented in **Fig. 5.6a-c**, and those for LSM-Y and LSM-Ti are provided **Fig. 5.7**. The peaks at ~529.7 eV, 531.2 eV and 532.2 eV are ascribed to the lattice oxygen (named as O_α), oxygen defect (i.e., oxygen vacancy; O_β) and surface adsorbed oxygen species (e.g. hydroxides; O_γ), respectively [153–156]. After fitting the spectra, the relative amount of oxygen vacancy is quantified by $[O_\beta]/([O_\alpha]+[O_\beta]+[O_\gamma])$, which is named as O_β^*. As shown in **Fig. 5.5d**, two different trends in the evolution of O_β^* are clearly visible. OMCs (i.e., LSM-

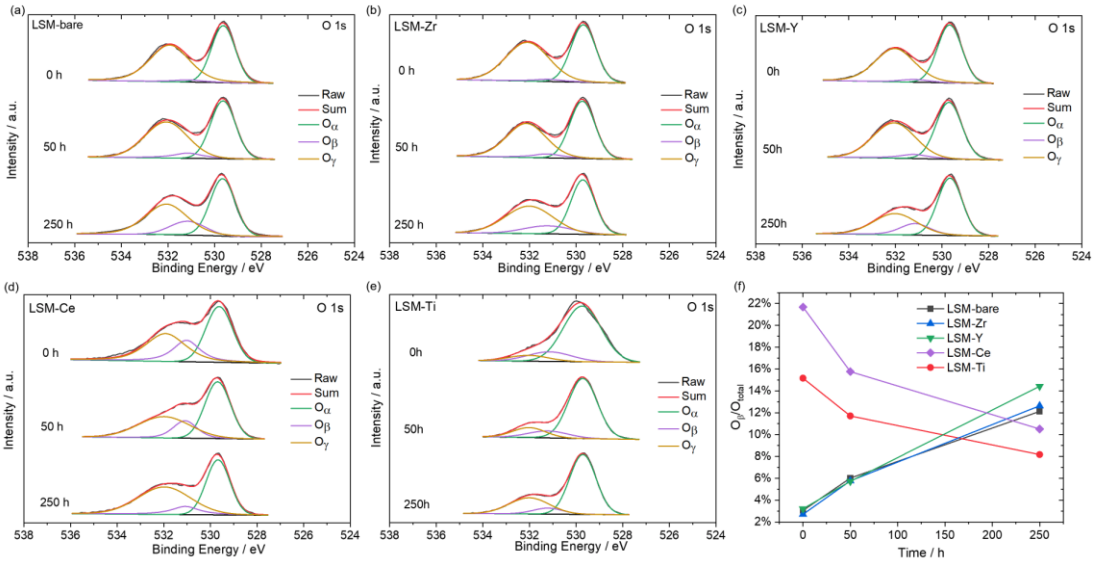

Fig. 5.8 O 1s spectra of (a) LSM-bare, (b) LSM-Zr, (c) LSM-Y, (d) LSM-Ce, and (e) LSM-Ti after exposing them to air at 750°C for 0, 50, and 250 h, and (f) relative concentrations of oxygen vacancies. The XPS spectra are obtained at the collection angle of 60°.

Ce and LSM-Ti) start with a relatively high O_{β}^{*} but exhibit a decreasing trend while OSCs (i.e., LSM-Zr and LSM-Y) show a clear increasing trend with a low starting value. The same trend is visible from the O 1s peak observed at the collection angle of 60° (**Fig. 5.8**), which is supposed to reveal a more surface-specific information.

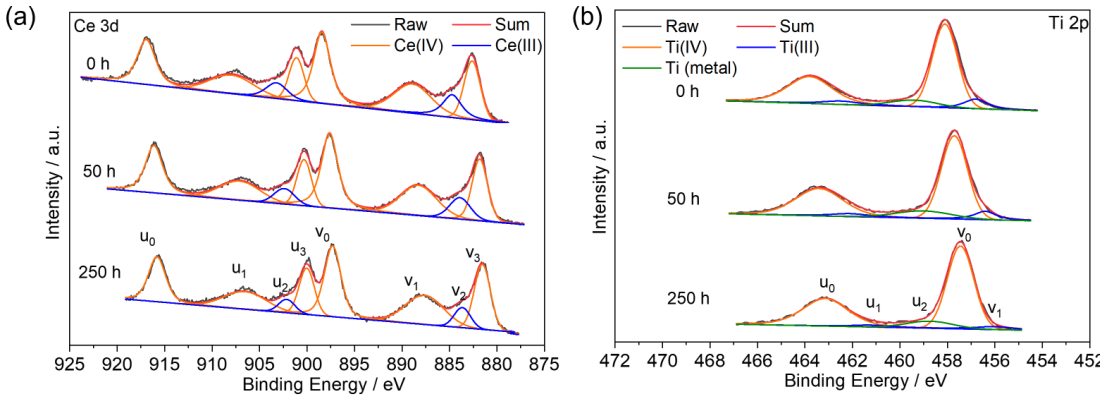

Fig. 5.9 XPS spectra of (a) Ce 3d and (b) Ti 2p after a thermal exposure at 750°C for 0, 50, and 250 h. The XPS spectra are obtained at the collection angle of 60°.

Table 5.1 Relative amount of trivalent Ce and Ti species determined by XPS Ce 3d and Ti 2p, respectively. The raw XPS spectra are provided in Fig. 5.9.

Sample	Time	$p(Ce^{3+})$	Sample	Time	$p(Ti^{3+})$
	0 h	13.3%		0 h	12.7%
LSM-Ce	50 h	11.2%	LSM-Ti	50 h	10.9%
	250 h	8.4%		250 h	7.4%

The high initial O_{β}^{*} values of OMCs are ascribed to the oxygen defects formed by the overcoat rather than the underlying LSM. This is supported by the considerable amount of trivalent Ce and Ti as detected by the Ce 3d and Ti 2p spectra (**Fig. 5.9**; **Table 5.1**). On the other hand, the inflexible valence states of Zr and Y in OSCs would incur little formation of oxygen vacancies within the overcoat. Therefore, the finite amount of initial O_{β}^{*} values of OSCs shown in Fig. 5(b), albeit small, are likely to be detected from LSM lattice in the vicinity of surface, not from the overcoat layer. This is further supported by the Mn valence state around the surface of LSM (**Fig. 5.10b**). Mn valence states can be estimated by Mn 3s spectra (Fig. S6) where the peak splitting in Mn 3s has a linear relationship with the Mn valences state [157]. The Mn valence state can be quantified from:

$$Diff_{peaks} = a \times \widetilde{Mn} + b \tag{5.2}$$

Where $Diff_{peaks}$ is the peak splitting (eV) in Mn 3s spectra, and $\widetilde{Mn}$ indicates the Mn valence state; a = -0.859, b = 7.869.

The Mn valence states of OSCs are initially in the range of 3.3 – 3.5 while those of OMCs are significantly higher than these values (LSM-Ce = 3.6; LSM-Ti =4.1). In the context of charge neutrality requirement, a lower Mn valence state indicates the existence of more of oxygen vacancies in the lattice. It is noted that the Mn valence state of OMCs at collection angle of 0° (which probes a deeper depth from the surface; **Fig. 5.10a**) are lower than those measured at 60°. This indicates that oxygen vacancies in LSM are less populated in the vicinity of its surface compared to the bulk (i.e., within the lattice). Therefore, it can be deduced that a proper ALD coating, even with an angstrom-level thickness, has distinctly affected the migration of oxygen species around the overcoat-LSM interface; the overcoat of OMCs attracts oxygen vacancies from the bulk of LSM to the interface while those of OSCs do not.

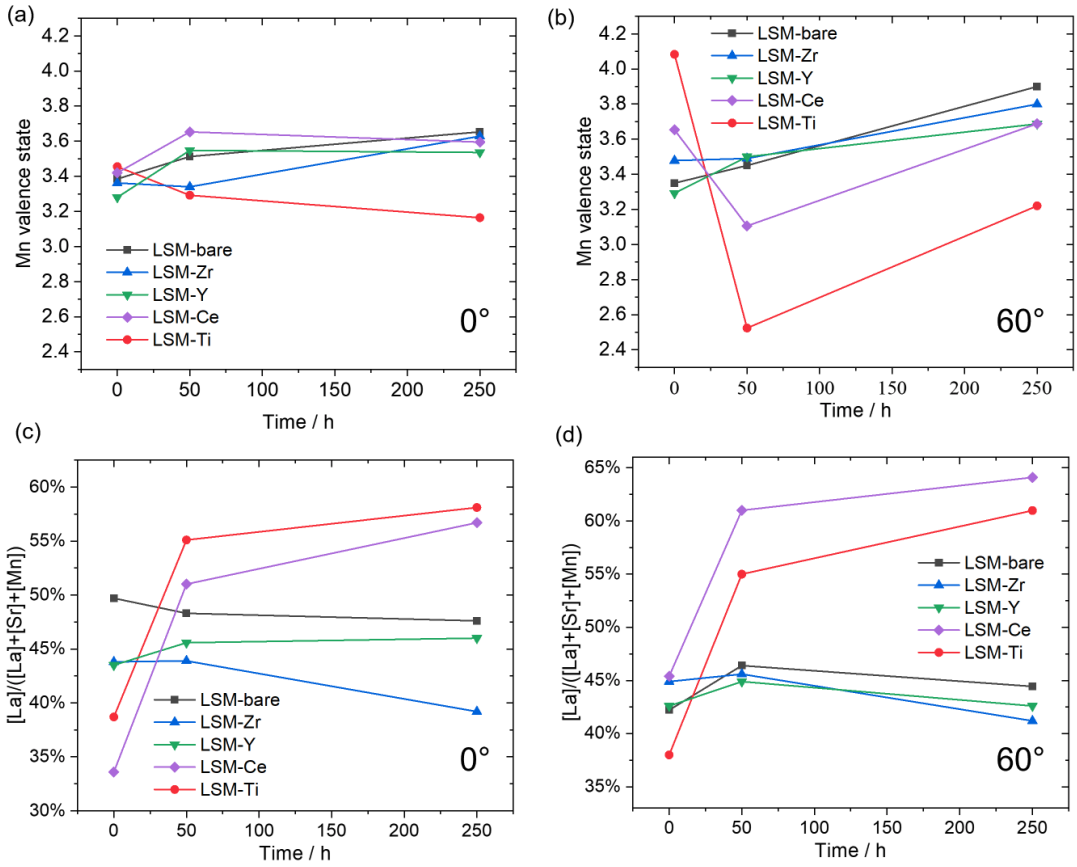

Fig. 5.10 (a,b) Mn valence states based upon XPS Mn 3s using the collection angle of (a) 0° and (b) 60°. (c,d) Relative concentration of La with respect to the total concentration of all A-site and B-site species, quantified at (c) 0° and (d) 60°. All Mn 3s spectra are provided in Fig. 5.11.

To summarize the XPS observations, OMCs show a significant desegregation of Sr species and a drastic decrease of oxygen vacancy concentration from the surface during their exposure to 750 °C. On the other hand, OSCs exhibit a minor change in

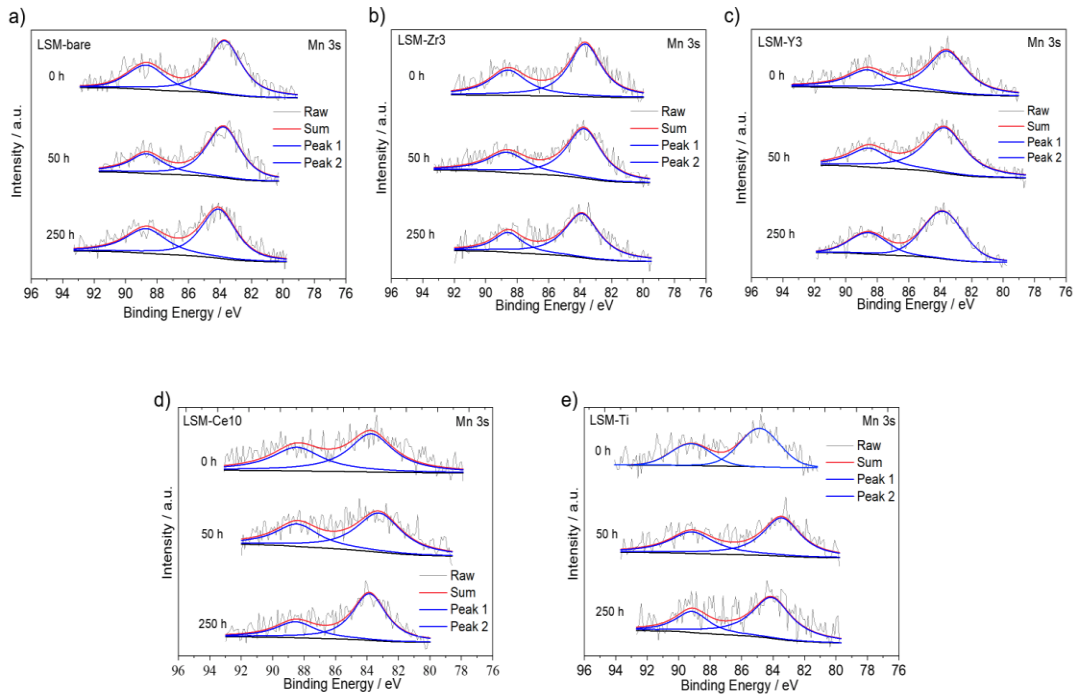

Fig. 5.11 XPS Mn 3s spectra of (a) LSM-bare, (b) LSM-Zr, (c) LSM-Y, (d) LSM-Ce, and (e) LSM-Ti.

surface Sr content and a considerable increase of oxygen vacancy concentration during the same period. **Fig. 5.12** presents a schematic diagram depicting the conjectured movements of ionic species around the surface based upon these observations.

First, in OMCs, the initially formed oxygen vacancies within the overcoat diffuses into the bulk of LSM. Simultaneously, Sr species from the SrO layer are incorporated into the LSM lattice while La species are segregated to the surface as shown in **Fig. 5.10c-d**, probably forming an oxide (La_2O_3). Within the LSM close to the surface, Mn species are reduced significantly for the first 50 h and subsequently oxidized for the remaining hours at a mild rate (**Fig. 5.10b**). The change in the Mn valance state evolution can be partially explained by the decelerated oxygen vacancy incorporation (**Fig. 5.6d**) after 50 h due to the limited amount of available oxygen vacancies. In the overcoat layer, the loss of oxygen vacancies is charge-balanced by the oxidation of overcoat cations, which is supported by XPS observations (summarized in **Table 5.1**). In the LSM surface layer, the incorporation of Sr species is charge-balanced by the introduction of oxygen vacancies from the overcoat.

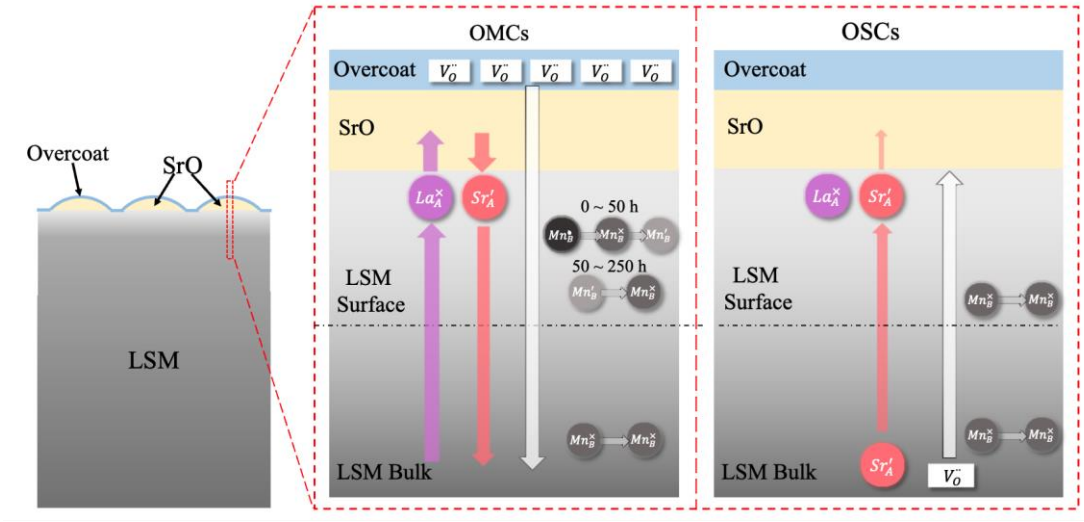

Fig. 5.12 A simplified schematic drawing to present the conjectured movements of ionic species during thermal exposure at 750 °C.

On the other hand, in OSCs, the overall movement of ionic species are relatively weak compared to those observed in OMCs. There is little oxygen vacancy present in the overcoat from the start whereas they are more populated in the LSM lattice compared to OMCs. It is conjectured that both oxygen vacancies and Sr species segregate to the surface side, which will satisfy the local charge neutrality requirement in each layer. According to **Fig. 5.3d**, there is not an appreciable change in the surface Sr content, indicating the segregated Sr does not form additional Sr oxide (e.g., SrO) on the surface of OSCs.

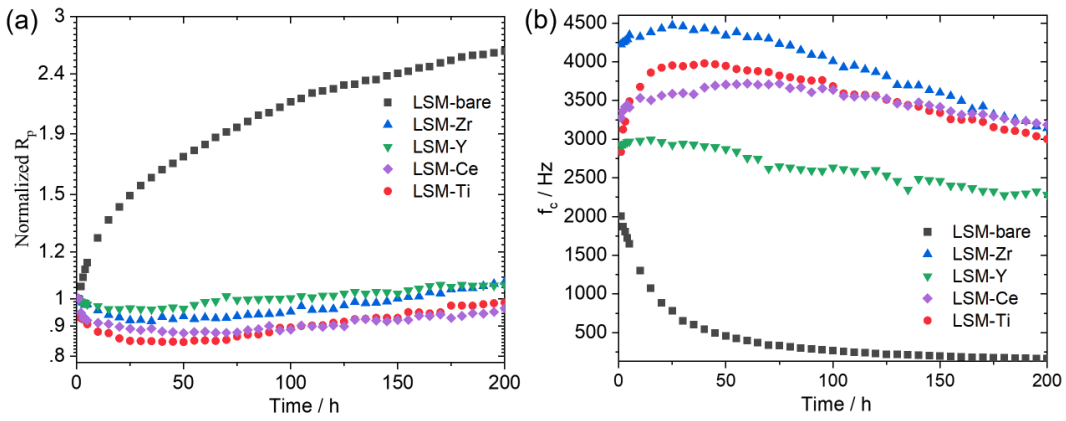

Fig. 5.13 Time evolution of normalized R_p (a) and characteristic frequency, (f_c). The normalized R_p is obtained by dividing R_p by the initial value for each sample. All the data are deduced from the EIS data shown in Fig. S6.

5.3.3 Electrochemical properties

Fig. 5.13 shows the time evolution of normalized polarization resistances (R_p) at 750 °C. LSM-bare shows a dramatic degradation in electrode performance by changing R_p from 1.87 to 4.90 Ω cm^2 and the characteristic frequency (f_c) from ~2,000 Hz to 164 Hz after 200 h. The f_c change indicates that the rate-determining step (RDS) of the electrode reaction shifted from a fast process (e.g., charge transfer reaction) to a slow process (e.g., molecular adsorption or diffusion) [115]. Compared to the LSM-bare that degraded by a factor of 2.62, all the samples with an ALD overcoat exhibit a much more stable performance. This is mainly ascribed to the excellent efficacy of ALD overcoat in suppressing agglomeration of LSM backbone [151].

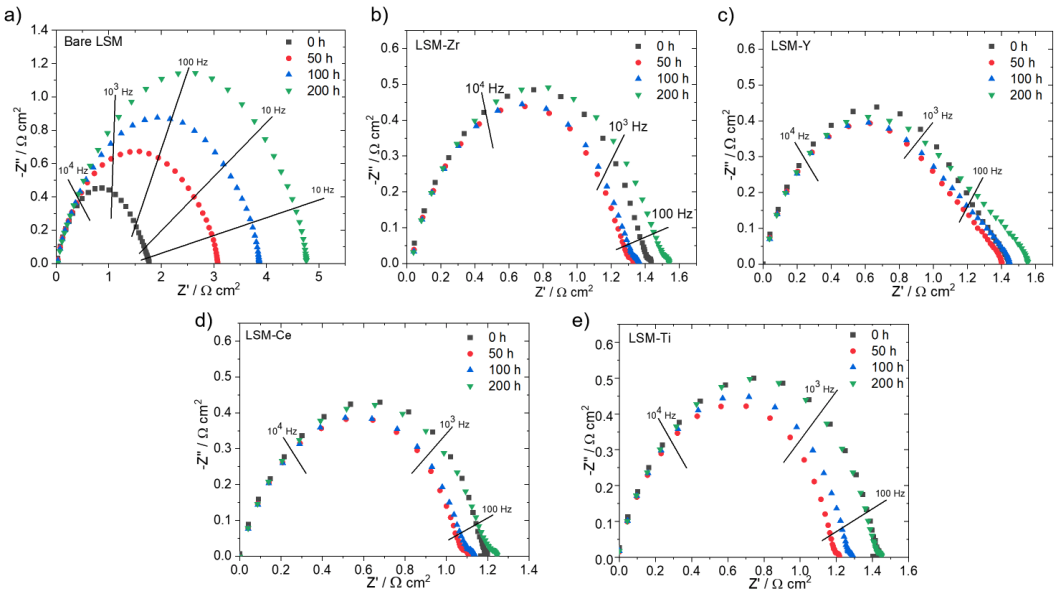

Fig. 5.14 EIS curves of each sample obtained at 750 °C. Ohmic resistance is deducted from the original data for a facile comparison.

The size distribution estimation is based on a 1100 × 760 nm^2 field emission SEM image shown in **Fig. 5.16** and **Fig. 5.17**. The total amount of LSM in this area is > ~150, indicating it can provide a meaningful size distribution. We first enlarge the SEM image as shown the **Fig. 5.15** below, then a black outline is drawn for each individual particle. Since it is difficult to quantify the area of the particles as they are, we estimate the size by redrawing a red circle which best matches the area of the black outline. For a particle whose shape deviates significantly from a circle, the size was taken from the average between its longest length and the length in the direction perpendicular to the longest side. Due to the size of LSM particle is relatively large, we group them in the size with step of 4 nm, resulting an error tolerance of ±2 nm (e.g. 52±2 nm, 56±2 nm, 60±2 nm, …).

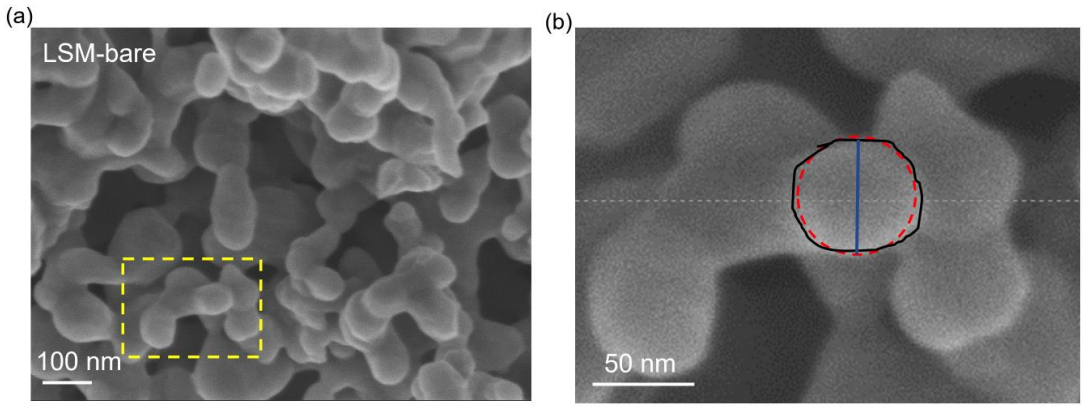

Fig. 5.15 (a) An SEM image of LSM-bare and (b) a close-up image in the yellow area in (a). The size of LSM particle was defined by the diameter of red circle (length of blue line), an artificial circle that best represents the actual LSM particle to the eyes.

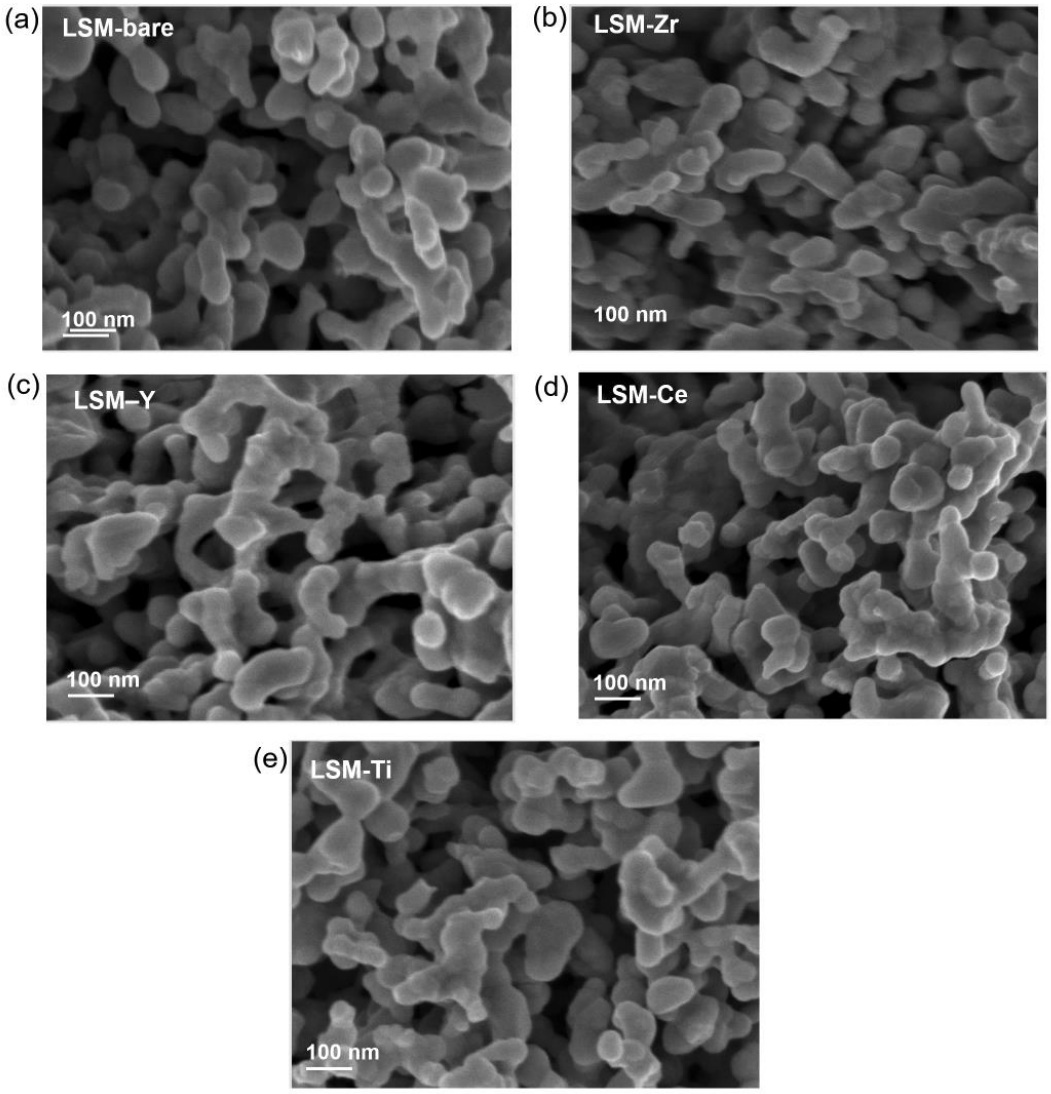

Fig. 5.16 (a-e) FE-SEM micrographs of bare LSM and ALD-treated LSM samples before operating at 750 °C.

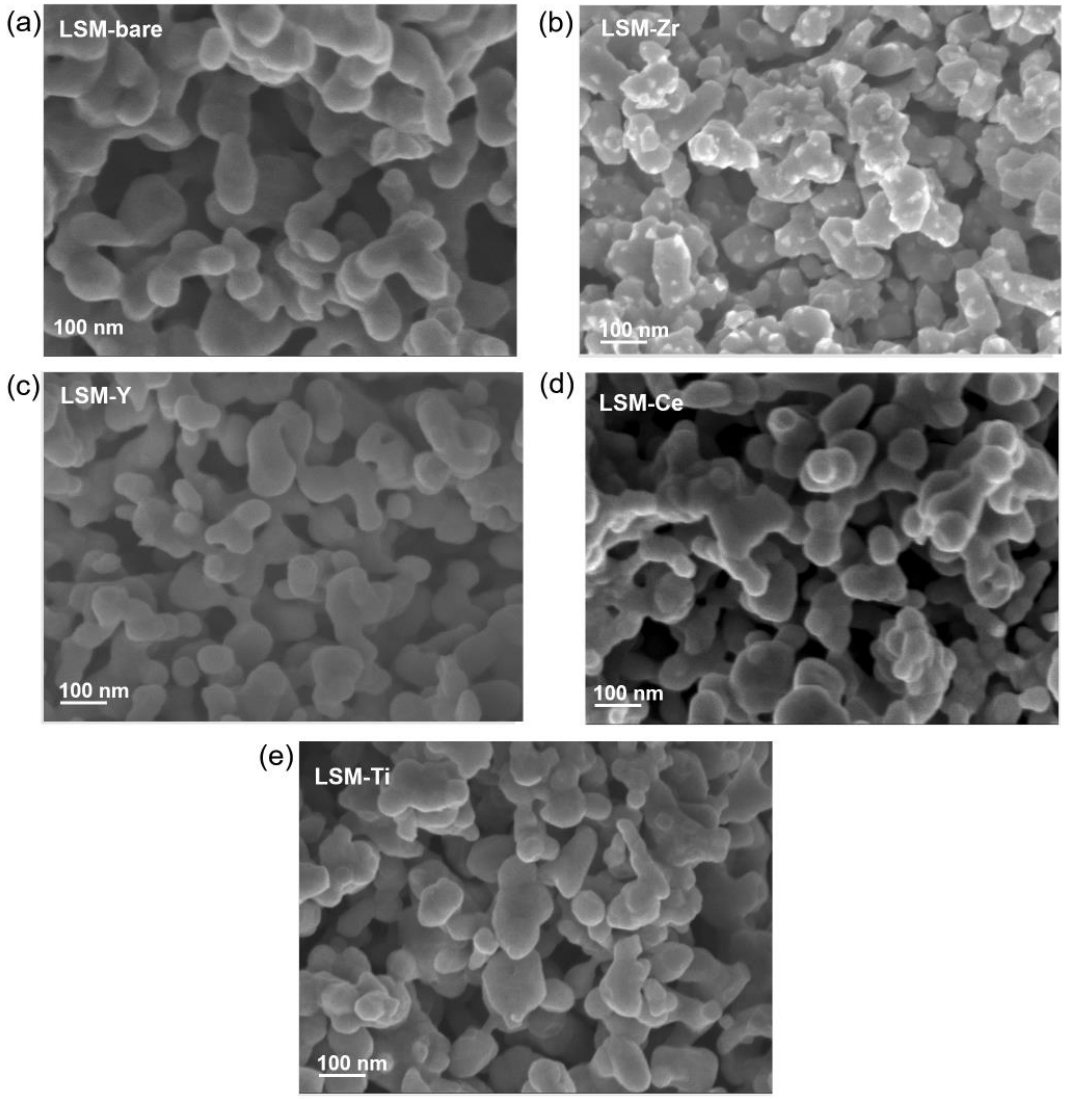

Fig. 5.17 (a-e) FE-SEM micrographs of bare LSM and ALD-treated LSM samples after exposing them to air at 750 °C for 200 h.

As shown in **Fig. 5.18**, the median LSM particle size of LSM-bare changed from 52.8 nm to 71.1 nm for 200 h at 750 °C. On the other hand, all the ALD-coated samples maintained the size to be smaller than ~ 60 nm (LSM-Zr = 57.9 nm; LSM-Y = 60.4 nm; LSM-Ti = 50.6 nm; LSM-Ce = 51.0 nm) during the same thermal exposure. The close correlation between the particle size and electrode performance can be ascribed to the reasoning that a smaller particle size would render a larger amount of oxygen adsorption sites and triple phase boundary regions.

It is noteworthy that the LSM particle size of OMCs become even smaller after 200 h of thermal exposure (from 52.8 nm to 51.0 nm for LSM-Ce, and to 50.6 nm for LSM-Ti), which is unexpected in the context of thermally driven sintering process. We

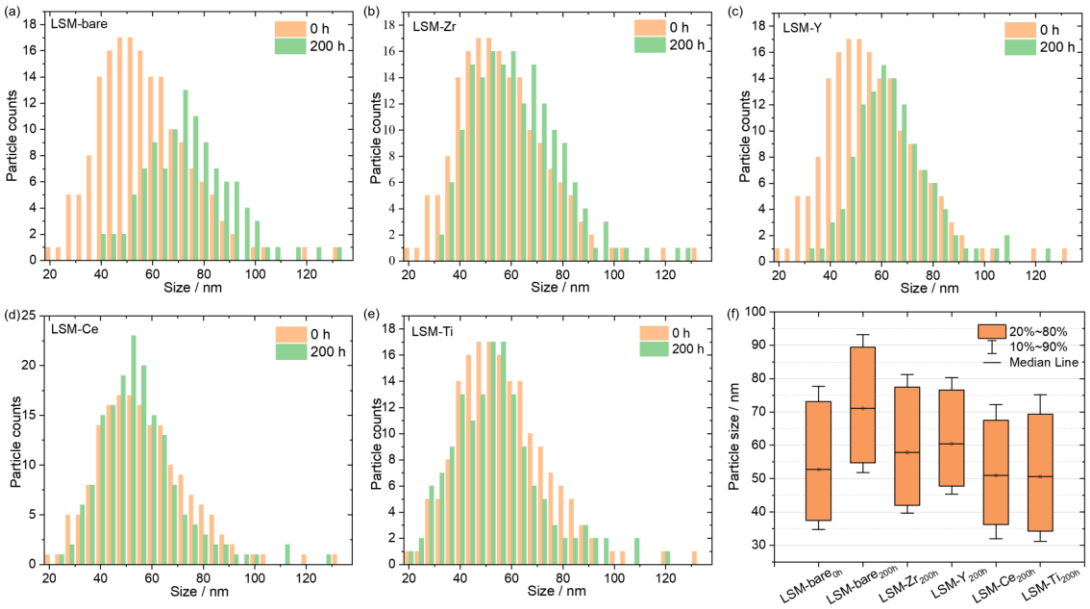

Fig. 5.18 (a-e) Size distribution of LSM particles in initial stage (0 h) and final stage (200 h) at 750 °C, and (f) the corresponding box chart of LSM particle sizes. Graphs are based upon the FE-SEM images shown in Fig. 5.16 and Fig. 5.17.

ascribe the phenomena to the incorporation of surface Sr species (such as $Sr(OH)_2$ and SrO) back into the LSM lattice. Since an incorporation of a mole of SrO would accompany a formation of a half mole of La_2O_3 as shown below (Kröger-Vink notation), it is reasonable to assume the initial presence of A-site vacancies provided the sites for incorporating some Sr species from the surface.

$$2SrO + 2La_{A(LSM)}^{\times} + O_{O(LSM)}^{\times} \rightarrow La_2O_3 + 2Sr'_{A(LSM)} + V_{O(LSM)}^{\bullet\bullet} \qquad (5.3)$$

As revealed by Sr 3d spectra in **Fig. 5.3**, the as-prepared LSM-bare has appreciable amount of surface Sr species, and the OMCs show an explicit desegregation behaviour, well aligned with the trend of LSM particle size evolution (i.e., the particles of OMCs became smaller while those for OSCs grew). However, the correlation between the evolutions of R_p and particle size is less explicit among ALD-coated samples than that between LSM-bare and ALD-coated samples. As shown in **Fig. 5.19**, all the samples show an initial drop in R_p for the first ~50 h followed by a gradual and consistent increase, and the amount of the initial R_p drop is somewhat larger in OMCs.

5.4 Conclusion

In this paper, we demonstrate that an atomic-scale overcoat with a nominal thickness of 2 – 3 Å is an effective approach of tuning Sr segregation behavior in LSM. Considering the extreme thickness of the overcoat, this method is a highly promising route in controlling the migration of ionic species and the formation/annihilation of surface oxides, which are highly correlated to the surface kinetics of an electrode. An

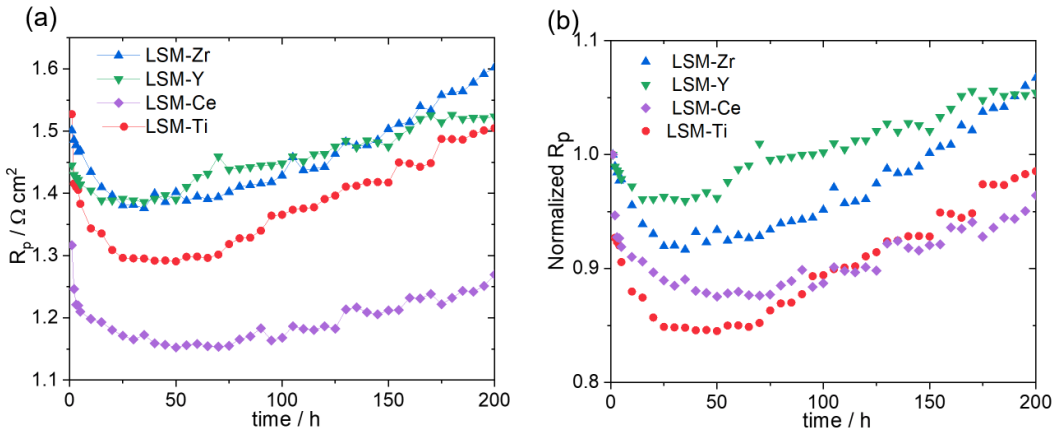

Fig. 5.19 (a) Polarization resistances (R_p) and (b) its normalized values with time at 750 °C. The normalized R_p is obtained by dividing R_p by the initial value for each sample.

overcoat of binary oxide with a multi-valent cation (CeO_2 and TiO_2) tends to drive Sr species into the lattice of LSM while an overcoat with a single valent cation (ZrO_2 and Y_2O_3) exhibits little effect on Sr segregation. This is tentatively ascribed to the initial differences in the amount of surface oxygen vacancies and resulting chemical potential gradient around the surface.

Chapter 6: Ultra-thin Metallic Ruthenium on Solid Oxide Electrolysis Cells.

6.1 Introduction

In this Chapter, I present the effect of an ultra-thin metallic ruthenium (Ru) catalyst on $(La_{0.6}Sr_{0.4})_{0.95}Co_{0.2}Fe_{0.8}O_{3-\sigma}$ (LSCF) air electrode by using PE-ALD, focusing on both ORR and OER activity as well as cell durability in the electrolysis mode of IT-SOCs. LSCF is a conventional air electrode material with a mild catalytic activity toward OER but is prone to Sr segregation[20]. However, the effect of an ultra-thin layer of catalyst by ALD for SOEC application is still rarely reported. Ru is a widely used noble metal for low-temperature solid oxide fuel cells (LT-SOFCs), mainly in fuel electrodes [21–23]. According to the volcano theory for OER, RuO_2 is the best candidate among various metal oxide catalysts (e.g. TiO_2, PtO_2, NiO, etc.)[24,25]. But the effect of RuO_2 overcoat as a surface catalyst for Intermediate-temperature solid oxide cells (IT-SOCs) has never been reported. Since the air electrode of SOCs is constantly exposed to an oxidized environment, metallic ruthenium will eventually oxidize, becoming RuO_2 on the electrode surface. The electrochemical, physical, and surface-specific characterization reveal that even an angstrom-thick Ru overcoat significantly improves both ORR and OER reactions. Interestingly, Ru tends to react with surface-segregated Sr species, forming a secondary perovskite phase, which suppresses further Sr segregation and improves cell sustainability. Furthermore, a detailed electrochemical analysis is performed throughout the durability testing process, which additionally reveals that the additional secondary phase is highly effective in maintaining oxygen desorption kinetics in the electrolysis mode.

6.2 Experimental

6.2.1 Cell Preparations

The cells used in the experiment are anode-supported full cells, with each cell diced from a commercialized anode-supported half-cell (Kceracell, 11 cm×11 cm) to a dimension of 2 cm × 2 cm. The anode-supported cell consists of a 600 μm NiO-YSZ composite support, a 30 μm NiO-YSZ functional layer, and a 5 μm dense YSZ electrolyte. For the air electrode, $(La_{0.6}Sr_{0.4})_{0.95}Co_{0.2}Fe_{0.8}O_{3-\sigma}$ (LSCF) is used, and a GDC interlayer (20% Gd) is placed between the YSZ and LSCF to prevent the degradation caused by the formation of an insulating phase, $LaSrO_3$[158,159], and improve contact between the electrode with electrolyte[160]. To fabricate the GDC interlayer, a GDC slurry is first prepared by mixing Hypermer KD-1 (Croda, dispersant) for 24 h at 50 °C. GDC nano-powders (FuelCellMaterials; 20 wt% GDC; surface area: 35.3 $m^2 g^{-1}$) and ethyl cellulose (Sigma Aldrich, binder) are then added to the mixture and stirred for another 24 h at 50 °C. The final slurry is composed of 40 wt% terpineol, 10 wt%

Hypermer KD-1, 2 wt% ethyl cellulose, and 48 wt% GDC nano-powder. LSCF slurry is prepared using the same method as the GDC slurry but with different compositions. It consists of 35 wt% of terpineol, 5 wt% of Hypermer KD-1, 3 wt% of ethyl cellulose, and 57 wt% of LSCF powers (FuelCellMaterials). After preparing the slurry, the GDC slurry is screen printed on the YSZ side with a specific area and then sintered at 1150 °C for 5 h at a rate of 3°C/min, with additional stops at 80 °C for 1 h and 500 °C for 30 mins to evaporate the solvent and binders, respectively. LSCF slurry is then screen printed on the GDC and sintered at 850 °C for 3 h, with the same stops with sintering GDC slurry.

On the top of the LSCF electrode, atomic-scale metallic Ru is overcoated by plasma-enhanced atomic layer deposition (PE-ALD), where performed in a customized PE-ALD system. (Carbonyl cyclohexadiene)Ru is used as the precursor, while hydrogen plasma is (150W, RF-sputtered source) used as the reactant. The canister temperature for Ru is 45 °C, with a chamber temperature of 250 °C. The deposition of Ru and H_2 plasma is in 'emerge mode' where all the valve is closed before the release of the precursor and preserve a hold-on of 10 s in between the release of the precursor and purge. The release time for Ru precursor is 1 s, while H_2 plasma is created by applying a 150W RF-sputtered source for 20 s. Argon gas is used as the purging gas, and a purge time of 30 s is applied to the PE-ALD. The growth rate for the metallic Ru is ~ 1.5 Å/cycle, and the details of the deposition characterization can be found in the previous work.

The platinum mesh (GoodFellow) was used as the current collector for the air electrode, while porous nickel foam served as the current collector for the fuel electrode. A 3 kg load was applied through the cell to ensure solid contact between the electrodes and the current collecting mesh/foam.

A separate set of samples was prepared for X-ray diffraction (XRD) analysis to examine the oxidation state of the Ru overcoat. Since this study is mainly focused on the air electrode, without being obscured by the present of NiO-YSZ and GDC. To make LSCF pallet-supported sample for this purpose, LSCF powders were first ball-milled and pressed under a uniaxial press with a pressure of 30 Mpa. The pressed pallet is then sintered at 850 ºC for 10 h. 200 cycles of Ru precursor (~30 nm) are deposited on the surface of LSCF pallet to have a decent Ru loading. Transmission electron microscopy (TEM) samples were prepared by grinding LSCF with Ru overcoat into powders, dissolving into ethanol, and drop-casting the particle suspension upon a 3mm lacey-carbon grid (TED Pella).

6.2.2 Physical Characterization

A field-emission scanning electron microscopy (FE-SEM, Zeiss Gemini 500) was used at 3 kV to observe the microstructure. X-ray photoelectron spectroscopy (XPS) was performed on a Nexus system (Thermo Fisher Scientific) using monochromated, micro-focused, low power Al Kα X-ray source for excitation and a 180º, double-focusing, hemispherical analyzer with 128-channel detector (10-400 μm spot size with

adjustable sample holder incident to X-ray beam from 0º to 60º). The phase and composition of samples were evaluated by XRD using a PANalytical X'Pert Pro system with Co Kα radiation (λ = 1.78897 Å). Scanning transmission electron microscopy (STEM, Talos) is used to characterize the structure and size of atomic-scale Ru/RuO overcoat, which was operated on a Talos F200C G2 TEM system. The energy dispersive X-ray spectroscopy (EDS) (Oxford X-max SDD 127 eV at 50 kcps) was performed on the TEM system.

6.2.3 Electrochemical Characterization

Electrochemical characterization was performed by electrochemical impedance spectroscopy (EIS; Bio-Logic SP-200) with different overpotentials (-0.5, -0.3,-0.1, and 0 V with respect to OCV for fuel cell mode; +0.2, 0.4, and 0 V with respect to OCV for electrolysis mode) with 20 mV of AC perturbation. Cell performance was measured by linear sweep voltammetry (LSV; Bio-Logic SP-200), with a scan rate of 20 mV/s, ranging from OCV to 0.3V for the fuel cell and 0.9 V to 1.6V for the electrolysis cell.

The cell is firstly heated to 700 °C at a rate of 2.5 °C/min, while dry hydrogen is supplied at the fuel electrode with a flow rate of 100 cm^3 min^{-1} (sccm). The cell is continuously reduced until the OCV of the cell is stabilized at ~1.1V. After NiO on the fuel side was completely reduced to Ni metal, fuel cell performance was initially investigated at different operating temperatures with 100 sccm O_2 on the air electrode and 100 sccm H_2 on the fuel electrode. The bottleneck process of the air electrode is estimated by evaluating the polarization resistances at different oxygen partial pressures and achieved by combining the O_2 with N_2 with a total flow rate of 100 sccm, while fixing the H_2 flow at the air electrode.

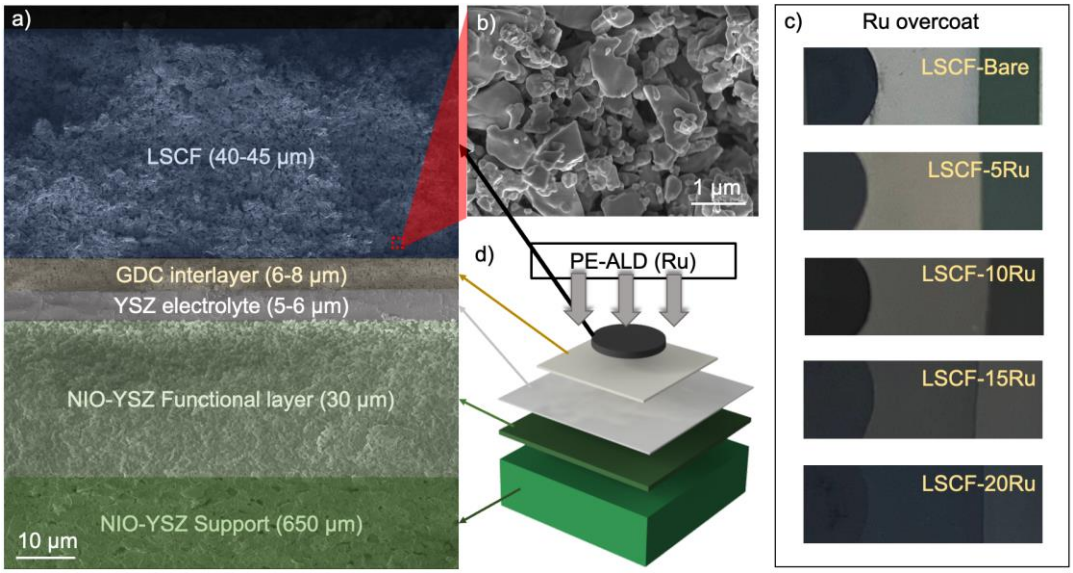

Fig. 6.1 (a) cross-sectional SEM image of the LSCF-Bare full cell (b) Zoom-in image of the LSCF electrode. (c) Top-view of the As-deposited cells d) A schematic diagram of the cell configuration

After the electrochemical testing in fuel cell mode, the cells were then tested in the electrolysis mode at 700°C. On the fuel electrode, H_2 flow rate is decreased to 50 sccm through a water bath. Relative humidity was controlled to ~50% by adjusting the temperature of the water bath to 82 °C. The entire fuel channel was covered by a heating tape (160 °C at the inlet and 170°C at the outlet) to prevent the condensation of steam. On the air electrode, O_2/ N_2 with a ratio of 21:79 was supplied to simulate the constant flow of ambient air with a total flow rate of 100 sccm.

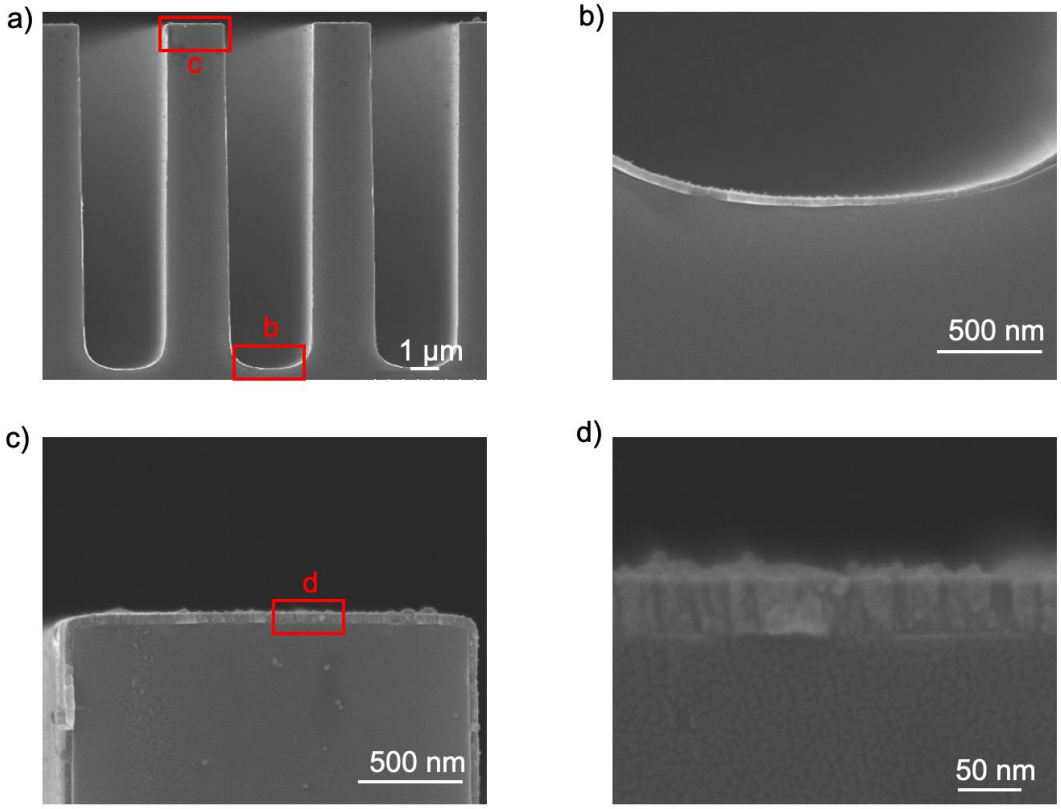

Fig. 6.2 (a-d) SEM image of trench structure Si wafer with 300 cycles of (Chorus)ruthenium deposited by PE-ALD

Durability tests for electrolysis cells were performed in galvanostatic mode at a constant current density of 500 mA cm^{-2}. OCV, LSV, and EIS with different overpotentials were measured every 5 h.

6.3 Result and Discussion

6.3.1 Cell set-up

An ultra-thin coating of metallic Ru species is deposited onto the surface of the LSCF backbone using PE-ALD, as demonstrated in **Fig. 6.1d**. The impact of the Ru overcoat is analyzed using 5 thickness levels: 0, 5, 10, 15, and 20 cycles, represented by LSCF-Bare, LSCF-5Ru, LSCF-10Ru, LSCF-15Ru, and LSCF-20Ru, respectively, with a nominal growth rate of 1.5 Å $cycle^{-1}$ on a silicon wafer substrate. The characterization of the Ru PE-ALD is depicted in **Fig. 6.2**, which reveals that the Ru

overcoat is predominantly of metallic phases and is distributed evenly over the surface. Multiple studies have demonstrated that the reduction of ALD precursors decreases with depth[161]. Considering the majority of ORR and OER occur at the electrode region in the vicinity of the electrode/electrolyte interface, a rather thin (40 µm) LSCF electrode with a high porosity is utilized as the electrode backbone to ensure that the ALD precursor penetrates throughout the entire backbone. **Fig. 6.1c** shows the top view of an as-prepared cells, and with increased cycles of Ru PE-ALD overcoat, specifically 15 and 20 cycles of metallic Ru (corresponding to a nominal thickness of 2.25 and 3 nm, respectively), the surface exhibits a distinct metallic gleam. To determine if the effect of Ru ALD on the electrode performance, EIS was performed with different overpotentials (**Fig. 6.3**). The data shows that for an overcoat of > 3 nm of metallic Ru (LSCF-20Ru), the effective surface area is no longer confined to the LSCF electrode, and the OCVs deviate from their theoretical values. As a result, LSCF-20Ru was excluded from the discussion of this study.

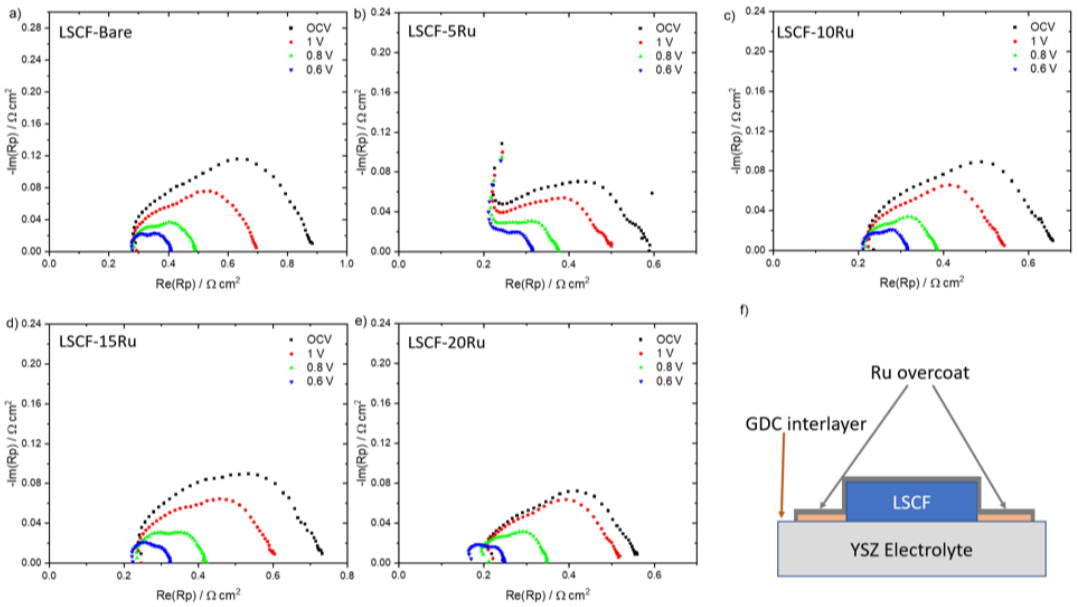

Fig. 6.3 EIS measurement for (a)LSCF-Bare, (b)LSCF-5Ru, (c)LSCF-10Ru, (d) LSCF-15Ru, and (e)LSCF-20Ru with different overpotential. (f) schematic diagram of the cell from side view

6.3.2 Physical properties

SEM images (**Fig. 6.4**) were employed to examine the surface characteristics of cells before and after a durability test in the electrolysis mode at 700 °C. Results

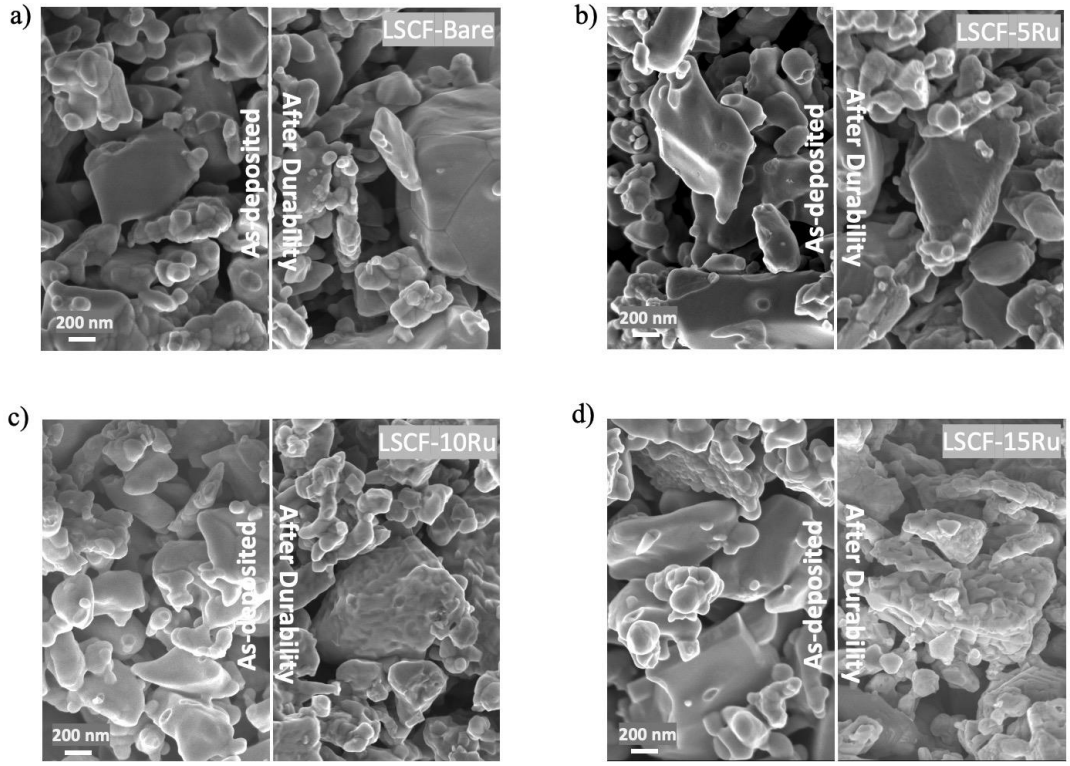

Fig. 6.4 SEM image of (a)LSCF-Bare, (b)LSCF-5Ru, (c)LSCF-10Ru, and (d) LSCF-15Ru for as-deposited cells (left) and cells with durability under electrolysis mode (right).

indicate that the Ru PE-ALD overcoat exhibits a consistent and uniform appearance across the LSCF electrode in all as-deposited cells, without any noticeable features. However, after undergoing a long-term electrolysis test (100 h at 700 °C with 500 mA

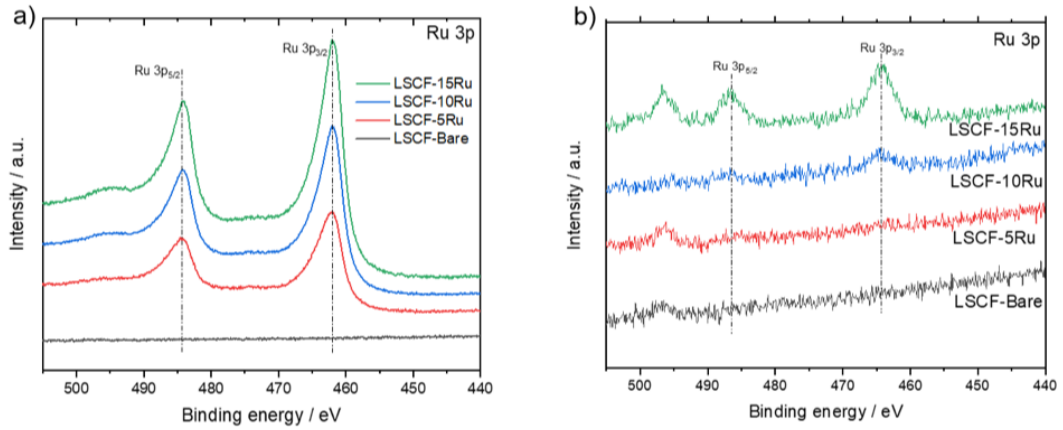

Fig. 6.5 XPS analysis on Ru 3p spectra for (a) as-deposited cells and (b) cells subjected to a durability test in electrolysis mode.

cm^{-2}), the cell's surface exhibits a greater degree of crystallization, along with a thicker Ru overcoat. Particularly for cells with 15 cycles of Ru overcoat (with a nominal thickness of 2.25 nm), the additional layer exhibits crystal features that range in length from 100-200 nm, whereas such crystallization is not observed in cells without a Ru overcoat.

XPS analysis was conducted to reveal the surface chemistry of the air electrode before and after a 90 h-long durability test under electrolysis mode. The presence of Ru species in as-deposited cells and those after durability tests is determined using Ru 3p spectra (**Fig. 6.5**) as Ru 3d spectra are obscured by C 1s spectra. A significant decrease in the amount of Ru species is observed. This is attributed to a strong oxidation of Ru and subsequent evaporation of the oxidized Ru during operation because the evaporation point of RuO_4 (130 °C[162]) is significantly higher than 700 °C. By reacting with diffused oxygen ions, Ru is oxidized into RuO_2, RuO_3, RuO_4, or a mixture of these, which is significantly more susceptible to evaporation. In parallel, Sr 3d spectra are deconvoluted into two peaks using sets of doublets with an energy difference of ~1.8 eV and an intensity ratio of 1.5 (**Fig. 6.6**). The lower binding energy Sr_α (131.8 - 132.1 eV) is assigned to lattice Sr peaks within the perovskite structure, while the higher binding energy Sr_β (133.3 - 133.6 eV), corresponding to SrO, $Sr(OH)_2$ and $SrCO_3$[163], is assigned to surface Sr peaks[164,165]. The relative amount of surface Sr quantified by

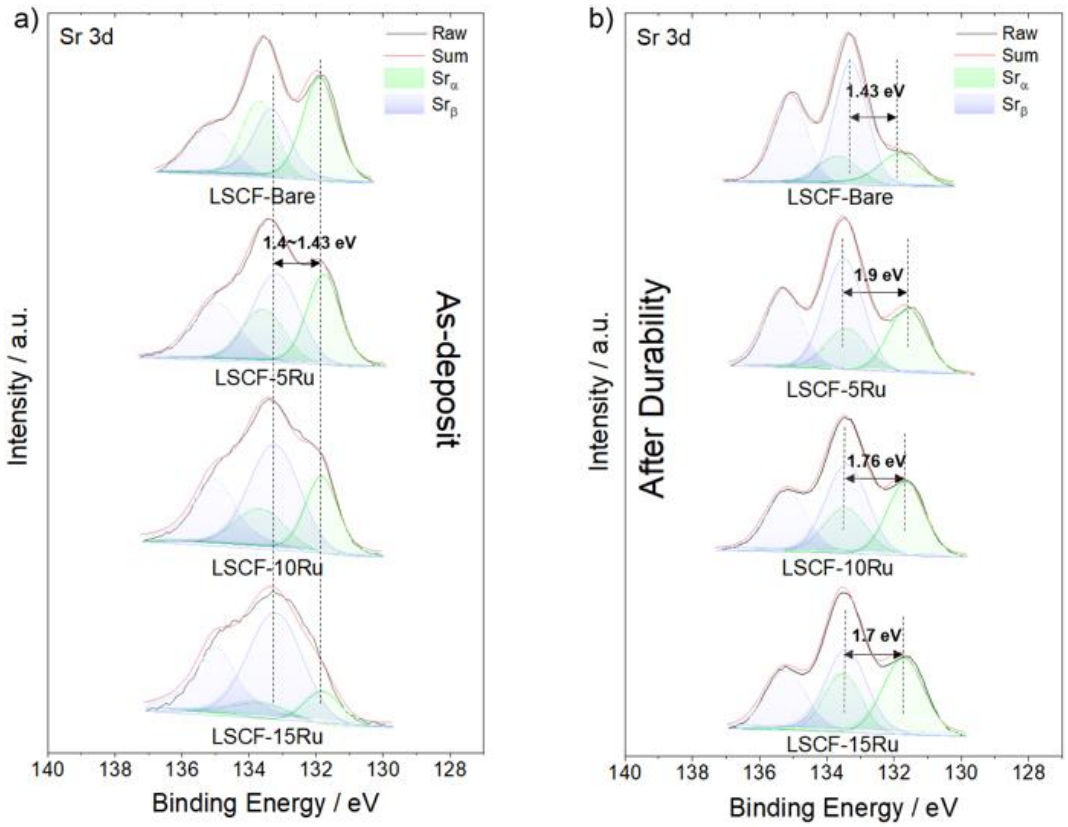

Fig. 6.6 The XPS spectra of Sr 3d for (a) as-deposited cells and (b) cells subjected to a durability test in electrolysis mode.

$[Sr_\beta]/([Sr_\alpha]+[Sr_\beta])$ is named as Sr_β^* (**Fig. 6.7a**). As shown in **Fig. 6.6** and **Fig. 6.7a**,

the Sr_β peak dominates with increasing thickness of Ru overcoat while the total amount of La, Sr, Co and Fe contents decrease significantly with an increasing amount of Ru overcoat; The La 3d, Sr 3d, Co 2p, and Fe 2p spectra were obtained for the as-prepared cells without normalization as **Fig. 6.8**, where the intensity of each element decrease significantly with a thicker Ru overcoat. However, after the durability test in the

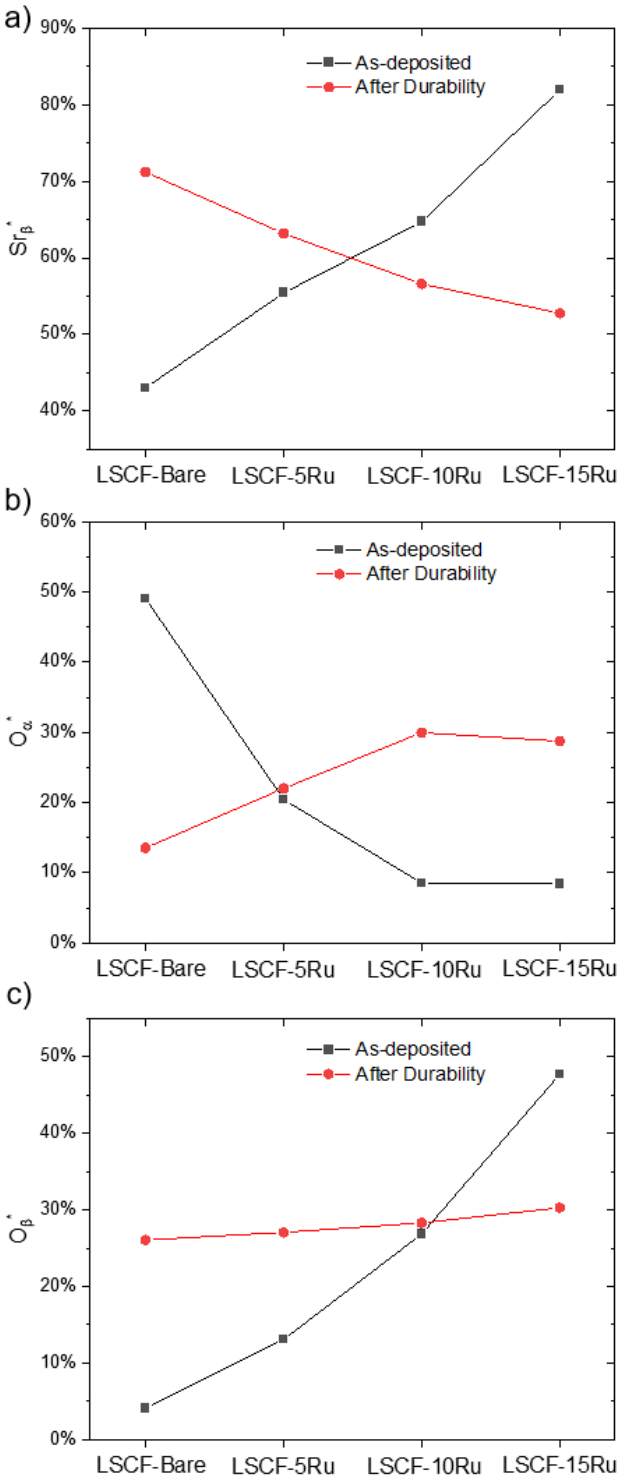

Fig. 6.7 The concentration of (a)Surface Sr, (b) Lattice oxygen, and (c) oxygen vacancies.

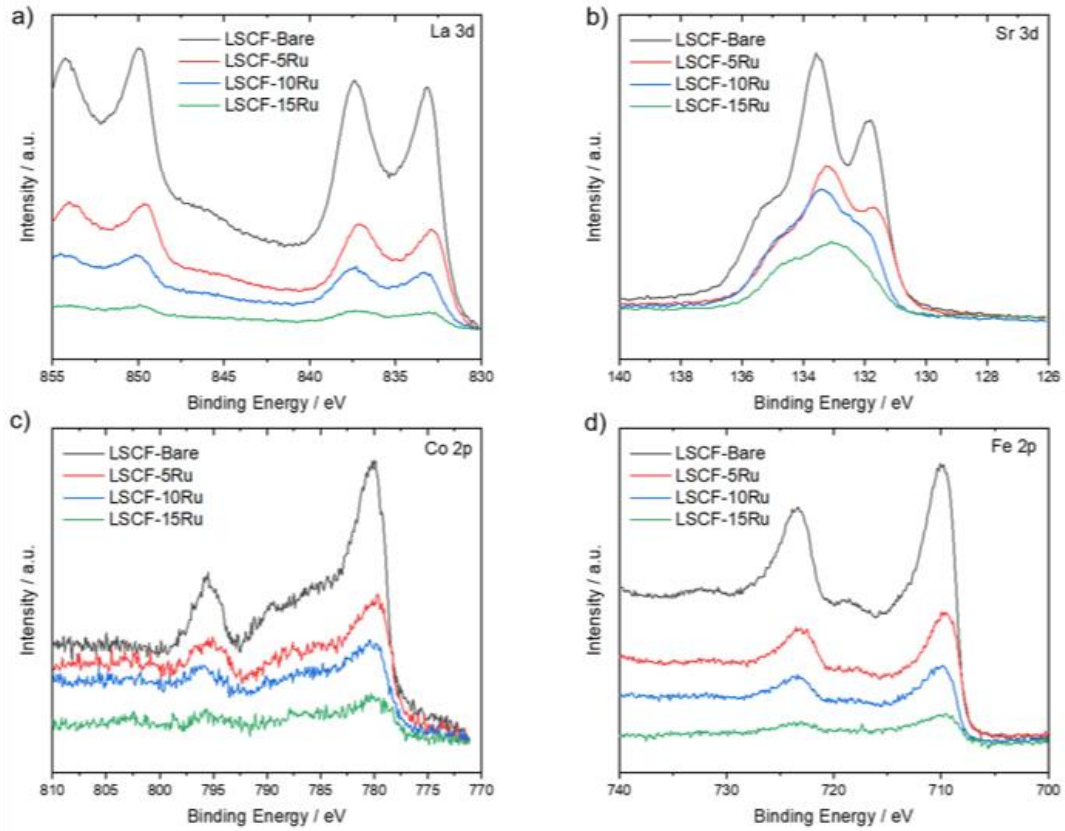

Fig. 6.8 The XPS spectra of (a) La 3d, (b) Sr 3d, (c) Co 2p, and (d) Fe 2p were obtained for the as-deposited cells. To match the intensity at the lowest binding energy, an additional offset value was applied to LSCF-5Ru, LSCF-10Ru, and LSCF-15Ru.

electrolysis mode, the surface Sr concentration shows a reversed relationship with the thickness of Ru overcoat. Furthermore, the Sr_{α} peak shifts to lower binding energies (131.6~131.8 eV), resulting in a larger difference of 1.6~1.9 eV between Sr_{α} and Sr_{β} peaks compared to the normal situation of 1.43 eV, particularly for the sample with 5 cycles of Ru overcoat. The significant shift in lower binding energy (Sr_{α}) in Sr spectra indicates a strong bonding of Sr with other elements, as observed by previous researchers. To gain further insight into the surface bonding condition, the O 1s spectra are also examined and fitted, as shown in **Fig. 6.9**. The peaks at approximately 528.3 eV, 530 eV, 530.9 eV, and 532.4 eV are ascribed to lattice oxygen (namely O_{α}), oxygen defect (namely O_{β}), surface adsorbed oxygen species (namely O_{γ}), and surface hydroxyls (namely O_{δ})[166], respectively. The relative amount of lattice oxygen, and that of oxygen vacancy is quantified by $[O_{\alpha}]/[O_{sum}]$ and $[O_{\beta}]/[O_{sum}]$ which named as O_{α}^{*} and O_{β}^{*} respectively (**Fig. 6.7b,c**), where $[O_{sum}] = [O_{\alpha}] + [O_{\beta}] + [O_{\gamma}] + [O_{\delta}]$. As shown in **Fig. 6.9a**, for the as-deposited cells, the lattice oxygen (O_{α}^{*}) decreased with increasing thickness of the Ru overcoat, indicating a significant decline in the perovskite phase, while the defect oxygen (O_{β}^{*}) increased dramatically, implying a high ratio of oxygen non-stoichiometry within the detection area of XPS. **Fig. 6.9b** shows that the Ru-overcoated cells exhibit a more pronounced presence of lattice oxygen (O_{α}^{*})

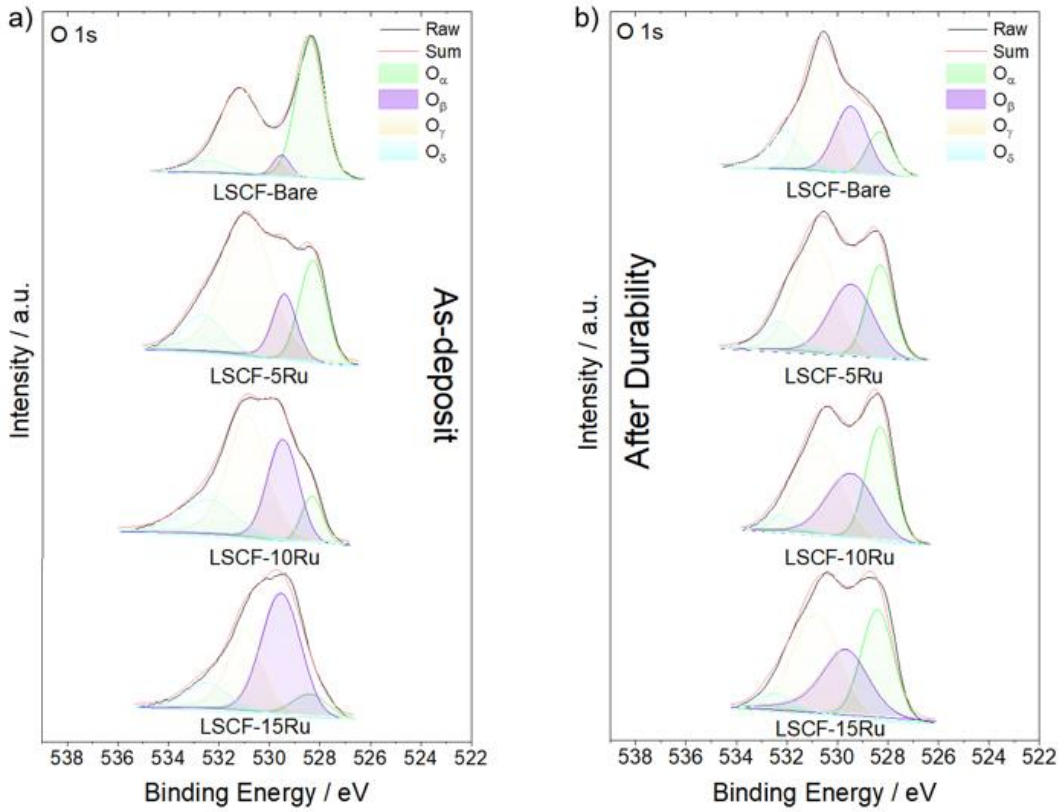

Fig. 6.9 The XPS spectra of O 1s for (a) as-deposited cells and (b) cells subjected to a durability test in electrolysis mode.

compared to the bare sample. This suggests the formation of an additional perovskite phase beyond the segregated SrO species that was observed on the surface of the LSCF-Bare cell.

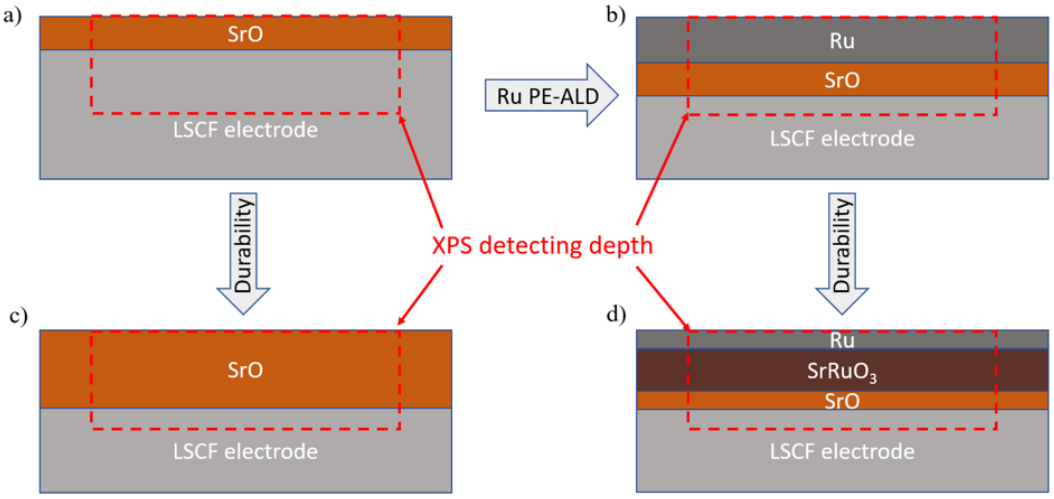

Fig. 6.10 Schematic diagrams of Cross-sectional views for as-deposited (a) LSCF-Bare cell, and (b) cells with Ru overcoat, as well as cross-sectional views for (c) LSCF-Bare cell, and (b) cells with Ru overcoat after durability test at electrolysis mode.

Schematic diagrams (**Fig. 6.10**) are depicted to describe the evolution of surface chemistries for cells with/without Ru overcoat based on all the physical characterizations mentioned above. As depicted in **Fig. 6.10c**, the sample without Ru overcoat shows significant Sr segregation[167,168] after the durability test, which is related to the increase in Sr_{β}^{*} and decrease in O_{α}^{*}. On the other hand, as shown in **Fig. 6.10b**, cells with Ru overcoat shows the higher Sr_{β}^{*} due to the additional metallic Ru overcoat, leading to a decrease in lattice Sr phase within the XPS detecting area. However, after durability (**Fig. 6.10d**), surface SrO is combined with the surface Ru, forming an extra $SrRuO_3$ phase.

6.3.3 Electrochemical properties

Fig. 6.11 depicts the electrochemical data obtained from both bare and Ru-overcoated samples in fuel cell mode, and all the cells are tested at an operating temperature of 700 °C. The open circuit voltage (OCV) closely matches the theoretical value for SOFC at this temperature, which is approximately 1.1 V. This suggests a high level of cell tightness and minimal current crossover through the electrolyte. Notably, the additional Ru overcoat significantly improves the initial cell performance, as indicated in **Fig. 6.11b**. Compared to the cell with bare LSCF as the electrode, cells

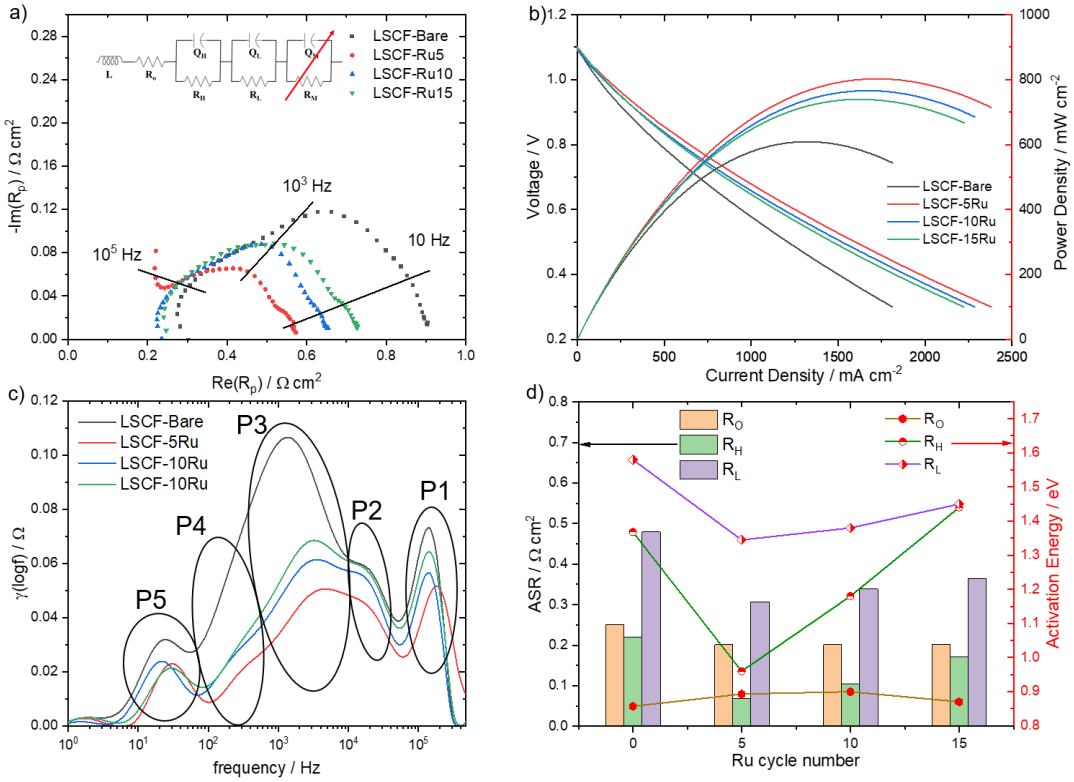

Fig. 6.11 (a) Nyquist plot of all the samples (in fuel cell mode) and the equivalent circuit used for fitting. (b) I-V curve of all the samples (c) DRT plot of all the samples (d) The fitted ohmic resistances (R_O) and polarization resistance (R_H, R_L) and their activation energies (E_a). All the samples are tested at 700 ºC with pure hydrogen and oxygen. Arrhenius relationship is used to determine the E_a as shown in Fig. 6.12.

with 5, 10, and 15 cycles of Ru overcoat by PE-ALD show enhancements in power density, with maximum values of 803 mW cm^{-2}, 766 mW cm^{-2}, and 739 mW cm^{-2}, respectively, compared to 609 mW cm^{-2} for bare LSCF. For the cell with 5 cycle Ru overcoat, with a nominal thickness of 7.5 Å, leads to a 31.9 % increase in performance, highlighting the effectiveness of an angstrom-level metallic Ru overcoat. However, thicker Ru overcoats lead to gradual performance reduction.

To gain further insight into the electrochemical properties, EIS analysis is conducted on all the cells. **Fig. 6.11a** presents the Nyquist plots for all the studied samples, while **Fig. 6.11c** shows the (distribution of relaxation time) DRT obtained based on both the real and imaginary impedances of the Nyquist plots. Based on the DRT calculations, I distinguished five notable peaks (P1-P5), each corresponding to a separate electrochemical process according to their characteristic frequencies (f_c)[169]. Since the fuel electrode for all the cells is nearly identical, the impact of surface treatment on the air electrode will mostly affect the electrochemical process corresponding to the air electrode, with minor influence on the others. The electrochemical process at very high f_c (P1) at around 10^5 Hz can be assigned to the transportation of oxygen ions within the air/fuel electrode framework and across the electrode and electrolyte interface. Within the range of 10^4-10^5 Hz (P2), the electrochemical process shows minor affection and can be attributed to hydrogen oxidation reaction (HOR). The resistance under such f_c significantly drops within the

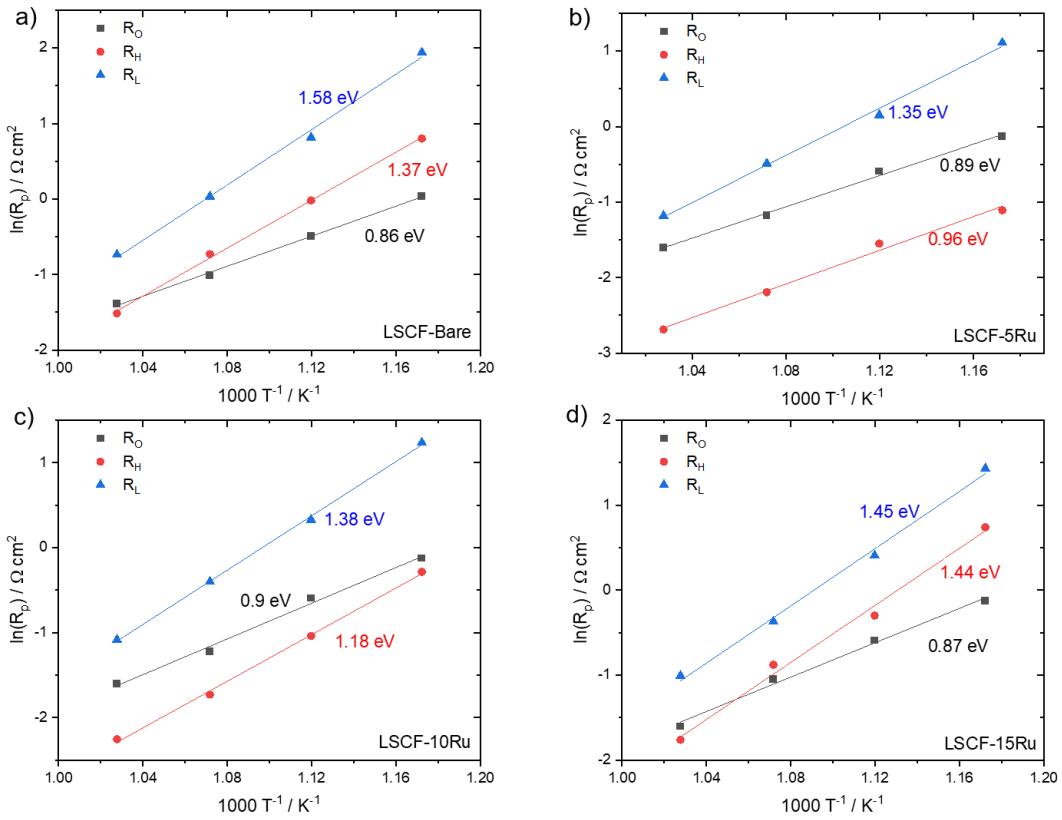

Fig. 6.12 Arrhenius plots of R_O, R_H, and R_L with their corresponding calculated activation energies for (a)LSCF-Bare, (b)LSCF-5Ru, (c)LSCF-10Ru, and (d)LSCF-15Ru

range of 10^3-10^4 Hz (P3) and that of 10^2-10^3 Hz (P4), where the electrochemical process is thus ascribed to the oxygen reduction reaction (ORR) and absorption of oxygen within the air electrode, respectively. As the peak at the lowest f_c (P5), 10-10^2 Hz, exhibits no temperature dependency, it thus can be assigned to the mass transportation in both the air/fuel electrodes.

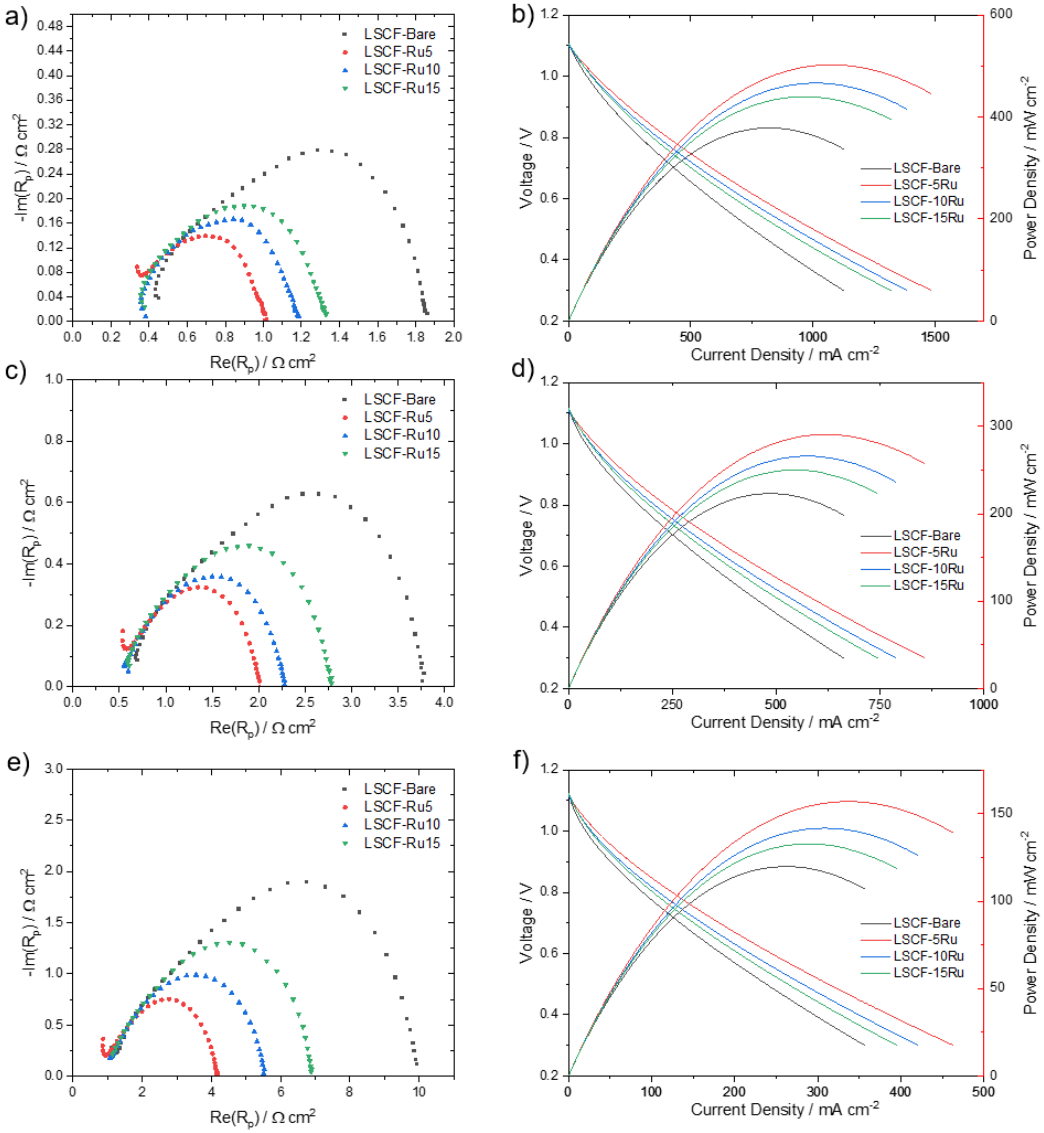

Fig. 6.13 Nyquist plots for all types of samples in (a)660 ºC, (c)620 ºC, and (e)580 ºC. I-V curves (left axis) and their corresponding power density (right axis) for all types of samples in (b)660 ºC, (d)620 ºC, and (f)580 ºC.

Based on the Nyquist plot shown in **Fig. 6.11a**, the impedance data can be fitted into three RC-coupled semicircles, which can be simulated by the equivalent circuit as *L-R_0-(R_H//Q_H)-(R_L//Q_L)-(R_M//Q_M)*. In this circuit, L, R, and Q are inductance, resistance, and constant phase element (CPE), respectively. R_O represents ohmic resistance sourced from the ionic movement within electrolyte material (YSZ, GDC, and electrode framework) and connectivity between the electrolyte and electrodes. The term (R_H//Q_H)

denotes the RC couples within the high f_c range of 10^3-10^4 Hz, corresponding to the electrochemical process P3 in DRT analysis, where the R_H is the polarization resistance of the ORR reaction. Similarly, (R_L//Q_L) symbolizes the RC couple within the low f_c range of 10^2-10^3 Hz, corresponding to the electrochemical process P4 in DRT analysis, where the R_L is the polarization resistance corresponding to oxygen absorption within the air electrode. The term (R_M//Q_M) reflects the RC couple within an extremely low f_c range of 10-10^2 Hz, which has no temperature dependency and is related to P5 in DRT analysis, where R_M is the polarization resistance of mass transportation. Since R_M is very small and has no temperature dependency, it is fitted but excluded from further electrochemical analysis. All the resistance and equivalent capacitance values are presented after normalization by the cell area for a facile comparison. R_O, R_H and R_L, along with their corresponding activation energy (E_a) is presented on **Fig. 6.11d**; The Arrhenius plots for all the studied samples are shown in **Fig. 6.13**; The fitted parameters are listed in **Table 6.1**.

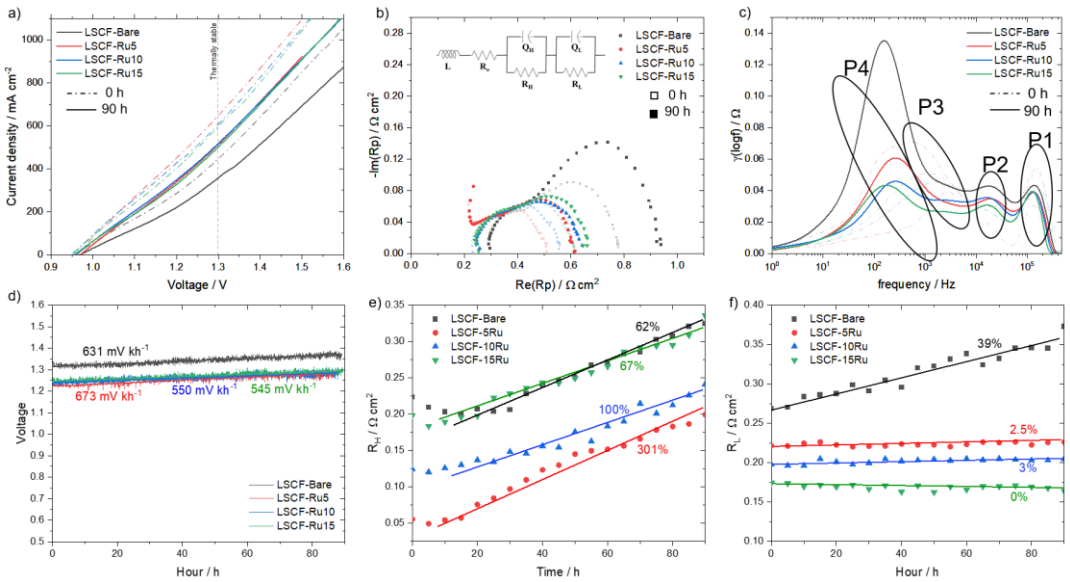

Fig. 6.14 (a) I-V curve of all the samples. (b) Nyquist plot of all the samples (in electrolysis cell mode) and the equivalent circuit used for fitting. (c) DRT plot of all the samples. (d) Durability test at 500 mA cm^{-2}. Evolution of fitted (e)R_H and (f)R_L over time. All the sample is tested at 700 ºC with 50% RH of hydrogen in the fuel electrode and 21% Oxygen/ 79% Nitrogen in the air electrode.

Further analysis reveals that all the Ru overcoated cells exhibit nearly the same R_O (0.2 Ω cm^2 at 700 °C) and a 20 % reduction compared with the bare sample (0.25 Ω cm^2 at 700 °C). Since the E_a for R_O for all the samples are in a very close range (0.87~0.9 eV), which is very close to the thermotical activation energy of YSZ (0.89 eV), the decrease in R_O can be attributed to enhanced connectivity between the electrolyte and electrode. On the other hand, the bare samples (without Ru overcoat) exhibit high R_H and R_L (0.22 and 0.48 Ω cm^2 at 700 °C, respectively), and their corresponding E_a (1.37 eV for R_H, and 1.58 eV for R_L). This is mainly due to the relatively low surface oxygen vacancies on the surface of bare LSCF. However, by

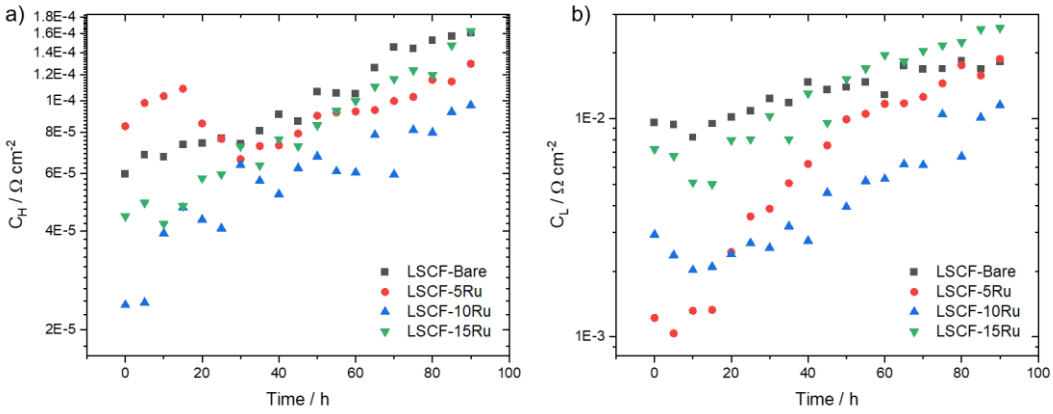

Fig. 6.15 Evolution of fitted (e)C_H and (f)C_L over time.

applying a 7.5 Å Ru overcoat using PE-ALD, the R_H and its E_a were significantly reduced (to R_H = 0.07 Ω cm^2 at 700 °C and E_a = 0.96 eV), accompanied by a minor reduction in R_L and its corresponding E_a (to R_L = 0.31 Ω cm^2 at 700 °C and E_a = 1.345 eV), as shown in **Fig. 6.12d**. This can be attributed to the well-known characteristics of RuO_2, where it shows pronounced catalytic activity for both ORR and even more for OER[19]. But it should be noted that a thicker Ru overcoat can lead to higher polarization resistance and its corresponding E_a, especially for the ORR reaction. This is because the excessive ALD overcoat will entirely block the LSCF catalytic surface and prohibit oxygen ion transfer from the surface Ru site into the LSCF lattice, thereby decreasing the area of the triple phase boundary [170]

The electrochemical data in electrolysis mode is also obtained at 700 °C, both before and after the short-term durability test (**Fig. 6.14a-c**), in which all the samples were tested under galvanostatic mode with a constant current density of 500 mA cm^{-2} for 90 h; As-deposited cells were indicated by light hollow points and 'line-dot' curves, while cells after the durability test were represented by heavy points and curves. The OCV for all the samples in **Fig. 6.14a** ranged between 0.95-0.97 V, consistent with other studies on SOECs with 50% relative humidity hydrogen flow, indicating gas tightness and little current crossover throughout the entire durability testing process. The current density at 1.3V was selected as the performance indicator because it is considered as the thermal stable operating voltage for water electrolysis applications. The bare sample with only LSCF as an air electrode showed decent performance (440 mA cm^{-2} at 1.3V at 700°C). Surprisingly, with only 5 cycles of Ru overcoat, the cell exhibits a 46.6% increase in initial performance (656 mA cm^{-2} at 1.3V at 700°C). Like the pattern of performance in FC mode, a thicker Ru overcoat results in a decrease in initial performance. However, a bulkier Ru overcoat on the electrode was found to improve the sustainability of the LSCF electrode. As shown in **Fig. 6.14d**, all the cells

Table 6.1 Summary of fitted R_O, R_H, and R_L, and their corresponding pseudo-capacitance C_H and C_L.

Temperature [°C]	Sample	R_{ohm} [Ω cm^2]	$R_{polarization\_1}$ [Ω cm^2]	C_1 [μF cm^{-2}]	$R_{polarization\_2}$ [Ω cm^2]	C_2 [mF cm^{-2}]
700	LSCF-Bare	0.25	0.22	27.52	0.48	1.56
	LSCF-5Ru	0.20	0.07	45.27	0.31	0.67
	LSCF-10Ru	0.20	0.11	40.74	0.34	1.07
	LSCF-15Ru	0.20	0.17	24.00	0.37	0.82
660	LSCF-Bare	0.36	0.48	21.94	1.03	1.09
	LSCF-5Ru	0.31	0.11	25.15	0.61	0.23
	LSCF-10Ru	0.30	0.18	23.43	0.67	0.35
	LSCF-15Ru	0.30	0.42	18.34	0.69	0.46
620	LSCF-Bare	0.61	0.98	19.43	2.26	0.67
	LSCF-5Ru	0.55	0.21	43.26	1.16	0.22
	LSCF-10Ru	0.55	0.35	28.55	1.39	0.30
	LSCF-15Ru	0.55	0.74	21.88	1.50	0.41
580	LSCF-Bare	1.04	2.23	15.05	6.97	0.39
	LSCF-5Ru	0.88	0.33	17.08	3.03	0.13
	LSCF-10Ru	0.88	0.75	33.18	3.44	0.24
	LSCF-15Ru	0.88	2.09	42.02	4.19	0.31

preserve a nearly linear degradation pattern, in which LSCF without Ru overcoat exhibits a durability rate of 631 mV kh^{-1}. Conversely, cells with thicker Ru overcoats of 5,10,15 cycles exhibited decreasing durability rates of 673, 550, and 545 mV kh^{-1}, respectively. The slight degradation in durability behavior observed for 5 cycles of Ru overcoat can be attributed to the loss of active Ru site on the electrode surface (refer to **Fig. 6.5b**). However, with thicker Ru overcoat (10 and 15 cycles Ru), cells show improved durability behavior. As mentioned in the former content, the Ru species on the surface tend to react with the Sr species in the vicinity of the LSCF electrode, forming a secondary perovskite phase, $SrRuO_3$, which in turn reduces the rates of cation segregation as well as particle agglomeration.

To gain further insight into the specific electrochemical behavior before and after the durability test, I present Nyquist and corresponding DRT plots in **Fig. 6.14b** and **Fig.6.14c**, respectively. The DRT plot reveals four peaks that can be attributed to four different electrochemical processes based on their f_c, as circled in **Fig. 6.14c**. Similar to the FC analysis, the electrochemical process at very high f_c (P1) at around 10^5 Hz can be assigned to the transportation of oxygen ions within the air/fuel electrode framework as well as that across the electrode/electrolyte interface. Within the range of 10^4-10^5 Hz (P2), the electrochemical process can be attributed to the hydrogen evolution reaction (HER) at the fuel electrode, which shows minor enhancement by additional surface treatment on the air electrode. Noticeably, the electrochemical processes are significantly facilitated within the f_c range of 10^3-10^4 Hz (P3) and that of 10^2-10^3 Hz (P4) by the Ru overcoat, where the electrochemical process is thus ascribed to the oxygen evolution reaction (OER) and the desorption of oxygen molecules on the electrode surface, respectively. However, unlike in FC mode, there is no prominent peak within the f_c range of 10-10^2 Hz, indicating that the ability of mass transport is not a problem in electrolysis mode.

The impedance data on the Nyquist plot can be simulated by two RC-coupled semicircles, which correspond to an equivalent circuit as *L-R_0-(R_H//Q_H)-(R_L//Q_L)*, in line with the assumption in FC mode. Here, R_O stands for ohm resistance, while R_H and R_L correspond to polarization resistance (R_p) related to high and low f_c, respectively. Based on the f_c of the two RC circuits, R_H//Q_H can be assigned to the electrochemical process of P3, whereas R_H//Q_H denotes to that of P4. From the Nyquist plot and DRT plot at 0 and 90 h for each sample, R_O remains constant over time, whereas the f_c for both R_H and R_L decreases substantially for all the cells. To gain a deeper understanding of the electrochemical processes during the entire durability test, EIS was measured and fitted using an equivalent circuit at 5-hour intervals. The R_H and R_L, along with their corresponding pseudo-capacitance (C_H and C_L), are shown in **Fig. 6.14 e,f**, and **Fig. 6.15**; the Pseudo Capacitance was calculated based on the CPE. In the absence of a Ru overcoat, both R_H and R_L exhibited high initial polarization resistance (R_H = 0.22 Ω cm^2 and R_L = 0.27 Ω cm^2) and high degradation rate (62% increase in R_H, and 39% increase in R_L). As NiO-YSZ fuel electrodes are incapable of causing such high degradation within such a short period of time, the degradation can be attributed mainly to cation segregation (Sr, in this case) on the air electrode, resulting in the formation of a SrO layer in the vicinity of the electrode that blocks the TPB and reduces both PER and the oxygen desorption. However, the initial resistance was significantly reduced for both R_H and R_L upon applying a Ru overcoat. The R_H and R_L displayed a contrasting trend with respect to the number of Ru cycles. The R_H, which respected to the R_p in high f_c, decreased in the order of 5Ru < 10Ru < 15Ru < bare (R_H = 0.05, 0.12, 0.19, and 0.22 Ω cm^2, respectively), emphasizing the effectiveness of angstrom-level Ru overcoat on OER. On the other hand, the R_L, which respected to the R_p in low f_c, decreased in the order of 15Ru < 10Ru < 5Ru < bare (R_L = 0.17, 0.20, 0.22, and 0.27 Ω cm^2, respectively), indicating that a thicker Ru overcoat would decrease OER but enhance the oxygen desorption form the electrode.

Apparently, polarization resistance related to OER (R_H) dramatically increases with thinner Ru overcoat (301%,100%, and 67% increase for 5,10, and 15 cycles of Ru, respectively). The increase in R_H is more pronounced with thinner Ru film and can be explained by the reduction in surface Ru catalytic site by either combining with Sr, forming secondary perovskite phase $SrRuO_3$, which have a lower activity on OER, or the evaporation of Ru species by super-oxidized the Ru. Surprisingly, polarization related to oxygen desorption (R_L) is significantly maintained (2.5%, 3%, and 0% increase for 5,10, and 15 cycles of Ru, respectively) by the additional Ru overcoat, even with angstrom-level of Ru overcoat. The retention of R_L can also be to the formation of the $SrRuO_3$ phase, which suppresses the Sr segregation to the electrode surface.

6.4 Conclusion

In this Chapter, an ultra-thin layer of metallic Ru (7-30 Å) is applied to a conventional air electrode (LSCF) via PE-ALD. I demonstrated that an angstrom-level Ru overcoat significantly enhances electrode performance in terms of polarization

resistance and its activation energy in fuel cell mode. The improved electrode activity resulting from ALD treatment can be primarily attributed to substantial facilitation in the charge transfer reaction during ORR, with a minor improvement in oxygen absorption kinetics. On the other hand, the electrolysis performance exhibits even greater improvement with the Ru overcoat, which can be ascribed mainly to the fact that Ru possesses superior OER kinetics compared to ORR. Furthermore, while the LSCF electrode is known to suffer from Sr segregation, leading to a considerable decrease in performance in electrolysis mode, the Ru overcoat is believed to react with surface-segregated Sr species forming a secondary perovskite phase, which enhances cell durability by suppressing further Sr segregation. Analysis also indicates that the newly formed perovskite phase maintains oxygen desorption kinetics from the air electrode.

Chapter 7: Conclusion and Future work

7.1 Conclusion

ALD has emerged as a powerful surface treatment technique for enhancing the performance and durability of SOCs. This dissertation presents a series of experimental studies and analysis based on the utilization of ALD technique for the purpose. Stemming from the research approaches detailed in Chapter 1, three types of surface treatments are performed with distinct objectives for SOFCs in Chapter 4 and 5, as well as SOECs in Chapter 6.

In Chapter 4, upon infiltrated CeO_2 nanoparticles, an additional angstrom-level of CeO_2 and Y_2O_3 overcoat is deposited, resulting in improved catalytic activity and enhanced durability. Chapter 5 investigates the impact of angstrom-level oxide layers on A-site dopant segregation with two categories of surface metal oxide coatings: oxides with single-valent cations (OSC) and those with multi-valent cations (OMC). The results revealed that OMC overcoats, such as CeO_2 and TiO_2, are highly effective in suppressing Sr segregation and even de-segregating Sr back into the backbone lattice, while OSCs affect little to the dopant segregation behavior.

Lastly, Chapter 6 presents that a metallic Ru-dispersion by plasma-enhanced ALD on a perovskite electrode sample significantly enhances catalytic activity in both fuel cell and electrolysis modes. The study also reveals that the atomically dispersed Ru forms a barrier layer to prevent further Sr segregation toward the surface of the underlying perovskite, thereby improving cell durability.

The objectives outlined in Chapter 1 were successfully achieved:

1. Investigating the effect of atomic-scale metal oxide overcoats on nanodot-decorated electrodes concerning cell performance and durability.
2. Examining and analyzing A-site dopant segregation with the aid of angstrom-level ALD of metal oxides.
3. Custom-building ALD system and an SOEC test station with flexible channel addition and operation.
4. Applying PE-ALD of metallic catalysts on SOECs to enhance cell performance and durability.

The assertion on the beneficial effect of ALD is supported by the enhancement of cell performance and durability. The use of ALD allows for the atomic control of the thickness and conformality of surface coatings, which can improve the electrochemical activity and stability of SOCs. Additionally, ALD can be used to maintain the microstructure of materials, which can lead to improved durability along with often enhanced catalytic activity. Moreover, ALD can create protective layers that prevent the degradation of the electrode materials over time. Overall, these advantages of ALD demonstrate its critical role in the advancement of SOCs.

7.2 Future Work and Perspective

SOCs are a superior candidate for energy conversion and storage compared to other types of fuel cells and electrolysis cells due to their high kinetics. However, their poor durability is the key factor preventing widespread commercialization of this technology, primarily due to the high operating temperatures required. Traditional oxygen-ion conducting systems, such as those employing YSZ electrolytes, necessitate a very high temperature to achieve decent cell performance. At these temperatures, degradation of electrodes by particle agglomeration, dopant segregation, and surface poisoning is accelerated as the processes are thermally activated. Furthermore, when operating in electrolysis mode with an oxygen-conducting electrolyte, an additional mechanism of degradation - electrode/electrolyte delamination - becomes highly problematic.

To lessen the concern regarding the operational temperature, proton conducting SOCs are emerging as a promising alternative, owing to their potential for reduced operating temperatures and enhanced performance, as well as providing a solution for the electrode/electrolyte delamination problem in SOECs. In this context, the electrochemical catalyst on the electrode becomes particularly important. Traditional bulky catalysts, such as those deposited by wet processes, are no longer efficient at the lower operating temperatures required by proton-conducting SOCs.

To address this challenge, ALD technology can play a crucial role in the development of next generation proton conducting SOCs. By enabling the deposition of ultra-thin, conformal layers of catalyst materials onto the electrode surfaces, ALD can enhance the electrocatalytic activity, stability, and durability of proton-conducting SOCs under the desired lower-temperature conditions. Furthermore, the scalability of ALD technique, along with its unique capability, can lead to the advancement of high-performance, sustainable, and commercially viable SOCs.

References

1 D. J. Deka, J. Kim, S. Gunduz, M. Ferree, A. C. Co and U. S. Ozkan, , DOI:10.1016/j.apcata.2020.117697.

2 A. S. Ali and A. S. Ali, *Nanotechnology and the Environment*, , DOI:10.5772/INTECHOPEN.91438.

3 D. Gielen, E. Taibi and R. Miranda, .

4 Global Solid Oxide Fuel Cell Market Size Report, 2030, https://www.grandviewresearch.com/industry-analysis/solid-oxide-fuel-cells-market, (accessed 30 March 2023).

5 S.Korea to foster hydrogen economy as new growth engine - Xinhua | English.news.cn, http://www.xinhuanet.com/english/2019-01/17/c_137752001.htm, (accessed 31 March 2023).

6 DOE awards Cummins $5M for automation of electrolyzer cell and stack assembly - Green Car Congress, https://www.greencarcongress.com/2021/09/20210928-cummins.html, (accessed 31 March 2023).

7 I. Chang, S. Ji, J. Park, M. H. Lee and S. W. Cha, *Adv Energy Mater*, 2015, **5**, 1402251.

8 J. W. Shin, S. Oh, S. Lee, D. Go, J. Park, H. J. Kim, B. C. Yang, G. Y. Cho and J. An, *Int J Hydrogen Energy*, 2021, **46**, 20087–20092.

9 A. Karimaghaloo, A. M. Andrade, S. Grewal, J. H. Shim and M. H. Lee, *ACS Omega*, 2017, **2**, 806–813.

10 T. Matsui, M. Komoto, H. Muroyama, K. Kishida, H. Inui and K. Eguchi, *J Power Sources*, 2016, **312**, 80–85.

11 B. Koo, K. Kim, J. K. Kim, H. Kwon, J. W. Han and W. C. Jung, *Joule*, 2018, **2**, 1476–1499.

12 J. Y. Koo, H. Kwon, M. Ahn, M. Choi, J. W. Son, J. W. Han and W. Lee, *ACS Appl Mater Interfaces*, 2018, **10**, 8057–8065.

13 N. Tsvetkov, Q. Lu, L. Sun, E. J. Crumlin and B. Yildiz, *Nat Mater*, 2016, **15**, 1010–1016.

14 S. P. Jiang and X. Chen, *Int J Hydrogen Energy*, 2014, 39, 505–531.

15 A. v. Virkar, *Int J Hydrogen Energy*, 2010, **35**, 9527–9543.

16 S. N. Rashkeev and M. v. Glazoff, *Int J Hydrogen Energy*, 2012, **37**, 1280–1291.

17 M. S. Khan, X. Xu, R. Knibbe, A. ur Rehman, Z. Li, A. J. Yago, H. Wang and Z. Zhu, *Energy Technology*, 2020, **8**, 2000241.

18 C. E. Frey, Q. Fang, D. Sebold, L. Blum and N. H. Menzler, *J Electrochem Soc*, 2018, **165**, F357–F364.

19 Y. Yan, Q. Fang, L. Blum and W. Lehnert, *Electrochim Acta*, 2017, **258**, 1254–1261.

20 Y. Li, W. Zhang, Y. Zheng, J. Chen, B. Yu, Y. Chen and M. Liu, *Chem Soc Rev*, 2017, **46**, 6345–6378.

21 S. Kye, H. J. Kim, D. Go, B. C. Yang, J. W. Shin, S. Lee and J. An, *ACS Catal*, 2021, **11**, 3523–3529.
22 W. Kobsiriphat, B. D. Madsen, Y. Wang, M. Shah, L. D. Marks and S. A. Barnett, *J Electrochem Soc*, 2010, **157**, B279.
23 T. Takeda, R. Kanno, Y. Kawamoto, Y. Takeda and O. Yamamoto, *J Electrochem Soc*, 2000, **147**, 1730.
24 I. C. Man, H. Y. Su, F. Calle-Vallejo, H. A. Hansen, J. I. Martínez, N. G. Inoglu, J. Kitchin, T. F. Jaramillo, J. K. Nørskov and J. Rossmeisl, *ChemCatChem*, 2011, **3**, 1159–1165.
25 H. Sun and W. C. Jung, *J Mater Chem A Mater*, 2021, **9**, 15506–15521.
26 W. Winkler and P. Nehter, *SOFC in brief*, Springer, 2008.
27 G. Pudmich, B. A. Boukamp, M. Gonzalez-Cuenca, W. Jungen, W. Zipprich and F. Tietz, *Solid State Ion*, 2000, **135**, 433–438.
28 C. Sun, R. Hui and J. Roller, *Journal of Solid State Electrochemistry*, 2010, **14**, 1125–1144.
29 A. Weber and E. Ivers-Tiffée, in *Journal of Power Sources*, Elsevier, 2004, vol. 127, pp. 273–283.
30 Z. Cai, M. Kubicek, J. Fleig and B. Yildiz, *Chemistry of Materials*, 2012, **24**, 1116–1127.
31 D. A. Osinkin, D. I. Bronin, S. M. Beresnev, N. M. Bogdanovich, V. D. Zhuravlev, G. K. Vdovin and T. A. Demyanenko, *Journal of Solid State Electrochemistry*, 2014, **18**, 149–156.
32 V. Gil, C. Moure and J. Tartaj, *J Eur Ceram Soc*, 2007, **27**, 4205–4209.
33 O. Yamamoto, *Electrochim Acta*, 2000, **45**, 2423–2435.
34 H. Yahiro, Y. Eguchi, K. Eguchi and H. Arai, *J Appl Electrochem*, 1988, **18**, 527–531.
35 M. B. Mogensen, T.; Lindegaard, U. R. Hansen and G. Mogensen, *J Electrochem Soc*, 1994, **141**, 2122.
36 H. Ullmann, N. Trofimenko, F. Tietz, D. Stöver and A. Ahmad-Khanlou, *Solid State Ion*, 2000, **138**, 79–90.
37 L. W. Tai, M. M. Nasrallah, H. U. Anderson, D. M. Sparlin and S. R. Sehlin, *Solid State Ion*, 1995, **76**, 273–283.
38 R. Chiba, F. Yoshimura and Y. Sakurai, 1999, **124**, 281–288.
39 M. Nishi, T. Horita, K. Yamaji, H. Yokokawa, T. Shimonosono, H. Kishimoto, M. E. Brito, D. Cho and F. Wang, , DOI:10.1149/1.3701306.
40 J. M. Clomburg, A. M. Crumbley and R. Gonzalez, *Science*, , DOI:10.1126/SCIENCE.AAG0804.
41 L. Chen, F. Chen and C. Xia, *Energy Environ Sci*, 2014, **7**, 4018–4022.
42 K. S. Exner and H. Over, *ACS Catal*, 2019, **9**, 6755–6765.
43 A. Grimaud, F. Mauvy, J. M. Bassat, S. Fourcade, L. Rocheron, M. Marrony and J. C. Grenier, *J Electrochem Soc*, 2012, **159**, B683–B694.
44 N. M. Sammes and C. Zhihong, *Solid State Ion*, 1997, **100**, 39–44.

45 Z. Shao, W. Zhou and Z. Zhu, *Prog Mater Sci*, 2012, **57**, 804–874.
46 H.-S. Kang, S. Grewal, H. Li and M. H. Lee, *J Electrochem Soc*, 2019, **166**, F255–F263.
47 X. Wang, M. Qin, F. Fang, B. Jia, H. Wu, X. Qu and A. A. Volinsky, *J Alloys Compd*, 2017, **719**, 288–295.
48 A. S. Deepi, S. Dharani Priya, A. Samson Nesaraj and A. I. Selvakumar, *https://doi.org/10.1080/15435075.2021.2018320*, 2022, **19**, 1600–1612.
49 S. P. Jiang, *Int J Hydrogen Energy*, 2012, **37**, 449–470.
50, DOI:10.1149/1.1497982.
51 T. Z. Sholklapper, C. Lu, C. P. Jacobson, S. J. Visco and L. C. De Jonghe, , DOI:10.1149/1.2206011.
52 C. Lu, T. Z. Sholklapper, C. P. Jacobson, S. J. Visco and L. C. De Jonghe, *J Electrochem Soc*, 2006, **153**, A1115.
53 W. Li, Z. Lü, X. Zhu, B. Guan, B. Wei, C. Guan and W. Su, *Electrochim Acta*, 2011, **56**, 2230–2236.
54 J. H. Shim, G. D. Han, H. J. Choi, Y. Kim, S. Xu, J. An, Y. B. Kim, T. Graf, T. D. Schladt, T. M. Gür and F. B. Prinz, *International Journal of Precision Engineering and Manufacturing - Green Technology*, 2019, **6**, 629–646.
55 J. Hämäläinen, M. Ritala and M. Leskelä, *Chemistry of Materials*, 2013, **26**, 786–801.
56 Nishinaga, *Handbook of crystal growth*, 2014.
57 M. Gonon, *Encyclopedia of Materials: Technical Ceramics and Glasses*, 2021, **1–3**, 560–577.
58 K. Chen and S. P. Jiang, *Electrochemical Energy Reviews*, 2020, **3**, 730–765.
59 Z. Lu, S. Darvish, J. Hardy, J. Templeton, J. Stevenson and Y. Zhong, *J Electrochem Soc*, 2017, **164**, F3097–F3103.
60 K. Sasaki, K. Haga, T. Yoshizumi, D. Minematsu, E. Yuki, R. Liu, C. Uryu, T. Oshima, T. Ogura, Y. Shiratori, K. Ito, M. Koyama and K. Yokomoto, *J Power Sources*, 2011, **196**, 9130–9140.
61 Y. Cao, M. J. Gadre, A. T. Ngo, S. B. Adler and D. D. Morgan, *Nat Commun*, 2019, **10**, 1–15.
62 D. Zhang, M. L. Machala, D. Chen, Z. Guan, H. Li, S. Nemsak, E. J. Crumlin, H. Bluhm and W. C. Chueh, *Chemistry of Materials*, 2020, **32**, 2926–2934.
63 V. Sharma, M. K. Mahapatra, P. Singh and R. Ramprasad, *Journal of Materials Science 2015 50:8*, 2015, **50**, 3051–3056.
64 Z. He, L. Zhang, S. He, N. Ai, K. Chen, Y. Shao and S. P. Jiang, *J Power Sources*, 2018, **404**, 73–80.
65 A. K. Huber, M. Falk, M. Rohnke, B. Luerssen, M. Amati, L. Gregoratti, D. Hesse and J. Janek, *J Catal*, 2012, **294**, 79–88.
66 B. B. Ebbinghaus, *Combust Flame*, 1993, **93**, 119–137.
67 M. C. Tucker, H. Kurokawa, C. P. Jacobson, L. C. De Jonghe and S. J. Visco, *J Power Sources*, 2006, **160**, 130–138.

68 C. Gindorf, L. Singheiser and K. Hilpert, *Steel Research*, 2001, **72**, 528–533.
69 X. Chen, B. Hua, J. Pu, J. Li, L. Zhang and S. P. Jiang, *Int J Hydrogen Energy*, 2009, **34**, 5737–5748.
70 N. Li, A. Verma, P. Singh and J. H. Kim, *Ceram Int*, 2013, **39**, 529–538.
71 Y. Sakaki, Y. Takeda, A. Kato, N. Imanishi, O. Yamamoto, M. Hattori, M. Iio and Y. Esaki, *Solid State Ion*, 1999, **118**, 187–194.
72 S. Carter, A. Selcuk, R. J. Chater, J. Kajda, J. A. Kilner and B. C. H. Steele, *Solid State Ion*, 1992, **53–56**, 597–605.
73 E. P. Murray, T. Tsai and S. A. Barnett, *Solid State Ion*, 1998, **110**, 235–243.
74 E. Perry Murray and S. A. Barnett, *Solid State Ion*, 2001, **143**, 265–273.
75 Y. Chen, H. Teílez, # Mónica, M. Burriel, F. Yang, N. Tsvetkov, Z. Cai, D. W. Mccomb, J. A. Kilner and B. Yildiz, , DOI:10.1021/acs.chemmater.5b02292.
76 P. Decorse, G. Caboche and L. C. Dufour, *Solid State Ion*, 1999, **117**, 161–169.
77 Z. Li, M. Li and Z. Zhu, *Electrochemical Energy Reviews 2021*, 2021, **1**, 1–49.
78 D. Lee, D. Kim, S. J. Son, Y. il Kwon, Y. Lee, J. H. Ahn and J. H. Joo, *J Power Sources*, 2019, **434**, 226743.
79 R. Merkle, Y. A. Mastrikov, E. A. Kotomin, M. M. Kuklja and J. Maier, *J Electrochem Soc*, 2011, **159**, B219–B226.
80 H. Li, H.-S. Kang, S. Grewal, A. J. Nelson, S. A. Song and M. H. Lee, *J Mater Chem A Mater*, , DOI:10.1039/d0ta02915g.
81 H. Jalili, J. W. Han, Y. Kuru, Z. Cai and B. Yildiz, *Journal of Physical Chemistry Letters*, 2011, **2**, 801–807.
82 S. P. Jiang and W. Wang, *Solid State Ion*, 2005, **176**, 1351–1357.
83 X. Xu, C. Wang, M. Fronzi, X. Liu, L. Bi and X. S. Zhao, *Mater Renew Sustain Energy*, 2019, **8**, 1–8.
84 M. Sahibzada, S. J. Benson, R. A. Rudkin and J. A. Kilner, *Solid State Ion*, 1998, **113–115**, 285–290.
85 J. Chen, F. Liang, B. Chi, J. Pu, S. P. Jiang and L. Jian, *J Power Sources*, 2009, **194**, 275–280.
86 S. Wang, T. Kato, S. Nagata, T. Honda, T. Kaneko, N. Iwashita and M. Dokiya, *Solid State Ion*, 2002, **146**, 203–210.
87 K. Chen, N. Ai, L. Zhao, al -, C. Cheng Wang, D. Luo, S. Ping Jiang, J. Ju, Y. Xie and Z. Wang, *J Electrochem Soc*, 2009, **156**, B1182.
88 F. Liang, J. Chen, S. P. Jiang, B. Chi, J. Pu and L. Jian, *Electrochemical and Solid-State Letters*, 2008, **11**, B213.
89 F. Liang, J. Chen, J. Cheng, S. P. Jiang, T. He, J. Pu and J. Li, *Electrochem commun*, 2008, **10**, 42–46.
90 L. Ge, K. Sun, Y. Gu, Q. Ni and X. Huang, *Energy Convers Manag*, 2021, **249**, 114873.
91 Y. Tan, S. Gao, C. Y. Xiong and B. Chi, *Int J Hydrogen Energy*, 2020, **45**, 19823–19830.

92 X. Tong, Y. Xu, Đ. Tripković, P. V. Hendriksen, W. R. Kiebach and M. Chen, *J Mater Chem A Mater*, 2020, **8**, 9039–9048.
93 S. L. Zhang, H. Wang, M. Y. Lu, C. X. Li, C. J. Li and S. A. Barnett, *J Power Sources*, 2019, **426**, 233–241.
94 S. il Lee, J. Kim, J. W. Son, J. H. Lee, B. K. Kim, H. J. Je, H. W. Lee, H. Song and K. J. Yoon, *J Power Sources*, 2014, **250**, 15–20.
95 K. Joong Yoon, M. Biswas, H. J. Kim, M. Park, J. Hong, H. Kim, J. W. Son, J. H. Lee, B. K. Kim and H. W. Lee, *Nano Energy*, 2017, **36**, 9–20.
96 R. Wang, E. Dogdibegovic, G. Y. Lau and M. C. Tucker, *Energy Technology*, 2019, **7**, 1801154.
97 H. Fan, Y. Zhang and M. Han, *J Alloys Compd*, 2017, **723**, 620–626.
98 T. Chen, Y. Zhou, M. Liu, C. Yuan, X. Ye, Z. Zhan and S. Wang, *Electrochem commun*, 2015, **54**, 23–27.
99 Y. Gong, D. Palacio, X. Song, R. L. Patel, X. Liang, X. Zhao, J. B. Goodenough and K. Huang, *Nano Lett*, 2013, **13**, 4340–5.
100 Y. Gong, R. L. Patel, X. Liang, D. Palacio, X. Song, J. B. Goodenough and K. Huang, *Chemistry of Materials*, 2013, **25**, 4224–4231.
101 I. Chang, S. Ji, J. Park, M. H. Lee and S. W. Cha, *Adv Energy Mater*, 2015, **5**, 1402251.
102 I. Chang, D. Kim, Y. Lee, S. H. Hong and S. W. Cha, *International Journal of Precision Engineering and Manufacturing 2016 17:5*, 2016, **17**, 691–694.
103 K. C. Neoh, G. D. Han, M. Kim, J. W. Kim, H. J. Choi, S. W. Park and J. H. Shim, *Nanotechnology*, 2016, **27**, 185403.
104 Y. K. Li, H. J. Choi, H. K. Kim, N. K. Chean, M. Kim, J. Koo, H. J. Jeong, D. Y. Jang and J. H. Shim, *J Power Sources*, 2015, **295**, 175–181.
105 T. P. Holme, C. Lee and F. B. Prinz, *Solid State Ion*, 2008, **179**, 1540–1544.
106 X. Jiang, H. Huang, F. B. Prinz and S. F. Bent, *Chemistry of Materials*, 2008, **20**, 3897–3905.
107 F. Shen, M. Reisert, R. Wang, P. Singh and M. C. Tucker, *ACS Appl Energy Mater*, 2022, **5**, 9383–9391.
108 Z. Jiang, C. Xia and F. Chen, *Electrochim Acta*, 2010, **55**, 3595–3605.
109 S. P. Jiang, *Int J Hydrogen Energy*, 2012, **37**, 449–470.
110 A. Karimaghaloo, J. Koo, H.-S. Kang, S. A. Song, J. H. Shim and M. H. Lee, *International Journal of Precision Engineering and Manufacturing-Green Technology*, 2019, **6**, 611–628.
111 Y. Li, W. Zhang, Y. Zheng, J. Chen, B. Yu, Y. Chen and M. Liu, *Chem Soc Rev*, 2017, **46**, 6345–6378.
112 T. Ohzeki, T. Hashimoto, K. Shozugawa and M. Matsuo, *Solid State Ion*, 2010, **181**, 1771–1782.
113 T. Komatsu, H. Arai, R. Chiba, K. Nozawa, M. Arakawa and K. Sato, *J Electrochem Soc*, 2007, **154**, B379.
114 N. Q. Minh, *Journal of the American Ceramic Society*, 1993, **76**, 563–588.

115 H.-S. Kang, S. Grewal, H. Li and M. H. Lee, *J Electrochem Soc*, 2019, **166**, F255–F263.
116 T. A. Schmauss, J. G. Railsback, M. Y. Lu, K. Y. Zhao and S. A. Barnett, *J Mater Chem A Mater*, 2019, **7**, 27585–27593.
117 X. Wang, Y. Jin and X. Liang, *Nanotechnology*, 2017, **28**, 505709.
118 A. Gupta, T. S. Sakthivel, C. J. Neal, S. Koul, S. Singh, A. Kushima and S. Seal, *Biomater Sci*, 2019, **7**, 3051–3061.
119 J. W. Shin, S. Oh, S. Lee, J.-G. Yu, J. Park, D. Go, B. C. Yang, H. J. Kim and J. An, *ACS Appl Mater Interfaces*, 2019, **11**, 46651–46657.
120 M. Rahmanipour, Y. Cheng, T. M. Onn, A. Donazzi, J. M. Vohs and R. J. Gorte, *J Electrochem Soc*, 2017, **164**, F879–F884.
121 J. Niinistö, M. Putkonen and L. Niinistö, *Chemistry of Materials*, 2004, **16**, 2953–2958.
122 J. H. Shim, C. Chao, H. Huang, F. B. Prinz, S. U. V, R. V April, V. Re, M. Recei and V. May, *Chemistry of Materials*, 2007, **19**, 3850–3854.
123 P. De Rouffignac, J. S. Park and R. G. Gordon, *Chemistry of Materials*, 2005, **17**, 4808–4814.
124 A. Gupta, T. S. Sakthivel, C. J. Neal, S. Koul, S. Singh, A. Kushima and S. Seal, *Biomater Sci*, 2019, **7**, 3051–3061.
125 K. I. Maslakov, Y. A. Teterin, A. J. Popel, A. Yu. Teterin, K. E. Ivanov, S. N. Kalmykov, V. G. Petrov, P. K. Petrov and I. Farnan, *Appl Surf Sci*, 2018, **448**, 154–162.
126 P. A. Connor, X. Yue, C. D. Savaniu, R. Price, G. Triantafyllou, M. Cassidy, G. Kerherve, D. J. Payne, R. C. Maher, L. F. Cohen, R. I. Tomov, B. A. Glowacki, R. V. Kumar and J. T. S. Irvine, *Adv Energy Mater*, 2018, **8**, 1800120.
127 J. Y. Chen, J. Rebello, V. Vashook, D. M. Trots, S. R. Wang, T. L. Wen, J. Zosel and U. Guth, *Solid State Ion*, 2011, **192**, 424–430.
128 M. Bevilacqua, T. Montini, C. Tavagnacco, E. Fonda, P. Fornasiero and M. Graziani, *Chemistry of Materials*, 2007, **19**, 5926–5936.
129 S. P. Jiang and W. Wang, *J Electrochem Soc*, 2005, **152**, A1398.
130 Z.-K. Han, L. Zhang, M. Liu, M. V. Ganduglia-Pirovano and Y. Gao, *Front Chem*, 2019, **7**, 436.
131 S. Zhao, L. Yan, H. Luo, W. Mustain and H. Xu, *Nano Energy*, 2018, **47**, 172–198.
132 J. Paier, C. Penschke and J. Sauer, *Chem Rev*, 2013, **113**, 3949–3985.
133 R. A. Budiman, T. Miyazaki, S. Hashimoto, T. Nakamura, K. Yashiro, K. Amezawa and T. Kawada, *J Electrochem Soc*, 2015, **162**, F1445–F1450.
134 E. P. Murray, T. Tsai and S. A. Barnett, *Solid State Ion*, 1998, **110**, 235–243.
135 J. Van Herle, A. J. McEvoy and K. R. Thampi, *Electrochim Acta*, 1996, **41**, 1447–1454.
136 Y. Gong, X. Li, L. Zhang, W. Tharp, C. Qin and K. Huang, *J Electrochem Soc*, 2014, **161**, F226–F232.

137 Y. Takeda, *J Electrochem Soc*, 1987, **134**, 2656.
138 E. Perry Murray, *Solid State Ion*, 2001, **143**, 265–273.
139 S. P. Jiang and X. Chen, *Int J Hydrogen Energy*, 2014, **39**, 505–531.
140 J. T. S. Irvine, D. Neagu, M. C. Verbraeken, C. Chatzichristodoulou, C. Graves and M. B. Mogensen, *Nat Energy*, 2016, **1**, 15014.
141 B. Koo, K. Kim, J. K. Kim, H. Kwon, J. W. Han and W. Jung, *Joule*, 2018, **2**, 1476–1499.
142 R. D. Shannon, *Acta Crystallographica Section A*, 1976, **32**, 751–767.
143 B. Koo, H. Kwon, Y. Kim, H. G. Seo, J. W. Han and W. Jung, *Energy Environ Sci*, 2018, **11**, 71–77.
144 N. Tsvetkov, Q. Lu, L. Sun, E. J. Crumlin and B. Yildiz, *Nat Mater*, 2016, **15**, 1010–1016.
145 W. Lee, J. W. Han, Y. Chen, Z. Cai and B. Yildiz, *J Am Chem Soc*, 2013, **135**, 7909–7925.
146 T. T. Fister, D. D. Fong, J. A. Eastman, P. M. Baldo, M. J. Highland, P. H. Fuoss, K. R. Balasubramaniam, J. C. Meador and P. A. Salvador, *Appl Phys Lett*, 2008, **93**, 151904.
147 J. Kuyyalil, D. Newby, J. Laverock, Y. Yu, D. Cetin, S. N. Basu, K. Ludwig and K. E. Smith, *Surf Sci*, 2015, **642**, 33–38.
148 M. Choi, I. A. M. Ibrahim, K. Kim, J. Y. Koo, S. J. Kim, J.-W. Son, J. W. Han and W. Lee, *ACS Appl Mater Interfaces*, 2020, **12**, 21494–21504.
149 A. Karimaghaloo, J. Koo, H.-S. Kang, S. A. Song, J. H. Shim and M. H. Lee, *International Journal of Precision Engineering and Manufacturing-Green Technology*, 2019, **6**, 611–628.
150 S. J. Skinner and J. A. Kilner, *Materials Today*, 2003, **6**, 30–37.
151 H. Li, H.-S. Kang, S. Grewal, A. J. Nelson, S. A. Song and M. H. Lee, *J Mater Chem A Mater*, 2020, **8**, 15927–15935.
152 Z. Sha, E. Cali, G. Kerherve and S. J. Skinner, *J Mater Chem A Mater*, 2020, **8**, 21273–21288.
153 X. Li, J. Ma, L. Yang, G. He, C. Zhang, R. Zhang and H. He, *Environ Sci Technol*, 2018, **52**, 12685–12696.
154 J. Jia, P. Zhang and L. Chen, *Appl Catal B*, 2016, **189**, 210–218.
155 S. Jain, J. Shah, N. S. Negi, C. Sharma and R. K. Kotnala, *Int J Energy Res*, 2019, **43**, 4743–4755.
156 Z. Liu, A. M. Andrade, S. Grewal, A. J. Nelson, K. Thongrivong, H. Sen Kang, H. Li, Z. Nasef, G. Diaz and M. H. Lee, *Int J Hydrogen Energy*, 2021, **46**, 38258–38269.
157 E. S. Ilton, J. E. Post, P. J. Heaney, F. T. Ling and S. N. Kerisit, *Appl Surf Sci*, 2016, **366**, 475–485.
158 J. Matsuda, S. Kanae, T. Kawabata, J.-T. Chou, Y. Inoue, S. Taniguchi and K. Sasaki, *ECS Trans*, 2017, **78**, 993–1001.

159 Z. Lu, S. Darvish, J. Hardy, J. Templeton, J. Stevenson and Y. Zhong, *J Electrochem Soc*, 2017, **164**, F3097–F3103.
160 A. Tsoga, A. Gupta, A. Naoumidis and P. Nikolopoulos, *Acta Mater*, 2000, **48**, 4709–4714.
161 T. A. Schmauss, J. G. Railsback, M. Y. Lu, K. Y. Zhao and S. A. Barnett, *J Mater Chem A Mater*, 2019, **7**, 27585–27593.
162 Y. Koda, *J. CHEM. SOC., CHEM. COMMUN*.
163 K. Chen, J. Hyodo, N. Ai, T. Ishihara and S. P. Jiang, *Int J Hydrogen Energy*, 2016, **41**, 1419–1431.
164 Y. Liu, F. Zhou, X. Chen, C. Wang and S. Zhong, *J Appl Electrochem*, 2021, **51**, 425–433.
165 P. A. W. Van Der Heide, *Surface and Interface Analysis*, 2002, **33**, 414–425.
166 A. K. Opitz, C. Rameshan, M. Kubicek, G. M. Rupp, A. Nenning, T. Götsch, R. Blume, M. Hävecker, A. Knop-Gericke, G. Rupprechter, B. Klötzer and J. Fleig, *Top Catal*, 2018, **61**, 2129–2141.
167 N. Ai, S. He, N. Li, Q. Zhang, W. D. A. Rickard, K. Chen, T. Zhang and S. P. Jiang, *J Power Sources*, 2018, **384**, 125–135.
168 B. Koo, K. Kim, J. K. Kim, H. Kwon, J. W. Han and W. C. Jung, *Joule*, 2018, **2**, 1476–1499.
169 P. Caliandro, A. Nakajo, S. Diethelm and J. Van herle, *J Power Sources*, 2019, **436**, 226838.
170 H. Li, H. Sen Kang, S. Grewal, A. J. Nelson, S. A. Song and M. H. Lee, *J Mater Chem A Mater*, 2020, **8**, 15927–15935.
171 Scanning Electron Microscope (SEM)- Definition, Principle, Parts, Images - Microbe Notes, https://microbenotes.com/scanning-electron-microscope-sem/, (accessed 20 March 2023).
172 Transmission Electron Microscope (TEM)- Definition, Principle, Images, https://microbenotes.com/transmission-electron-microscope-tem/, (accessed 22 March 2023).